Copyright is owned by the Author of the thesis. Permission is given for a copy to be downloaded by an individual for the purpose of research and private study only. The thesis may not be reproduced elsewhere without the permission of the Author.

SOME STUDIES ON DIFFUSION IN MACROMOLECULAR SOLUTIONS

A thesis presented in partial fulfilment
of the requirements for the degree of
Doctor of Philosophy at Massey University

CRAIG MALCOLM TROTTER

1980

ABSTRACT

The construction and performance of a Pulsed Field Gradient system for use with a commercial, high-resolution, Fourier-Transform NMR spectrometer is described. The self-diffusion coefficient of benzene as measured by the calibrated system is in agreement with the current literature value, within the overall experimental error of the system (±2%). The use of an external lock in conjunction with signal averaging facilitates the measurement of self-diffusion coefficients for solution components in small concentrations. During signal accumulations, the system exhibits freedom from the spin-echo phase and envelope instabilities mentioned as sources of error even in recent publications dealing with the Pulsed Field Gradient technique (e.g. von Meerwall et al., 1979). The ability of the system to investigate dilute solutions is demonstrated by measurements made on 0.5% (w/v) solutions of polystyrene in carbon tetrachloride. Homogeneity coils included in the NMR probe have allowed the self-diffusion coefficients of some single components in multi-component systems to be investigated, and results for the binary system butanol-benzene are presented.

Polymer self-diffusion coefficients have been obtained for 110,000 molecular weight random-coil polystyrene in the solvents carbon tetrachloride, deuterated-chloroform and deuterated-toluene. The Pulsed Field Gradient NMR method was used for the measurements, and the polystyrene concentrations ranged from 0.5% (w/v) to 25% (w/v). For each solvent a concentration regime is found in which the de Gennes' polymer self-diffusion scaling law is obeyed; and the upper concentration limit at which this scaling law breaks down is defined. The self-diffusion coefficient of polystyrene in the solvent deutero-benzene has also been determined, and is shown to agree with Forced Rayleigh Scattering self-diffusion results for similar molecular weight polystyrenes in normal benzene. In contrast, values of the self-diffusion coefficient obtained for polystyrene random-coils by calculation from sedimentation data are shown to differ significantly from those directly determined. The mutual diffusion coefficients of the polystyrene solutions have been obtained from Quasi-Elastic Laser Light-Scattering experiments. These mutual diffusion coefficients do not approach the directly measured self-diffusion coefficients even at concentrations where the random-coils are on average well separated. It is proposed that migrating polymers must suffer transient entanglement effects over the experimental time scales

employed in the diffusion measurements.

Quasi-Elastic Laser Light-Scattering has also been used to measure the diffusion coefficient of polystyrene latex spheres in 0.01M and 0.001M sodium chloride. Experiments were conducted over the latex sphere concentration range 0.004% (w/v) to 4.46% (w/v), and several measurements were also made for low concentrations of latex spheres in triply distilled water. The diffusion coefficient was found to be ionic strength dependent over the entire concentration range studied. Solutions of polystyrene spheres at moderate concentrations exhibit the phenomenon of multiple scattering. The available literature on multiple scattering is reviewed and criteria adopted for the reliable interpretation of data collected during experiments on these solutions. The diffusion coefficients so obtained show substantial agreement with the mutual-diffusion coefficient results of Anderson et al., obtained by a capillary penetration technique. The conclusion reached in this section of the work is that Quasi-Elastic Laser Light-Scattering is able to provide a measure of the mutual diffusion coefficient in the presence of interactions between charged macromolecules. This conclusion is seen to be in accord with earlier laser light-scattering studies on solutions of the protein Bovine Serum Albumin, provided that a reassessment of available mutual diffusion data on these systems is undertaken.

ACKNOWLEDGEMENTS

I wish to express my sincere appreciation for the guidance and careful instruction given by my Chief Supervisor, Dr D.N. Pinder, during the course of this research project. It is also a pleasure to thank Dr P.T. Callaghan, not only for his invaluable advice during the joint supervision of this work, but also for constructing part of the Pulsed Field Gradient apparatus.

I am indebted to many members of the Science Faculty for helpful discussions, and I would particularly like to thank Mr R.C. O'Driscoll for advice concerning the electronic projects undertaken. The financial support of Massey University during the course of this thesis is also appreciated.

I am grateful to Mr N. Foote of the Mechanical Workshop for his cheerful co-operation in performing many tasks requiring his considerable technical expertise. The assistance of Mr R. Parsons and the Electronic Workshop staff is also appreciated.

The typists, Mesdames Maryanne Nation and Wendy Sigvertson are thanked for their patience and assistance. Particular thanks are due to Maryanne Nation for concluding the typing of this thesis.

TABLE OF CONTENTS

	PAGE
ABSTRACT	ii
ACKNOWLEDGEMENTS	iv
TABLE OF CONTENTS	v
LIST OF FIGURES	ix
LIST OF TABLES	xii
LIST OF PLATES	xiii
LIST OF SYMBOLS	xiv
CHAPTER 1 - INTRODUCTION	1
1.1. RESEARCH GOALS	1
1.2. DIFFUSION IN MACROMOLECULAR SOLUTIONS	3
1.2.a. Definition of Diffusion Coefficients	3
1.2.b. The Direct Measurement of Macromolecular Diffusion Coefficients	5
1.2.c. Diffusion Coefficient Measurement in This Thesis	7
CHAPTER 2 - THE LASER LIGHT-SCATTERING EXPERIMENT	12
2.1. HISTORICAL SKETCH AND INTRODUCTION	12
2.2. THEORY REVIEW	15
2.2.a. The Laser Light-Scattering Experiment	15
2.2.b. The Homodyne Intensity Autocorrelation Function for a Very Dilute, Monodisperse Solution of Small Macromolecules	17
2.2.c. The Photocount Analysis Method	19
2.2.d. The Method of Cumulants: Application to Data Obtained from Concentrated Solutions of Macromolecules	23
2.2.e. Implications of the Angular Dependence of the Intensity Autocorrelation Function Decay Rate	26
2.3. INSTRUMENTATION	29
2.3.a. A Digital Correlator with Blinker Facility	29
2.3.b. Considerations for Photomultipliers as Photodetectors	32
2.3.c. The Laser Spectrometer	33

PAGE

CHAPTER 3 - THE PULSED FIELD GRADIENT EXPERIMENT

3.1. INTRODUCTION: THE NUCLEAR MAGNETIC RESONANCE EXPERIMENT 39
3.1.a. Nuclear Magnetic Resonance 39
3.1.b. The Formation of Spin-Echoes 43
3.2. DIFFUSION COEFFICIENT MEASUREMENT BY NUCLEAR MAGNETIC RESONANCE 45
3.2.a. The Attenuation of Spin-Echoes Due to Diffusion 45
3.2.b. The Pulsed Field Gradient Nuclear Magnetic Resonance Experiment 46

CHAPTER 4 - INSTRUMENTATION FOR A PULSED FIELD GRADIENT EXPERIMENT 51
4.1. INTRODUCTION 51
4.2. DESIGN AND CONSTRUCTION OF INSTRUMENTATION 54
4.2.a. Probe and Gradient Coil Design 54
4.2.b. A Digital Pulse Programmer for Pulsed Field Gradient Experiments 62
4.2.c. A Power Supply for Pulsed Field Gradient Generation 65
4.2.d. The NMR Spectrometer 71
4.3. EXPERIMENTAL CONSIDERATIONS 75
4.3.a. Sample Related Considerations 75
4.3.b. Signal Related Considerations 75
4.3.c. Restrictions on Gradient Pulse Parameters 76
4.3.d. Accumulation and Pulse Repetition Time Effects 80
4.4. MAGNETIC FIELD GRADIENT CALIBRATION 82
4.4.a. Field Gradient and RF Pulse Profiles 82
4.4.b. Calibration and Reproducibility of the Field Gradient 84
4.4.c. Concluding Remarks 88

CHAPTER 5 - THE STUDY OF DIFFUSION IN RANDOM-COIL POLYSTYRENE SOLUTIONS: EXPERIMENTAL DETAILS 93
5.1. INTRODUCTION 93
5.2. THE PULSED FIELD GRADIENT NUCLEAR MAGNETIC RESONANCE EXPERIMENTS 94
5.2.a. Preparation of Samples for the PFGNMR Study 94
5.2.b. Analysis of PFGNMR Data 94

PAGE

5.2.c. The Polystyrene Self-Diffusion Coefficients 95
5.2.d. Self-Diffusion of Chloroform in Polystyrene 98
5.3. THE QUASI-ELASTIC LASER LIGHT-SCATTERING EXPERIMENTS 103
5.3.a. Application of the Blinker to Concentrated Polymer Solutions 103
5.3.b. Preparation of Samples for the QELS Study 104
5.3.c. Spectrometer Related Considerations 106
5.3.d. Spurious Contributions to the Intensity Autocorrelation Function 107
5.3.e. Analysis of QELS Data 108
5.3.f. The Polystyrene Solution Mutual Diffusion Coefficients 114

CHAPTER 6 - DIFFUSION IN RANDOM-COIL POLYSTYRENE SOLUTIONS: DISCUSSION OF RESULTS 118
6.1. INTRODUCTION 118
6.2. THE dE GENNES' SCALING LAW FOR POLYMER SELF-DIFFUSION 119
6.3. DIFFUSION IN RANDOM-COIL POLYSTYRENE SOLUTIONS: DISCUSSION OF RESULTS 122
6.3.a. Experimental Results and the de Gennes' Scaling Law 122
6.3.b. Direct and Indirect Measurements of Polystyrene Self-Diffusion Coefficients 124
6.3.c. A Comparison of Macroscopic and QELS Determinations of the Mutual Diffusion Coefficient 126
6.3.d. A Comparison of Self and Mutual Diffusion Coefficients in Polymer Solutions 128

CHAPTER 7 - POLYSTYRENE LATEX SPHERE DIFFUSION: A LASER LIGHT-SCATTERING STUDY 135
7.1. INTRODUCTION 135
7.2. THE EFFECT OF MULTIPLE SCATTERING 137
7.3. THE EXPERIMENTAL STUDY 139
7.3.a. Sample Preparation 139
7.3.b. Use of the Blinker 140
7.3.c. Data Analysis 141
7.3.d. The Concentrated Solution Results 147
7.3.e. The Very Dilute Solution Results 151

PAGE

7.4. COMPARISON OF RESULTS 158

7.4.a. Theories of Macro-ion Transport in the Presence of a Concentration Gradient 158

7.4.b. Application of Macro-ion Transport Theories to Latex Sphere Solutions 161

7.4.c. Interpretation of Data Obtained at High Ionic Strength 163

7.4.d. Interpretation of Data Obtained at Low Ionic Strength 165

7.4.e. Comparison with Other Work 167

CHAPTER 8 - CONCLUSIONS 169

8.1.a. Concluding Remarks 169

8.1.b. Towards an Improved PFGNMR Experiment 172

APPENDICES

Appendix 1 - The Magnetic Field Due to an Opposed Helmholtz Pair in the Presence of Magnet Pole-pices 176

Appendix 2 - The Digital Pulse Programmer 179

Appendix 3 - Auxilary Tables 181

Appendix 4 - Auxilary Figures 189

Appendix 5 - A 20MHz Digital-Analogue Ratemeter 192

Appendix 6 - A Pulsed Magnetic Field Gradient Sequence for Eddy Current Minimisation 195

Appendix 7 - Published Work 199

BIBLIOGRAPHY 220

LIST OF FIGURES

		PAGE
Figure 1.1.	A comparison of QELS and diffusion cell measurements.	9
Figure 2.1.	A schematic representation of the laser light scattering experiment.	16
Figure 2.2.	The relationship between the full and clipped photocount.	22
Figure 2.3	A schematic circuit diagram of the digital autocorrelator	30
Figure 2.4	A schematic diagram of the laser spectrometer	34
Figure 2.5.	The photomultiplier tube and housing.	36
Figure 3.1.	The spin-echo experiment.	41
Figure 3.2.	The pulsed magnetic field gradient experiment.	47
Figure 4.1.	The NMR probe circuitry.	56
Figure 4.2.	The coil shape for the generation of uniform magnetic field gradients.	59
Figure 4.3.	The sample space geometry, and sample holder.	60
Figures 4.4.	The TTL pulse timer schematic circuit diagram.	63,64
Figure 4.5.	A schematic circuit diagram of the Kepco power supply.	67
Figure 4.6.	Programming the output current of the Kepco power supply by stepping the reference voltage.	68
Figures 4.7.	The circuitry used in this work for the generation of magnetic field gradient pulses.	70
Figure 4.8.	A block diagram of the JEOL JNM-FX 60 NMR spectrometer.	72
Figure 4.9.	Investigation of the effect of eddy currents on the PFGNMR experiment.	78
Figure 4.10.	Magnetic field gradient and rf field magnitude-profiles along the sample y-axis.	83
Figure 4.11.	The magnetic field gradient calibration experiment: the spin-echo attenuation plot for water.	85
Figure 4.12.	The spin-echo attenuation plot for Analar benzene.	87
Figure 4.13.	The spin-echo attenuation plot for Analar glycerol.	89

		PAGE
Figure 4.14.	The ^1H frequency domain NMR spectrum of an equi-molar mixture of benzene and butanol.	91
Figure 4.15.	Spin-echo attenuation data for pure benzene, pure butanol and an equi-molar mixture.	92
Figure 5.1.	The ^1H frequency domain NMR spectrum of 0.75gm% polystyrene in D-toluene.	96
Figure 5.2.	The spin-echo attenuation plot for 1.5gm%, 110,000M_w polystyrene in D-toluene.	97
Figure 5.3.	The self-diffusion coefficients of 110,000M_w polystyrene, as a function of concentration, in the solvents CCl_4, $CDCl_3$ and D-toluene.	99
Figure 5.4.	The spin-echo attenuation plot for "doped" water.	100
Figure 5.5.	The self-diffusion coefficients of chloroform in polystyrene solutions.	102
Figure 5.6.	The diffusion coefficients of 390,000M_w polystyrene in butanone, measured by QELS in the very dilute concentration regime.	109
Figure 5.7.	The signal-to-noise ratio obtainable in QELS experiments at the lowest polystyrene concentration studied.	111
Figure 5.8.	Plots showing the multi-exponential nature of the IAFs encountered in the study of the sample 2.0gm% 110,000M_w polystyrene in CCl_4.	113
Figure 5.9.	Cumulant plots for the sample 2.0gm% polystyrene in CCl_4.	115
Figure 5.10.	Mutual diffusion coefficients obtained by QELS for solutions of 110,000M_w polystyrene in the solvents $CDCl_3$ and CCl_4.	116
Figure 6.1.	Entanglement phenomena in the polymer gel regime: the de Gennes' model.	120
Figure 6.2.	The self-diffusion coefficients of 110,000M_w polystyrene in various solvents, normalised to solvent viscosity.	123
Figure 6.3.	A comparison of directly and indirectly measured self-diffusion coefficients of random-coil polystyrene.	125

PAGE

Figure 6.4. A comparison of D_0 values obtained by wedge interferometry with results from QELS studies. 127

Figure 6.5. A comparison of mutual- and self-diffusion coefficients for 110,000M_w polystyrene in CCl_4. 129

Figure 6.6. A comparison of mutual- and self-diffusion coefficients for 110,000M_w polystyrene in $CDCl_3$. 130

Figure 6.7. A comparison of mutual- and self-diffusion coefficients for 110,000M_w polystyrene in the solvents toluene and D-toluene. 131

Figure 7.1. Plots showing the presence of both long and short decays in the NIAFs obtained from a QELS study of a concentrated solution of polystyrene latex spheres. 142

Figure 7.2. A plot showing the linear dependence of the long-time decay rate on $\sin^2(\theta/2)$, for a concentrated solution of polystyrene latex spheres. 145

Figure 7.3. The concentration dependence of the quantity with the dimensions of a diffusion coefficient which was obtained from QELS studies of concentrated polystyrene latex sphere solutions. 148

Figure 7.4. Plots showing the linear dependence of the long-time decay rate on $\sin^2(\theta/2)$, for representative samples. 149

Figure 7.5. As for Figure 7.4.

Figure 7.6. The very dilute regime latex sphere diffusion coefficients. 152

Figure 7.7. The diameter distribution of the nominally 0.085μm diameter latex spheres as determined by transmission electron microscopy. 156

Figure 7.8. A comparison of QELS measurements from the concentrated latex sphere solution study with D_M values obtained by the technique of capillary penetration. 166

Figure 8.1. A ramped-pulse, field gradient pulse sequence for eddy-current minimisation. 174

LIST OF TABLES

		PAGE
Table 2.1.	Specifications of the laser light-scattering spectrometer.	35
Table 4.1.	The effect of eddy currents on the measured diffusion coefficient.	79
Table 4.2.	Checks for the consistency of the attenuation ratio under various rf and magnetic field gradient pulse conditions.	81
Table 4.3.	Gradient coil calibration experimental data.	86
Table 5.1.	Details of the data analysis from the samples 0.26gm% and 2.0gm% polystyrene in CCl_4.	112
Table 6.1.	A comparison of intermolecular spacings, radii of gyration, and experimental molecular displacements encountered at two different concentrations in 110,000M_w polystyrene solutions.	133
Table 7.1.	Examples of correlator off-to-on times encountered in a study of concentrated latex sphere solutions.	143
Table 7.2.	Details of the data analysis for the sample 2.15gm% polystyrene latex spheres in 0.001M sodium chloride.	146
Table 7.3.	Diffusion coefficients determined by QELS in the very dilute latex sphere concentration regime.	154
Table 7.4.	Theoretical and experimental values of k.	164

LIST OF PLATES

PAGE

Plate 1 - The low resolution NMR probe used in this work. 61

Plate 2 - The JEOL JNM-FX60 spectrometer, and instrumentation for the PFGNMR experiment. 73

LIST OF SYMBOLS

D_S	-	macromolecular self-diffusion coefficient.
D_{Solv}	-	solvent self-diffusion coefficient.
D_M	-	macromolecular solution mutual-diffusion coefficient.
$\overline{r^2}$	-	mean-squared displacement.
J	-	the flow of solute molecules, per unit time, across a unit area perpendicular to that flow.
c	-	macromolecular concentration.
D_0	-	infinite dilution macromolecular diffusion coefficient.
k_B	-	Boltzmann constant (1.38×10^{-23} joule.deg^{-1}).
T	-	absolute temperature, or correlator sample time.
f_0	-	frictional coefficient per macromolecule at infinite solute dilution.
R	-	non-hydrated hard sphere radius.
π	-	the constant 3.14159.
η_0	-	the solvent viscosity.
M_w, M_n	-	the weight and number average molecular weights.
R_H	-	the hydrodynamic sphere radius.
D_S^+	-	indirectly determined self-diffusion coefficient.
$\bar{v}$	-	solute partial specific volume.
s	-	sedimentation coefficient.
ρ	-	solution density.
θ	-	the scattering angle (except in Chapter 3 where θ is the magnetisation rotation angle).
$\underset{\sim}{q}$	-	the scattering vector.
$\underset{\sim}{k}_i, \underset{\sim}{k}_s$	-	initial and scattered wave vectors.
q	-	magnitude of the scattering vector.
λ_0	-	vacuum wavelength of the incident laser radiation.
$\hbar$	-	Planck's constant (6.6256×10^{-34} joule.deg^{-1}) divided by 2π.
$E_S(0)$	-	magnitude of the total scattered electric field at the photodetector at time t′.
$E_S(t)$	-	E_S at the later time t′+t.
I(0)	-	the scattered intensity, defined similarly to $E_S(0)$.
I(t)	-	the scattered intensity, defined similarly to $E_S(t)$.
*	-	indicates that the complex conjugate has been taken (Chapter 2 only).

$g^{(2)}(t)$ - the normalised intensity autocorrelation function (second order electric field autocorrelation function).

$g^{(1)}(t)$ - the normalised first order electric field autocorrelation function.

ω_0 - incident electric field angular frequency.

$I(t,T)$ - the average intensity during the short time interval T which is centred on the time $t'+t$.

$n(t,T)$ - number of photodetections during T.

$C_p(t,T)$ - the un-normalised, full photocount autocorrelation function.

$\eta_k(T)$ - the clipped count.

k - clipping level.

$C_k(t), C_k(mT)$ - single-clipped, un-normalised photocount autocorrelation function.

$g_k^{(2)}(t,T)$ - normalised, single-clipped photocount autocorrelation function.

Γ - the decay rate of a photocount autocorrelation function.

$\bar{\Gamma}$ - average decay rate of a photocount autocorrelation function.

$G(\Gamma)$ - normalised distribution of the decay rates.

$\mu_r/\bar{\Gamma}^r$ - rth normalised moment of $G(\Gamma)$.

D_{ML} - the quantity extracted by a cumulants analysis of QELS data obtained from concentrated, non-random-coil, macromolecular solutions.

Q' - the variance of the decay rate distribution.

$G_k^{(2)}(\infty)$ - the calculated baseline: the value of the normalised, single-clipped autocorrelation function at infinite time.

A_{coh} - the detector coherence area.

Ω - the solid angle subtended by the source, at the detector (Chapter 2 only; otherwise an Ohm symbol).

I - nuclear spin quantum number (Chapter 3 only; otherwise symbolises current).

B_0 - magnitude of the steady magnetic field.

γ - nuclear gyromagnetic ratio.

$\underset{\sim}{i},\underset{\sim}{j},\underset{\sim}{k}$ - laboratory frame unit vectors

$\underset{\sim}{i}',\underset{\sim}{j}',\underset{\sim}{k}'$ - rotating frame unit vectors.

μ - magnitude of the nuclear magnetic moment (Chapter 3 only; otherwise the multiplier "micro" i.e. $x10^{-6}$).

M	-	the magnitude of the macroscopic magnetisation.
ω_L	-	Larmor frequency.
B_1	-	the magnitude of a magnetic field applied along the x´-axis.
t_p	-	the time for which $\underset{\sim}{B}_1$ is applied.
τ	-	the 90^o-180^o rf pulse spacing.
G	-	the magnitude of the magnetic field gradient.
$A(0)$	-	the magnitude of the spin-echo at $t=2\tau$ in the absence of an applied magnetic field gradient.
$A(G)$	-	the magnitude of the spin-echo when the field gradient is applied.
T	-	the time for which a nucleus remains at a position z.
ζ	-	the rms jump displacement of a nucleus.
Δ	-	the magnetic field gradient pulse separation.
δ	-	the magnetic field gradient pulse width.
d	-	the separation between the 90^o rf pulse and the first gradient pulse.
$P(\phi_D)$	-	the probability of obtaining a phase difference ϕ_D.
Q_T	-	quality factor of the transmitter circuit.
L_1, L_2, L_3	-	inductances in the NMR probe circuitry.
R_{in}, R_1, R_2, R_3	-	resistances in the NMR probe circuitry.
C_1, C_2, C_3	-	capacitances in the NMR probe circuitry.
D_1-D_4	-	diodes in the NMR probe circuitry.
$2l$	-	separation of the magnet pole-pieces.
Q_A, Q_B	-	sets of Darlington connected transistors.
R_S	-	the Kepco sensing resistor.
R_{CC}	-	Kepco current control potentiometer.
g_0	-	residual field gradients due to inhomogeneities in the steady field $\underset{\sim}{B}_0$.
g_e	-	the eddy current induced gradient.
$\Delta\nu$	-	the off-resonant frequency.
Aco	-	the ratio of the correlator off-to-on times.
S_M	-	the slope of a ln(NIAF-1) vs. time plot; or the initial slope of such a plot if the plot is multi-exponential.
R_F	-	the radius of random-coils in the very dilute regime.
ℓ	-	the Kuhn statistical segment length.
M	-	the polymer molecular weight.
m	-	molecular weight of ℓ.
ν	-	Flory number (except in Chapter 3 where $\Delta\nu$ denotes the off-resonant frequency).

c^* - the polymer concentration such that the average distance between two neighbouring coil centres is equal to $2R_F$.

ξ - the average distance between polymer entanglements in the gel regime.

T_r - the chain disentanglement time.

S_L - the long time decay rate.

D_L - the quantity with the dimensions of a diffusion coefficient, calculated from the long-time part of a ln(NIAF-1) vs. time plot.

R_S - the calculated mean latex sphere separation.

σ - latex sphere surface charge density.

ε - permittivity of the latex sphere.

a - latex sphere radius.

B_M - latex sphere bulk modulus.

ε_0 - the permittivity of free space.

k - defined through the equation

$$D_M = D_0(1 + k.c + \text{---})$$

E(r) - the pair potential energy for two charged particles separated by a centre-to-centre distance r.

ψ_0 - the surface potential of a charged sphere.

R - the normalised intersphere separation (Chapter 7 only).

κ^{-1} - the Debye-Hückel shielding length.

e - electronic charge (1.602×10^{-19}C).

f,Ξ - parameters used to evaluate equation 7.6.

$(\frac{\partial \pi}{\partial c})_{p,T}$ - isothermal osmotic compressibility.

Φ - volume fraction.

β - the rise-time of a ramped magnetic field gradient pulse.

CHAPTER 1

INTRODUCTION

1.1 RESEARCH GOALS

The first objective of this study was to develop a pulsed field gradient facility for the measurement of liquid-component diffusion coefficients by the technique of Pulsed Field Gradient Nuclear Magnetic Resonance (PFGNMR). The pulsed field gradient apparatus was designed to be interfaced to an existing, commercial Nuclear Magnetic Resonance (NMR) spectrometer. It has been previously held (Tanner[1], 1966; von Meerwall et al.[2], 1979) that the PFGNMR technique gives rise to systematic errors in the self-diffusion coefficient of about 10%. Prudent design of the PFGNMR instrumentation developed in this work has reduced this error to 1%.

The second intention of this thesis was to study diffusion in some well-defined macromolecular solutions and to compare macromolecular diffusion coefficients measured by different techniques. Specifically, measurements were to be made by the techniques of both PFGNMR and Quasi-Elastic Laser Light Scattering (QELS), and the following comparisons undertaken. QELS diffusion measurements made on concentrated solutions of polystyrene latex spheres were compared with capillary penetration, mutual diffusion coefficients obtained from similar solutions: this comparison indicates that QELS measures the mutual diffusion coefficient of a concentrated, solution of charged macromolecules. For random-coil polymer solutions, self-diffusion coefficients measured by PFGNMR were compared with those calculated from sedimentation coefficients: marked disagreement was found in this comparison, with a positive indication that it is the sedimentation-derived diffusion coefficient which is in error. A comparison of mutual (by QELS) and self (by PFGNMR) diffusion coefficients obtained from the same random-coil polymer solution indicates that polymer entanglement phenomena play an important role in polymer diffusive motion even at high polymer dilutions. Finally, PFGNMR measurements made on concentrated random-coil polymer solutions were compared with the theory of de Gennes'[3] for self-diffusion in

polymer gels: considerable agreement between measurement and theory is evident.

1.2 DIFFUSION IN MACROMOLECULAR SOLUTIONS

1.2.a Definition of Diffusion Coefficients

Of interest to this thesis are three diffusion coefficients related to diffusive motions in solutions containing a single macromolecular solute and a single solvent species. These are the macromolecular self-diffusion coefficient D_S, the solvent self-diffusion coefficient D_{Solv} and the macromolecular solution mutual-diffusion coefficient D_M. These diffusion coefficients are now defined.

According to the theory of Brownian motion, the mean-square-displacement, $\overline{r^2}$, of the centre-of-mass of a freely diffusing macromolecule during the time t is given by [4]

$$\overline{r^2} = 6D_S t \qquad 1.1$$

Thus, D_S gives a direct measure of the laboratory frame translational motion of the macromolecule. The self-diffusion coefficient of the solvent is also defined by equation 1.1 if $\overline{r^2}$ is taken to be the mean-squared-displacement of the solvent molecules during the time t.

Concentration gradients in the macromolecular solution give rise to flows of matter which tend to relax those gradients. These randomly distributed flows are the process of mutual diffusion. For a one-dimensional concentration gradient along the x-axis the flow of solute molecules, J, per unit time across a unit area perpendicular to the x-axis is given by Fick's equation [4]

$$J = -D_M \frac{\partial c}{\partial x} \qquad 1.2$$

where c is the solute concentration and the negative sign indicates that matter flows in the direction of decreasing concentration. The mutual diffusion coefficient D_M thus characterises the relaxation of concentration gradients in the macromolecular solution.

When the macromolecular concentration becomes so small that solute-

solute interactions cease to make a significant contribution to macromolecular diffusive motion, D_S and D_M become indistinguishable and are both denoted by D_0, the infinite dilution macromolecular translational diffusion coefficient. Einstein has shown that [4]

$$D_0 = k_B T/f_0 \qquad 1.3$$

where k_B is Boltzmann's constant, T the absolute temperature and f_0 is the frictional coefficient per macromolecule at infinite solute dilution. For non-hydrated hard spheres of radius R, f_0 is accurately represented by[4]

$$f_0 = 6\pi\eta_0 R \qquad 1.4$$

where η_0 is the solvent viscosity. Equation 1.4 is known as Stokes' law. A measurement of D_0, together with equations 1.3 and 1.4, can be used to define the apparent hydrodynamic radius, R_H, of a solvated macromolecule through the equation[4]

$$D_0 = k_B T/(6\pi\eta_0 R_H) \qquad 1.5$$

Equation 1.5 is known as the Stokes-Einstein equation.

For the purposes of this thesis, two macromolecular concentration regimes are defined. The very dilute regime should be taken to mean those macromolecular concentrations at which solute-solute interactions do not make a significant contribution to macromolecular diffusive motion. The concentrated regime consists of those macromolecular concentrations other than very dilute. D_0 is measured only in the very dilute regime, whereas macromolecular diffusion in the concentrated regime is characterised by D_S and D_M.

D_S is a parameter of fundamental importance in directly describing macromolecular dynamics and a knowledge of D_S enables important tests of theoretical models concerning macromolecular solutions. However, due to experimental difficulties, very few direct measurements of D_S have been reported in the literature. The more accessible quantities D_M and D_0 (D_0 by extrapolation of D_M to c = 0) have been obtained for many macromolecular solutions by observing the relaxation of

one-dimensional concentration gradients[4]. Although D_M is a function of macromolecular motion, solution thermodynamic parameters also make an important contribution to D_M. Thus, macromolecular dynamics are only observed indirectly in measurements of D_M.

When D_M and appropriate thermodynamic data are available for a macromolecular solution, D_S can be obtained from the equation[5]

$$D_S^+ = D_M[(1 - \bar{v}c)(1 + 2A_2c + 3A_3c^2 + ...)]^{-1} \qquad 1.6$$

where $\bar{v}$ is the solute partial specific volume and A_n are virial coefficients, obtained from osmotic pressure measurements. The symbol D_S^+ is used here to represent the self-diffusion coefficient obtained in this indirect manner (in order to distinguish it from the directly determined D_S).

Another indirect determination of the self-diffusion coefficient involves the sedimentation coefficient, s, obtained from ultracentrifugation studies. In this instance the calculated self-diffusion coefficient is given by[5]

$$D_S^+ = sk_BT/(1 - \bar{v}\rho) \qquad 1.7$$

where ρ is the solution density. This equation is derived under the assumption that the macromolecular frictional coefficients in sedimentation and diffusion are identical[5].

1.2.b The Direct Measurement of Macromolecular Diffusion Coefficients.

There are various methods available for the direct measurement of the diffusion coefficients D_S, D_M and D_0. The particular measurement techniques referred to in disussions in this thesis are now briefly reviewed.

D_S characterises the random motions of an (average) individual macromolecule in an isotropic solution. To follow such individual motions it is necessary to label the macromolecules in some manner.

The long-established radio-tracer technique employs the label of radioactivity provided by tritiating some of the macromolecular sample. Countervailing gradients of labelled and unlabelled macromolecules are established such that the total concentration of macromolecules is everywhere the same. The relaxation of the labelled gradient is then monitored to provide a measure of D_S. The principle disadvantage of the radiotracer method is that macroscopic displacement of the macromolecules is necessary to measure D_S, with such displacements taking several days[4].

In 1965 Stejskal and Tanner developed the PFGNMR technique[6], which can be used to measure the D_S of random-coil macromolecules. PFGNMR employs the intrinsic molecular label provided by the characteristic Larmor frequencies of the macromolecular ^1H nuclei. This label is given a spatial dependence by applying a magnetic field gradient in the form of two pulses, with molecular displacement during the inter-pulse period being detected. An average macromolecular displacement of a few hundred nanometres can be detected by the PFGNMR method, enabling relatively rapid measurements of D_S.

Recently, Hervet et al.[7] have reported a new technique for D_S measurement. They call their approach Forced Rayleigh Scattering (FRS) and labelling is achieved by exciting, with spatial periodicity, a photochromic dye attached to a small proportion of the macromolecules. The intensity of laser light scattered by the macromolecular solution varies according to the relaxation of this spatially periodic excitation, which is in turn governed by the self-diffusion coefficient of the labelled macromolecules. Average macromolecular displacements of a few hundred nanometres can be detected by FRS allowing D_S to be rapidly measured to a reported accuracy of about 10%[7].

The mutual diffusion coefficient D_M characterises the relaxation of concentration gradients in the macromolecular solution. Direct measurement of D_M involves setting up a one-dimensional concentration gradient on a macroscopic scale, and monitoring the relaxation of the gradient as a function of time. Three methods of D_M measurement of interest to this work are the diffusion cell technique, where two stirred solutions of initially differing macromolecular concentration are separated by a rigid permeable membrane; the capillary penetration

technique, where a capillary containing a macromolecular solution is immersed in a solution of differing concentration; and interferometric techniques, which follow the relaxation of concentration gradients by monitoring changes in solution refractive index. The above methods of D_M measurement require macroscopic displacement of the solute, giving rise to rather long experimental times.

Values for the diffusion coefficient D_0 have long been reported in the literature[4]. D_0 was usually obtained by extrapolation of D_M measurements to zero macromolecular concentration. In 1964, Cummins et al.[8] first used QELS to measure D_0. The QELS experiment involves illuminating a macromolecular solution with a laser beam, and light scattered (largely) by dielectric discontinuities at solvent/macromolecular interfaces is then collected by a photodetector. The total scattered intensity at the photodetector fluctuates on a timescale determined by the diffusive displacements of the macromolecules, and characterisation of the intensity fluctuation timescale is sufficient to determine D_0[8]. QELS is sensitive to macromolecular displacements of several hundred nanometres, and experimental times of one minute can be sufficient to determine D_0 to $\pm 1\%$ in some instances.

In the work which follows the term "macroscopic D_M (or D_S, D_0) measurement" should be taken to mean that the diffusion coefficient was measured by a technique requiring macroscopic solute displacement.

1.2.c Diffusion Coefficient Measurement in This Thesis.

The techniques of PFGNMR and QELS were chosen for diffusion coefficient measurement in this thesis. The reasons for this choice were two-fold. First, the QELS facility was already in existence in the Chemistry, Biochemistry and Biophysics department at Massey University, and a commerical NMR spectrometer was also available to serve as the basis for development of the PFGNMR experiment. Second, both the PFGNMR and QELS techniques exhibit various deficiencies which merit further investigation. An outline of these deficiencies is now given, and their relevance to the research goals of this thesis explained.

The QELS technique only provides a well-defined macromolecular diffusion coefficient measurement in the very dilute macromolecular concentration regime, where D_0 is measured. Sample polydispersity and molecular anisotropy can be accounted for in the analysis of QELS data and the technique is equally applicable to either random-coil or globular-macromolecular solutions. The intensity of the light scattered by a solution varies as r^6, where r is the radius of the scattering particles. In the case of a solution containing relatively massive macromolecules, the scattered light can be considered as arising from the macromolecular component alone.

In the concentrated macromolecular solution regime, where solute-solute interactions become important, it is no longer possible to rigorously relate the experimental quantity obtained from an analysis of QELS data to a well-defined property of the diffusing system. However, the experimental quantity has the dimensions of a diffusion coefficient, and has been shown by several authors to exhibit a concentration dependence similar to values of D_M determined by macroscopic diffusion studies. Therefore, to define the measurement made by QELS in the concentrated regime, the approach has been to compare QELS results with macroscopic diffusion coefficient measurements made on similar systems. In the case of random-coil macromolecular solutions Roots et al.[9] have recently demonstrated that macroscopic mutual diffusion coefficients of concentrated polystyrene/toluene solutions are in good agreement with the QELS measurements made by Pusey et al.[10] on the same system. This agreement is in accord with earlier QELS/macroscopic-D_M comparisons which used non-identical (but similar) polymer/solvent systems[11,12].

Comparisons have also been made between QELS and macroscopic D_M measurements obtained from the study of solutions of the charged, globular-macromolecules Bovine Serum Albumin (BSA) and Cyanomethemoglobin. The BSA comparison is shown in Figure 1.1, where a strong disagreement between QELS and D_M measurements is evident. Similar disagreement is also found for the Cyanomethemoglobin comparison suggesting, perhaps, that QELS does not measure a macroscopic D_M in the case of solutions of charged, globular macromolecules. However, protein solutions are not ideal systems for comparative studies. The difficulties associated

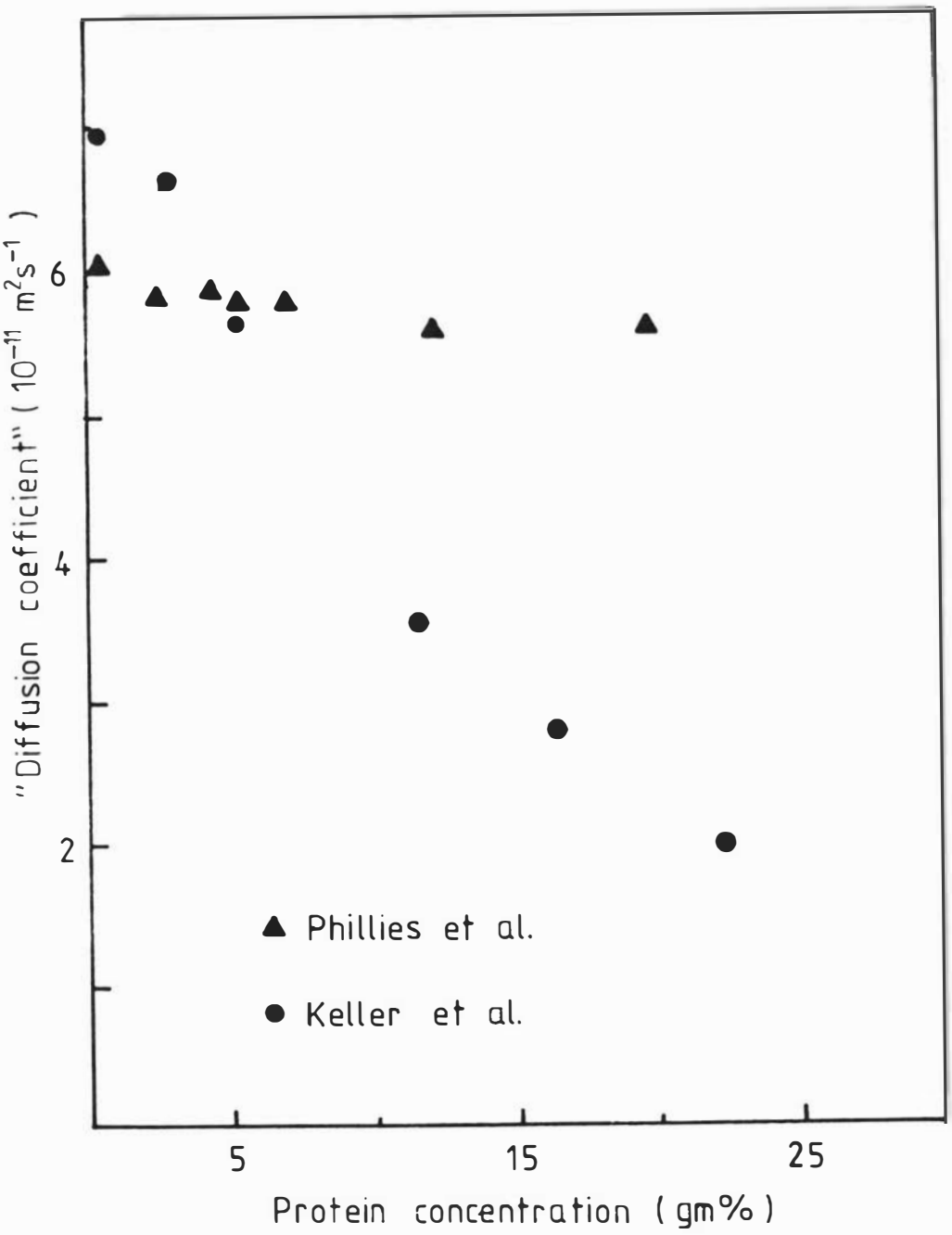


Figure 1.1. A comparison of QELS (Phillies et al.) and diffusion cell (Keller et al.) measurements made on solutions of Bovine Serum Albumin in acetate buffer (at pH≈5) - after Phillies et al., reference 13. It is evident that a substantial discrepancy exists between the D_M values of Keller et al. and the quantity measured in the QELS experiment. This discrepancy can not be explained by the differing samples or slightly different salt concentrations employed.

with the preparation of monodisperse protein solutions are well known, and samples with some degree of polydispersity are usually presented for study. Sample variability can also be a problem and diffusion coefficient variations of up to ten percent have been observed for samples prepared in an identical manner, but obtained from different sources[13, 15]. The complications caused by polydispersity and sample variability, together with possible protein aggregation effects and the dependence of protein charge on pH, all lead to uncertainties in the interpretation of comparative diffusion results. Clearly more comparative diffusion measurements need to be made, particularly on charged globular-macromolecules, and it may be that polystyrene latex spheres would be a more useful system for such comparative studies. These synthetic latex spheres are monodisperse, relatively free from aggregation effects and possess a fixed charge little affected by pH changes. It was for these reasons that latex spheres were selected for a study by QELS, with the intention of assessing the suitability of latex sphere solutions for use as a comparative system.

We now return to the PFGNMR technique, which in this thesis will always be concerned with the study of ^1H nuclei in the sample. To avoid complicating the PFGNMR experiment, solvents containing ^1H must be avoided. (If necessary deuterated solvents can be employed.) The PFGNMR technique possesses the advantage of direct and rapid measurement of D_S. However, in the past this advantage has been offset by poor experimental accuracy, a typical figure being $\pm 10\%$[2]. This inaccuracy has two major components. First, the magnitude of the applied field gradient, G, encountered by the sample must be accurately known (since $D_S \propto G^2$). It is now recognised that G is best determined by calibration using a sample with a well-known diffusion coefficient; usually benzene or water[16,17]. Using such a calibration routine it is possible to obtain G to an accuracy of about 0.5%[17]. The second source of inaccuracy arises from time-domain instability of the NMR signal during signal averaging, a problem which has been encountered since the first PFGNMR experiments were performed[1]. Even in recent papers on the PFGNMR technique (for example reference 2, published 1979) signal instability has been a problem, leading to the conclusion that systematic errors of ± 5 - 15% are present whenever signal accumulation is used. Reduction of the error even to this level requires that an experienced operator visually inspect the NMR signal

and make an acceptance/rejection decision based on the appearance of the signal. The requirement that a signal should be discernable after a single accumulation precludes the study of very dilute samples. The PFGNMR technique, then, requires considerable improvement if D_S measurements are to be made to good ($\pm$1%) accuracy. It was one of the aims of this thesis to improve the accuracy of the PFGNMR technique through careful experimental design, in order to fully realise the potential of PFGNMR as a direct D_S measurement technique.

CHAPTER 2

THE LASER LIGHT-SCATTERING EXPERIMENT

2.1 HISTORICAL SKETCH AND INTRODUCTION

The advent of the laser in the early 1960s provided the long awaited ideal of a narrow-band, high power light source for light-scattering experiments. In 1964, Pecora[18] showed that the Rayleigh component of the light scattered by a very dilute macromolecular solution would be broadened by macromolecular translational diffusion. The mathematical formalism used by Pecora was partially based on the earlier formalism of Van Hove[19], developed for neutron scattering. Pecora showed that the broadening of the Rayleigh line might also be used to study rotational motion and molecular flexation.

The frequency shifts involved in the broadening of the Rayleigh line, which have their origins in the Doppler shifts associated with macromolecular Brownian motion, are so small that conventional interferometers can not be used to resolve the frequency distribution of the scattered light. However, Forrester[20] had previously pointed out that if a narrow-band light source containing several frequency components was incident upon a photodetector, the frequency components would beat together to provide a photocurrent containing the component difference frequencies. The photocurrent could then be examined by a spectrum analyser. This process afforded a much improved resolution over interferometric methods; as was first demonstrated for a laser light source by Javan et al.[21].

In 1964, Cummins, Knable and Yeh[22] used such an optical mixing technique to observe the spectrum of laser light scattered by dilute solutions of polystyrene latex spheres, and the broadening of the Rayleigh line was found to be in quantitative agreement with theory. Pecora's theories have since been validated for a wide range of very dilute, macromolecular systems.

In the early 1970s the analysis of the photocurrent was shifted from the frequency domain into the time domain. The range in time over which intensity fluctuations in the scattered light were correlated was now

determined by forming the intensity autocorrelation function. The origin of the intensity fluctuations in the light scattered by a solution of macromolecules can be seen by analogy with the scattering of X-rays by a crystal. An ordered crystalline array scatters X-rays to give a diffraction pattern with relatively few, but intense, maxima. In contrast, macromolecules in solution are, at any instant, randomly located. The diffraction pattern arising from the scattering of laser light by such a solution thus consists of a superposition of many randomly placed maxima and minima of varying intensity and size. Since the macromolecules are free to diffuse through the solution, the diffraction pattern of the scattered light will fluctuate with time. A photodetector having a photosensitive area approximately equal to the extent of one diffraction maximum (a coherence area) will thus record a randomly fluctuating light intensity whose time evolution is related to the diffusive displacements of the macromolecules. An estimate of the timescale of these fluctuations is the average time (a coherence time of the scattered light) taken for a diffraction minimum to replace a maximum at the detection point. A coherence time is of order of the time taken for a macromolecule to diffuse over the distance of one wavelength of light.

The time domain approach was formalised in an extended series of papers by Jakeman and Pike[23], with several important contributions also being made by Koppel[24,25]. The time domain and frequency domain data form a Fourier-transform pair, and so the information obtained by either analysis method is equivalent. However, in practice time domain analysis is preferred since it offers freedom from errors associated with non-linearities in the analogue spectrum analysis method.

The range of systems to which the laser light scattering technique could be applied was also extended in the early 1970s, when Koppel[25] provided a theoretical interpretation for data collected from very dilute, polydisperse macromolecular solutions. Brown, Pusey and Dietz[26] provided experimental confirmation of Koppel's work, and also provided a more practical method of analysis which could be used to characterise the intensity autocorrelation functions obtained from studies on polydisperse systems. This development released many interesting biological systems for study since these systems can not usually be prepared to contain a single component. (The reasons for this may either be strictly preparative considerations, or may be due to the

presence of complex equilibria in the solution.) The analysis method developed for polydisperse solutions can also be used to characterise the intensity autocorrelation functions obtained from concentrated macromolecular solutions[10,11].

The remaining contents of this chapter will be devoted to a review of the theoretical basis required for the characterisation of intensity autocorrelation functions of the type encountered in QELS studies on concentrated macromolecular solutions.

2.2 THEORY REVIEW

2.2.a. The Laser Light-Scattering Experiment

This section defines a laser light-scattering experiment, and introduces terminology used in discussion of the experiment.

In Figure 2.1 the laser light-scattering experiment is presented schematically. A narrow beam of laser light passes through the macromolecular solution of interest and the scattered light is intercepted by a photodetector (a photomultiplier in the case of this work). The position of the photodetector relative to the emergent unscattered beam defines the scattering angle, θ, while the intersection of the incident and scattered beams defines the scattering volume.

Figure 2.1 actually defines a homodyne scattering experiment; that is only light scattered by the macromolecular component impinges upon the photodetector. An alternative QELS experiment, the heterodyne experiment, colinearly mixes a portion of the unscattered beam with the scattered light at the photodetector.

In the following discussion it will be assumed that the light from a laser can be considered as a single frequency, constant amplitude, plane wave of coherence time long compared with any requirements for phase stability of the incident light. The photodetector is assumed to have a photosensitive area of less than a coherence area. Also, the photodetector is assumed to have a finite quantum efficiency, and it is further assumed that only one anode-pulse is emitted per detected photoevent at the photocathode. These assumptions are met by commercial lasers and photodetectors of the type employed in this thesis[27]. Furthermore, QELS experiments are arranged so that the number of detected photoevents is well within the count-rate capacity of the photodetector.

For the geometry shown in Figure 2.1, the scattering vector, $\underset{\sim}{q}$, is defined by

$$\underset{\sim}{q} = \underset{\sim}{k}_i - \underset{\sim}{k}_s$$

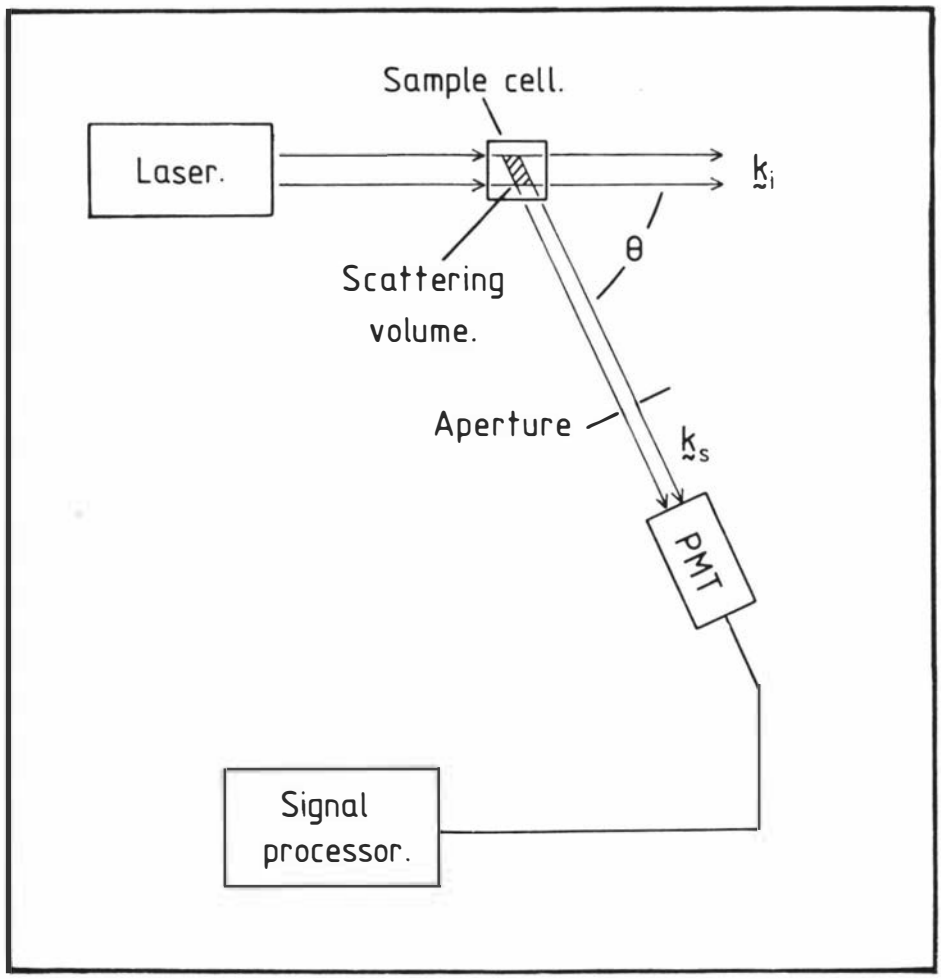


Figure 2.1. A schematic representation of the laser light scattering experiment, using a photomultiplier (PMT) as a detector. $\underset{\sim}{k}_i$ and $\underset{\sim}{k}_s$ are the wave vectors of the incident and scattered light respectively, and n_0 is the refractive index of the scattering medium. θ is the scattering angle, and the moduli of the wave vectors are given by $|\underset{\sim}{k}_i| = 2\pi n_0/\lambda_i$ and $|\underset{\sim}{k}_s| = 2\pi n_0/\lambda_s$.

where $\underset{\sim}{k}_i$ and $\underset{\sim}{k}_s$ are the wave vectors given in Figure 2.1. The magnitude of $\underset{\sim}{q}$ is given by [27]

$$q \equiv |\underset{\sim}{q}| = 4\pi n_0 . \sin(\theta/2)/\lambda_0 \qquad 2.1$$

where n_0 is the solution refractive index and λ_0 is the vacuum wavelength of the incident laser radiation. In the case of a massive macromolecule scattering visible light, the magnitude of the momentum change ($\hbar q$ where $\hbar$ is Planck's constant divided by 2π) suffered by the macromolecule during a scattering event is so small that the macromolecular momentum can be considered unchanged[28]. Light of the wavelength used in a QELS experiment is not usually absorbed by the scattering particles, and so energy and momentum transfer considerations due to absorption need not be considered. It is because the momentum changes associated with a scattering event are so small that the laser light scattering experiment is termed quasi-elastic, and hence the acronym QELS was coined. This acronym will be used henceforth to denote the homodyne experiment shown in Figure 2.1.

2.2.b. The Homodyne Intensity Autocorrelation Function for a Very Dilute, Monodisperse Solution of Small Macromolecules.

The very dilute macromolecular solution is considered here in order to relate the diffusive motions of macromolecules to fluctuations in the total scattered intensity. These dilute solutions provide the basis for discussion of the more interesting concentrated macromolecular solutions.

The magnitude of the scattered intensity impinging upon a photodetector as a result of scattering from a macromolecular solution would show random fluctuations with time (as discussed in section 2.1) such that a recording of the intensity would closely resemble a noise pattern. The theory of noise and stochastic processes indicates that such a time-varying intensity can be characterised by forming the intensity autocorrelation function (IAF) or, more usually, the normalised intensity autocorrelation function (NIAF). If the scattered intensity at the photodetector is stationary (a stationary scattered intensity has the same average value regardless of the time at which the average is initiated), the NIAF is defined as[29]

$$\langle I(0)I(t)\rangle/\langle I(0)\rangle^2 = \langle E_S(0)\, E_S^*(0)\, E_S(t)E_S^*(t)\rangle/\langle E_S(0)E_S^*(0)\rangle^2 \equiv g^{(2)}(t) \qquad 2.2$$

where $E_S(0)$ represents the magnitude of the total scattered electric field at the photodetector at a time t' and $E_S(t)$ represents E_S at a later time $t'+t$. $I(0)$ and $I(t)$ are similarly defined. The symbol * indicates that the complex conjugate has been taken, the angular brackets indicate a time average and the symbol $g^{(2)}(t)$ is used to denote the NIAF as defined by equation 2.2.

The average intensity scattered by a solution of diffusing macromolecules is indeed stationary, and so equation 2.2 is valid for a macromolecular solution[29]. Furthermore, although the macromolecular solutions under consideration are termed very dilute, there are still sufficient scatterers in the scattering volume for the Central Limit theorem to be valid[29]. According to this theorem $E_S(t)$ will be a Gaussian distributed random variable, for which the normalised first and second order electric field autocorrelation functions are related by[28]

$$g^{(2)}(t) = 1 + |g^{(1)}(t)|^2$$

where 2.3

$$g^{(1)}(t) = \langle E_S(0)\, E_S^*(t)\rangle/\langle E_S(0)\, E_S^*(0)\rangle$$

Thus, in the case of a very dilute macromolecular solution the problem of characterising the scattered intensity fluctuations has been reduced to that of finding the first order electric field autocorrelation function, $g^{(1)}(t)$.

The model under consideration here is that of homodyne scattering from a very dilute solution of identical, small (i.e. macromolecular radius less than $\lambda_0/20$), Brownian macromolecules immersed in an invisible solvent. The assumptions built into this model are as follows. Each macromolecule is assumed to interact independently with the incident electric field (of frequency ω_0), and so the amplitude of the total scattered electric field at the detector is the superposition of the fields from the individual scatterers. The condition that the macromolecules be small precludes intramolecular interference effects and also ensures that the macromolecules are optically isotropic, even if they are not physically isotropic[28].

The optical isotropy of the macromolecules means that the amplitude of the scattered electric field due to each macromolecule is independent of time. This scattered amplitude is the same for all macromolecules since the macromolecules are identical. The Brownian motion assertion means that diffusion governs the conditional probability of macromolecular displacement, and the very dilute assumption implies that the macromolecules undergo independent displacements.

For the above model, the normalised electric field autocorrelation function is given by[18]

$$g^{(1)}(t) = \exp(-q^2 D_0 t).\exp(-i\omega_0 t)$$

whence

$$g^{(2)}(t) = \langle I(0)I(t)\rangle / \langle I(0)\rangle^2 = 1 + \exp(-2q^2 D_0 t) \qquad 2.4$$

Thus, in a homodyne laser light-scattering experiment construction of the normalised intensity autocorrelation function $g^{(2)}(t)$ is sufficient to determine D_0. It should be noted that equation 2.4 is an adequate representation for many macromolecular solutions of interest. Most macromolecules are sufficiently small to be optically isotropic, and they usually scatter sufficient light to allow studies to be conducted in the very dilute concentration regime.

2.2.c. The Photocount Analysis Method

To measure the diffusion coefficient of macromolecules in solution it is first necessary to obtain the NIAF, which can be formed very efficiently by using the technique of photocount autocorrelation. This technique has been discussed in detail by, among others, Jakeman and Pike[23], Foord et al.[30], and Koppel[24]. The application of photocount autocorrelation to the study of light scattered by a macromolecular solution is now considered.

The intensity fluctuations in the scattered light can be characterised by using a photodetector as an intermediate processor. For those photodetectors which work by photon annihilation (such as photomultipliers) the probability per unit time of detecting a photon is directly proportional to the intensity incident upon the detector[31].

The NIAF is formed by calculating the products I(0)I(t), where I(0) and I(t) are intensities measured at instantaneous times. However, in the context of a QELS experiment, the term instantaneous means a time interval very short compared with the coherence time of the scattered intensity. Thus, the intensity I(t) can be defined as

$$I(t) \simeq I(t,T) = n(t,T) \qquad 2.5$$

where I(t,T) is the average intensity during the short time interval T centred on t´+t, and n(t,T) is the number of photodetections which are encountered in the time T. The NIAF is then given by

$$\langle I(0)I(t)\rangle/\langle I(0)\rangle^2 \simeq \langle I(0,T)I(t,T)\rangle/\langle I(0,T)\rangle^2$$

$$\simeq \langle n(0,T)n(t,T)\rangle/\langle n(0,T)\rangle^2 \qquad 2.6$$

where $\langle n(0,T)n(t,T)\rangle$ is known as the (un-normalised) full photocount autocorrelation function, denoted by $C_p(t,T)$. In practice $C_p(t,T)$ would be calculated at a number of discrete points which are usually multiples of the sampling period T; that is the following function would be formed

$$C_p(mT,T) = \langle n(0,T)n(mT,T)\rangle \quad m=1,2,3,.....p$$

However, there are severe computational difficulties associated with constructing the above full photocount autocorrelation function in real-time[32]. These problems have been overcome by adopting a technique known as clipping (or one-bit quantisation).

Originally developed for use in the microwave region, the technique of clipping makes use of the fact that most of the spectral information conveyed in a randomly fluctuating Gaussian signal is contained in the distribution of the mean-value-crossings of that signal[33]. That is, such a signal can be represented by just two values, 0 and 1, depending upon whether the amplitude of the signal is less than or greater than the mean. (In general the mean value is not the only preset amplitude criterion that can be utilised[33].) The optical analogue of this microwave technique was developed by Jakeman and Pike[23]. The clipped count, $n_k(T)$, is defined as

$$n_k(T) = 1 \quad \text{if} \quad n(T) > k$$

$$n_k(T) = 0 \quad \text{if} \quad n(T) \leq k \qquad 2.7$$

where the non-negative integer k is termed the clipping level. The effect of clipping a typical distribution of photocounts at two is shown in Figure 2.2.(iii). Fluctuations in the photocount rate can now be characterised by forming the single-clipped autocorrelation function, $C_k(t)$, defined by [23]

$$C_k(mT) = \langle n(0,T)n_k(mT,T)\rangle \qquad 2.8$$

The advantage of single-clipped over full photocount autocorrelation is that by clipping the input signal, the history of the photocount rate can be stored as a linear chain of 0's and 1's, and so can be simply held in a shift register. The products $n(0,T)n_k(mT,T)$ can now be formed by using AND gates as multiplicative elements and so both the circuit complexity and time required for multiplication are greatly reduced. This makes practicable the construction of an inexpensive, real-time autocorrelator.

The normalised, single-clipped photocount autocorrelation function (the acronym NIAF will henceforth denote this function) is then defined as[23]

$$g_k^{(2)}(t,T) = \langle n(0,T)n_k(t,T)\rangle / (\langle n_k\rangle\langle n\rangle) \qquad t \neq 0 \qquad 2.9$$

For Gaussian scattered-light fields $g_k^{(2)}(t,T)$ is related to the scattered electric field autocorrelation function, and hence to the diffusion coefficient of the macromalecules, by[23]

$$g_k^{(2)}(t,T) = 1 + C\left|g^{(1)}(t)\right|^2 = 1 + C.\exp(-2D_0q^2t) \qquad t \neq 0 \qquad 2.10$$

The parameter C is a complicated function of the counting and clipping parameters ($\langle n\rangle$, $\langle n_k\rangle$ and k). The effect of using sample periods T which are not very small compared with the coherence time of the scattered intensity is only to add a term which can be included in C[34]. Further, the parameter C includes the effect of exposing more than one

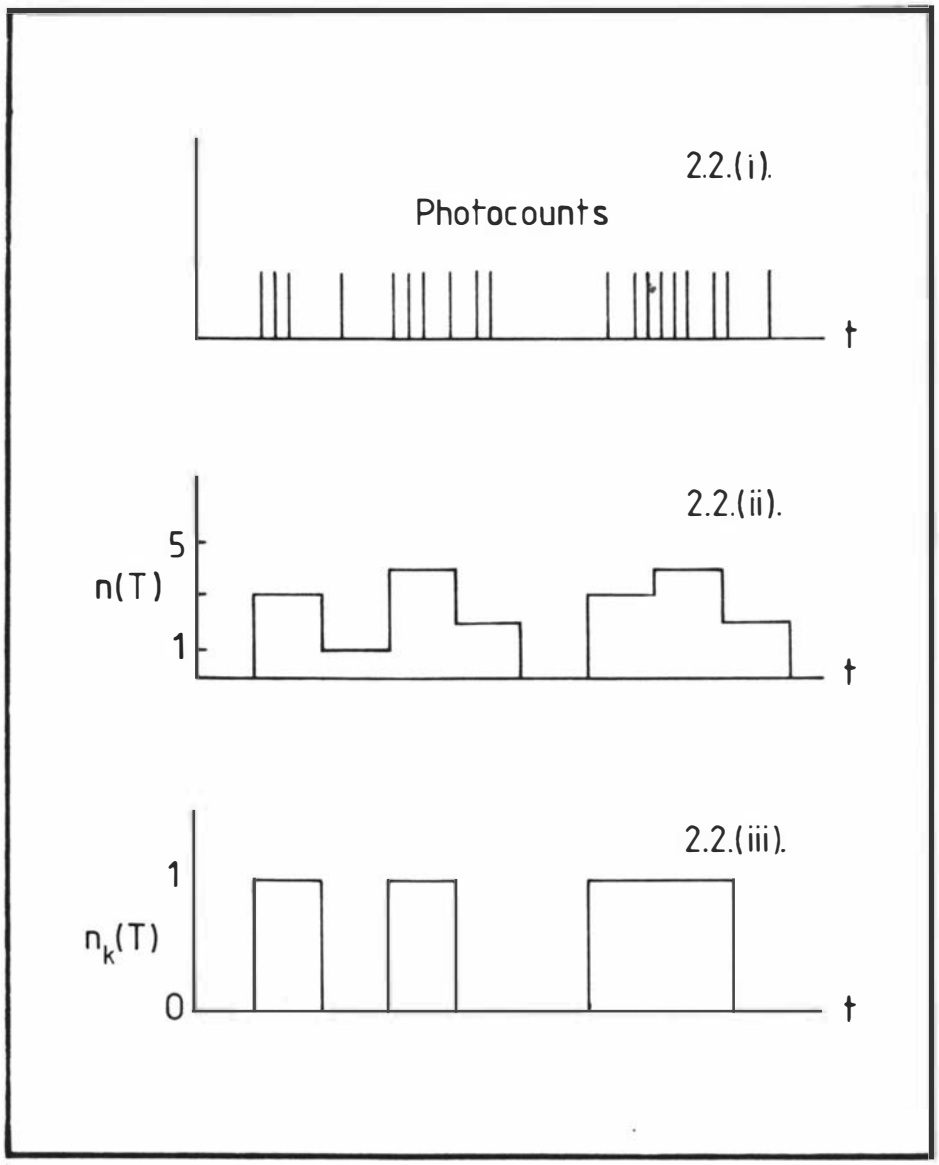


Figure 2.2. The relationship between the full and clipped photocount.

2.2.(i) A typical distribution of photocounts.

2.2.(ii) The number of photocounts, n(T), per sample time T.

2.2.(iii) The result of clipping the photocount distribution at two. If more than two photocounts are recorded during T, the clipped photocount, $n_k(T)$, has a value of one; otherwise $n_k(T) = 0$.

coherence area of the photodetector to the scattered light.

In any particular experiment the parameter C can be regarded as a constant. The light scattering experiment, shown schematically in Figure 2.1, can thus be set up non-critically with respect to the exposed detector area and the sample period T. A single-clipping autocorrelator can then be used to determine $g_k^{(2)}(t,T)$ and the diffusion coefficient of macromolecules in very dilute solution calculated via equation 2.10.

2.2.d. The Method of Cumulants: Application to Data Obtained from Concentrated Solutions of Macromolecules.

Single-exponential NIAFS can be interpreted in terms of a single diffusion coefficient D_0, as indicated by equation 2.10. An analysis method suitable for characterisation of multi-exponential NIAFs, such as those encountered in QELS studies on concentrated, monodisperse macromolecular solutions, is now discussed.

For a monodisperse solution[29]

$$|g^{(1)}(t)| = \exp(-\Gamma t)$$

where

$$\Gamma = D_0 q^2 \qquad 2.11$$

For polymer systems whose NIAFs are characterised by a distribution of decay rates, Γ_i, the above equation can be generalised in the following manner[25,26].

$$|g^{(1)}(t)| = \int_0^\infty G(\Gamma).\exp(-\Gamma t)d\Gamma \qquad 2.12$$

with

$$\int_0^\infty G(\Gamma)d\Gamma = 1$$

$G(\Gamma)$ is the normalised distribution of the decay rates, and $G(\Gamma)d\Gamma$ can be interpreted as the fraction of the total intensity scattered on average by scattering centres whose average decay rate lies between Γ and $(\Gamma + d\Gamma)$ [26].

Experimental determinations of $G(\Gamma)$ would contain information about the mean and variance of the decay rates in the system under investigation. Equation 2.12 indicates that $G(\Gamma)$ may be obtained by inverse Laplace transformation of $|g^{(1)}(t)|$. However, experimental estimates of $|g^{(1)}(t)|$ obtained in a QELS experiment are not sufficiently precise to allow the characterisation of $G(\Gamma)$ by this method. Koppel[25], and Pusey and co-workers [26,29] have proposed and developed an alternative analysis scheme which allows a broad range of multi-exponential NIAFs to be characterised.

The analysis scheme proceeds by first defining the mean decay rate, $\overline{\Gamma}$, as

$$\overline{\Gamma} = \int_0^\infty \Gamma G(\Gamma) d\Gamma \qquad 2.13$$

Also

$$\exp(-\Gamma t) = \exp(-\overline{\Gamma} t)\, \exp[-(\Gamma-\overline{\Gamma})t]$$

Expanding $\exp[-(\Gamma-\overline{\Gamma})t]$ and substituting into equation 2.12, together with rearrangment into a form commonly encountered in statistical theory eventually yields [29]

$$\ell n|g^{(1)}(t)| = -\overline{\Gamma} t + \mu_2(\overline{\Gamma} t)^2/(2!\overline{\Gamma}^2) - \mu_3(\overline{\Gamma} t)^3/(3!\overline{\Gamma}^3) + \ldots. \qquad 2.14$$

where

$$\mu_r = \int_0^\infty (\Gamma-\overline{\Gamma})^r\, G(\Gamma) d\Gamma$$

The terms $\mu_r/\overline{\Gamma}^r$ are known as the normalised moments of the distribution $G(\Gamma)$. The first three moments provide estimates of the distribution mean, variance and skewdness. Formally, $\ell n|g^{(1)}(t)|$ is the cumulant generating function for $G(\Gamma)$[25], and hence this method of analysis is usually referred to as being the method of cumulants or just cumulants analysis.

Equation 2.14 is exact provided that all terms are kept. However, the usefulness of the above approach derives from the fact that for many $G(\Gamma)$'s of interest the terms in equation 2.14 fall off very rapidly with increasing order in $\overline{\Gamma} t$ [29]. Thus, a second or third order

polynomial in t is usually an adequate approximation to equation 2.14. Having measured the single-clipped, normalised photocount autocorrelation function it is necessary to perform a least-squares fit to plots of $\ell n[g_k^{(2)}(t,T)-1]$ versus time in order to obtain $\overline{\Gamma}$, μ_2 etc.; where (from equations 2.11 and 2.14)

$$\ell n[g_k^{(2)}(t,T)-1] = \ell n\ C - 2\overline{\Gamma}t + 2\mu_2(\overline{\Gamma}t)^2/(2!\overline{\Gamma}^2) - 2\mu_3(\overline{\Gamma}t)^3/(3!\overline{\Gamma}^3)+... \qquad 2.15$$

Since the signal-to-noise ratio deteriorates as $g_k^{(2)}(t)$ decays, it is usual to employ a weighting scheme in the sums of squares minimisation [35,36].

The problem of deciding whether a second, third or fourth order polynomial in $\overline{\Gamma}t$ best describes a given set of data can be circumvented by making use of the fact that as $t \to 0$, the higher terms in equation 2.15 become progressively less important [26]. Thus, a series of measurements are made for a range of T and for each value of T, $\ell n[g_k^{(2)}(t,T)-1]$ is fitted to linear, quadratic and cubic functions in t. The values of $\overline{\Gamma}$ and the μ_n obtained from each of these fits are plotted against T, and extrapolation to T=0 yields values for these variables free of systematic error. An example of such a plot can be seen on p115 of this thesis.

Signal-to-noise considerations will generally prevent the use of very small T values, but spanning a range of times such that $0.4 \leq \overline{\Gamma}t_{max} \leq 4.0$ usually enables reliable extrapolation to T = 0 [26]. Here, t_{max} is the maximum time at which the autocorrelator computes a value of the intensity autocorrelation function.

QELS experiments have shown that the NIAFs obtained from studies on concentrated, monodisperse macromolecular solutions are multi-exponential [10, 11, 12]. The distribution of decay rates implied by such NIAFs can, perhaps, be thought of as arising from local solution inhomogeneties (i.e. local areas of excess macromolecules and other areas of excess solvent which persist for a time comparable to the coherence time of the scattered light). It has not yet proved possible to derive an expression for the total scattered electric field originating from concentrated macromolecular solutions. Thus, while $\overline{\Gamma}$ and the μ_n can be obtained from a cumulants analysis of the QELS data obtained from

a study of such solutions, it is not possible to directly assign these quantities to properties of the interacting system. Further, the QELS measurement obtains an apparant mean decay rate, $\bar{\Gamma}$, on a timescale comparable to that required for changes to occur in the local solution environment, whereas a macroscopic diffusion coefficient measurement on the same solution averages over a very much longer period. Thus, although in the case of a QELS study on a concentrated macromolecular solution it is possible to define a quantity D_{ML} where by analogy with equation 2.12

$$\bar{\Gamma} = D_{ML}q^2 , \qquad 2.16$$

this quantity is not necessarily related to a macroscopically measured diffusion coefficient.

Thus, multi-exponential NIAFs can be characterised by finding the mean decay rate $\bar{\Gamma}$ and the variance of the decay rate distribution $\mu_2/\bar{\Gamma}^2$, by utilising the method of cumulants for data analysis. The precision of the QELS technique only allows $\bar{\Gamma}$ and μ_2 to be determined with a reasonable degree of accuracy[26] (typically $\pm$ (1-5)% for $\bar{\Gamma}$, and $\pm$ (5-30)% for μ_2). In the case of concentrated macromolecular solutions it is not possible to place a direct physical interpretation on the quantities $\bar{\Gamma}$ and $\mu_2/\bar{\Gamma}^2$. However, experiments on concentrated solutions of random-coil polystyrenes have shown that the diffusion coefficient D_{ML} calculated via equation 2.16 appears to be equivalent to the macroscopically measured mutual diffusion coefficient (as discussed in Chapter 1). Thus, the term D_M will be used to denote the diffusion coefficient measured by QELS under a cumulants analysis of concentrated, random-coil macromolecular solution data. For concentrated solutions containing other than random-coil macromolecules, the term D_{ML} will be used to denote the quantity measured by QELS using cumulants analysis.

2.2.e. Implications of the Angular Dependence of the Intensity Autocorrelation Function Decay Rate

Plots of Γ (or $\bar{\Gamma}$) versus q^2 should yield a straight line of slope D_0 (or D_M, D_{ML} for concentrated macromolecular solutions) provided, of course, that the process characterised by Γ or $\bar{\Gamma}$ is not a function

of q. The expression for q is, from equation 2.1

$$q = 4\pi n_0 . \sin(\theta/2)/\lambda_0$$

In this work only θ can be easily changed, and so it is the invariance of D_0 (or D_M, D_{ML}) with $\sin^2(\theta/2)$ which is the important test of experimental reliability.

The resolution of the QELS experiment is taken to be of order 1/q. This can be seen by noting that for photodetection purposes the NIAF, $g^{(2)}(t)$, varies as

$$g^{(2)}(t) \sim |g^{(1)}(+)|^2$$

and it can be shown that [18]

$$|g^{(1)}(t)|^2 \sim \langle \exp(2i\underset{\sim}{q}.[\underset{\sim}{r}(t)-\underset{\sim}{r}(0)]) \rangle$$

where $[\underset{\sim}{r}(t)-\underset{\sim}{r}(0)]$ is the displacement of a scattering particle during the time t. Thus, $g^{(2)}(t)$ suffers a significant change in magnitude as the average scattering particle traverses a distance of order 1/q (in the direction of $\underset{\sim}{q}$), hence defining the resolution of the QELS experiment. For the macromolecules and scattering angles of interest to this work, the macromolecular radius is always much less than 1/q and so the QELS experiment only probes the macromolecular centre-of-mass motion.

There are only two effects of concern to this thesis which can engender anomolous non-linear q^2 versus $\overline{\Gamma}$ plots: the presence of heterodyne components in the scattered light, or the presence of dust in the scattering volume. Heterodyne components arise when stray light is scattered into the photomultiplier tube during small angle studies (scattering from the sample-cell walls for example). For a pure heterodyne experiment the NIAF decays as [18]

$$\Gamma = D_0 q^2/2 \quad \text{or} \quad \overline{\Gamma} = D_{ML} q^2/2$$

Significant heterodyne components in the scattered light will cause

the NIAF to decay more slowly then in a pure homodyne experiment, and so could lead to a smaller diffusion coefficient being calculated in the case of a cumulants analysis of QELS data. Significant heterodyne components in the NIAF of a very dilute, monodisperse macromolecular solution are easily detectable since the NIAF will deviate from single-exponentiality at low scattering angles, and so such data can be readily rejected.

Dust in the scattering solution poses a major problem in all light scattering experiments. As the massive dust particles traverse the scattering volume the amount of light scattered to the photomultiplier increases greatly, and serves to introduce large components into the NIAF which decay on a timescale much slower than that of experimental interest. Dust further disturbs the QELS experiment by introducing a non-stationary term into the NIAF, since dust particles are not always present in the scattering volume. Provided that only small quantities of dust are present in the scattering solution, satisfactory QELS measurements can usually be made at large scattering angles because the scattering of light from the massive dust particles is subject to intra-particle interference effects[29]. These interference effects serve to enhance the intensity of the light scattered by the dust to small scattering angles, thus making large scattering angle QELS studies on macromolecular solutions possible. However, weakly scattering systems, where study at large scattering angles is not possible due to limited signal-to-noise, pose severe cleanliness requirements. For dilute, monodisperse macromolecular solutions the effect of dust is easily detectable as a deviation from single-exponential NIAFs. In the case of concentrated macromolecular solutions, low values of D_{ML} could be calculated.

2.3 INSTRUMENTATION

2.3.a. A Digital Correlator with Blinker Facility

The basic principles of photocount autocorrelation were outlined in section 2.2.c. Suitable circuitry for the implementation of data collection and processing rates of up to 20MHz was made possible by the development of high-speed digital integrated circuits. The (auto) correlator used for data processing in this thesis was of an original design by O'Driscoll and Pinder[37]. The complete correlator was electronically designed and constructed in this laboratory by R. C. O'Driscoll, and a description of the circuitry and operating principles has recently been published[37]. This correlator is very similar, both in specifications and operating modes, to commerically available correlators. There is, however, one very important difference: the incorporation of a dust effect minimising device (known as a blinker) into the O'Driscoll-Pinder correlator. The blinker is essentially an automated data rejection scheme which is triggered by abnormally high scattered-intensity levels, such as those associated with the passage of a dust particle through the scattering volume. The blinker is of central importance to much of the work performed in this thesis, and it is thus appropriate to give a brief description of it's operation.

A block diagram of the essential features of the correlator is shown in Figure 2.3 where, for simplicity, the three additional monitor channels which record the total counts, total clipped counts and total elapsed sample times have been omitted (these channels are used to calculate the NIAF, as will shortly be described). The circuit blocks labelled delay, and intensity monitor, form the basis of the blinker. The delay circuitry postpones the arrival of the input pulses to the clipper in order to allow the intensity monitor time to examine the incoming data for spurious intensity fluctuations. A signal is designated spurious if $n(t,T)$ exceeds a preset number, the blinker level, for each of three consecutive sample periods. When met, this condition generates a correlator stop command. To ensure that the dust has left the scattering volume one second is allowed to elapse before the system

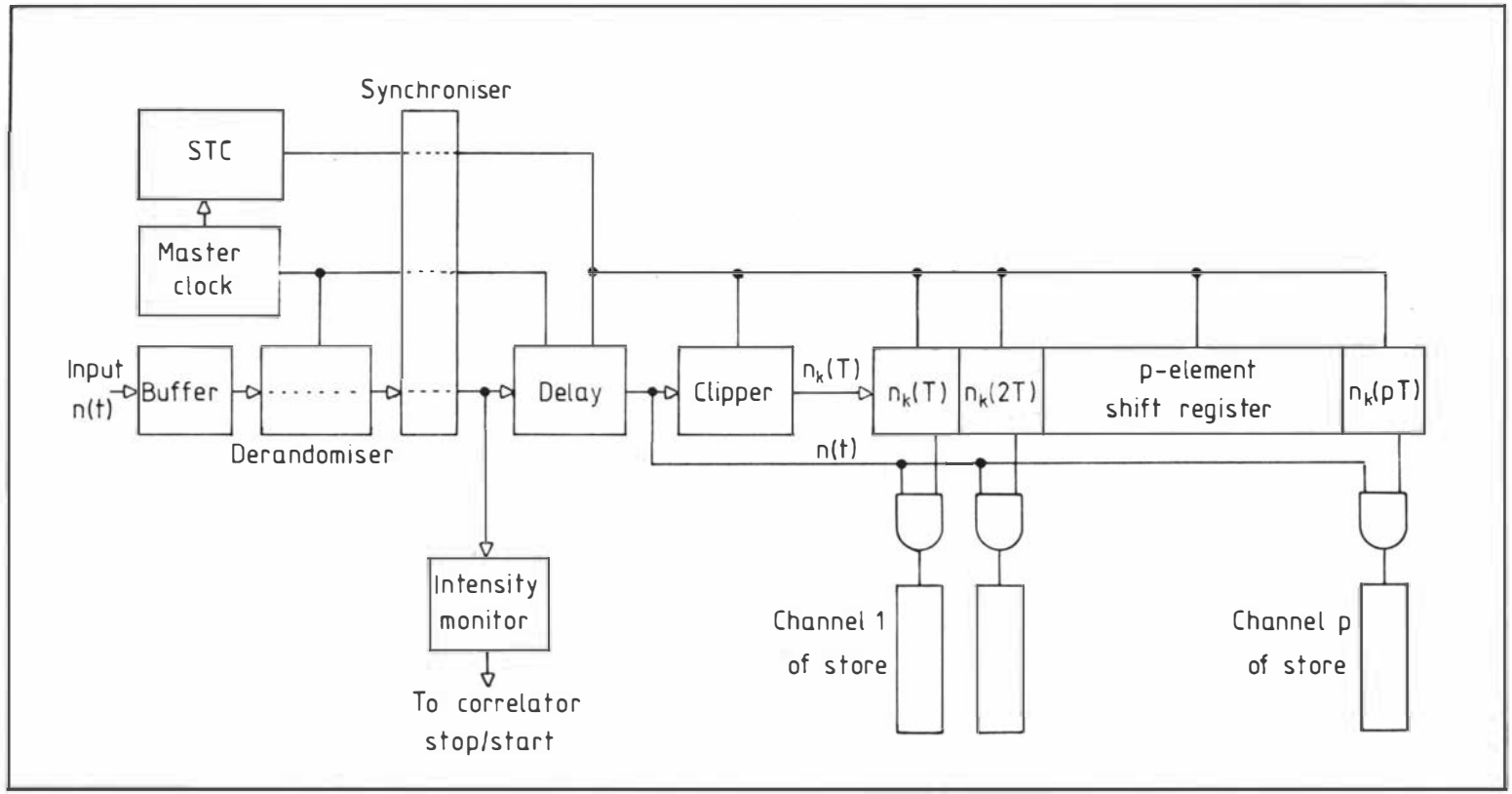


Figure 2.3. A schematic circuit diagram of the digital autocorrelator used in this work - after O'Driscoll and Pinder, reference 37. The circuit blocks labelled Delay and Intensity monitor form the "blinker".

checks for a correlator start command. A start command consists of four sample periods each with n(t,T) less than the blinker level, and when encountered allows the main shift register to fill. Correlation then proceeds.

The correlator may be stopped and restarted many times during an experimental run, so it is important that the randomly blinker-generated stop-start commands in no way interfere with the function of the correlator. These commands must not cause ambiguous interpretation of any photocount data arriving near to the time when the correlator is stopped or started. Also, photocounts arriving close to the end of a sample period must be treated just the same as photocounts arriving in the middle of the sample period (and not, for example, ignored while n(t,T) is loaded into a subsequent processor). It is the function of the circuit blocks labelled derandomiser, and synchroniser, to obviate any data processing problems associated with the random arrival of either input photocounts or blinker-generated correlator stop-start commands; thus allowing the photocount autocorrelation function to be correctly determined.

The acceptance or rejection of input data by the correlator depends on n(t,T) relative to the blinker level setting. If this level is set too high then the high count rates associated with dust will be processed. If set too low, large intensity fluctuations statistically associated with the solution under study will also be removed. The choice of a suitable blinker level is only straightforward for a dilute, monodisperse macromolecular solution, as such solutions are characterised by single exponential NIAFs. The blinker level is thus adjusted until the plot of $\ell n(g_k^{(2)}(t,T)-1)$ versus t becomes a straight line [37]. Consideration of the signal-to-noise typically encountered in a QELS experiment leads to the conclusion that an NIAF can be considered a single-exponential if the experimental estimate of the decay rate variance, $\mu_2/\bar{\Gamma}^2$, is less than 0.02[26]. The term $\mu_2/\bar{\Gamma}^2$ is given the symbol Q´ in this work.

Finally in this section the calculation of the NIAF is considered. After M sample periods the contents of channel m of the store represent the un-normalised, clipped IAF, $G_k^{(2)}(mT)$. The normalised, single-clipped IAF, $g_k^{(2)}(mT)$, is then obtained by dividing $G_k^{(2)}(mT)$ by the calculated baseline, $G_k^{(2)}(\infty)$, where

$$G_k^{(2)}(\infty) = (\text{total counts}) \times (\text{total clipped counts})/(\text{total sample periods}) \quad 2.17$$

It is the function of the monitor channels mentioned earlier to provide the various counts which enable $G_k^{(2)}(\infty)$ to be calculated. When the blinker is being used these monitor channels must not record any information during correlator off times, otherwise an incorrect $G_k^{(2)}(\infty)$ will be calculated.

2.3.b. Considerations for Photomultipliers as Photodetectors.

In this work a photomultiplier tube (PMT) was employed as a photodetector. Several precautionary points concerning the application of commercial PMT assemblies to photocounting experiments are now discussed.

The first problem considered is that of correlated after-pulses. Amplification of a photoelectron ejected at the photocathode of a PMT relies on a statistical secondary emission process. The time of arrival of the secondary emission electrons at the anode will depend on the particular transit path taken by individual electrons down the amplifying sections of the phototube. The time taken by different groups of electrons travelling by different paths can lead to correlated after-pulses, an occurence that is particularly damaging to correlation experiments. Apart from variations in transit times, correlated after-pulses can also be caused by optical, soft X-ray or positive ion feedback; induced by the arrival of large pulses at the anode[27]. Correlated after-pulses can be effectively eliminated by imposing a dead-time upon the PMT output electronics such that after-pulses which occur within a certain time of the parent pulse are prevented from passing to the output circuitry. For the carefully selected PMTs used in photocount experiments, the dead-time is quite small (50ns for the commonly employed ITT FW130 PMT, for example), and for normal count-rates does not interfere with collection of data. However, the transit time of the PMT is dependent on the high voltage applied to the PMT. Changing the high voltage away from the manufacturers recommended setting (as is sometimes necessary to reduce the input count-rate for example) may so alter the PMT characteristics that correlated after-pulses appear outside the PMT dead-time, and so become included in the experimental data comprising the NIAF. It is thus important to consider

this source of error if the high voltage applied to the PMT is altered from the recommended setting.

The second problem considered in this section is the manipulation of the exposed photocathode area to provide the maximum signal-to-noise from the PMT. Consider two distinct points, A and B, on a photocathode which receives light from a source of finite dimensions. The amplitude of the total scattered electric field at A, E_A, will differ from the field amplitude at B, E_B, since the pathlengths from various points on the source to the two points A and B will differ. When A and B are coincident, E_A and E_B will be identical. When A and B are distinct E_A will be correlated to E_B, and as A and B move far apart E_A and E_B will eventually become uncorrelated. In fact, E_A and E_B will be correlated only when the points A and B are separated by less than the linear dimensions of a coherence area. Thus, exposing an area of the photocathode which is larger than a coherence area will not further increase the signal-to-noise ratio obtainable from the PMT. By making the coherence area as large as possible, the maximum amount of correlated, scattered light can be collected. For a three-dimensional source radiating onto a two-dimensional detector, it can be shown that the expression for a coherence area is [27]

$$A_{coh} = \lambda_0^2/\Omega$$

where Ω is the solid angle subtended by the source at the detector. Decreasing Ω obviously increases A_{coh}, and it is for this reason that (consistent with the requirements of the Central Limit theorem) the laser beam is focused into the scattering cell (see Figure 2.4).

2.3.c. The Laser Spectrometer

The components which comprise the laser spectrometer are shown schematically in Figure 2.4, with relevant specifications given in Table 2.1. The block labelled PMT in Figure 2.4 is shown in more detail in Figure 2.5. The laser, and components contained in the dashed outline in Figure 2.4, are mounted on a two tonne steel reinforced concrete table. The table is isolated from building vibrations by placing

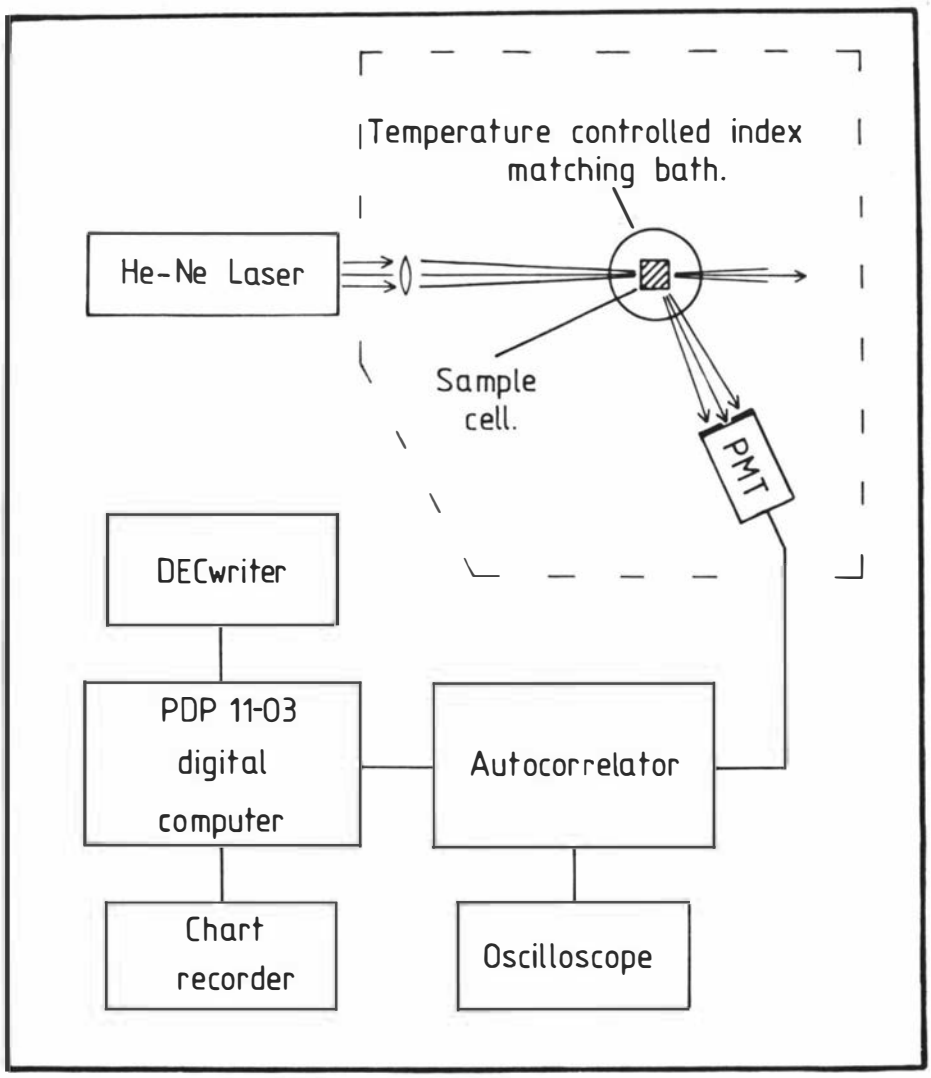


Figure 2.4. A schematic diagram of the laser spectrometer. The focal length of the lens is 20cm, with the sample cell located at the focal point. The oscilloscope is used to monitor the accumulation of the IAF. Data accumulated by the correlator is passed to the PDP 11-03 digital computer for analysis.

Component	Specifications
He-Ne laser.	Output power: 55mW at 632nm. Amplitude stability: better than 3% per hour
Temp. control.	Precision: $\pm$ 0.03^{o}C; accuracy: $\pm$ 0.01^{o}C.
Photomultiplier tube and associated electronics.	Quantum efficiency: 0.46%. Dark count: ~10 per second at 25^{o}C. Correlated after-pulses: <1 per 10^{3} pulses. Dead time: 50ns. Output pulse width: 25ns. Optimum HV: 1750V.
Correlator	48 data channels of 10^{8} count capacity. 4 monitor channels of 10^{10} count capacity. Sample time presettable with 2½ digit mantissa. Sample times available: 0.05μs to (9.95)x10^{5}μs. Clipping level adjustable in unity steps: 00-99. Blinker level adjustable in steps of 2^{n}:n=1-8. The correlator also functions in other modes (multi-scaling, double-clipping), and has other features (cross-correlation, probability analysis).

Table 2.1. Specifications of the laser light-scattering spectrometer.

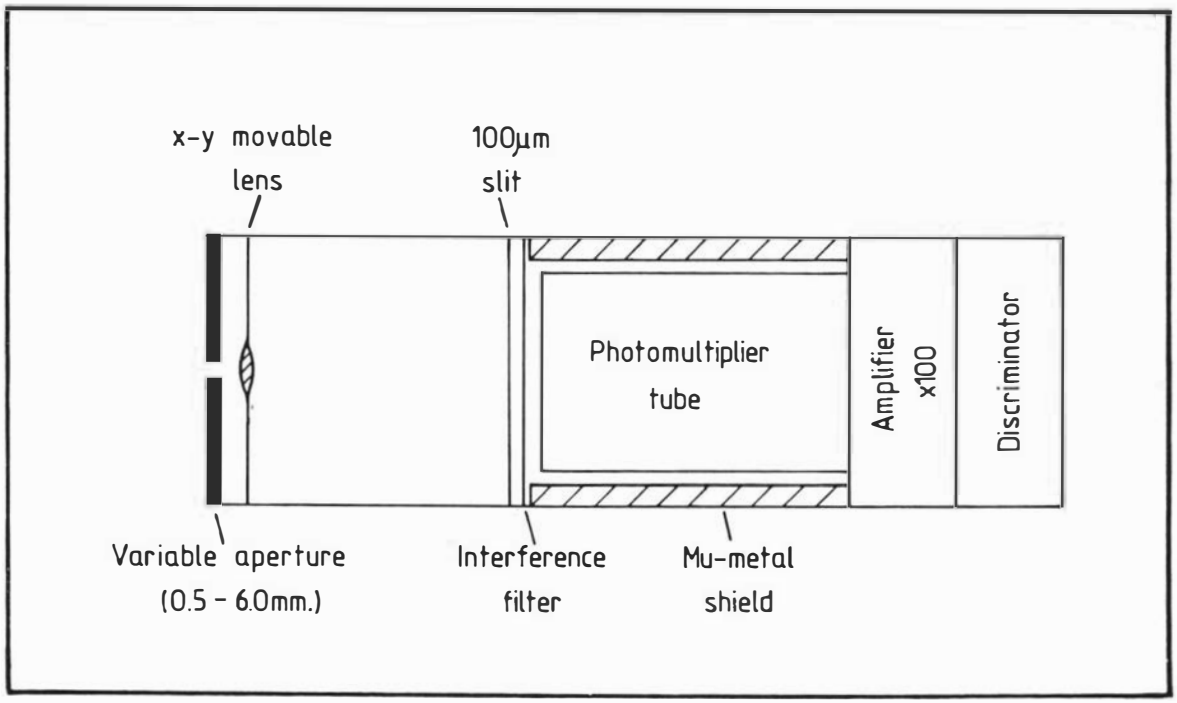


Figure 2.5. The photomultiplier tube and housing. The front of the housing is located about 10cms from the centre of the sample cell. Light from the sample cell is imaged on to the vertically orientated 100µm slit, located 10cms from the lens which has a 5cm focal length.

slabs of 10cm thick foam rubber between the floor stands and the table.

The helium-neon laser used to carry out QELS experiments in this thesis was a Spectra Physics (California, U.S.A.) model 125A, chosen for it's amplitude stability. The components inside the dashed outline in Figure 2.4 comprise the Precision Devices (Malvern, England) 4300 spectrometer. The PMT assembly is mounted on an arm free to rotate concentrically about the sample cell. Scattering angles can be read to a precision of 0.1^{o} with the aid of a vernier scale mounted around the outside of the index matching bath. The accuracy of the scattering angles depends on the precise setting of the zero degree position, which corresponds to the position of the emergent, un-scattered laser beam. The angular alignment scheme adopted in this work is discussed in Chapter 6.

The photomultiplier tube used in the 4300 spectrometer is the ITT (Indiana, U.S.A.) FW130; the tube commonly employed for photocount experiments. The high voltage is supplied to the tube by an EMI (Hayes, Middlesex, England) PM25A power supply. The temperature of the index matching bath is controlled by a Precision Devices temperature controller, while actual temperature measurements were made with a calibrated HP(Hewlett-Packard, U.S.A) 2801A quartz crystal oscillator thermometer.

The data in the correlator storage channels is acessible via the correlator data bus for output (following D/A conversion) to an oscilloscope. The oscilloscope display is updated at a 9kHz rate, allowing the accumulation of the IAF to be observed. A serial interface, also connected to this data bus, is used to transfer data to a DEC (Digital Equipment Corporation, U.S.A) PDP-1103 digital computer for analysis pruposes. A DEC-writer was utilised for hardcopy computer input/output, and the computer was also interfaced[38] to an HP (Hewlett-Packard, U.S.A.) 7015B chart recorder for visual display of $\ell n(g_k^{(2)}(t,T)-1)$ versus t plots.

Several types of high optical quality scattering cells were used in the QELS experiments. Most experiments were performed using 1.000cm square fluorimeter cells (Helma, England) which were polished on four sides. However, several experiments utilised 1cm wide by 0.500cm path length cells (Spectrosil, U.S.A.) with "frosted sides". Evaporation of solvent from

either type of stoppered cell was negligible during the time taken to complete a set of experiments on the solution under study.

CHAPTER 3

THE PULSED FIELD GRADIENT EXPERIMENT

3.1 INTRODUCTION: THE NUCLEAR MAGNETIC RESONANCE EXPERIMENT

3.1 a. Nuclear Magnetic Resonance

It is well known that a nucleus with nuclear spin quantum number I, immersed in a magnetic field of magnitude B_0, has 2I+1 energy levels (the Zeeman levels) equally spaced with a separation[39]

$$\Delta E = \hbar\gamma B_0$$

where γ is the nuclear magnetogyric ratio (a constant for a given nucleus). Associated with each nuclear spin is a nuclear magnetic moment, of magnitude μ given by[39]

$$\mu = \gamma\hbar I$$

The ^1H nuclei of interest to this thesis are particles with $I = \frac{1}{2}$. In the remainder of this section a classical treatment of the behaviour of spin ½ particles placed in a steady magnetic field $\underset{\sim}{B}_0$ is given. This field is considered to lie along the laboratory z-axis, that is $\underset{\sim}{B}_0 = B_0\underset{\sim}{k}$, where $\underset{\sim}{k}$ is the z-axis unit vector.

At thermal equilibrium the nuclear spin ensemble can be described in terms of the occupancy of the Zeeman levels. This occupancy has the form of a Boltzmann distribution. For spin ½ particles there are only two energy levels whose relative populations are given by[39]

$$n_1/n_0 = \exp[-\hbar\gamma B_0/(k_B T)] \qquad 3.1$$

where n_1 and n_0 are the number of nuclear magnetic moments aligned against and with the steady field $\underset{\sim}{B}_0$ respectively, and T is the absolute temperature. As can be seen from equation 3.1, a measurable

polarisation of the nuclear spins can be achieved by making B_0 large. In NMR experiments B_0 is usually arranged so that the frequency of the electromagnetic radiation necessary to cause transitions between the Zeeman levels is in the radiofrequency (rf) range.

Significant polarisation of the nuclear spins gives rise to a macroscopic magnetisation of magnitude M (the magnitude of the net magnetic moment per unit volume). For the NMR experiments of interest to this thesis, it is sufficient to deal entirely with this macroscopic magnetisation. At thermal equilibrium $\underset{\sim}{M}$ is aligned along the steady field axis, that is $\underset{\sim}{M} = M\underset{\sim}{k}$. If B_0 is constant in magnitude (homogeneous) over the ensemble of nuclear spins, the magnetic moments comprising M all precess about $\underset{\sim}{k}$ at the angular frequency

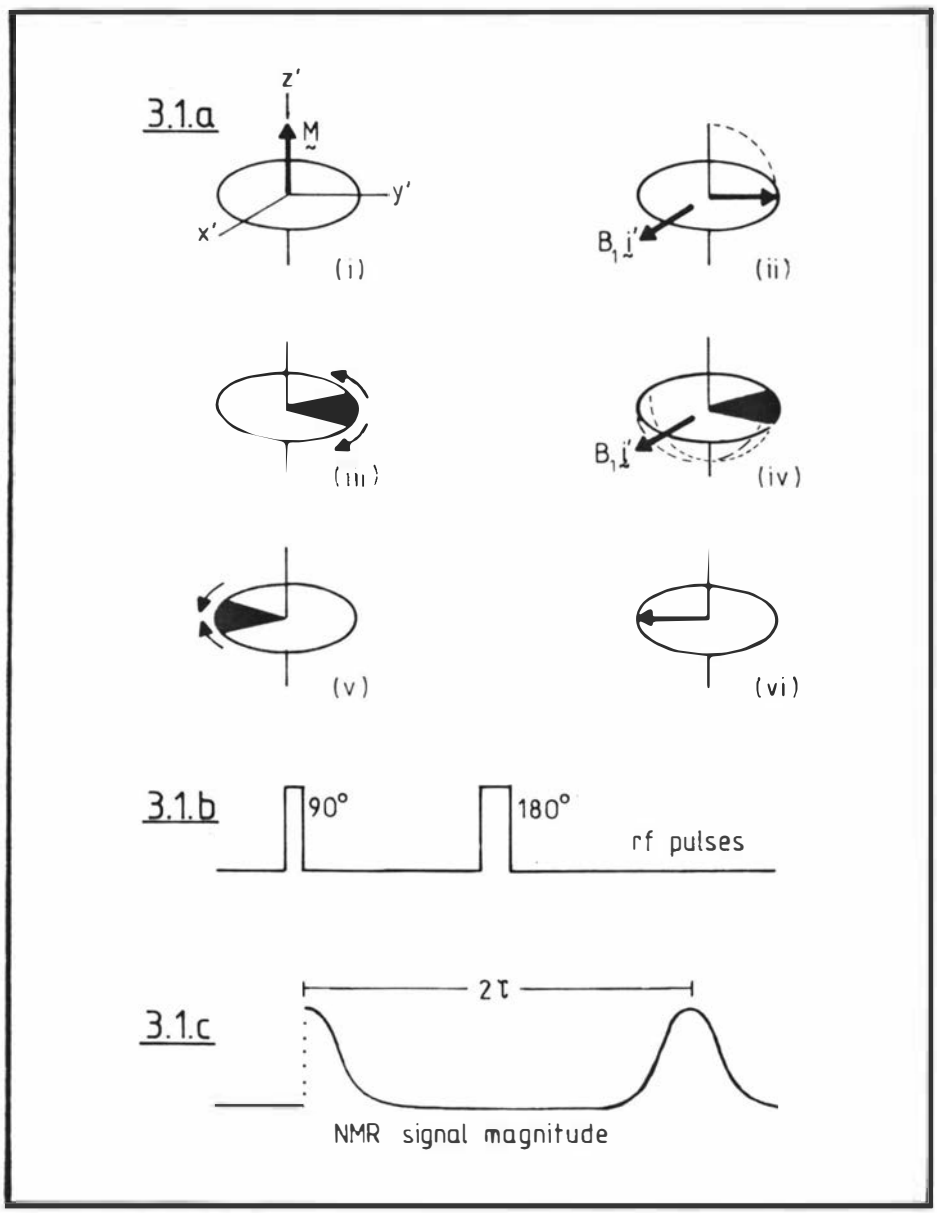
$$\omega_L = -\gamma B_0$$

where ω_L is known as the Larmor frequency. The equation of motion of $\underset{\sim}{M}$ in the rotating frame (a frame of reference rotating about the steady field direction at an angular frequency ω) is [39]

$$\partial\underset{\sim}{M}/\partial t = \gamma\underset{\sim}{M}\times\underset{\sim}{k}(B_0+\omega/\gamma)$$

when $\omega = \omega_L$, the magnetic moments become stationary with respect to the rotating frame, thus giving the appearance (in the rotating frame) of having set B_0 to zero.

Manipulation of $\underset{\sim}{M}$ can be achieved by applying a small field of magnitude $B_1 (<<B_0)$ that rotates in the x-y plane at the Larmor frequency[39], a field which is considered to lie along the x´-axis of the rotating frame as shown in Figure 3.1.a.(ii). Classically, $\underset{\sim}{M}$ will precess about $B_1\underset{\sim}{i}'$ ($\underset{\sim}{B}_0$ being "absent" in a frame rotating at ω_L), where $\underset{\sim}{i}'$ is a unit vector along the x´-axis of the rotating frame. Significant reorientation of $\underset{\sim}{M}$ occurs only when the small field $B_1\underset{\sim}{i}'$ is applied at the Larmor frequency of the magnetic moments[39]. This situation is analogous to many resonant systems where the presence of a small "driving force" (the rf field $B_1\underset{\sim}{i}'$ in this case) applied in the presence of much larger static forces can cause a significant response in a system when the frequency of the driving force is equal to the "natural frequency" (ω_L in this case) of the system. Thus the


3.1.a
z'
M
y'
x'
(i)
B1 i'
(ii)
(iii)
B1 i'
(iv)
(v)
(vi)
3.1.b
90°
180°
rf pulses
3.1.c
2τ
NMR signal magnitude

term Nuclear Magnetic Resonance was coined for experiments involving reorientation of $\underset{\sim}{M}$ by a small, rf magnetic field applied in the presence of a much stronger, static magnetic field.

In practice, the field $B_1\underset{\sim}{i}'$ is generated by passing an rf current oscillating at ω_L through a coil located coaxially about the sample x-axis. However, if an oscillating magnetic field of magnitude $2B_1$ is applied along the laboratory x-axis, this field can be considered as being composed of two counter-rotating fields of magnitude B_1; that is

$$2B_1\underset{\sim}{i}\cos(\omega_L t) = B_1[\underset{\sim}{i}\cos(\omega_L t)+\underset{\sim}{j}\sin(\omega_L t)]+B_1[\underset{\sim}{i}\cos(\omega_L t)-\underset{\sim}{j}\sin(\omega_L t)]$$

where $\underset{\sim}{i}$ and $\underset{\sim}{j}$ are unit vectors along the laboratory x and y axes respectively. If $B_1 << B_0$ (the case in an NMR experiment), the effect of a rotating magnetic field on a nuclear magnetic moment is negligible unless the frequency of rotation approaches the Larmor frequency, and so only the component rotating in the same sense as the precession of $\underset{\sim}{M}$ can cause reorientation of the magnetic moments.

In an NMR experiment it is not possible to make a magnetic field $B_0\underset{\sim}{k}$ which has a perfectly homogeneous magnitude over the sample, with the result that a distribution of Larmor frequencies is present in the sample. A measure of the variation in the steady field magnitude is given by the root-mean-square deviation of B_0, $\sqrt{(\Delta B_0)^2}$. In a frame rotating at the average Larmor frequency $\omega_L = -\gamma B_0$, components of $\underset{\sim}{M}$ located in a field possessing a deviation ΔB_0 will appear to precess about the z´-axis at the small angular frequency $\Delta\omega = -\gamma(\Delta B_0)$. When the field $B_1\underset{\sim}{i}'$ is applied to the sample, the net field $\underset{\sim}{B} = (\Delta B_0\underset{\sim}{k}' + B_1\underset{\sim}{i}')$ will determine the precession axis of the components of $\underset{\sim}{M}$. However, if the magnitude of the rf field is made sufficiently large ($B_1 >> \sqrt{(\Delta B_0)^2}$), and the time ($t_p$) for which the rf field is applied is made sufficiently short [$t_p << 1/(\gamma\sqrt{(\Delta B_0)^2})$], then the precession about the net field is equivalent to precession about $B_1\underset{\sim}{i}'$. With these restrictions on the rf field, all components of $\underset{\sim}{M}$ will rotate together as a single total magnetic moment vector. In the time t_p, the angle of rotation of $\underset{\sim}{M}$ is $\theta = \gamma B_1 t_p$ radians[39].

Consider the situation when the rf field $\underset{\sim}{B}_1$ is applied for a time sufficient to rotate $\underset{\sim}{M}$ through 90°, that is a pulse of rf current is applied to a coil surrounding the sample (the coil is oriented coaxially about the sample y-axis). Following the 90° rf pulse, $\underset{\sim}{M}$ precesses in the x-y plane, about $\underset{\sim}{B}_0$. The precession of $\underset{\sim}{M}$ in this plane induces an rf voltage in the coil surrounding the sample (the same coil that was used to generate $\underset{\sim}{B}_1$ is usually used). The rf voltage induced in the coil decays as the precessing x-y magnetisation returns to the equilibrium situation $\underset{\sim}{M} = M\underset{\sim}{k}$, as illustrated in Figure 3.1.c. The signal induced in the coil is termed a free induction decay (FID) since it is a result of free (i.e. no applied rf field) precession of the magnetisation in the x-y plane.

If B_0 is homogeneous over a nuclear spin ensemble which has a single resonant frequency, the decay of the magnitude of the magnetisation in the x-y plane is characterised by two time constants, T_1 and T_2. T_1 is the longtitudinal relaxation time, which characterises the return to equilibrium of the z-axis component of $\underset{\sim}{M}$ (i.e. from zero just after the 90° rf pulse, to $\underset{\sim}{M} = M\underset{\sim}{k}$ at equilibrium). T_2 is the transverse relaxation time, which characterises the return to equilibrium of the x-y component of $\underset{\sim}{M}$ (i.e. from $M\underset{\sim}{j}'$ just after the 90° rf pulse, to zero at equilibrium). These decay rates are a sensitive function of the chemical environment of the particular resonant nuclei under study, and NMR studies are capable of yielding a wealth of chemical information about the nuclear spin ensemble. In liquid or liquid-like systems a study of the FID can also yield information concerning the laboratory frame motion of molecules containing the resonant nuclei. NMR is thus an important investigative technique which, since the first experiments by Bloch in 1946[40], has been widely applied in many sciences.

3.1 b. The Formation of Spin-Echoes.

In an inhomogeneous magnetic field, such as that encountered in NMR experiments, the precessional frequency of the magnetic moments varies over the sample. Thus, following a 90° rf pulse, the decay of the magnetisation in the x-y plane is augmented (over and above T_2

relaxation) by a loss of phase coherence among the magnetic moments, as illustrated in Figure 3.1.a. (iii). As was first pointed out by Hahn[41], a sequence of two rf pulses can be used to reverse these phase losses through the formation of a spin-echo, a phenomenon which is of central importance to the measurement of diffusion coefficients by NMR. For the purposes of the present discussion, the resonant nuclei are considered to be fixed in the magnetic field $\underset{\sim}{B}_0$. The rf two-pulse sequence usually employed to generate spin-echoes is due to Carr and Purcell[42]. This rf pulse sequence requires that at a time $t = \tau$ after the end of a 90° rf pulse, a second pulse be applied for a time sufficiently long to rotate $\underset{\sim}{M}$ through 180°, as shown in Figure 3.1.a.(iv). The magnetic moments, still retailing their unique, position dependent precessional frequencies, now begin to rephase as shown in Figure 3.1.a.(v), until at $t = 2\tau$ rephasing is complete. The rephased signal at $t = 2\tau$ (see Figure 3.1.c) is termed a spin-echo.

3.2 DIFFUSION COEFFICIENT MEASUREMENT BY NUCLEAR MAGNETIC RESONANCE

3.2 a. The Attenuation of Spin-Echoes Due to Diffusion

In any experiment on a liquid-like system, the molecules in the sample may diffuse appreciable distances during the time 2τ. Since B_0 is not homogeneous over the sample, the nuclear magnetic moments associated with the diffusing nuclei acquire a time-dependent precessional frequency. Consequently, phase losses which occur among the magnetic moments comprising $\underset{\sim}{M}$ during the time $t=0$ to $t=\tau$ are not completely reversed during the refocusing period $t=\tau$ to $t=2\tau$. As was first pointed out by Hahn[41], the magnitude of the spin-echo signal at $t=2\tau$ is additionally reduced (over and above any reduction due to relaxation processes), compared with the signal magnitude at $t=0$, by an amount which is dependent on the diffusion coefficient of the molecules containing the resonant nuclei. It was Carr and Purcell[42] who first provided a practical method for measuring self-diffusion coefficients by observing the attenuation of spin-echoes in an inhomogeneous magnetic field. This method is now described as it contains the fundamentals of the PFGNMR experiment.

The Larmor frequency of a nuclear spin is position-dependent in an inhomogeneous magnetic field, and diffusion of nuclear spins in such fields results in additional attenuation of the spin-echo. Carr and Purcell proposed that the intrinsic label provided by the Larmor frequency of a nuclear spin be used to define the spin's position. This can be achieved by placing a known, static, one-dimensional magnetic field gradient of magnitude G, (usually) along the z-axis of the sample[42], where G is much greater than the magnitude of any gradients due to inhomogeneities in B_0. Translation of a nuclear spin in the direction of the applied magnetic field gradient causes a well-defined change in the Larmor frequency of that spin. Since dephasing in the spin-echo experiment is now almost entirely due to the well-defined applied gradient, the factor A by which diffusion attenuates the amplitude of the spin-echo can be calculated. A is given by[42]

$$A = A(G)/A(0) = \exp(-2\gamma^2 G^2 D\tau^3/3)$$

where A(G) and A(0) represent the magnitude of the spin-echo at $t=2\tau$ in the presence and absence of magnetic field gradient respectively, and D is the self-diffusion coefficient.

There are, however, experimental limitations to the steady gradient experiment. These arise when the gradient magnitude is increased to make possible the measurement of smaller values of the self-diffusion coefficient. Increasing G shortens the interval over which the phase coherence of the spin-echo is partially restored, and so it becomes necessary to increase the bandwidth of the detection system in order to observe the spin-echo. This degrades the signal-to-noise ratio of the detected FID. Furthermore, increasing G usually increases the variation of the total magnetic field over the sample. As previously discussed, the manipulation of $\underset{\sim}{M}$ demands that B_1 be much greater than any variations in the magnitude of the total magnetic field, and so increasing G demands that the output power of the rf transmitter be increased. These limitations imposed by the requirement for larger values of G mean that it is not practical to measure diffusion coefficients smaller than about $10^{-11} m^2 s^{-1}$ by the steady gradient technique[43].

3.2 b. The Pulsed Field Gradient Nuclear Magnetic Resonance Experiment

In an attempt to eliminate the experimental problems associated with the steady gradient technique, Stejskal and Tanner[43] developed an experiment which utilised two identical pulses of magnetic field gradient to measure a diffusion coefficient. The timing of the gradient pulses relative to the rf pulses is shown in Figure 3.2, where the various pulse widths and separations are also defined. Since the gradient pulses are applied between the rf pulses, the requirements on B_1 are considerably reduced. A broad echo is also obtained because the refocusing (and defocusing) rate around $t=2\tau$ is now only determined by the small residual gradients which arise from the residual inhomogeneities in B_0. Values of the self-diffusion coefficient down to $10^{-14} m^2 s^{-1}$ have been measured by the PFGNMR method[44]. The derivation of the expression for the diffusive-attenuation of the spin-echo in a PFGNMR experiment is now briefly reviewed. For the moment, the sample under consideration is assumed to be a simple fluid.

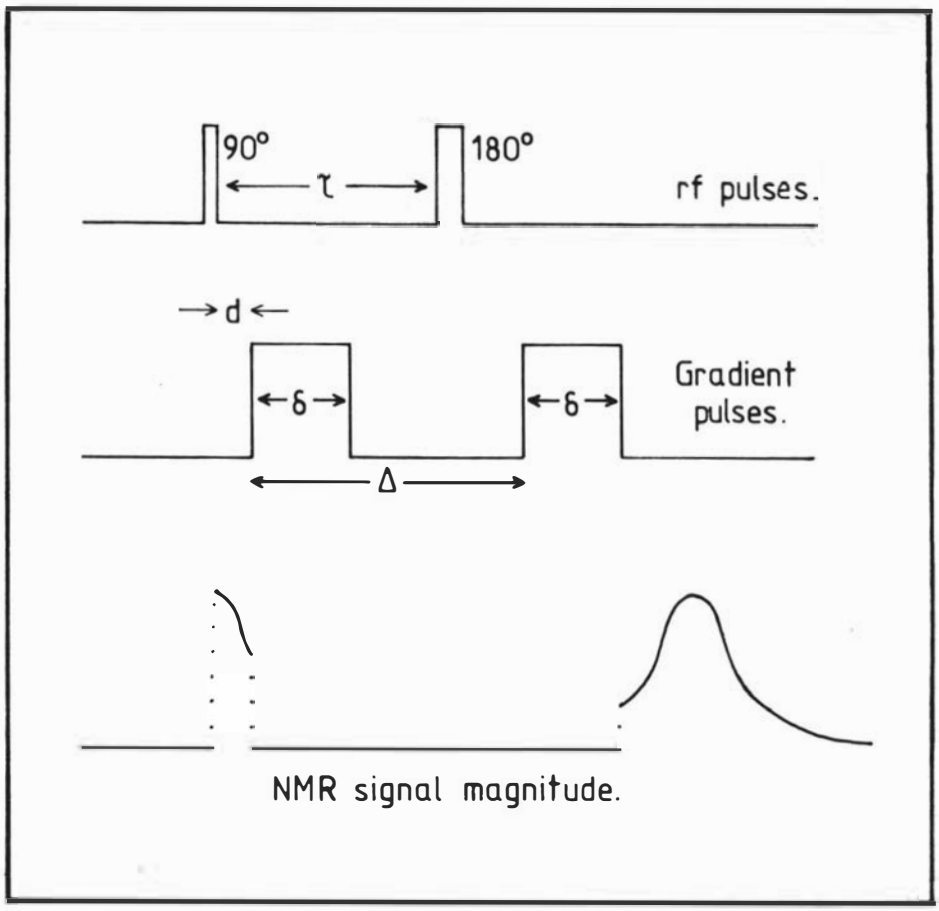


Figure 3.2. The pulse parameters, and timing relationships between the pulses used in a pulsed field gradient experiment, with an example of the magnitude of the NMR signal encountered with such a pulse sequence. The 180° rf pulse always occurs between the two gradient pulses. In this work, d is usually 500μs.

The random-walk nature of the diffusion process examined in a PFGNMR experiment is best viewed through the model first proposed by Carr and Purcell[42] for the steady-gradient experiment. Carr and Purcell considered an ensemble of spins with $\underset{\sim}{M}$ initially aligned along the y´-axis of the rotating frame (i.e. just after the 90° pulse) to be subject to a linear z-axis magnetic field gradient G. The phase history of a single diffusing spin was determined from a random walk model, and an average over the ensemble performed to determine the residual y´ component of magnetisation at $t=2\tau$.

If the z-axis magnetic field gradient has a magnitude much greater than the gradients due to inhomogeneities in B_0, we need only consider the one dimensional components of motion of magnetic moments along the gradient axis. The random walk model assumed is as follows: a nucleus remains at a given position z for T seconds, then suffers a rms jump displacement of ζ along the z-axis, where the new z-coordinate differs from the previous one by ζa_i, and a_i is a random variable whose value is either 1 or -1. If the magnitude of the field in which a nucleus finds itself at t=0 is $B_0(0)$, and if the z-axis field gradient has a constant magnitude G, then after $j = t/T$ jumps a nucleus will find itself in a field of magnitude

$$B_0(t) = B_0(jT) = B_0(0) + G\zeta \sum_{i=1}^{j} a_i$$

After N steps the phase ϕ of the precessing nuclear moment will differ from the value ϕ_0 it would have had in the absence of diffusion by an angle

$$\phi_D = \phi - \phi_0 = \sum_{j=1}^{N} \gamma T[B_0(jT) - B_0(0)] = G\zeta\gamma T \sum_{j=1}^{N} \sum_{i=1}^{j} a_i \qquad 3.2$$

The above model has been extended to the PFGNMR experiment[45] by noting the following facts. In the PFGNMR experiment (see Figure 3.2), the field gradient has a value of G only during the times $0 < t \leq \delta$ and $\Delta < t \leq \Delta + \delta$, being zero for all other times. The beginning of the first gradient pulse is taken as time zero since no significant dephasing occurs before then. The 180° rf pulse always falls between the two gradient pulses, and so the sign of all phase changes which occur during the second gradient pulse are reversed (with respect

to the first gradient pulse). For a PFGNMR experiment, equation 3.2 thus becomes[45]

$$\phi_D = G\zeta\gamma T\left(\sum_{j=1}^{N_1} \sum_{i=1}^{j} a_i - \sum_{j=N_2+1}^{N_2+N_1} \sum_{i=1}^{j} a_i \right) \qquad 3.3$$

where $N_1 = \delta/T$ and $N_2 = \Delta/T$.

The amplitude of the magnetisation at $t = 2\tau$ can be obtained by summing, over the ensemble, the normalised y'-components of the magnetisation[42]

$$M_{y'}(G) = M_{y'}(0) \int_{-\infty}^{\infty} \cos(\phi_D).P(\phi_D)d\phi_D \qquad 3.4$$

where $M_{y'}(G)$ and $M_{y'}(0)$ are the components of $\underset{\sim}{M}$ detected at $t=2\tau$ in the presence and absence of field gradient pulses respectively, and $P(\phi_D)$ is the probability of obtaining a phase difference ϕ_D. In the limit of large N_1, N_2 (the case in a PFGNMR experiment) the Central Limit theorem predicts that the distribution of ϕ_D will be Gaussian, that is

$$P(\phi_D) = (2\pi \langle\phi_D^2\rangle)^{-\frac{1}{2}} \exp[-\phi_D^2/(2\langle\phi_D^2\rangle)] \qquad 3.5$$

$\langle\phi_D^2\rangle$ can be calculated from equation 3.3. Recalling the Einstein definition of the self-diffusion coefficient, $D = \zeta^2/(2T)$, and substituting for N_1, N_2 in the series in equation 3.3 yields[45]

$$\langle\phi_D^2\rangle = 2\gamma^2G^2D\delta^2(\Delta-\delta/3) \qquad 3.6$$

Using equations 3.5 and 3.6, equation 3.4 can be evaluated to give the expression for the diffusion-attenuated spin-echo originally derived by Stejskal and Tanner from a macroscopic approach. This expression is[43]

$$M_y(G) = M_y(0) \exp[-\gamma^2G^2D\delta^2(\Delta-\delta/3)] \qquad 3.7$$

where D is the self-diffusion coefficient; D_S or D_{Solv} in this work.

When $\Delta >> \delta/3$, the time over which diffusive displacements are observed is well-defined as Δ. In the case of gradient pulses of larger width, the diffusion time is taken as being $(\Delta-\delta/3)$[43].

If the macromolecular self-diffusion coefficient D_S is being measured in a PFGNMR experiment, the value of D_S obtained via equation 3.7 must be interpreted with some caution. This is because the resonant nuclei in random-coil macromolecules can suffer z-axis displacements due to macromolecular rotation and intramolecular rearrangement, whereas equation 3.7 only takes into account the translation of the nuclear spins due to the centre-of-mass molecular motion. However, in practice the values of G, Δ and δ available in a PFGNMR experiment require $\bar{z}^2$ to be greater than $(50nm)^2$ for any significant (>1%) attenuation to be observed. Thus, for macromolecules with a radius of gyration less than 50nm, such as those used in this work, the PFGNMR experiment is only sensitive to the macromolecular centre-of-mass motion.

CHAPTER 4

INSTRUMENTATION FOR A PULSED FIELD GRADIENT EXPERIMENT

4.1. INTRODUCTION

The principal advantage of PFGNMR is the ability to directly measure self-diffusion coefficients. However, in the past the PFGNMR technique has been subject to several systematic errors, with the result that accuracy estimates of ±(5-20)% are commonly quoted for the self-diffusion coefficient[2]. Imprecision can increase this error even further. The main sources of error in the PFGNMR experiment have been associated with setting up the known, reproducible and uniform magnetic field gradient required by the experiment[17].

There are several coil configurations available for the generation of linear magnetic field gradients[46, 47]. The magnitude of the field gradient is commonly determined by one of several schemes: by theoretical calculation from a knowledge of gradient coil dimensions, by determination from the decay rate of the NMR signal following the 90° rf pulse (the larger the gradient, the more rapid the signal decay), or by utilising a substance whose diffusion coefficient is already well known. The difficulties with the theoretical calculation are that accurate winding of the coils is assumed, and the contribution from image currents induced in the nearby magnet pole pieces must be taken into account. Calculation of the magnitude of the magnetic field gradient from it's effect on the NMR signal is prone to many sources of systematic error[16]. Although some of these errors can be eliminated by careful adjustment of the sample position, and corrections can be made for other sources of error, the overall requirements of the calibration are too rigorous to allow the gradient to be simply determined. The most satisfactory method of calibrating the field gradient appears to involve the use of a substance of well known self-diffusion coefficient. The self-diffusion coefficients of both benzene and water are known to a few tenths of a percent[48-50], and both of these liquids are well suited to gradient calibration since they possess strong ^{1}H NMR signals thus providing good precision. By calibrating the gradient using benzene, it has recently been shown that a reproducibility of ±1%, and an overall

accuracy of ±2%, can be obtained for steady gradient diffusion coefficient measurements on water in various salt solutions[17].

The determination of the field gradient magnitude in a PFGNMR experiment is subject to several additional complications which are not present in the steady gradient experiment. The generation of a field gradient pulse is associated with rapid current changes during the rise and fall times of the pulse. This leads to the generation of eddy currents in nearby metal objects. There are two systematic errors associated with eddy current generation. First, the eddy current extended "tail" of the gradient pulse may still be present during the 180° rf pulse if the gradient pulse is placed too close to the rf pulse. This has the effect of adding a third, small gradient pulse to the sequence with the result that the spin-echo at $t=2\tau$ will be additionally attenuated, and in fact the spin-echo may not even reach a maximum at $t=2\tau$. The second error associated with eddy current generation arises from the contribution that eddy current induced magnetic fields make to the magnetic field gradient applied to the sample. Eddy currents will cause the gradient pulse shape to deviate from the ideal rectangular shape assumed during the derivation of the expression for the spin-echo attenuation. Thus, it is important to give careful consideration to the minimisation of eddy currents during construction of the NMR probe in which the gradient coils are housed. The effect that residual eddy currents have on the PFGNMR experiment must also be determined.

A review of the literature indicates that the PFGNMR experiment also suffers from several systematic errors whose causes are not well understood. First, experimenters often make a correction to the length of one of the gradient pulses in order to correctly position the spin-echo maximum at $t=2\tau$[1,2]. (This does not appear to be an eddy current effect.) Second, it has often been mentioned that there is some instability in the position and rf phase of the spin-echo[1,2], a fact which has led some experimenters to adopt a procedure in which the operator accepts or rejects spin-echos for height analysis on the basis of the echo's position and appearance. This necessarily requires that an experienced operator perform the experiments, although computerised echo inspection can also be used[2]. The problems of signal stability and gradient pulse length adjustment have been encountered since the

inception of the PFGNMR technique[1] and continue to be mentioned in even the more recent papers on the technique (see reference 2, published 1979). Even when "spurious" spin-echoes are rejected, it is estimated that the reproducibility of the measured self-diffusion coefficient lies only in the range ±5-15% if signal averaging is employed. Further investigation into the cause of these "spurious" spin-echoes is clearly required.

The remaining sections of this chapter are devoted to the design and construction details of the NMR probe, the magnetic field gradient coils, the gradient pulse timer and the gradient pulse power supply. Particular attention was paid to the minimisation of the various errors which have been discussed in this section. Preliminary experiments have indicated that there are a number of experimental precautions which must be observed if the spin-echo magnitude is to be accurately measured. These will be discussed in section 4.3. Finally, a section containing the gradient calibration and reproducibility experiments will be presented.

4.2. DESIGN AND CONSTRUCTION OF INSTRUMENTATION

4.2.a. Probe and Gradient Coil Design

The primary design criteria for the ^1H NMR probe are set by the commercial JEOL (Tokyo, Japan) JNM-FX60 high resolution spectrometer to which the probe is connected. The ^1H resonant frequency in the magnetic field (B_0 = 1.4 Tesla) of this spectrometer is 60MHz, and the probe must fit in the 32mm gap between the magnet pole pieces. The output impedance of the pulsed rf transmitter is 50Ω (which should be matched for maximum power transfer), while the receiving electronics require that the NMR signal be preamplified before being passed to the spectrometer for subsequent processing. Apart from these basic physical and electronic constraints, the design of the probe must also be consistent with the requirements for error minimisation, as outlined in section 4.1.

Various aspects of the design of NMR probe electronics have been covered in articles by Clark and McNeil[51], Lowe and Tarr[52], and Anderson[53]. The design of magnetic field gradient coils for PFGNMR experiments has been treated by, among others, Tanner[46], Odberg and Odberg[54], and Webster and Marsden[47]. Working from the design criteria set out in these articles, a 60MHz low-resolution probe containing 0.15 Tesla.$m^{-1}A^{-1}$ field gradient coils has been constructed by Dr P.T. Callaghan. Contributions from the author amount to construction of the sample-tube holder and homogeneity-coil constant current supply. The design criteria for probe construction are now reviewed.

One of the important components of a pulsed NMR spectrometer is the electronic circuitry which is used to couple power from the rf transmitter into the sample coil, and then to convert the precessing nuclear magnetisation into a signal at the input of the receiver preamplifier. The basic requirements for such a circuit are: efficient transfer of power from the transmitter to the sample coil, protection of the preamplifier from the destructive overloads of the transmitter, rapid ring-down (decay) of the transmitter pulse (60v-pp from the JEOL rf transmitter) to the milli- or microvolt levels of the FID signal, and a high signal-to-noise ratio for observation of the FID.

The above points are included in the design of a single coil (i.e. one coil used for both rf irradiation and reception) series resonant circuit presented in an article by Clark and McNeil[44].

Using the criteria set out by Clark and McNeil, the circuit shown schematically in Figure 4.1.a has been constructed. This circuit consists of three subsystems which are turned to the operating frequency: the transmitter output circuit (L_1, C_1, R_1), the sample coil circuit (L_2, C_2, R_2) and the preamplifier input circuit (L_3, C_3, R_3, R_{in}). C_1 includes any transmitter output capacitance, C_3 includes the preamplifier input capacitance, and R_{in} is the preamplifier input resistance. It was found advantageous to shield the discrete components in the circuit in order to minimise rf pick-up and noise.

The transmitter is connected to the sample coil L_2 via a coaxial cable which has a characteristic impedance of 50Ω. The length of this cable was chosen to lie in a range such that the cable acts as the inductor L_{1a}. The length of the cable within the inductive-range was set to give a circuit input impedance, when tuned by C_1, equal to the rf transmitter ouput impedance. When a transmitter pulse occurs, the diodes D_1-D_4 become short circuits. The tuned pair L_2C_2 represents a very low impedance in parallel with the much larger impedance of L_3, and so all the rf current appears in the sample coil L_2. The preamplifier is protected from damaging overloads by the effective short circuit diode pair D_3 and D_4, and by the high impedance of L_3.

Following the rf transmitter pulse, the circulating current in L_2 must quickly ring down so that the FID signal induced in L_2 can be observed. This requires that Q_T, the quality factor of the effective transmitter load circuit, be kept as small as possible. For the circuit shown in Figure 4.1.a,

$$Q_T \propto (L_1+L_2)/(R_1+R_2)$$

Since L_1 has already been determined, Q_T can be made small by keeping L_2 small or by increasing R_1 and R_2. However, any reduction in L_2 reduces the magnitude of the rf magnetic field, B_1 ($\propto L_2$). Increasing R_1 or R_2 limits the current through L_2 and so also reduces B_1. In

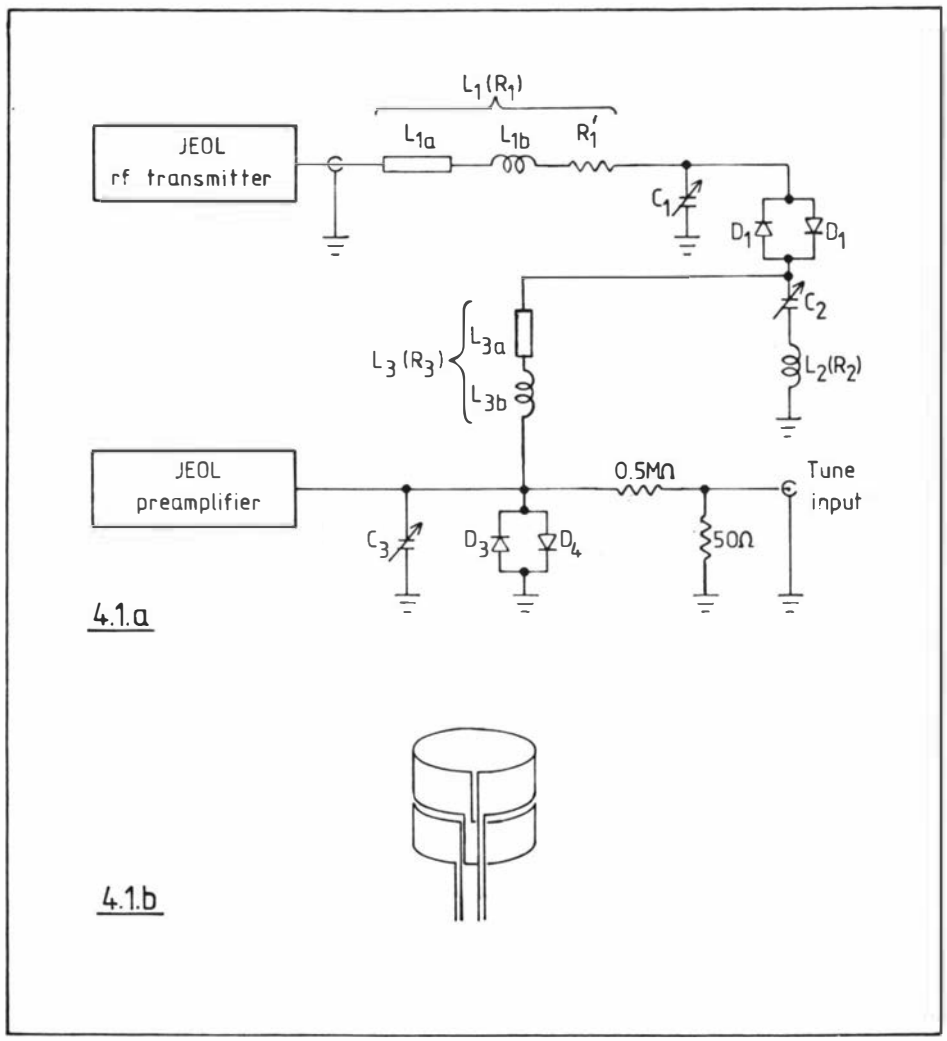


Figure 4.1.a. A single coil series resonant circuit - after Clark and McNeil, reference 51. The resistor R_1' is included to reduce the transmitter pulse decay time to ~1.5μs. L_1 is adjusted to present a 50Ω load to the rf transmitter (which has z_0=50Ω) when tuned by C_1. L_1C_1, L_2C_2 and L_3C_3 are tuned pairs. D_1-D_4 are high speed silicon diodes.

4.1.b. The configuration of the rf irradiation/reception coil - after Lowe and Tarr, reference 52. The coil is constructed from 0.17mm copper shim, and is 7mm long by 9mm in diameter.

practice, the values of L_2 and R_1 are arranged (R_1 by adding the resistor R_1') such that a sufficiently large B_1 is generated while Q_T is held to the desired low value. To be consistent with this compromise solution the inductance L_2 needs to be kept much smaller than is practical for a wire-wound coil of dimensions suitable for use as a sample coil. For this reason, following Lowe and Tarr[52], a 2 turn coil was wound from 0.17mm copper shim. This coil, which is illustrated in Figure 4.1.b., provides good rf field homogeneity over a sample volume equal to the coil's length[52].

Following the ring-down of the transmitter pulse, the small voltage levels induced in L_2 by the precessing magnetic moments can be observed. For small voltage levels the diodes D_1-D_4 behave as open circuits and so the receiver circuit consists of the preamplifier input stage and the elements L_2, C_2, L_3, C_3. The major problem during the FID reception stage lies in maximising the signal-to-noise ratio in the receiving circuit. A detailed Nyquist noise analysis of the circuit does not yield any generally applicable criteria for noise reduction[51], with Clark and McNeil suggesting that a low-noise, high input impedance preamplifier be employed, while keeping R_2 and R_3 as small as possible. Thus, L_3 should be chosen to minimise R_3 while ensuring that $Q_3(\propto L_3/R_3)$ remains sufficiently small for the receiver circuit to follow a rapidly decaying FID. Clark and McNeil suggest $Q_3 = 2Q_2$ as a practical design criteria. The preamplifier used in this work is a tuned, single stage JEOL 60MHZ FET preamplifier, although any other tuned, rf, low-noise preamplifier[55] would suffice.

A second aspect of importance in the design of an NMR probe for PFGNMR experiments is the provision of a large, uniform magnetic field gradient over the sample volume. It is well known[46] that two coaxial, circular coils with opposed magnetic fields (an opposed Helmholtz pair) produce the largest region of uniform field gradient along their common axis if their radius equals $2/\sqrt{3}$ times their separation distance. Other coil configurations can also be employed to provide uniform magnetic field gradients[47,54], but we have chosen the opposed Helmholtz pair for constructional simplicity.

In a PFGNMR experiment, the gradient coils are located between the pole-pieces of an electromagnet. The presence of nearby non-saturated magnetic material contributes an additional magnetic field by induced

dipole alignment, over and above the field due to conduction in the coils[46]. The above relationship between the coil radius and separation no longer describes an opposed Helmholtz pair giving the largest region of uniform field gradient over the sample when these induced fields are present[46]. However, by using the method of images (see, for example, reference 56), Tanner has calculated the optimum coil shape for an opposed Helmholtz pair placed between magnet pole-pieces located at $z = \pm 1$. The results of Tanner's calculations were presented in the graph reproduced here in Figure 4.2. A surface of revolution of curve A in Figure 4.2 about its abcissa has the correct shape for the gradient coils. A derivation of the equation describing curve A is given in Appendix 1. It is the midsurface of the windings which should coincide with curve A, and sufficient turns should be wound so that the field associated with the leads is unimportant: 18 turns has been found to be adequate[46].

In this work a pair of 19-turn coils were wound from 26-swg enamelled copper wire on a Teflon former, which was constructed to conform as closely as practically possible to the shape given in Figure 4.2. The approach of the coils used in this work to the optimum shape (curve A) is shown in Figure 4.2, and the variation in the magnitude of the field gradient over the z-axis of the sample volume was calculated to be $0.143 \leq G \leq 0.144$ Tesla.$m^{-1}A^{-1}$. The relative positions of the sample dewar, gradient coils and rf coil are shown in Figure 4.3. To ensure mechanical stability the rf coil was bound to the outside of the sample dewar with Teflon tape. Teflon tape also forms the insulation between the right hand lead and the lower turn of the rf coil (see Figure 4.1.b).

A photograph of the completed PFGNMR probe is shown in Plate 1. There are three sources of error in the PFGNMR experiment that can be minimised at the overall probe design stage. These are eddy current generation, spurious sample movements and variations in the magnitude of the steady magnetic field. Where possible Teflon, laminated plastic, glass and Perspex have been used as construction materials for the probe in order to reduce eddy currents. The NMR sample tubes are held firmly in place by a well-seated holding arrangment shown in Figure 4.3 and Plate 1. Variations in B_0 can be minimised by including in the probe an external lock. This device consists of a ^2H sample whose resonance frequency is compared with a frequency standard, with any frequency difference forming the error signal in a feedback loop controlling B_0.

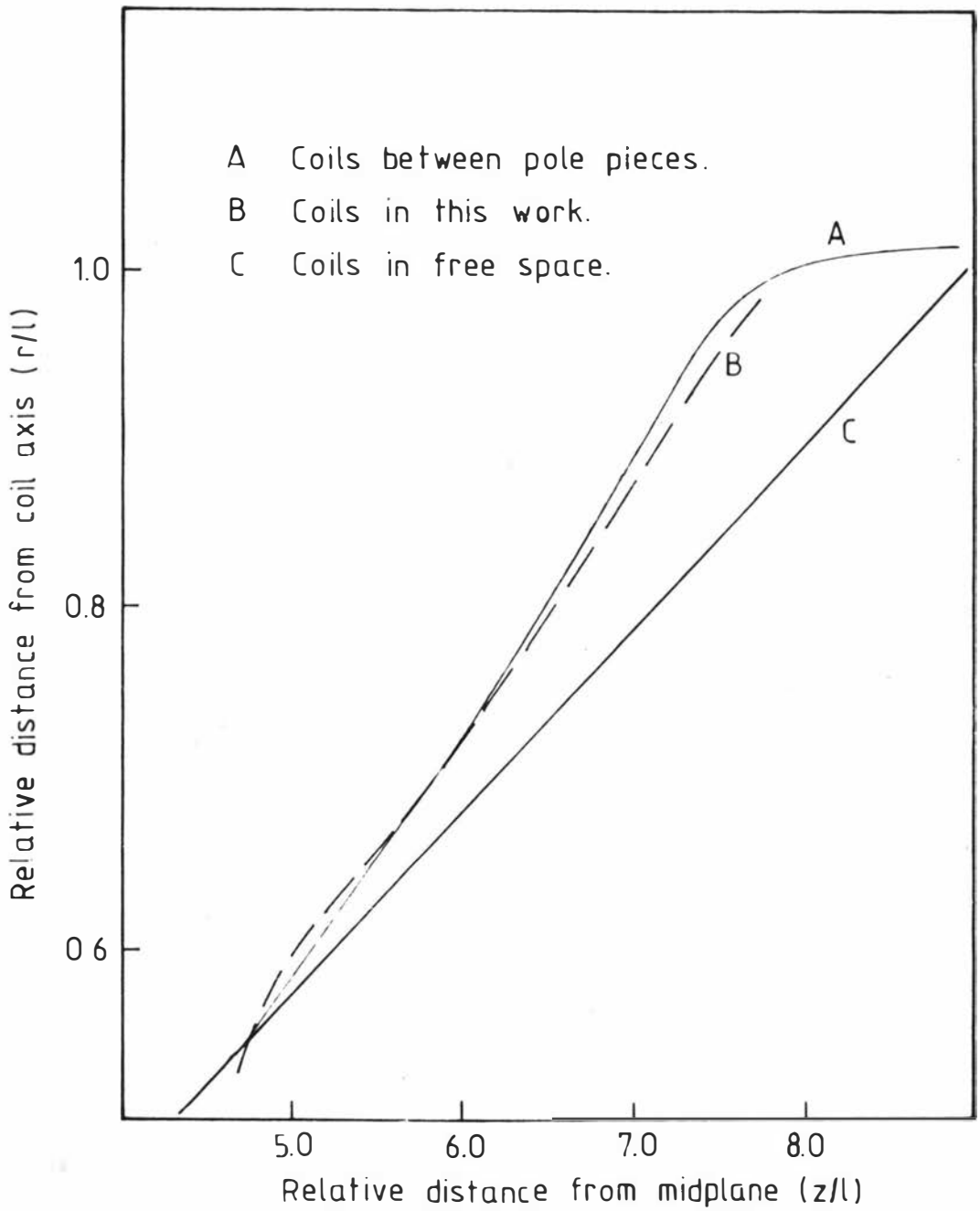


Figure 4.2. Coil shape for the generation of uniform magnetic field gradients. A surface of revolution of curve A about the abscissa has the required shape for coils in an opposed Helmholtz configuration to give the largest region of most homogeneous field gradient along the coil axis when the coils are located between magnet pole-pieces. r is the coil radius measured from the coaxial coil axis, and z is the distance to the coils as measured from a midplane centrally located between the coils at right angles to the coil axis. 2l is the z-axis separation of the magnet pole-pieces.

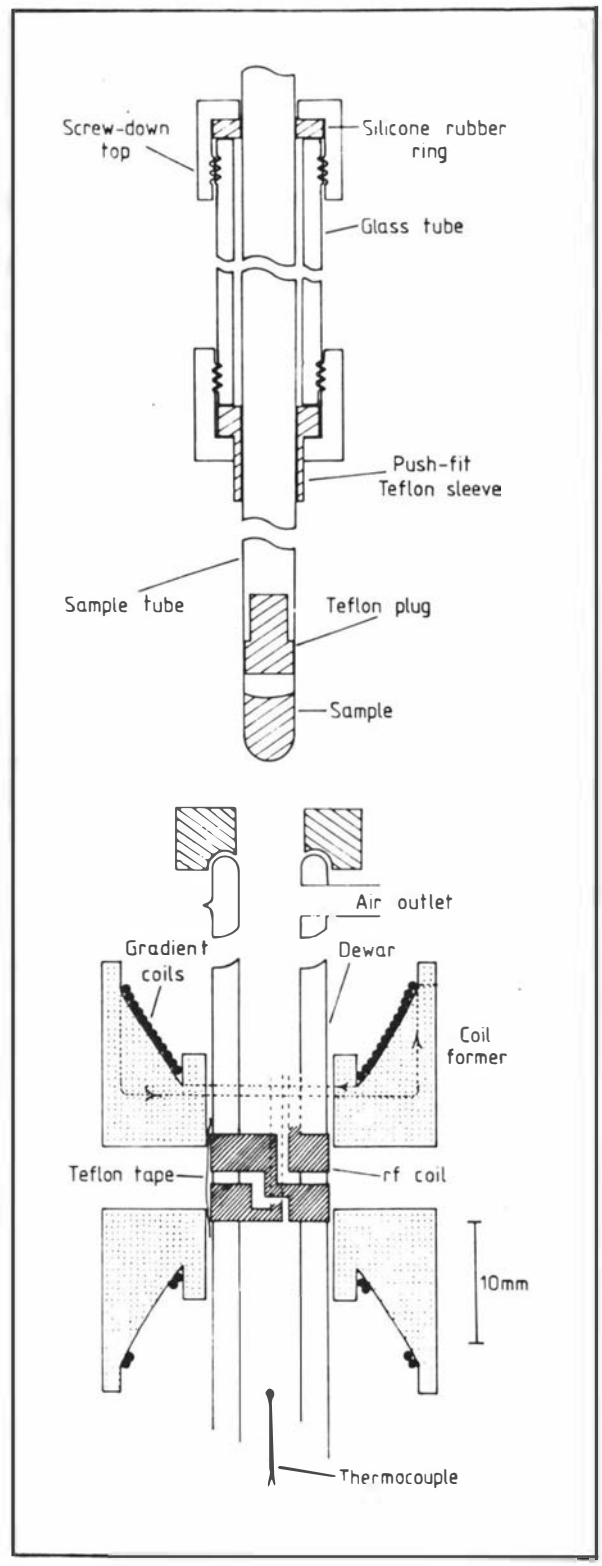


Figure 4.3. The sample space geometry, and sample holder. The viewing port along the axis of the Helmholtz coils allows the rf coil to be accurately centred. The sample dewar isolates the gradient coils from the sample temperature, and during experiments a stream of constant temperature air is directed at the coil base.

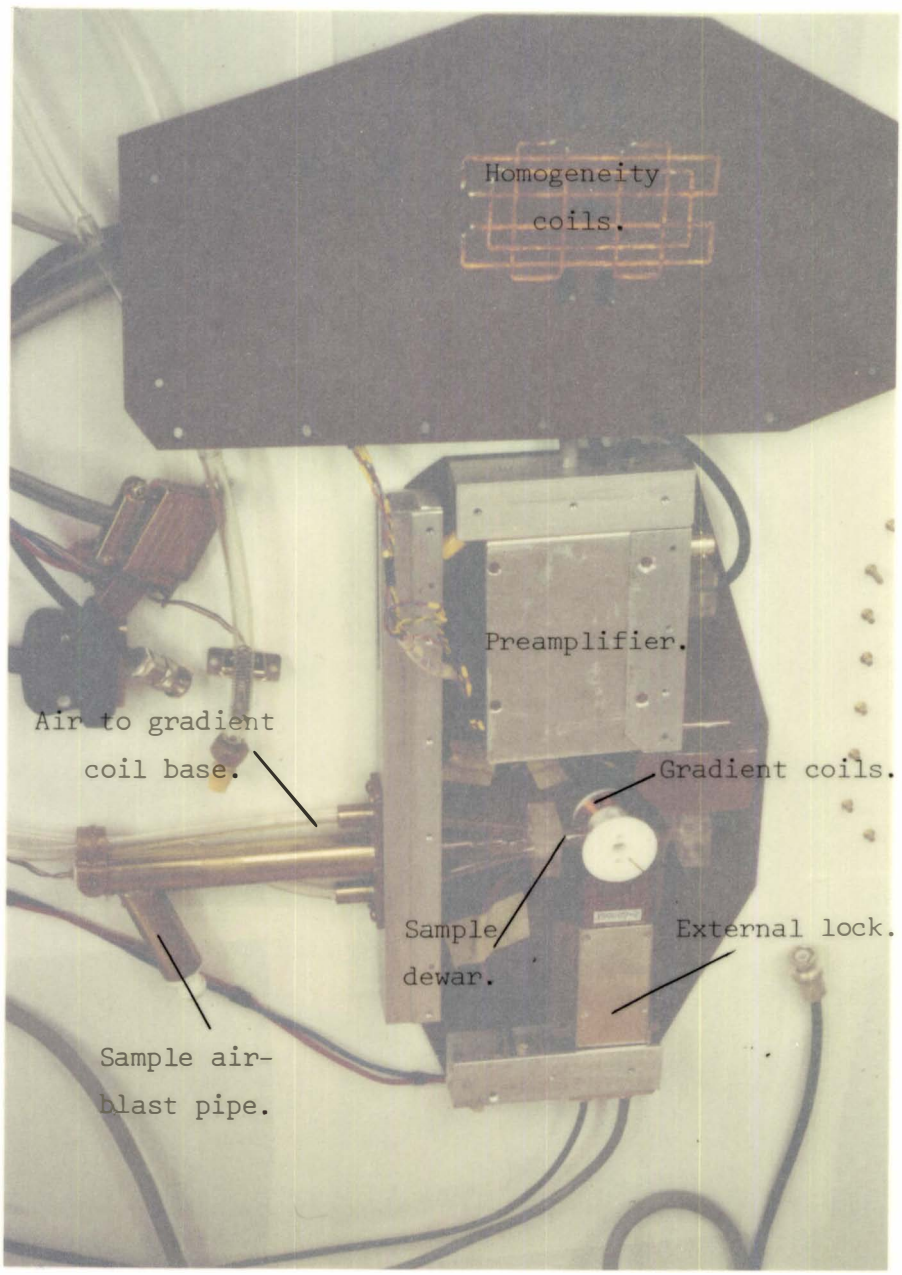


Plate 1. The low resolution probe used in the PFGNMR experiment.

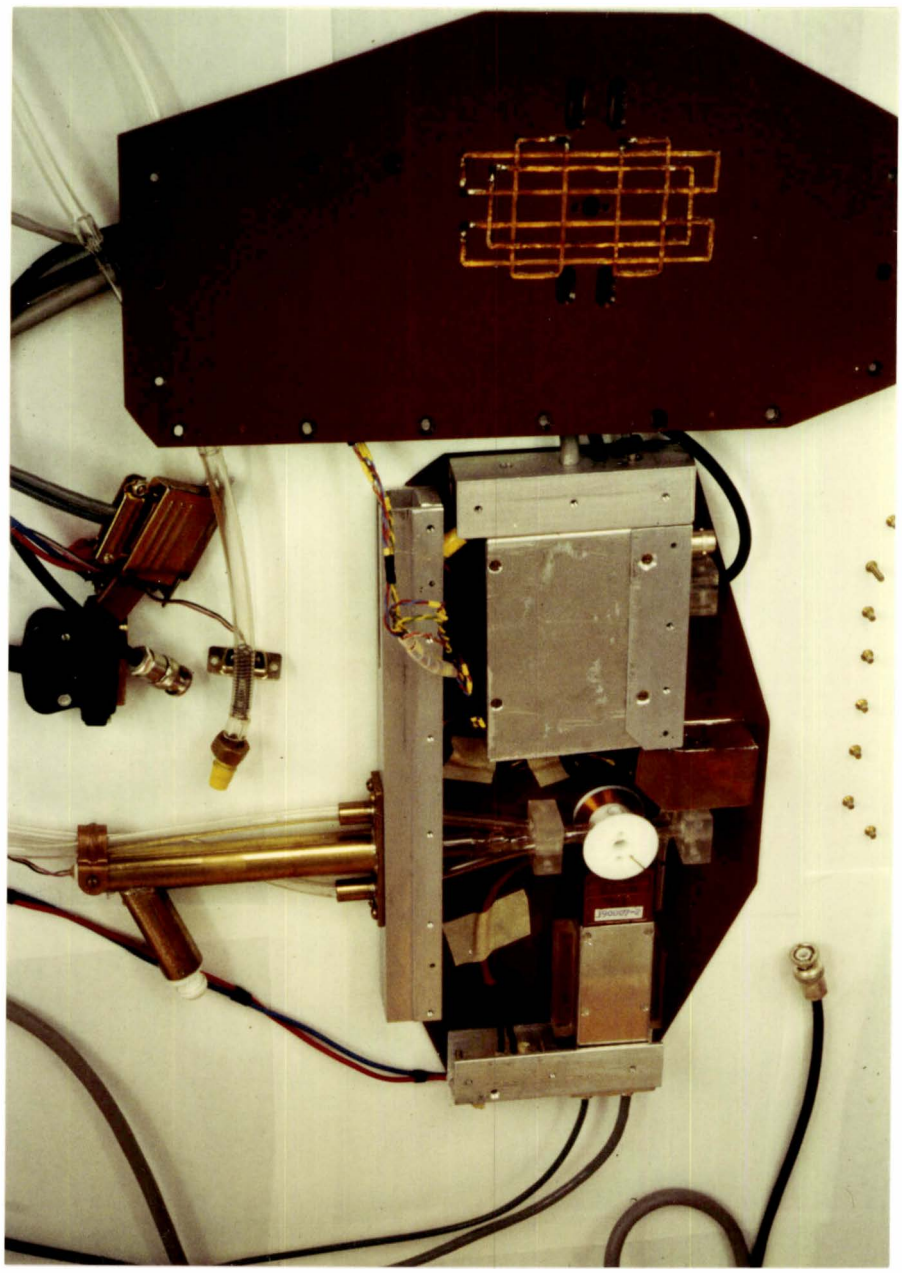


Plate 1. The low resolution probe used in the PFGNMR experiment.

Also shown in Plate 1 are the $\partial B_0\underset{\sim}{k}/\partial x$, $\partial B_0\underset{\sim}{k}/\partial y$ and $\partial B_0\underset{\sim}{k}/\partial z$ homogeneity coils included in the probe to aid the resolving of ^1H resonances in the frequency domain. The improved resolution afforded by these coils also provides a valuable increase in the signal-to-noise ratio when working with dilute molecular species. The homogeneity coils were designed according to the criteria set out by Anderson[53], and the coils were constructed by inlaying copper shim into the outer surface of the laminated plastic probe box sides. The current for the coils is provided by three constant current power supplies built around the Motorola MC1446 integrated circuit (a comprehensive power supply IC - see reference 57). The current is continuously variable in the range $\pm$(0-1) amps, with a current regulation of better than 0.01%.

4.2.b. A Digital Pulse Programmer for Pulsed Field Gradient Experiments.

It is the function of the pulse programmer to provide control pulses for the sequentially timed intervals d, Δ and δ(as defined in Figure 3.2). The experimentally important intervals δ and Δ must be both precise and accurate over a wide range of times (100's of microseconds to 100's of milliseconds), and also possess a high degree of reproducibility. The accuracy and reproducibility of the timing pulses is best acheived by using digital logic circuitry in combination with clock pulses derived from a quartz crystal. The schematic circuitry shown in Figures 4.4.a,b,c represents the essential features of a digital pulse timer designed and constructed as part of this work.

The circuit, which utilised 7400 series TTL integrated circuits throughout, has been designed so that the experimental parameters Δ and δ, as well as the time d, can be set directly on BCD coded thumbwheel switches. A 1MHz signal, derived from the JEOL spectrometer crystal clock, provides the clock pulses entering the divider chain. Timing pulses appropriate to any particular experiment can be selected using NAND gates as detailed in Figure 4.4.b. The precision of the output pulse timing is determined by the number of up/down counters (74190's) in cascade. Figure 4.4.a thus represents a programmer with a precision of two digits in each of the intervals d, Δ and δ. Such a precision has been found to be quite adequate for our PFGNMR experiments. The

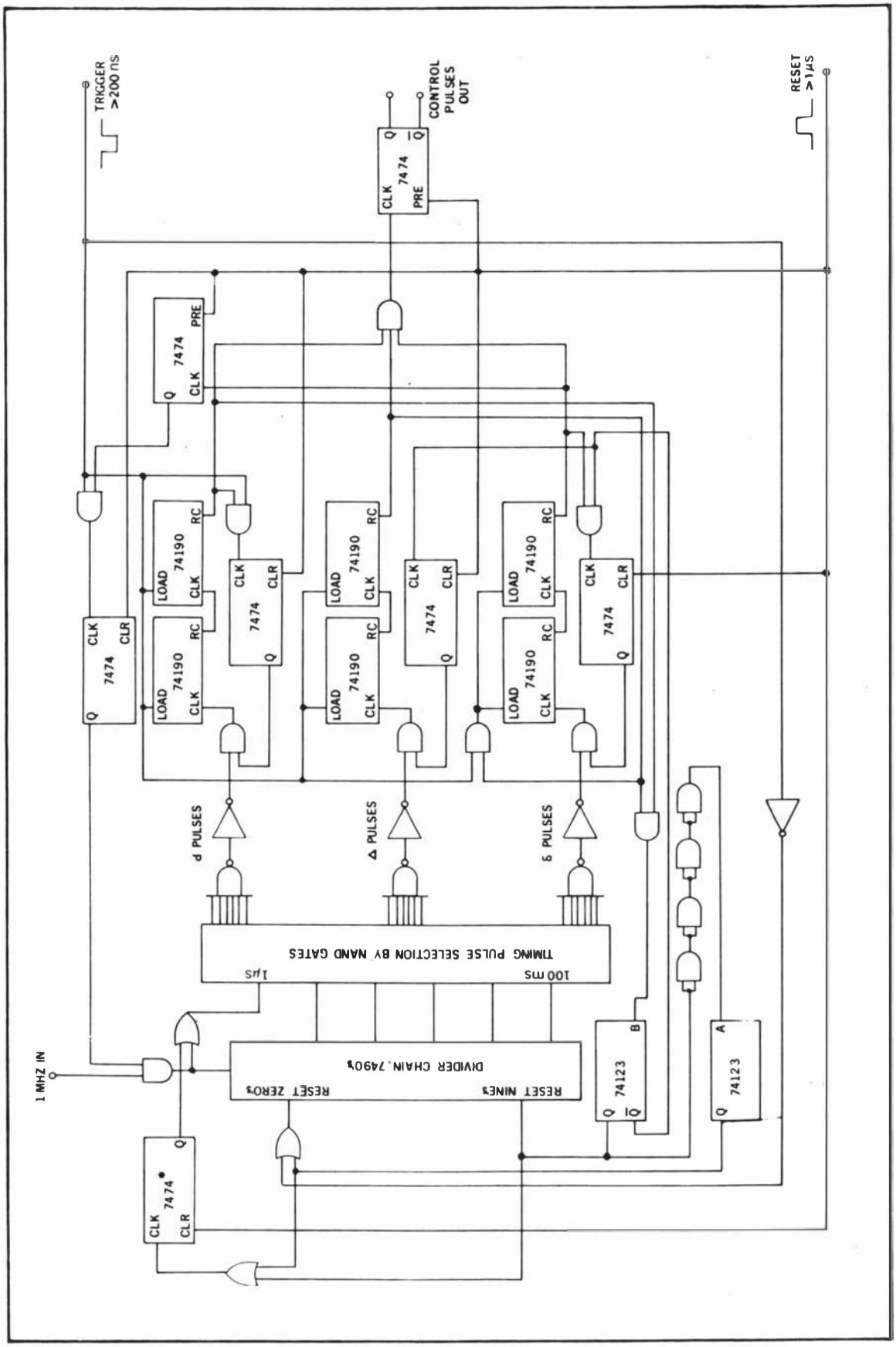


Figure 4.4.a. The TTL pulse timer schematic circuit diagram.

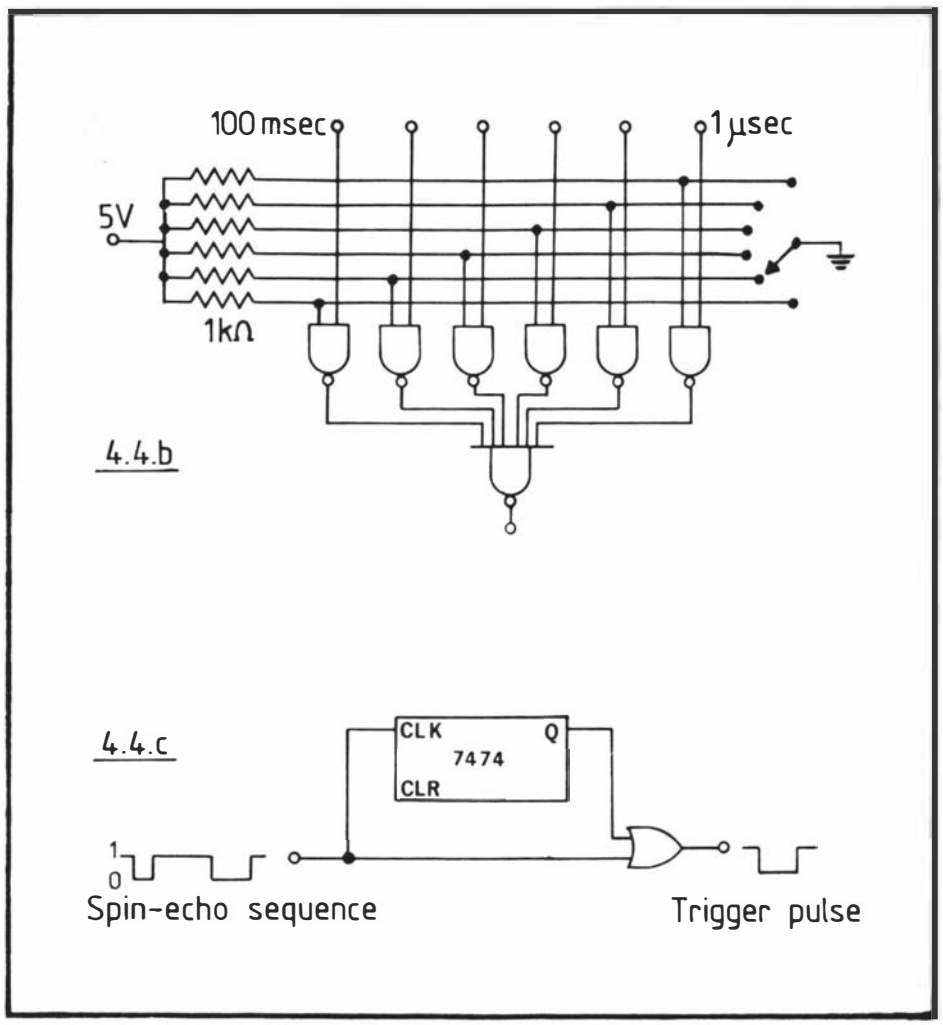


Figure 4.4.b. The timing pulse selection circuitry.

4.4.c. The circuit modification required when using a two-pulse, spin-echo sequence as a trigger.

up/down counters are used in the down counting mode, and are directly connected to the thumbwheel switches. A load command is provided by the trigger pulse (see Figure 4.4.a) to initially set the d, Δ and δ counter contents, and the δ counter is again loaded just before the end of the Δ interval in preparation for timing the second δ interval.

At power turn-on a reset pulse (> 1μs) must be provided to the appropriate PRE or CLR inputs of the D flip-flops (7474's) to set their initial output states. The circuit shown in Figure 4.4.a requires only a single trigger pulse to initiate timing. The two pulse spin-echo rf logic pulse sequence provided by the JEOL spectrometer (which is used as the trigger in this work) is easily converted into the required single trigger pulse by including the circuitry, shown in Figure 4.4.c, before the trigger input of Figure 4.4.a. When the gradient two-pulse sequence reaches completion, the 1MHz clock access to the divider chain is disabled. The appearance of the falling edge of the next trigger pulse readies the timer for a new sequence (i.e. loads the down counters, and sets the outputs of the divider chain to zero), and timing proceeds from the rising edge of the trigger pulse. In the JEOL spectrometer the 1MHz clock and rf logic pulses are independently generated, which results in there being an uncertainty of $\pm$1μs in the interval d. As the accurate timing of this interval has no experimental significance, this uncertainty is of no consequence. The circuit presented does not require the NAND gate range switches (see Figure 4.4.b) to be "debounced", or to make-before-break, as false clocking of the counters is prevented by their inhibited CLK inputs (inhibited by the 7474s shown beneath each counter set). Further details concerning the pulse programmer are given in Appendix 2.

4.2.c. A Power Supply for Pulsed Field Gradient Generation

The design of a power supply for the generation of current pulses, using the Helmholtz coils as a load, needs to be undertaken with considerable care as the PFGNMR experiment is very sensitive to any gradient pulse mismatch[58]. The PFGNMR experiment requires that current pulses of between about 0.5 and 10 amps be passed through an inductor, with the rise and fall times of the current pulses being sufficiently fast to be consistent with the rectangular shape assumed

during the derivation of equation 3.7. The current pulses must possess a well regulated and highly reproducible amplitude and width, and both pulse amplitude and width must be independent of pulse separation. Several designs for pulsed current supplies suitable for a PFGNMR experiment have appeared in the literature, where rechargable batteries and transistor switches comprise the power supply[46, 58, 59]. All of these designs have disadvantages, with the most suitable power supply[58] possessing only a limited current regulation (1%). In order to achieve the design criteria of high precision and accuracy for the PFGNMR experiment, a pulsed power supply offering current regulation of 0.02% and full power bandwidth of ~65kHz has been assembled. This power supply, which is built around a modified commercial operational power supply (essentially an operational amplifier with a 10 amp. output stage), is now described.

A Kepco (New York, USA) JQE25-10M low speed, unipolar, operational power supply was adapted for high speed operation by the removal of the output capacitor, and by the addition of several phase shifting networks around the error amplifier to prevent oscillation. Further modifications to various components brought the specifications of the altered JQE25-10M up to those of the equivalent high speed model, OPS25-10M. (The various modifications were based on the circuitry of the OPS25-10M.) The power supply which is shown schematically in Figure 4.5, is operated in the constant current mode by sensing the voltage developed across a 50 watt, 20ppm temperature coefficient, 0.1000Ω precision resistor in series with the load. This voltage is compared to a temperature compensated voltage reference by means of an error amplifier which drives the output power transistors. The phase shifting networks (lag I and II in Figure 4.5) are adjusted for minimum ringing of the current pulses, while retaining the maximum rise-time. The optimum value of the feedback capacitance was found to be zero.

One of the simplest methods of providing current pulses in the load of Figure 4.5 is to step the reference voltage from zero to V_r by means of the circuit shown in Figure 4.6. However the resultant current pulses possessed far from optimum shape, as illustrated in Figure 4.6, and although various other direct switching schemes were employed none were found to be satisfactory. The short ramp and long tail, at the beginning and end of the current pulse respectively, appear to be associated with the charging and discharging of capacitors around the error amplifier.

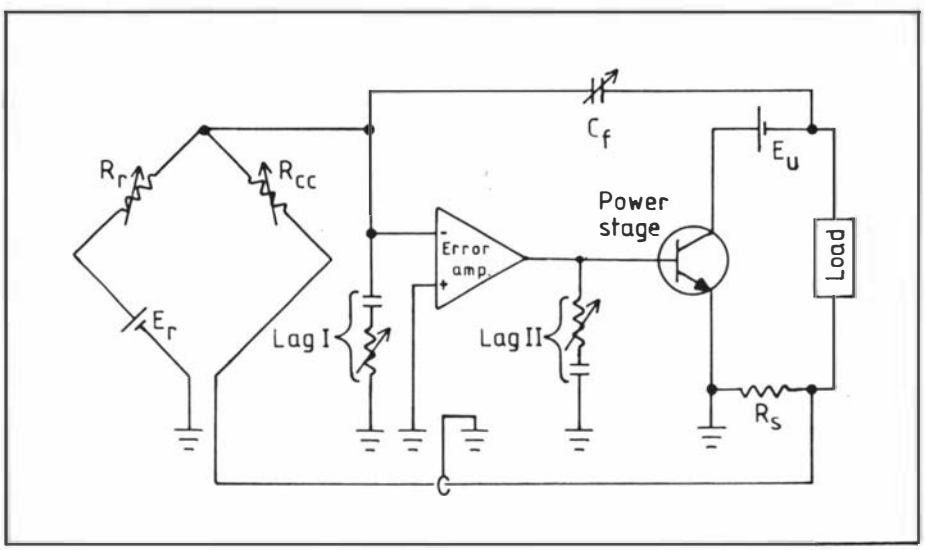


Figure 4.5. A schematic circuit diagram of the Kepco power supply, operating in the constant current mode. Lags I and II are phase shifting networks which are adjusted to prevent oscillation of the output current. The other components are the unregulated supply (E_u), sensing resistor (R_s), feedback capacitor (C_f), reference voltage (E_r), reference resistor (R_r) and current control resistor (R_{cc}).

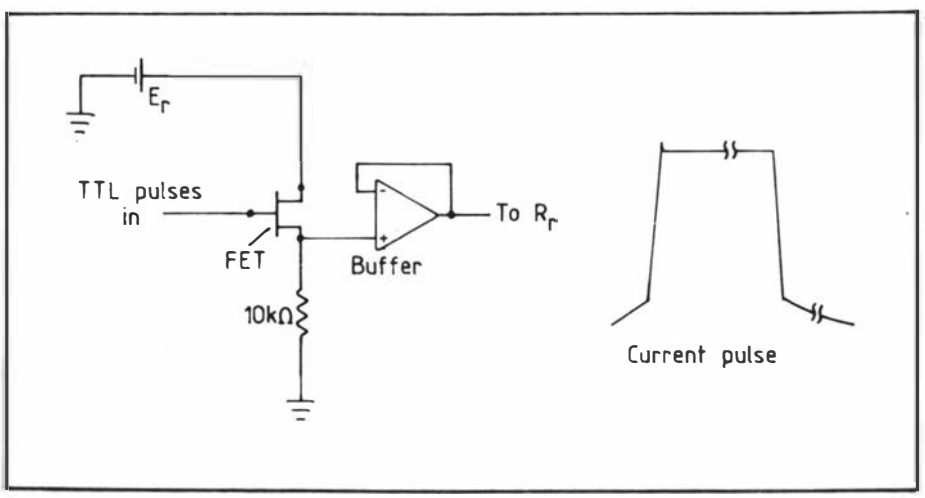


Figure 4.6. Programming the load current by stepping the reference voltage. The resultant current pulse observed in the load is also shown, where the small initial ramp is about 50μs long, the pulse width is 500μs and the long tail lasts about 1.5ms at an initial amplitude of 20mA. Such a pulse shape is unsatisfactory for accurate PFGNMR experiments.

By changing the time constants of lag I or lag II it is possible to alter the pulse shape.

Apart from non-ideal current pulse shape, a further problem was encountered with simple current switching schemes. During preliminary testing of the probe/power-supply/pulse-programmer / NMR-spectrometer system, the spin-echo was found to exhibit random variations in both phase and position (as previously noted by other authors). These spurious effects worsened as the magnitude of the current pulses was increased, but were not a function of rf-pulse/gradient-pulse separation and so were not eddy current effects. However, when the power supply was turned off, no random variations of the spin-echo were observed. Careful examination of the current flowing through the load with an oscilloscope, applied across R_S, revealed that small current pulses flowed through the load during the rf pulse. That the variations in the spin-echo phase and position are caused by rf pick-up, either at the sensing resistor or at some other part of the circuit, can be readily demonstrated by using longer rf pulses. If a 450°-τ-540° rf pulse sequence were used, the spurious gradient pulses became larger and the variations in the spin-echo worsened considerably. Why the variations should be random is not well understood, although Matson[57] notes that echo stability is improved if the gradient pulses are synchronised to the line frequency (50 Hz). This suggests that hum may also contribute to the pick-up in some manner. In any event it is apparent that the gradient coils should be isolated from the power supply at other than during the times δ.

Both the pulse shape and rf coupling problems are solved by the circuitry shown in Figure 4.7.a. The current pulses generated by this circuit have the shape shown in Figure 4.7.b. The width of the current pulses, as observed by monitoring the voltage across R (see Figure 4.7.a) via a storage oscilloscope with a differential input, shows excellent accuracy and reproducibility with the leading and trailing edges of sucessive pulse pairs coinciding over all pulse widths and spacings examined.

The current pulses in the load (the Helmholtz coils) are generated by externally switching the current path with the Darlington connected transistor sets Q_A and Q_B. During δ, the Q_A transistors are on and Q_B

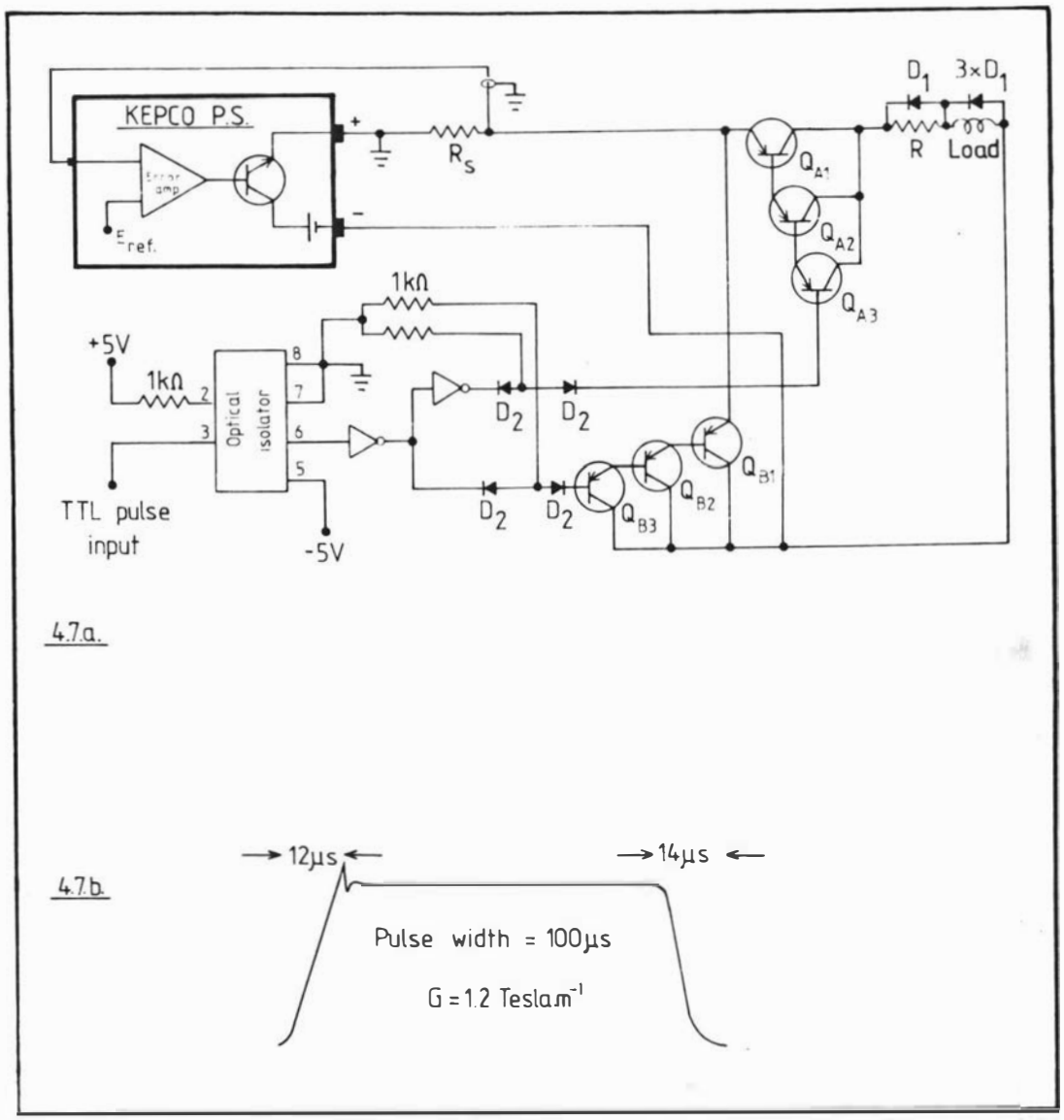


Figure 4.7.a. The circuitry used for the generation of gradient pulses in this work. The transistors are Texas Instruments TIP36A (Q_{A1}, Q_{B1}), TIP30A (Q_{A2}, Q_{B2}) and 2N3906 (Q_{A3}, Q_{B3}); D_1 is a high speed power diode (BYX55); D_2 are high speed signal diodes (1N4148) and R is a 30 Watt, 0.1Ω wirewound resistor. The optical isolator is a Hewlett-Packard HP4350, chosen for its 2MHz bandwidth.

4.7.b. Characteristics of the current pulse generated by the circuitry shown in Figure 4.7.a. The rise and fall times of the pulse do not change significantly with pulse magnitude. (The diagram is taken from an oscillograph, and has been drawn to scale.)

off, thus allowing current to flow through the gradient coils. At all other times Q_A are off and Q_B on, and the gradient coils are isolated from the circuit. The optical isolator (an HP4360, chosen for its 2MHz bandwidth) provides both a convienient (+5V, 0V) to (0V, -5V) logic voltage level translation as well as protection for the TTL pulse programmer in the event of transistor (Q_A or Q_B) failure. The transistors are protected from large inductive voltage spikes encountered during current turn-off by placing high speed power diodes in parallel with R and the gradient coils. The gradient coils, which would deform if a continuous current of ~10 amps were passed through them, are protected by a series 3 amp fuse. We have found, as have others [59], that some fuse holders do not afford adequate contact with the fuse which results in spurious pulse shapes. Fuse holders, and any plugs in series with the gradient coils, must therefore be chosen with some care.

The use of the Kepco constant current supply in the circuit configuration shown in Figure 4.7.a allows, then, the generation of current pulses which match the stringent requirements of a PFGNMR experiment. By switching the external current path and thus eliminating rf pick-up, the major problem of spin-echo position and phase instability has been eliminated, and so signal accumulation can be performed in a routine manner. Also, problems associated with capacitor charging and discharging around the Kepco error amplifier are circumvented by this circuit configuration since the system now suffers only minor excursions away from the equilibrium output current situation. The circuit shown in Figure 4.7.a also has the advantage that the magnitude of the current pulse in the coil can be determined at any time by measuring the voltage drop across the 0.1000Ω precision resistor, and in this work a 4½ digit calibrated DVM has been utilised for such measurements.

4.2.d. The NMR Spectrometer

The great advantage of interfacing the PFGNMR instrumentation to a computer controlled NMR spectrometer, in this case a JEOL JNM-FX60, is the ease and flexibility with which data can be accumulated, manipulated and analysed. A block diagram of the FX60 is shown in Figure 4.8, together with the additional instrumentation required for

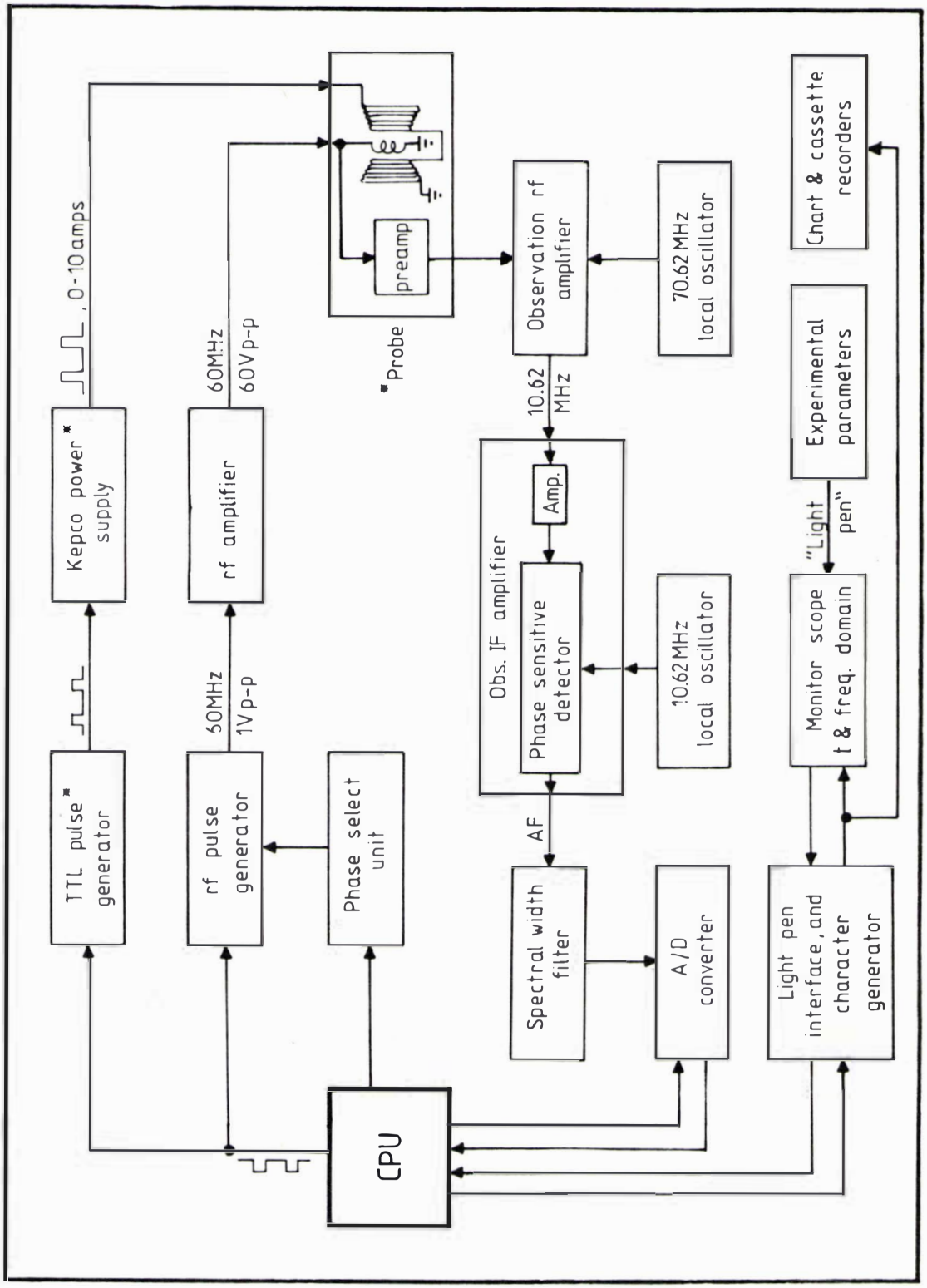


Figure 4.8. A block diagram of the JEOL JNM FX-60 NMR spectrometer. The instrumentation added for the PFGNMR experiment is shown with a * superscript.

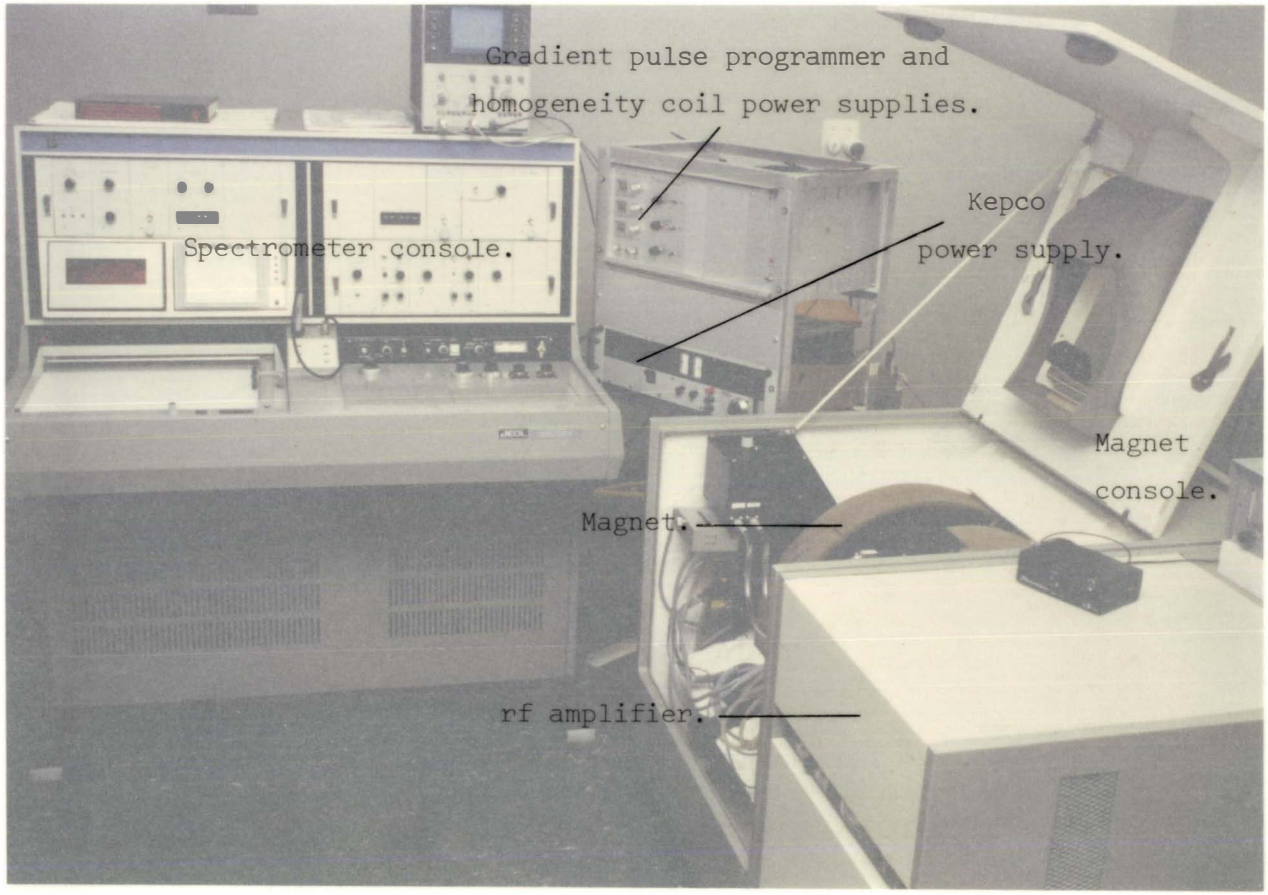


Plate 2. The JEOL JNM FX-60 NMR spectrometer, and the instrumentation for the PFGNMR experiment.

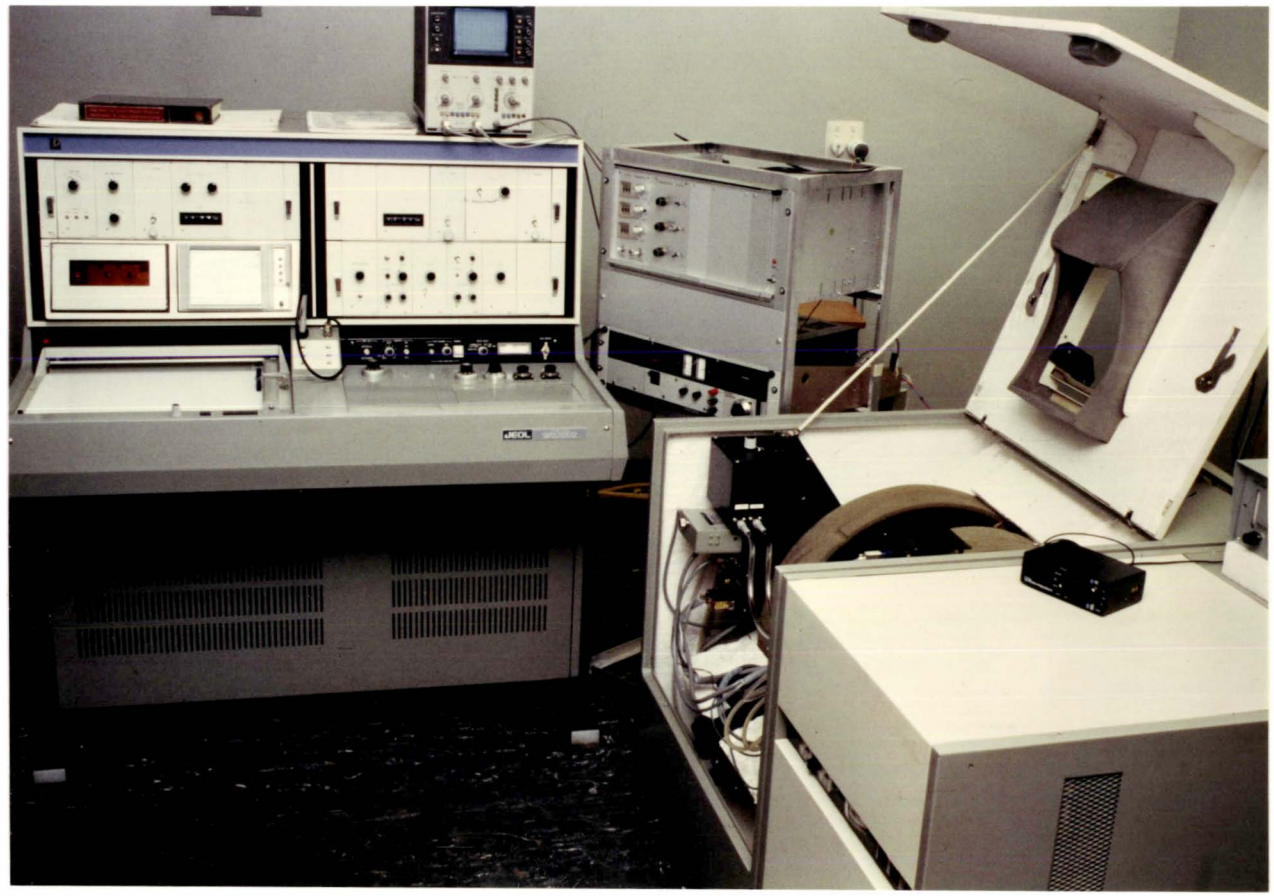


Plate 2. The JEOL JNM FX-60 NMR spectrometer, and the instrumentation for the PFGNMR experiment.

the PFGNMR experiment. Temperature control is achieved by a conventional hot air feedback system (JEOL JES VT-3) which uses a thermocouple as the sensing element (see Figure 4.3). A precision of better than $\pm 0.5^{o}C$ can be obtained with this system over a period of ten hours.

The rf experimental parameters (rf pulse widths etc) are entered into the spectrometer computer (a Texas Instruments 980-A model) via a light-pen system. Having adjusted the NMR signal to maximum resolution and stabilised B_0 by engaging the ^2H external lock, data aquisition proceeds routinely under computer control. Spin-echoes are phase-sensitive detected, digitised and accumulated in the computer memory (see Figure 4.8). In the case of PFGNMR experiments, phase-sensitive detection offers several advantages over alternative detection techniques[60]. First, phase-sensitive detection results in the NMR signal being shifted to the audio-frequency (AF)-range, where a low-pass filter can be used to improve the time-domain signal-to-noise ratio (see Figure 4.8). Second, phase-sensitive detection preserves the phase information in the rf NMR signal, and if time domain sampling of the spin-echo begins at $t=2\tau$, the time domain data can be Fourier-Transformed to the frequency domain. Frequency domain analysis considerably improves experimental signal-to-noise by effectively applying a band-pass filter. In the frequency domain spin-echo amplitudes are obtained by integrating the peak area. In this work the zero peak amplitude is set by placing a baseline through the centre of the noise on either side of the peak.

4.3. EXPERIMENTAL CONSIDERATIONS

4.3.a. Sample Related Considerations

In this work thin-wall sample tubes of 4.0mm external diameter were used, and the samples were ≤ 5mm in height as measured from the bottom of the tube. To prevent evaporation, small teflon plugs were made to press-fit into the sample tube (see Figure 4.3). A 0.2mm diameter hole was drilled through the plugs to allow pressure equalisation, and the plugs were located ~2mm above the sample miniscus. Apart from obviating sample evaporation during even the longest experimental runs, the plugs should also reduce temperature gradients in the sample.

To measure sample temperatures, the sample tube was replaced by a similarly teflon plugged tube containing a 5mm glycerol sample and a thermistor, with the bead of the thermistor located ~2.5mm from the bottom of the tube. The thermistor had previously been calibrated to $\pm 0.01^{\circ}C$ with the HP2801A thermometer mentioned earlier (Chapter 2). Measurements with the thermistor indicated that the sample reached thermal equilibrium ~10 minutes after being placed in the probe. Removal and replacement of the thermistor sample tube did not perturb the JEOL temperature control system, and the JEOL temperature control specification of $\pm 0.5^{\circ}C$ has been confirmed by measurements over a 10 hour period, with better short term precision observed.

4.3.b. Signal Related Considerations

For the experiments reported in this thesis the gain of the incoming signal was always adjusted to utilise at least 10 bits of the A/D converter, thus giving a digitisation precision of at least 0.1%. Spurious DC signal components arising from various amplifier offsets can reduce the effective A/D dynamic range available to the NMR signal, and also such components must be excluded when the NMR signal amplitude is being measured in a PFGNMR experiment. DC offsets can be a particular problem when weak signals are being studied since the requirement for adequate digitisation precision is only satisfied by

high amplifier gains, with a corresponding increase in the DC offset terms being presented to the A/D converter.

The JEOL spectrometer has two features which effectively eliminate DC offsets. First, the A/D converter has both coarse and fine offsets to balance incoming and internally generated DC terms. Second, a phase alternating pulse sequence (PAPS) was employed in which every second $90^{\circ}|_{x}$-τ-$180^{\circ}|_{y}$ rf pulse sequence is applied along the negative x' and y' axes by phase-shifting the rf pulses by π radians (see Figure 3.1, and caption), while at the same time alternating the sign of the A/D converter. This has the effect of cancelling any residual DC terms (such as those caused by thermal drifts of the amplifier offsets) and also provides cancellation of any coherent "noise" sources, such as stray rf pick-up in the necessarily unshielded rf irradiation/receiver coil in the probe. This last problem has been encountered when experiments were performed on systems with weak NMR signals.

During the course of a PFGNMR experiment, the magnitude of the NMR signal was sometimes found to exhibit a small drift which could not be attributed to sample evaporation. This small drift was compensated for by occasionally re-measuring the magnitude of the unattenuated [A(0)] signal (see equation 3.7). Small, long-term drifts were also observed in the output current of the Kepco power supply, and these were taken into account by directly measuring the voltage across R_S for each setting of R_{CC} (see Figure 4.5).

4.3.c. Restrictions on Gradient Pulse Parameters.

Any PFGNMR experiment is limited by the requirement that the contribution of G to the dephasing of the nuclear spins be much greater than the contribution from the residual inhomogeneities (g_0) in the steady field. In a PFGNMR experiment this is tantamount to ensuring that

$$\tau g_0 << \delta G. \qquad (4.1)$$

An estimation of g_0 can be obtained from the half-height linewidth of a simple molecular species, for example benzene. With the homogeneity coils adjusted for typical frequency resolution, the half-height

linewidth of an ~4mm benzene sample was 34Hz (see Figure 4.14) which corresponds to a residual gradient of 0.2 milli-Tesla.m^{-1}. Equation 4.1 should be considered whenever the combination of low currents, small gradient-pulse widths and large rf-pulse separations is employed.

Eddy currents, also, will place certain restrictions on the gradient pulses (as discussed in section 4.1). Although eddy currents have been minimised by appropriate probe design, the effect that any residual eddy currents have on the PFGNMR experiment must be ascertained. When eddy currents are present, the rate of decay of the FID in the "tail" of the gradient pulse is proportional to $g_0 + g_e$, where g_e is the eddy current induced gradient. By using the pulse sequence shown in Figure 4.9, the initial slope of an on resonance FID can be compared with and without a gradient pulse for a range of τ'. Following a 1.5 Tesla.m^{-1} field gradient pulse, with τ' = 1ms, no change was observed in the FID implying g_e was negligible compared with g_0, that is g_e certainly $\leq$ 0.01 milli-Tesla.m^{-1} at 1ms after the gradient pulse. When τ' = 0.5ms the FID shows a small initial slope change: at worst $g_e \sim 15\%$ of g_0 that is g_e certainly $\leq$ 0.03 milli-Tesla.m^{-1}. In PFGNMR experiments the gradient-rf pulse spacing is always $\geq$ 0.5ms (in this work), and so the problem of inversion of the eddy current "tail" by the 180° rf pulse in a normal PFGNMR experiment need not be considered. However, since eddy currents are present, even though they may be small, the gradient pulses will deviate from the rectangular shape assumed during theoretical derivations. The effect of the shape deviations can be assessed experimentally by performing a PFGNMR experiment on a given sample and observing the measured diffusion coefficient as a function of decreasing gradient pulse width. Such an experiment was performed using a 0.001M copper sulphate solution: so called doped water which has T_1, T_2 < 0.2s (due to dipolar relaxation) and so allows rapid accumulation of data for noise reduction purposes. As can be seen from Table 4.1, eddy current distortion has no effect on the measured diffusion coefficient (within $\pm$1%) down to the lowest gradient pulse widths likely to be experimentally encountered (0.5ms).

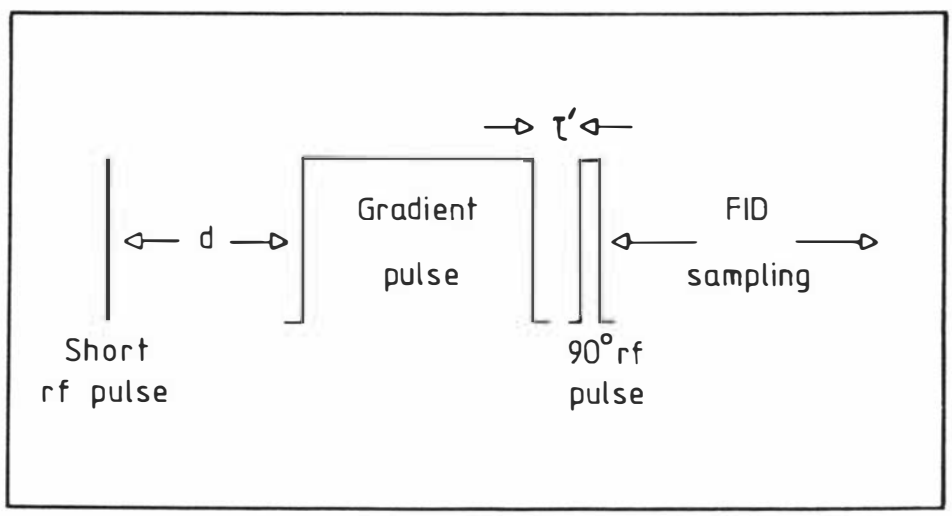


Figure 4.9. Field gradient and rf pulse sequences used to assess the effect of the eddy current "tail" on the PFGNMR experiment. A very short rf pulse is used to initiate timing in the pulse programmer, and d is sufficiently long to ensure that the nuclear spins have regained their equilibrium distribution before the gradient pulse is applied. The second gradient pulse occurs outside the FID sampling region.

Maximum current (A)	Δ (ms)	δ (ms)	τ-d-δ (ms)	D_{Solv} ($10^{-9} m^2 s^{-1}$)
5	6.0	2.0	3.5	2.31±0.03
9	3.5	1.0	3.0	2.35±0.02
9	15	0.5	14	2.34±0.03

Table 4.1. The effect of eddy currents on the measured diffusion coefficient. The values of D_{Solv} are not dependent on the gradient pulse width, indicating that the Stejskal-Tanner formula for the spin-echo attenuation is valid in the presence of the residual eddy currents encountered in this work. D_{Solv} was determined by an un-weighted least squares fit of 9 attenuation ratios to equation 3.1 (with the gradient coil factor set equal to 0.15 Tesla.$m^{-1}A^{-1}$, as determined from preliminary experiments). The error quoted for D_{Solv} was calculated from the standard deviation in the least-squares slope. Experiments were analysed in the time-domain, and the external lock was not used.

4.3.d. Accumulation and Pulse Repetition Time Effects.

When using data accumulation routines for noise reduction purposes it is important that the spectrometer system exhibit consistency over all rf pulse repetition rates, gradient pulse magnitudes and number of data accumulations used. In successive off-resonant ($\Delta\nu$ = 500Hz, 2τ = 30ms) accumulations under the action of gradient pulses (d = 0.5ms, Δ=15ms, δ=10ms and G=1.35 Tesla.$m^{-1}A^{-1}$) the echo maximum was stable to $\leq$20μs ($\leq 4^{o}$). This represents a spurious attenuation of ~0.25%. A further indication of the reliability of the experiment under accumulation is given by the accuracy of the accumulated echo height. Using frequency domain analysis on doped water, glycerol and random coil polystyrene samples; the data shown in Table 4.2 was obtained. These data clearly show that the system is free of any spurious effects associated with either the number of accumulations or the rf pulse repetition rate used.

It has been noted that if rf gradient pulse spacings of less than 5ms are used (with d=0.5ms) in conjunction with gradient pulse widths of greater than 10ms, spurious attenuation of the NMR spin-echo can be obtained. This appears in attenuation plots as a reduced intercept, although the attenuation plot remains a straight line. The reasons for this attenuation are not well understood, although this effect may be associated with interference of the magnetic field magnitude stabilisation circuitry by the gradient pulses. In any event, experiments in this work always employ (Δ-δ) > 5ms. For this condition, spin-echo formation and stability are well behaved (as discussed above), and attenuation plots have the required intercept of 1.0 (see, for example, Figure 4.13).

Sample	Number of accumulations.	Repetition rate (secs).	Attenuation ratio.
a...Doped water	4	1	0.419±0.002
(Δ=5ms, δ=1.5ms)	200	1	0.422
b...Glycerol	10	3	0.800±0.005
(Δ=25ms, δ=15ms)	100	3	0.796±0.002
	4	1	0.423±0.002
c...Doped water	4	5	0.421±0.002
(Δ=5ms, δ=1.5ms)	4	15	0.421±0.002
	250	1	0.662±0.009
d...Polystyrene in CCl_4.	250	2	0.668±0.009
(Δ=16ms, δ=10ms)	250	4	0.665±0.009

Table 4.2. Checks for consistency of the attenuation ratio under various rf and magnetic field gradient pulse conditions. No systematic variations are observed.

4.4 MAGNETIC FIELD GRADIENT CALIBRATION

4.4.a. Field Gradient and RF Pulse Profiles.

In a PFGNMR experiment the magnitudes of both the attenuated and unattenuated spin-echoes are measured at $t=2\tau$. The experimentally important ratio A(G)/A(0) is thus unaffected by small systematic errors in the 90° or 180° rf pulse lengths. The y-axis profile of the rf pulse length required to rotate the nuclear magnetic moments through 180° at various y-axis displacements from the centre of the irradiation coil is shown in Figure 4.10. The 180° rf pulse length was experimentally determined by using a doped water sample in a tube with a flattened bottom, the length of the sample being ≤1mm. In a PFGNMR experiment spurious attenuation of the spin-echo occurs if the resonant nuclei diffuse to a region of the sample having a different 90° rf pulse length, in the time τ. Figure 4.10 shows that B_1 easily satisfies the homogeneity requirements of the PFGNMR experiment.

The y-axis profile of the field gradient magnitude can also be experimentally determined with the 1mm sample by measuring the attenuation (for a given δ,Δ and G) at different positions. For each y-axis displacement the sample was allowed 5 minutes thermal equilibration and then 100 accumulations were performed, resulting in a noise-to-signal ratio of ~0.7%. The 90° and 180° rf pulse lengths were chosen according to Figure 4.10 in order to retain the same signal-to-noise at all y-axis positions. As can be seen from Figure 4.10, no systematic variations in the attenuation ratio were observed over the central region of the profile, with the data within $\pm$2mm of the zero displacement position all lying within a $\pm$0.8% range. Within $\pm$3mm of the centre position the data all lie in a $\pm$1% range, which is consistent within the combined errors of the experimental noise-to-signal ratio ($\pm$0.7%) plus the contribution from the $\pm 0.1^{\circ}$C temperature variation which occured during the experiment ($\pm$0.3%). Thus, the uniformity of the field gradient is consistent with the accuracy goals set for the PFGNMR experiment if samples of ≤ 6mm length are used.

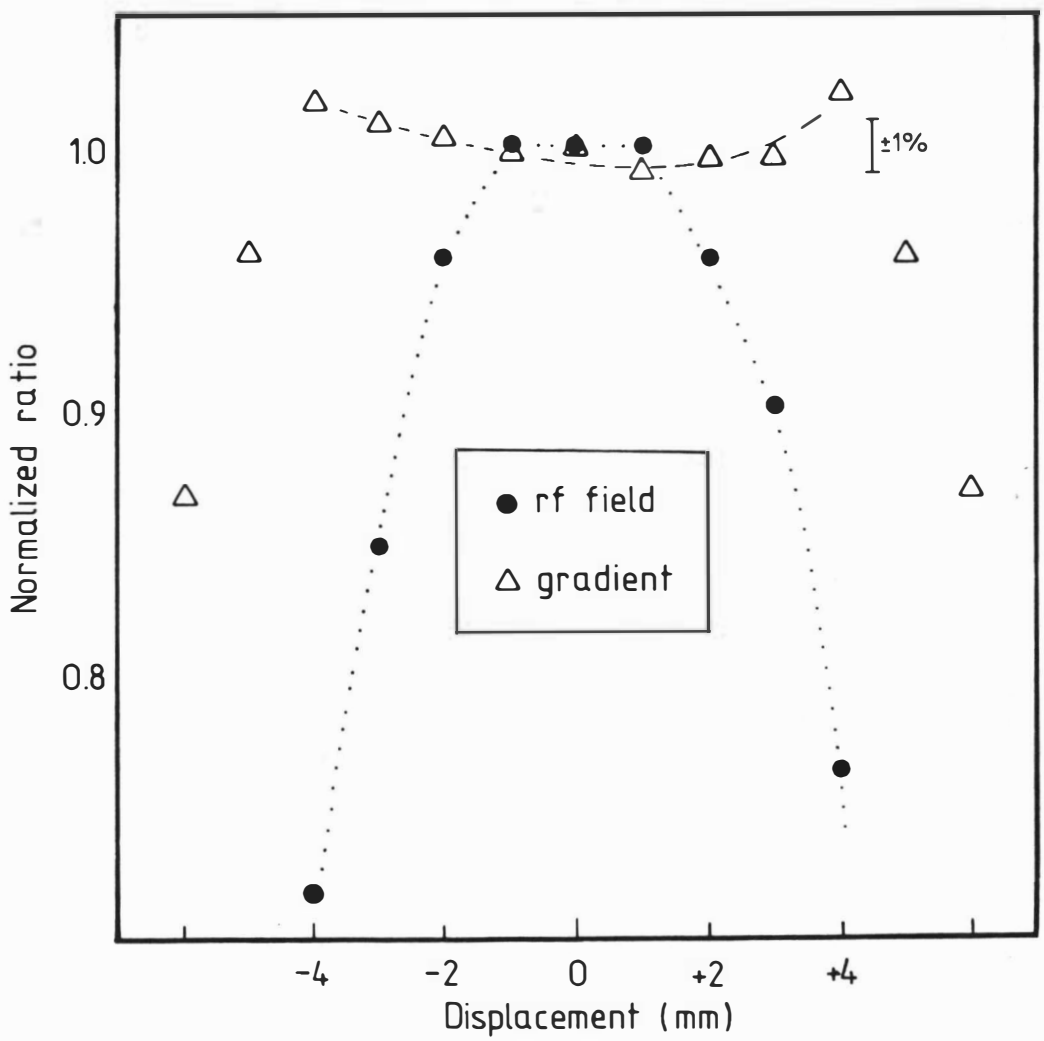


Figure 4.10. Magnetic field gradient and rf field magnitude-profiles along the sample y-axis. For the gradient profile experiment, d=0.5ms, Δ=0.5ms, δ=1ms and G=0.4 Tesla.m^{-1}. The field gradient is homogeneous to better than ±1% over the middle 6mm of the coils.

4.4.b. Calibration and Reproducibility of the Field Gradient.

Having now considered all the potential sources of error which can spuriously attenuate the NMR signal in a PFGNMR experiment, we are in a position to determine the field gradient magnitude. The field gradient magnitude can be obtained by performing a PFGNMR experiment on pure water, taking due regard of the various experimental considerations discussed in sections 4.3 and 4.4.a. Distilled, deionised water was re-distilled in a glass still and cooled under nitrogen. The conductivity measured by a GM4249 (Philips, Holland) conductivity bridge was $0.7 \times 10^{-8} \Omega^{-1} m^{-1}$. A 3mm (height) sample of this water contained in a 4mm diameter sample tube, with a Teflon plug inserted above the sample, was used in the experiment. In order to ensure good sample temperature stability, the JEOL temperature controller was set to ~25°C 12 hours before the experiment, thus allowing equilibration of all parts of the air-blast system. The spin-echo attenuation plot obtained for the water sample is shown in Figure 4.11 with the data, and experimental parameters used, listed in Table 4.3. More accumulations were used at high attenuation ratios to partially offset the effects of noise, and an unweighted least squares analysis was used to obtain the slope ($\pm$ the standard deviation) and intercept given in Figure 4.11. According to the results of Mills[41], the self-diffusion coefficient of water at 24.7$\pm$0.2°C is (2.28$\pm$0.01) $\times$ $10^{-9} m^2 s^{-1}$. Using the slope in Figure 4.11 the gradient coil factor, including the error due to temperature variations during the calibration run, is (0.1505$\pm$0.0009)Tesla.$m^{-1}A^{-1}$. This value is within 4% of the value calculated from a knowledge of the coil dimensions.

Since the gradient coil factor is now known, the reproducibility of the complete system can be checked by measuring the diffusion coefficient of benzene, which is known to better than 0.2%. Figure 4.12 shows the attenuation plot obtained by varying all three experimental parameters G, Δ and δ. Within the experimental precision (noise) the data obtained are consistent with the Stejskal-Tanner formula (equation 3.7). The least squares slope of the benzene attenuation plot, in conjunction with equation 3.7 and the above value for the gradient coil factor, yields a diffusion coefficient of (2.25$\pm$0.05) $\times$ $10^{-9} m^2 s^{-1}$, which is in good agreement with the accepted literature value of $2.210 \times 10^{-9} m^2 s^{-1}$[49]. The overall reproducibility of the PFGNMR system thus lies within the combined errors of gradient calibration and experimental precision.

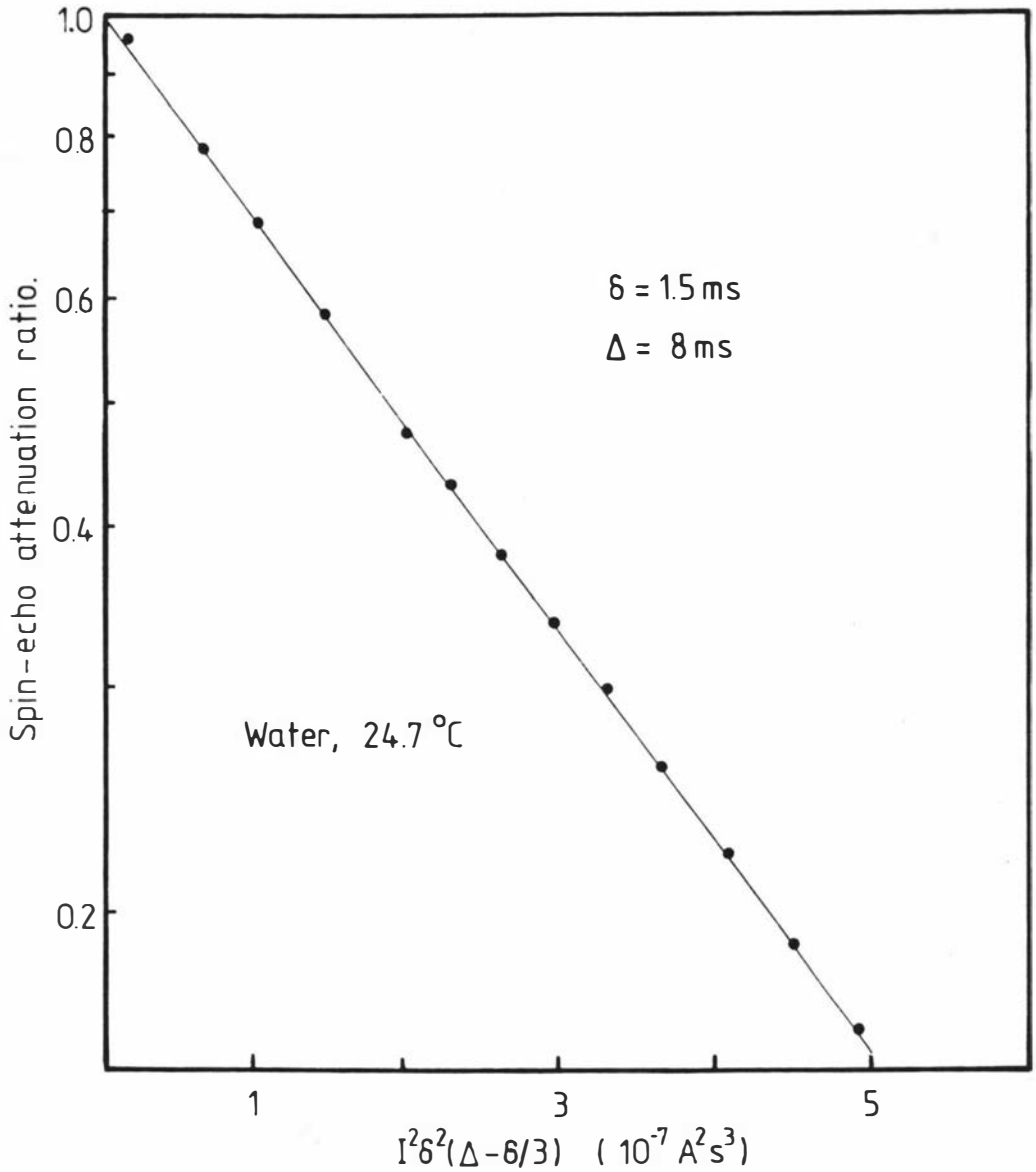


Figure 4.11. The spin-echo attenuation plot of pure water that was used to calculate the field gradient magnitude. The residual gradients due to inhomogeneities in the steady magnetic field $\underset{\sim}{B}_0$ do not make a significant contribution to the spin-echo attenuation for the gradient pulse parameters used. The plot has a least-squares intercept of 1.000 ± 0.007 and a slope of $-0.0624 A^{-2}$. The standard deviation in the slope is $0.0004 A^{-2}$.

Number of accumulations = 20.

1 kHz off-resonance.

AF filter at 2.5kHz width.

Number of time domain points = 512.

Spin-echo rf pulse sequence repetition time = 1s.

T_1 = 2.83 ± 0.02s from crossover point method.

Current (A).	Attenuation ratio.	± Noise contribution.
2.941	0.581	0.012
1.955	0.786	0.009
3.931	0.382	0.007
4.919*	0.216	0.005
5.413*	0.164	0.005
0.969	0.964	0.011
2.450	0.683	0.009
3.437	0.471	0.008
4.671	0.258	0.006
4.428	0.298	0.007
4.184	0.333	0.007
3.684	0.428	0.007
5.165*	0.187	0.005
5.413*	0.161	0.004
4.919*	0.224	0.005

Table 4.3. Gradient coil calibration experimental data. The experiment was conducted in the time domain. At larger attenuations (those marked with a *) 40 accumulations were used.

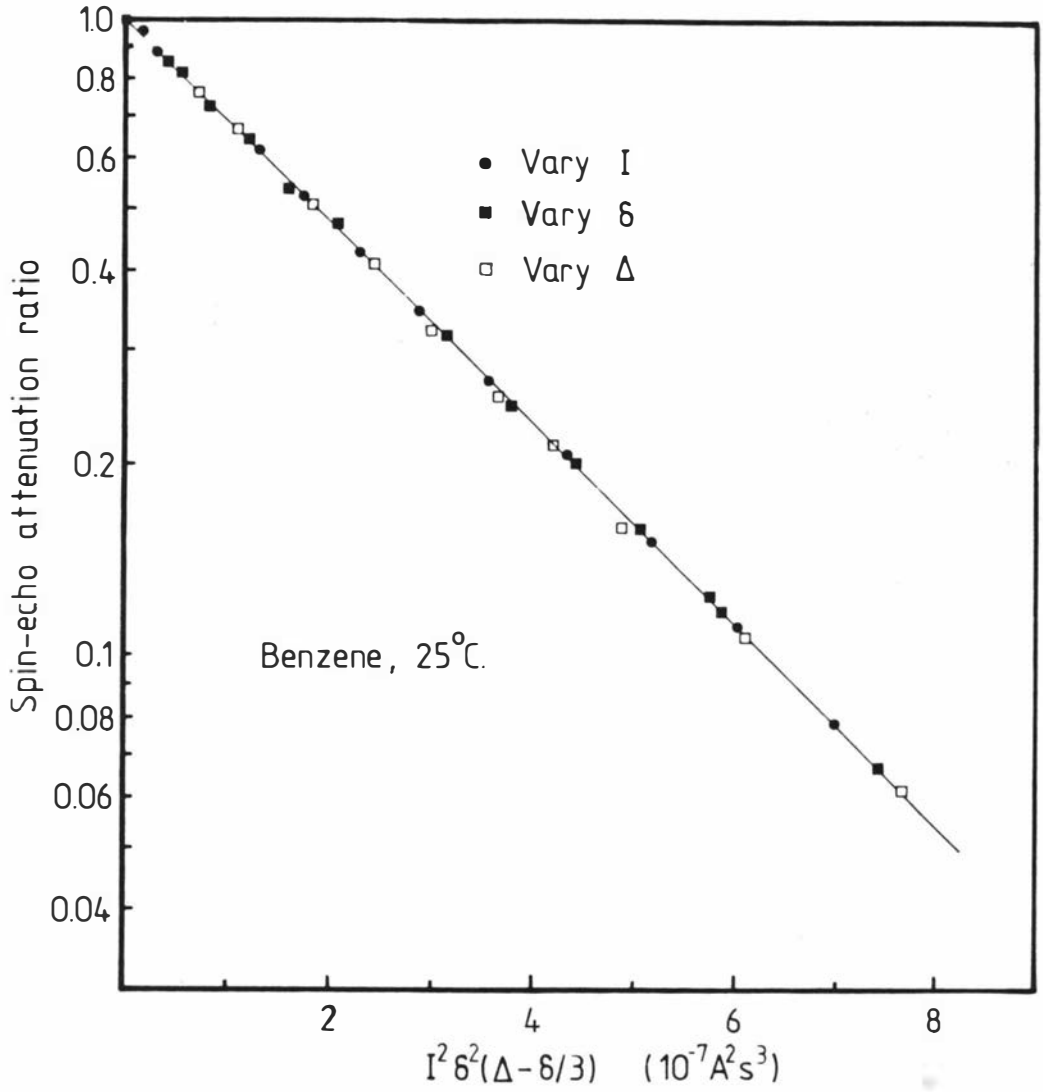


Figure 4.12. The spin-echo attenuation plot for Analar benzene in which all three experimental parameters G, Δ and δ, are varied. The resultant linear plot indicates that the PFGNMR apparatus is free of any systematic error in G, Δ or δ. During the experiment G varied from 0.15 to 1.05 Tesla.m^{-1}, Δ from 5 to 50ms and δ from 0.5 to 8ms. The diffusion coefficient of benzene determined from the above plot is within experimental error of the accepted literature value.

Finally, the reliability of the PFGNMR system was assessed at large field gradient magnitudes and pulse widths by measuring the diffusion coefficient of Analar glycerol at 25°C. The attenuation plot shown in Figure 4.13 yields a diffusion coefficient of $(2.15\pm0.06) \times 10^{-12} m^2 S^{-1}$ which is in good agreement with the value of $(2.1\pm0.1) \times 10^{-12} m^2 S^{-1}$ obtained from the data presented by Tomlinson[61].

4.4.c. Concluding Remarks

The gradient pulse switching scheme used in this work, in conjunction with careful probe design, has eliminated the problems which are cited in the literature as being responsible for the poor reproducibility of diffusion coefficients measured by PFGNMR[8,9]. In our system no gradient pulse width correction is over applied and automatic data accumulation is used under conditions of near perfect phase and envelope stability with correct echo formation at $t=2\tau$. Since data accumulation can proceed without the need for the echo inspection/rejection schemes commonly employed[2], very dilute samples which do not have a discernable echo even after several accumulations can be studied. The efficiency of the experiment is also considerably improved since spin-echoes no longer need be rejected, nor need time be taken to make acceptance/rejection decisions, thus allowing faster rf pulse repetition rates to be achieved for some systems (e.g. for polymer-dilutent systems where repetition times down to 1s can be used).

The PFGNMR system developed here possesses an accuracy of 1.2%, imposed by the field gradient calibration experiment. This brings the accuracy of the PFGNMR experiment up to the level recently attained for the steady gradient NMR experiment[17], and represents a very significant improvement over even the more recently published[2] estimations of PFGNMR measurement reliability.

The JEOL spectrometer has played a significant role in the development of the PFGNMR instrumentation by providing a stable base from which to judge the instrumentation performance. The Fourier-Transformation capability of the spectrometer also allows the diffusion coefficients of individual components in a multicomponent system to be determined

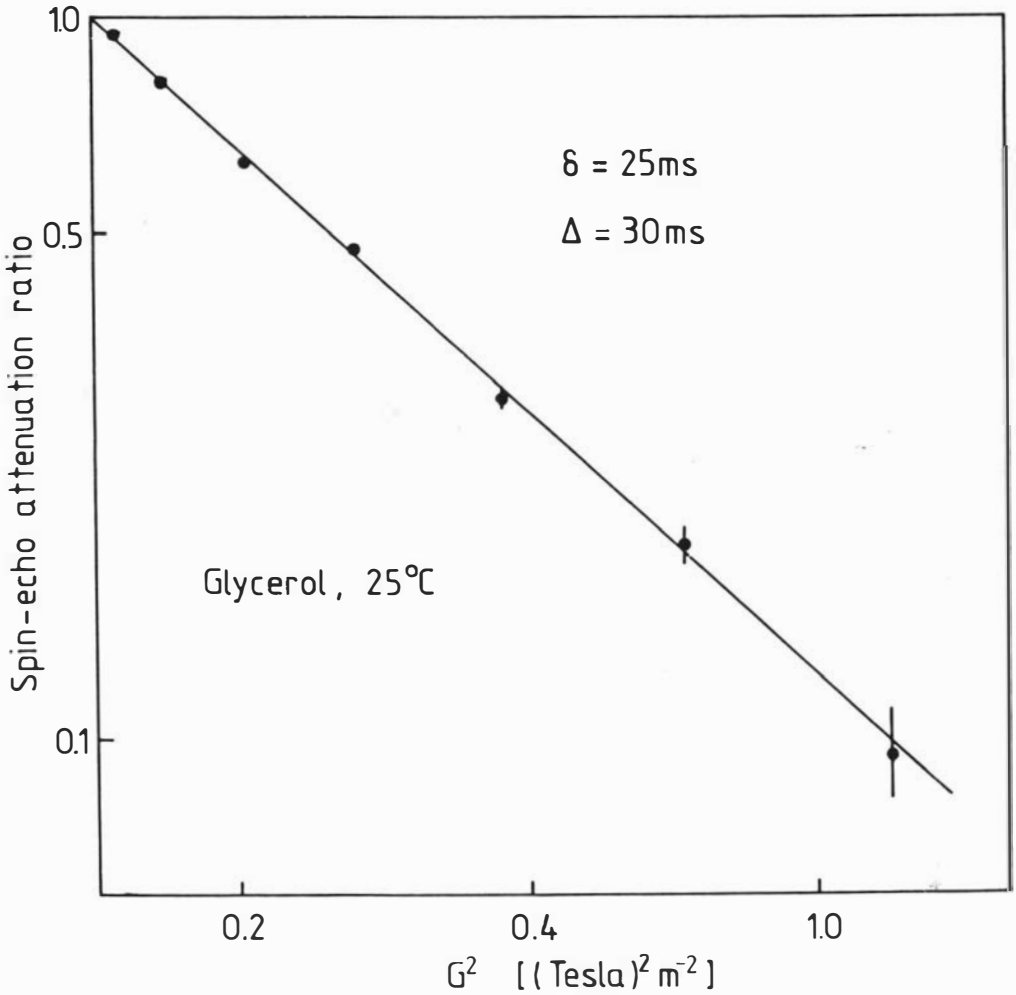


Figure 4.13. The spin-echo attenuation plot for Analar glycerol. The linear plot with an intercept of 1.0 (within experimental error) indicates satisfactory performance of the PFGNMR apparatus when large gradient pulse widths are used. The diffusion coefficient obtained from the above plot is in good agreement with literature values.

if the ^{1}H resonances are separable. The homogeneity coils built into the probe allow a frequency resolution of ~60Hz, as is demonstrated in Figure 4.14, and a study of individual component diffusion in a benzene-butanol mixture has been carried out using the PFGNMR system described in this chapter[62] (see Figure 4.15). Finally, it should be noted that diffusion coefficients which appear henceforth in this thesis have been calculated assuming a gradient coil factor of 0.1505 ± 0.0009 Tesla.$m^{-1}A^{-1}$, and any error quoted for the diffusion coefficient measurements will contain the error associated with gradient calibration.

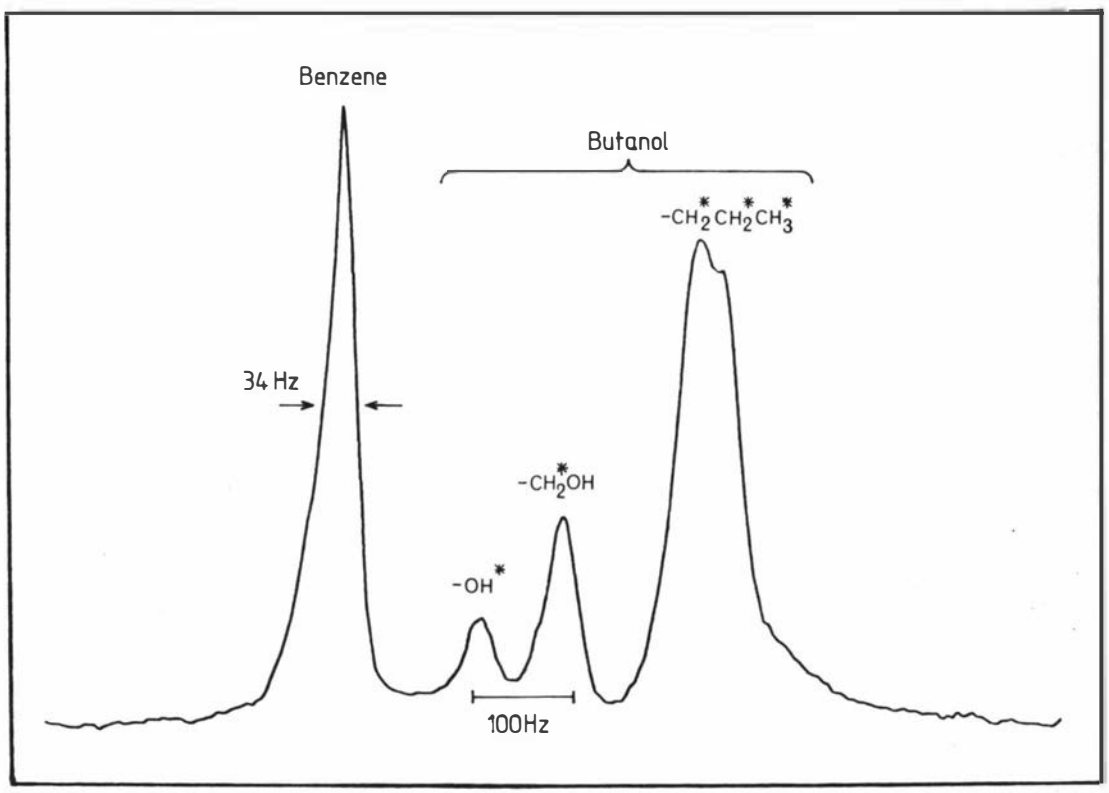


Figure 4.14. The ^{1}H frequency domain NMR spectrum of an equi-molar mixture of benzene and butanol, illustrating the resolution obtainable with the NMR probe used in this work.

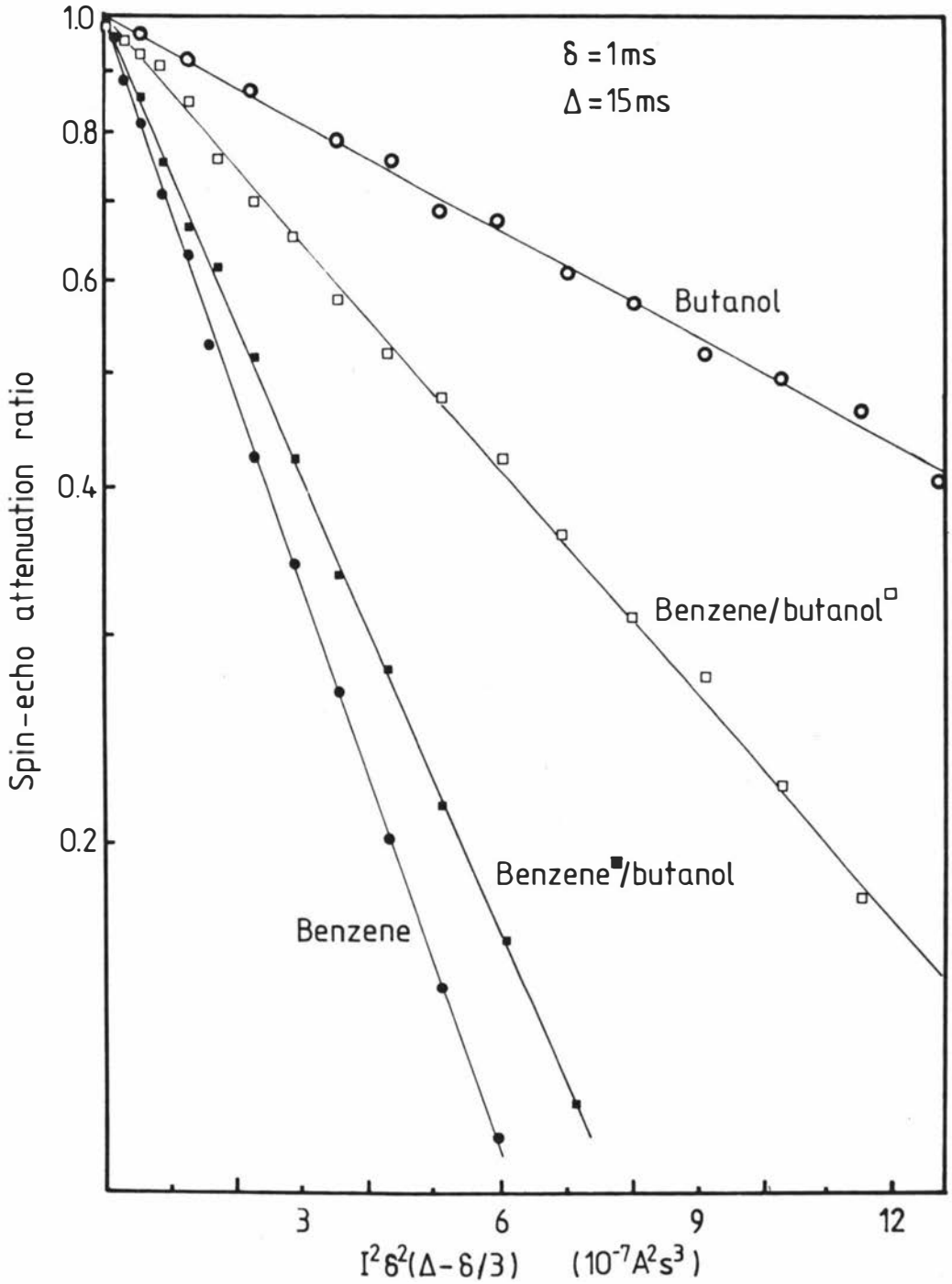


Figure 4.15. Spin-echo attenuation data for pure benzene, pure butanol, and the benzene and butanol components in an equimolar mixture; illustrating the measurement of single component diffusion coefficients in multi-component systems. All data were obtained at 25°C, and the self-diffusion coefficients are respectively $(2.23\pm0.04)\times10^{-9}$, $(0.43\pm0.01)\times10^{-9}$, $(1.83\pm0.04)\times10^{-9}$ and $(0.90\pm0.02)\times10^{-9}$ m^2s^{-1}.

CHAPTER 5

THE STUDY OF DIFFUSION IN RANDOM-COIL POLYSTYRENE SOLUTIONS: EXPERIMENTAL DETAILS.

5.1 INTRODUCTION

In this work, the diffusion coefficients D_S and D_M have been determined for various random-coil polystyrene/solvent systems; over a range of polystyrene concentrations. PFGNMR was used to measure D_S, with D_M being measured by QELS. This chapter details the experimental procedures associated with this study, and also presents both the QELS and PFGNMR experimental results.

The systems selected for study were those of 110,000 molecular weight polystyrene in the solvents carbon tetrachloride (CCl_4), deuterated-chloroform ($CDCl_3$) and deuterated-toluene (D-toluene; study by PFGNMR only). These solvents lack a ^1H signal, thus simplifying the PFGNMR experiment. The molecular weight of 110,000 was the smallest to provide an acceptable signal-to-noise ratio in the QELS experiment. Smaller (rather than larger) molecular weights are required so that the lowest polystyrene concentration accessible to the PFGNMR technique (~0.5gm% for the present apparatus) could approach the very dilute concentration regime. This regime is of great interest to the D_S/D_M comparison which was planned as part of this work, as in the very dilute regime D_S and D_M are expected to become indistinguishable.

Preliminary QELS experiments indicated that the very low scattered light levels encountered in a study of 110,000 molecular weight polystyrene would require the use of small scattering angles in order to obtain an acceptable signal-to-noise ratio. However, as discussed in Chapter 2, the combination of small scattering angles and low scattered light levels places severe restrictions on the QELS experiment in terms of solution cleanliness, with possible errors also being introduced by inadvertant heterodyning. These aspects of small angle studies have been given careful consideration in this work, as discussed in section 5.3 of this chapter.

5.2 THE PULSED FIELD GRADIENT NUCLEAR MAGNETIC RESONANCE EXPERIMENTS.

5.2.a. Preparation of Samples for the PFGNMR Study.

Monodisperse, 110,000 molecular weight, random-coil polystyrene was obtained from the Pressure Chemical Company (Pittsburgh, U.S.A), who give a value of 1.06 for M_n/M_w. (which is the ratio of the number-average to weight-average molecular weight) The carbon tetrachloride used was BDH (Poole, England) spectroscopic grade. The deuterated solvents were Merck (Darmstadt, Germany) spectroscopic grade, having ^1H contaminations of $< 0.1\%$ and $< 0.3\%$ for $CDCl_3$ and D-toluene respectively. These solvents were taken from sealed phials and between use stored under dry nigrogen to avoid further ^1H contamination.

Preparation of samples for study by PFGNMR was achieved as follows. The required quantity of polystyrene (dried at 40^oC for 48 hours) was accurately weighed into a volumetric flask and solvent added up to the $1cm^3$ mark. The flask was then sealed under dry nitrogen and the contents vigorously stirred by creating a vortex in the solution. Viscous samples were warmed to about 35^oC and stirred while cooling. 24 hours was allowed to elapse and the sample was again stirred shortly before an NMR sample was extracted by pipette. A sample of $\lesssim$ 5mm length was placed in a 4mm diameter NMR tube, and a tight-fitting Teflon plug was positioned ~2mm above the sample meniscus. NMR sample tubes that had previously contained polystyrene solutions were thoroughly cleaned, rinsed with spectroscopic grade CCl_4 and then heated to dryness (together with the Teflon plug) until just prior to use.

A study of the "solvent" diffusion in a solution of polystyrene was also planned. For this purpose chloroform ($CHCl_3$) was re-distilled under dry nitrogen and at low light levels (in order to prevent decomposition). The middle fraction boiling at 61.7^oC was taken, and stored under dry nitrogen in the dark.

5.2.b. Analysis of PFGNMR Data.

The sample 1.5gm% in D-toluene is used as an example in this section.

The T_1's of the polystyrene ^1H's were found to be less than 0.2s for this (and all other) samples, thereby allowing rf spin-echo pulse-pair repetition times of 1s. Spin-echoes were time-domain accumulated in the PAPS mode, and were subsequently Fourier-Transformed to take advantage of the band-pass characteristics of frequency-domain analysis. The frequency-domain NMR spectrum for the 1.5gm% sample is shown in Figure 5.1, and the area under the benzene-ring ^1H signal was determined from digitised data displayed by the spectrometer computer.

The attenuation plot ($\ell n[A(G)/A(0)]$ vs. I^2) for the 1.5gm% sample is shown in Figure 5.2, together with various signal accumulation parameters. To improve experimental reliability the number of signal accumulations was increased at smaller attenuation ratios, with 1.5 times the basic A(0) number of accumulations used for $0.4<[A(G)/A(0)]<0.5$ and twice the basic number for $[A(G)/A(0)]<0.4$. It is appropriate to analyse data obtained under these conditions by a non-weighted least-squares fit, and the slope and intercept given in Figure 5.2 were obtained in this way. The intercept apparent in Figure 5.2 is due to the residual protonated toluene. For polystyrene solutions with a residual solvent signal, the attenuation ratio in a PFGNMR experiment is given by

$$A(G)/A(0)=(1-x).\exp[-\gamma^2G^2D_S\delta^2(\Delta-\delta/3)]+x.\exp[-\gamma^2G^2D_{Solv}\delta^2(\Delta-\delta/3)] \quad 4.1$$

where x and (1-x) are the fractions of the spin-echo signal due to the solvent and polystyrene ^1H nuclei respectively. For the D-toluene used in this work, at a 1.5gm% polystyrene concentration, $x \lesssim 0.16$. The experiments reported in this thesis have $D_{Solv} > (100.D_S)$. Thus, under the action of gradient pulses suitable for the measurement of D_S ($\delta \geq 7ms, \Delta \geq 13ms$), the solvent term in equation 4.1 contributes less than 1% to the spin-echo attenuation ratio at even the smallest gradients used (0.15 Tesla.m^{-1}). Hence, the slope of the attenuation plot in Figure 5.2 correctly yields D_S, while the intercept gives a measure of x. The reliability of the signal attenuation plots was ensured by occassionally taking a new value for A(0), and due regard was also taken of the precautionary experimental points previously discussed in Chapter 4.

5.2.c. The Polystyrene Self-Diffusion Coefficients.

Tables of results and relevant experimental parameters are given in

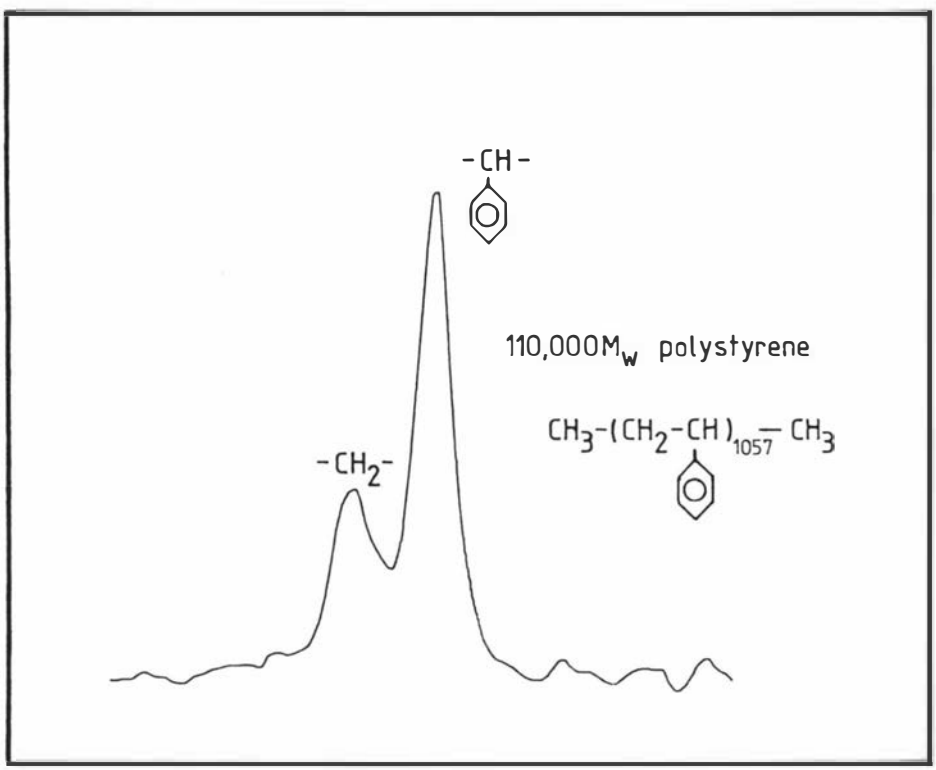


Figure 5.1. The ^{1}H frequency domain NMR spectrum of 1.5gm% polystyrene in D-toluene, as determined by the low resolution probe. 400 accumulations were used, and the area under the benzene-ring/CH peak was used to determine spin-echo amplitudes.

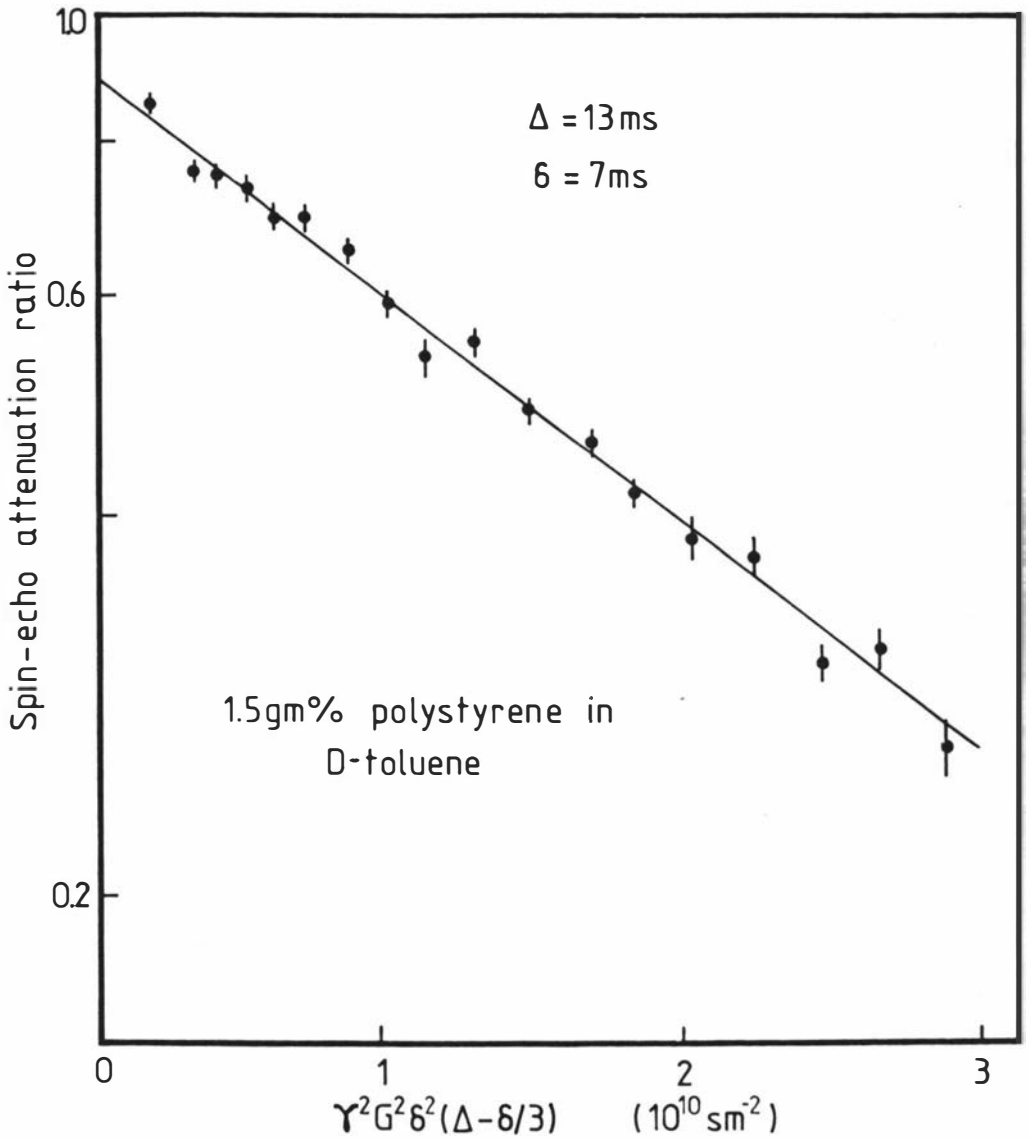


Figure 5.2. The spin-echo attenuation plot for 1.5gm%, 110,000M_w polystyrene in D-toluene. The y-axis intercept gives a measure of the fraction of toluene which is undeuterated. The slope of the plot yields the diffusion coefficient of the polystyrene.

Appendix 3 (Tables A.1, A.2 and A.3). Attenuation plots for the largest (25gm%) and smallest (0.5gm%) polystyrene concentrations studied are shown in Appendix 4(Figures A.1 and A.2). An accumulation repetition time of 1s was used for all samples studied while the basic A(0) number of accumulations varied from 250 to 400, depending on the particular polystyrene concentration used. The polystyrene D_S values are presented in graphical form [$\log(D_S)$ vs. $\log(c)$] in Figure 5.3. For the moment we merely note that the plots exhibit a linear region of slope -1.75. (These plots will be fully discussed in Chapter 6.)

The reliability of D_S values obtained from low signal-to-noise ratio experiments (< 1gm% polystyrene) was investigated by studying a doped water sample in a signal-to-noise ratio regime similar to that encountered for a 0.5gm% polystyrene sample. The attenuation plot for the water sample is shown in Figure 5.4, where the attenuation ratios >0.1 contain less than a 1% noise contribution. The attenuation ratios 0.036 and 0.025 were obtained from an average of six values, each with a noise-to-signal ratio contribution of about 8%. These high-noise, average attenuation ratios show excellent agreement with the extrapolated low-noise ratios, indicating an absence of systematic error in the calculation of polystyrene D_S values in low signal-to-noise ratio experiments.

The self-diffusion coefficients of two polystyrene samples (1.0gm% and 20gm%) were examined for any dependence on the effective experimental time ($\Delta-\delta/3$). Over the range of a few tens of milliseconds no dependence was found within experimental error. It should also be noted that the size of the molecular displacements necessary for detection by PFGNMR precludes any influence from intramolecular modes for polystyrenes with molecular weights as small as 110,000.

5.2.d. Self Diffusion of Chloroform in Polystyrene.

The limited resolution afforded by the present PFGNMR probe does not allow separation of the chloroform ($CHCL_3$) and polystyrene ^1H signals, thus complicating a study of solvent diffusion. However, field gradient pulse parameters appropriate for study of the solvent do not cause significant (< 1%) attenuation of the polystyrene signal. Under these conditions the expression for the total echo attenuation becomes

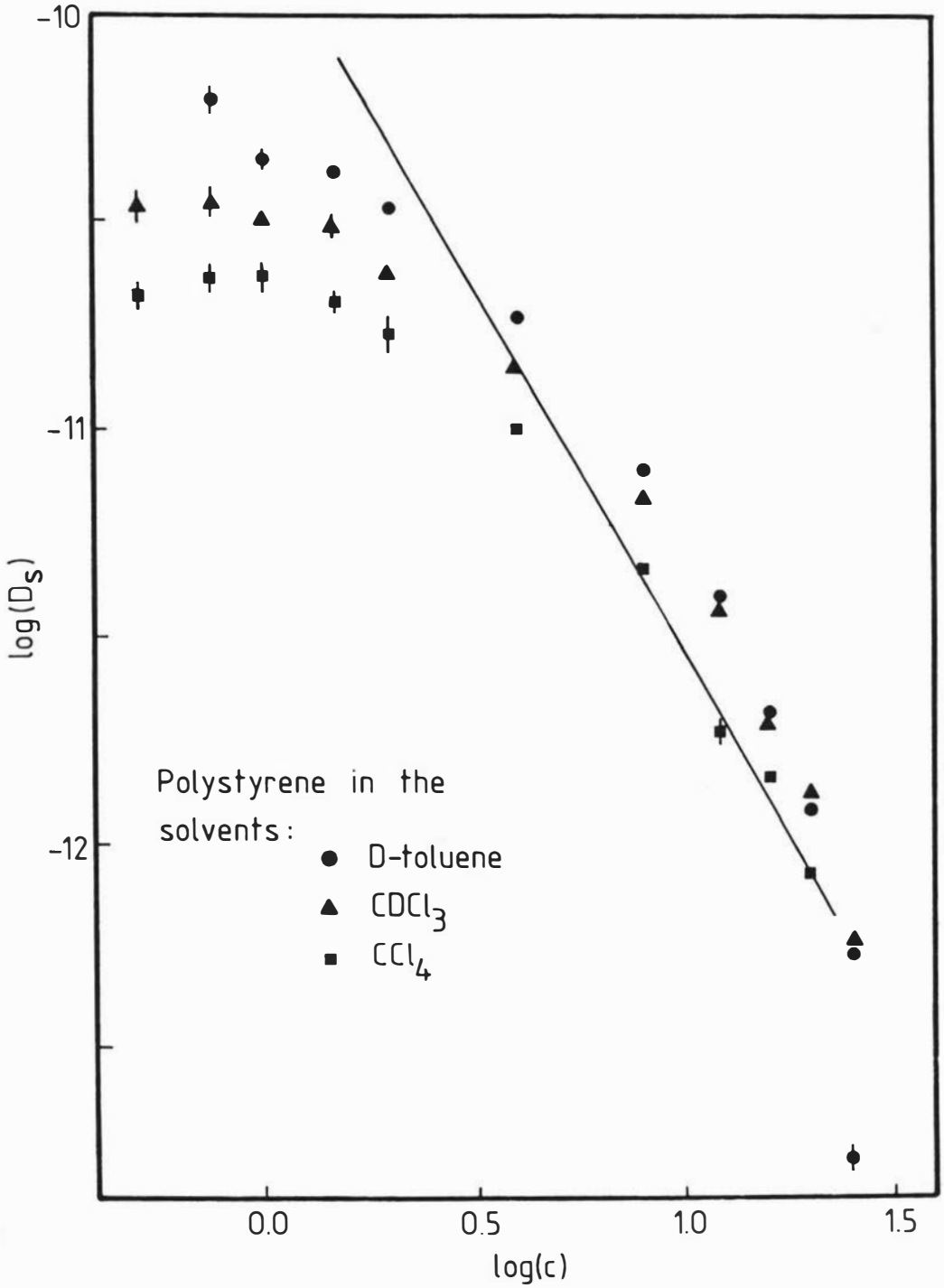


Figure 5.3. The self-diffusion coefficients of 110,000M_w polystyrene, as a function of concentration, in the solvents CCl_4, $CDCl_3$ and D-toluene. D_S and c (the polystyrene concentration) have units of $10^{-11} m^2 s^{-1}$ and gm% respectively, and all experiments were conducted at $25.0 \pm 0.5^{o}C$. Note that the log-log plot exhibits a linear region where D_S appears to vary as $c^{-1.75}$.

MASSEY UNIVERSITY
LIBRARY

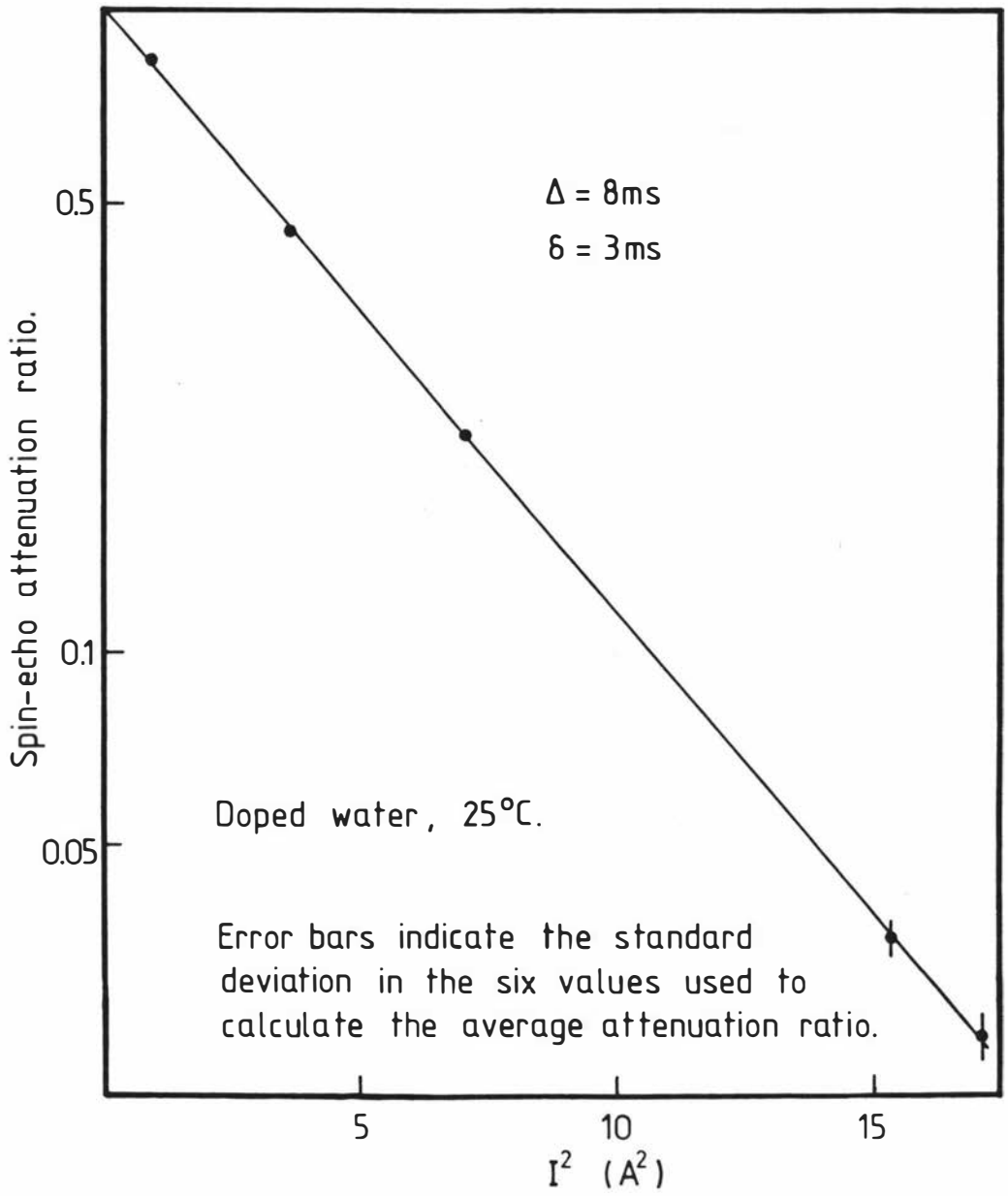


Figure 5.4. Spin-echo attenuation plot for doped water. The points with an attenuation ratio >0.1 contain <1% contribution from noise. The points with attenuation ratios <0.1 are averages obtained from six values, with each value having a noise-to-signal ratio of ~8%. This noise-to-signal ratio is similar to that encountered when studying 0.5gm% polystyrene solutions. The extrapolation of the low-noise ratios into the high-noise regime (attenuation ratios <0.1) gives excellent agreement with the averaged, high-noise ratios. This indicates an absence of systematic error in PFGNMR experiments conducted on dilute, low signal-to-noise ratio, polystyrene solutions.

$$A(G)/A(0)=\exp[-D_{Solv}.\gamma^2G^2\delta^2(\Delta-\delta/3)] + \text{constant}$$

where the term "constant" represents the polystyrene ^1H signal. D_{Solv} was calculated by subtracting constants from the experimental attenuation ratios until such time as a least squares fit to the data indicated the presence of a single exponential. The values of D_{Solv} obtained by this method are shown in Figure 5.5. The small concentration dependence of D_{Solv} is consistent with other work on solvent diffusion in polystyrene solutions[63]. From the spread of the D_{Solv} values the error in D_{Solv} appears to be about $\pm$3%.

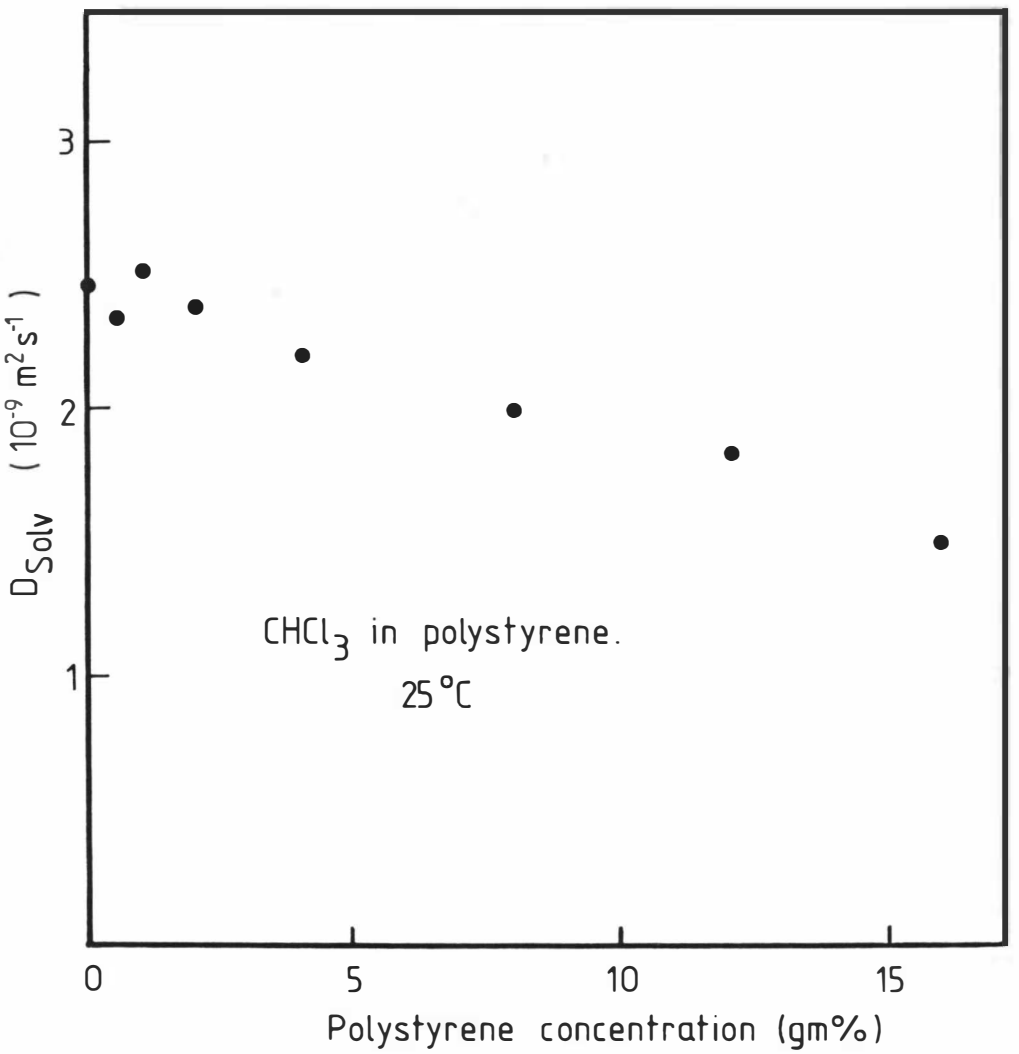


Figure 5.5. The self-diffusion coefficients of chlorofrom in polystyrene solutions. These values were determined by subtracting a "background" term from the attenuation ratios until the initially curved attenuation plot became a straight line. From the scatter on the data points, the error in determining diffusion coefficients by this method is about ±3%.

5.3 THE QUASI-ELASTIC LASER LIGHT-SCATTERING EXPERIMENTS.

5.3.a. Application of the Blinker to Concentrated Polymer Solutions.

Very dilute monodisperse random-coil polymer solutions (those free from significant polymer-polymer interactions) allow the blinker to be used as described by O'Driscoll and Pinder[37]; that is by assuming the plot of $\ell n(NIAF-1)$ versus time is a straight line, and by adjusting the blinker level until such a plot is experimentally obtained. This method of selecting the blinker level will henceforth be referred to as the blinker force-fitting (BFF) method. However, in a concentration regime where significant polymer-polymer interactions occur, the application of the blinker is not straightforward as the variance of $\overline{\Gamma}$, and hence Q', is not usually known a priori.

The following method was adopted for using the blinker to study concentrated polymer solutions. A suitable blinker level was selected and the IAF accumulation observed on the oscilloscope screen. The presence of dust in the scattering volume was indicated by an increase in the rate of accumulation of the IAF. The counts-per-sample-time were then increased (by small adjustments either to the correlator sample time or to the high-voltage applied to the photomultiplier), until careful observation of the IAF accumulation rate indicated that the blinker was activated before any noticeable increase in the count rate occured. The IAF accumulation was always observed for about 5 minutes to ensure a suitable counts-per-sample-time had been selected. This blinker setting method will henceforth be referred to as the ad hoc method.

The ad hoc method of setting the blinker can be rather tedious however, and it also relies considerably on the judgement of the operator. It is therefore advantageous to use the BFF approach whenever possible. The BFF method involves altering the blinker level until $Q' \lesssim 0.02$, and so any polymer solution which is expected to possess $Q' \lesssim 0.02$ can be studied using this method. Pusey et al.[10] give values of Q' versus polymer concentration obtained from a QELS diffusion study of $200{,}000 M_w$ polystyrene in toluene. At a polystyrene concentration such that the intermolecular spacing was about twice the polymer radius of gyration[64],

a value of $Q'=0.03\pm0.01$ was obtained. This implies that for the polymer/solvent combinations of interest to this work, the BFF method of blinker level setting should be valid for studying solutions having polystyrene concentrations $\lesssim$ 1gm%.

The fraction of the total experimental time the autocorrelator spends off (Aco) due to the blinker being triggered provides a measure of both the solution cleanliness and data collection efficiency. Recall that for each time the blinker is triggered, the correlator ceases data collection for one second. Aco is thus given by

$$\text{Aco} = (\text{total blinker counts})/(\text{total expt'l time})$$

The value of Aco obtained when the blinker is set by the BFF method also gives an estimate of the confidence that can be placed in the QELS data obtained. If a value of Aco approaching 1 is required to yield $Q'\lesssim 0.02$, the possibility that the blinker is being triggered by large "statistical" intensity fluctuations, rather than by dust, should be considered.

5.3.b. Preparation of Samples for the QELS Study.

The aim of any sample preparation scheme is to eliminate any spurious components in the solutions which might otherwise interfere with the extraction of reliable QELS data. In the case of monodisperse random-coil polystyrene solutions the only contaminant of any import is dust. Dust particles tend to be electrostatically charged and are also usually of low density. These properties must be taken into consideration when designing a solution cleaning scheme.

As a first step in sample preparation new glassware was scrupulously cleaned by ultrasonication in hot radioactive-decontamination detergent (DECON 75). This was followed by copious rinsing with hot tap water, distilled (glass still) water, re-distilled water and finally 0.22μm Millipore filtered (filters pre-rinsed) re-distilled water. Glassware was dried, wrapped in aluminium foil and stored at this stage if required for later use. Any glassware that had previously contained a polystyrene solution was rinsed out with some 10 volumes of chloroform (a good solvent for polystyrene) and soaked in hot chloroform together with a

5 minute period of ultrasonication. The glassware was then subjected to ethanol rinses followed by the water rinses detailed above.

Centrifugation was adopted for the preparation of dust-free light-scattering samples because the pore size of Millipore filters suitable for use with organic solvents is too large to allow effective solution cleaning by filtration. The scattering cells and any syringes (and needles) used for sample cell loading were rendered dust-free by rinsing with a centrifuged solvent. As far as dust minimisation is concerned a suitable solvent should be non-polar, and possess both a low viscosity and low surface tension. These properties will allow rapid sedimentation of dust particles, and also prevent particles from residing in the meniscus of the solvent. The most suitable solvent consistent with the health of the experimenter (that is, benzene should not be used) is cyclohexane.

A sample for study by QELS was prepared in the following manner, where all steps marked * were carried out in an atmosphere of 0.22μm filtered air.

1. $60cm^3$ of Analar cyclohexane was centrifuged at ~32,000g (15,000rpm) for 2 hours in $4 \times 15cm^3$ Teflon-stoppered glass centrifuge tubes, which had been loaded and sealed in 0.22μm filtered air. (These tubes were selected from a series of tubes recommended for use at no more than 12,000rpm by loading with the dense solvent CCL_4, spinning at 16,000rpm for 10 minutes, and accepting the survivors.)

2.* The centrifuged solvent was used to rinse the loading syringe plus needle four times, being careful not to touch the sides of the centrifuge tube nor to withdraw solvent from near the surface or bottom of the tube.

3.* The remaining centrifuged solvent was used to rinse the scattering cell, using the cleaned syringe for solvent transfer.

4.* Both scattering cell and syringe were placed in a clean dessicator (which was only opened in the filtered air atmosphere) and subsequently dried in vacuo.

5. $5cm^3$ of polystyrene solution was centrifuged for 2 hours at ~32,000g in Teflon-capped tubes. The centrifuge tubes were loaded in the filtered air atmosphere.

6.* The clean syringe was used to remove a $2cm^3$ middle portion from the polystyrene solution, about $0.5cm^3$ was expelled to remove any dust which had clung to the end of the syringe needle during removal through the meniscus, and about $1.5cm^3$ placed in the scattering cell. During entry into the solution in the centrifuge tube, a small amount of (the filtered) air was expelled through the syringe needle to avoid contamination of the syringe by dust trapped in the meniscus.

The above cleaning scheme produced appreciably cleaner solutions than any of the several alternative (combinations of filtering and centrifuging) schemes tried. The effect of residual dust in the solutions was eliminated by the use of the blinker. It should also be noted that when making up a polystyrene solution, the precaution of filtering the solvent through a 0.2μm fluoropore Millipore filter was employed.

5.3.c. Spectrometer Related Considerations.

To ensure that the average photocount rate does not vary during a QELS experiment, various warm-up times must be taken into consideration. The manufacturer's recommendation of 2 hours was utilised for the laser, while measurement showed that a solution in a sample cell (initially at $15^{\circ}C$) reached thermal equilibrium at $25^{\circ}C$ ~45 minutes after being placed in the index matching bath. There is also a characteristic warm-up time associated with the application of high-voltage to the photomultiplier tube (PMT), in that the photocount rate drifts appreciably over a period of about one hour after the voltage is applied (or changed significantly). Experiments were not conducted during this time.

It was found that the IAF could be effected by the level of particulate contamination in the index matching fluid, a problem also noted by others[65]. In this work the cleanliness of the index matching bath was

ensured by using 0.22μm Millipore filtered water as the index matching fluid, in conjunction with the anti-bacterial agent sodium azide which was added to the water at a level of 0.04gm%.

The direction of the unscattered laser beam defines the zero scattering angle position in the QELS experiment, and the zero angle as measured by the vernier scale around the outside of the index matching bath must coincide with this position. In this work the zero angle was set in the following manner. An appropriate neutral density filter was first placed in the incident beam, with careful adjustments made to ensure that the filter was perpendicular to the beam so that beam translation was avoided. The PMT mounting arm was then rotated to 0.0° as indicated by the angular scale, and the smallest operture (0.5mm) selected to limit the PMT acceptance angle. Using the x-y motions available to the lens mounted in the PMT housing (as shown in Figure 2.5) the unscattered beam intensity was then adjusted to a maximum as determined by observing the count-rate on a 20MHz digital-analogue ratemeter constructed as part of this thesis. (A schematic circuit diagram of the ratemeter is given in Appendix 5.) The reproducibility of the zero-angle setting was limited only by the precision of the vernier scale (0.1°). When this alignment procedure was complete, placing a sample cell in the index matching bath did not detectably alter the position of the unscattered beam intensity maximum.

5.3.d. Spurious Contributions to the Intensity Autocorrelation Function.

When homodyne experiments are conducted at small scattering angles, heterodyne components can be introduced into the IAF by stray scattering from, for example, the sample-cell walls. Heterodyne components in the IAF would lead to an artifically decreased diffusion coefficient being determined, particularly at small scattering angles.

A check for heterodyne components was carried out by measuring the diffusion coefficient of 390,000M_w random coil polystyrene in butanone. A dilute polystyrene solution (concentration <0.1gm%) was prepared according to the scheme given in section 5.3.b, and the diffusion coefficient determined as a function of scattering angle. The effect of the PMT acceptance angle (determined by the aperture setting) was also

studied. The BFF method of blinker level setting was used, resulting in Aco ≈ 1/3 for a Q' $\lesssim$ 0.02. The results of this study are shown in Figure 5.6, and indicate that within ±2% the diffusion coefficient is independent of both angle and aperture for those values studied. The diffusion coefficient obtained at 25°C was $(3.99\pm0.08)\times10^{-12}m^2s^{-1}$, which is in good agreement with the value of $(3.95\pm0.15)\times10^{-12}m^2s^{-1}$ reported by King et al.[64]. The angular independence of the diffusion coefficient indicates an absence of heterodyning effects. This conclusion is supported by the fact that for acceptable values of Aco, single-exponential NIAFs were obtained (Q' $\lesssim$ 0.02), whereas multi-exponential NIAFs are expected if the scattered light contains heterodyne components. The presence of dust in the scattering volume prevented scattering angles below 10° being examined. Diffusion coefficient measurements have been carried out only at scattering angles above 10° in this thesis.

A spurious contribution to the IAF was encountered when the voltage applied to the photomultiplier tube was reduced below the recommended 1750V in order to finely adjust the input count rate; in order to allow correct operation of the blinker. Under these conditions the initial part of the NIAF contained a short up-turn; or down-turn, depending upon the applied voltage magnitude. This effect was only noticeable at small sample times (T of order μs), and was confined to the first and second data channels of the correlator. This effect is due to correlated or anti-correlated photomultiplier tube after-pulses, and so when working at small timescales and reduced high-voltage settings, the first two data channels of the IAF were discarded.

To examine the effect of IAF accumulation time on the measured diffusion coefficient the dilute solution of 390,000M_w polystyrene in butanone was re-examined. The diffusion coefficient determined from a 3 hour IAF accumulation was found to agree with the earlier D_0 determinations that were obtained from 20 minute IAF accumulations. The average scattered intensity varied by <1% over the 3 hour period.

5.3.e. Analysis of QELS Data

In this section some relevant details of the analysis of QELS data obtained from 0.26gm% and 2.0gm% solutions of 110,000M_w polystyrene in

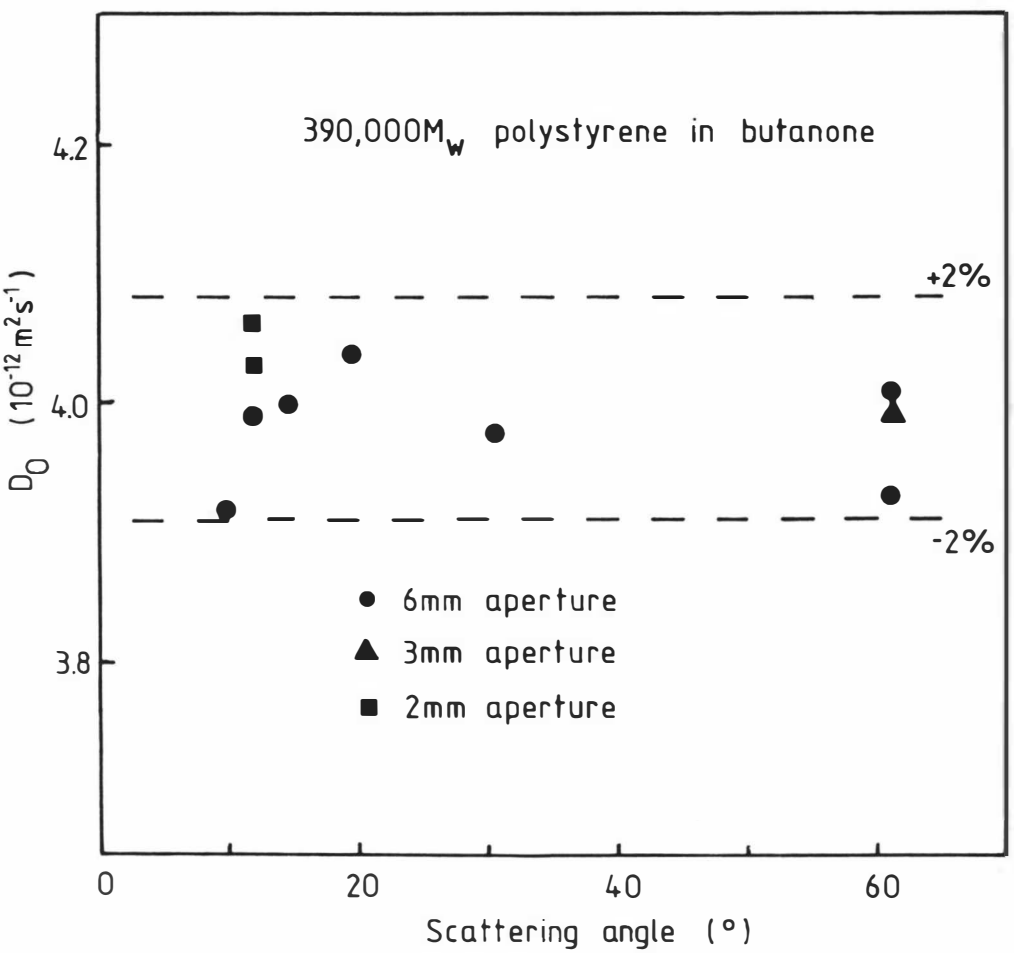


Figure 5.6. The diffusion coefficient of 390,000M_w polystyrene in butanone as measured by QELS in the very dilute concentration regime, at 25.0°C. Within ±2% no variations were observed with aperture or scattering angle changes. The value of D_0 determined in this experiment shows good agreement with that obtained by King et al.[64].

CCl_4 are presented. The 0.26gm% sample is representative of these solutions possessing polymer concentrations $\lesssim$ 1gm% for which the blinker was set according to the BFF method (as discussed in section 5.3.a.). The 2.0gm% solution represents those solutions where Q'>0.02, requiring analysis by the method of cumulants in conjunction with blinker setting by the ad hoc method. The above samples, as with all random-coil polystyrene samples studied in this work, were prepared by the scheme outlined in section 5.3.b.

The 0.26gm% sample is first considered. For this sample scattering angles below 30° provided an NIAF with an acceptable signal-to-noise ratio. Individual IAFs were accumulated over 3 hour periods, and Figure 5.7 details the resultant signal-to-noise ratio obtained for an NIAF at $\theta=13.7^{\circ}$. The small values of Aco encountered in the study of this sample (see Table 5.1) indicate that the intensity fluctuations removed by the blinker were indeed spurious. This is because an average correlator accumulation period of 4 seconds (Aco=1/5) represents a time extremely long compared with any statistical fluctuations (of order 10's of milliseconds) in the light intensity incident upon the photomultiplier tube. The scattering angles at which this sample was studied are given in Table 5.1, together with the mutual diffusion coefficients as determined by the QELS technique. The scattering angles have been corrected for refraction at the polystyrene-solution/glass/water interface. The refractive index of the polystyrene solution was determined with a calibrated Abbe(Tokyo, Japan) refractometer. The values of D_M were calculated assuming that the IAF decays as a single exponential with exponent $(-2D_Mq^2)$. No systematic variations in D_M were observed with scattering angle which implies that for the 0.26gm% sample, a Brownian diffusion process was being studied.

Data obtained from concentrated polymer solutions, such as the 2.0gm% sample, can be analysed by the method of cumulants. Plots of ℓn(NIAF-1) versus channel number for the 2.0gm% sample are shown in Figure 5.8, illustrating the signal-to-noise ratio obtainable at both the largest and smallest timescales used in the $\theta=13.7^{\circ}$ study. Analysis of this data by the method of cumulants involves plotting the initial slope, obtained from a ℓn(NIAF-1) versus time plot, against the experimental sample time T. NIAFs are obtained for a range of T, and

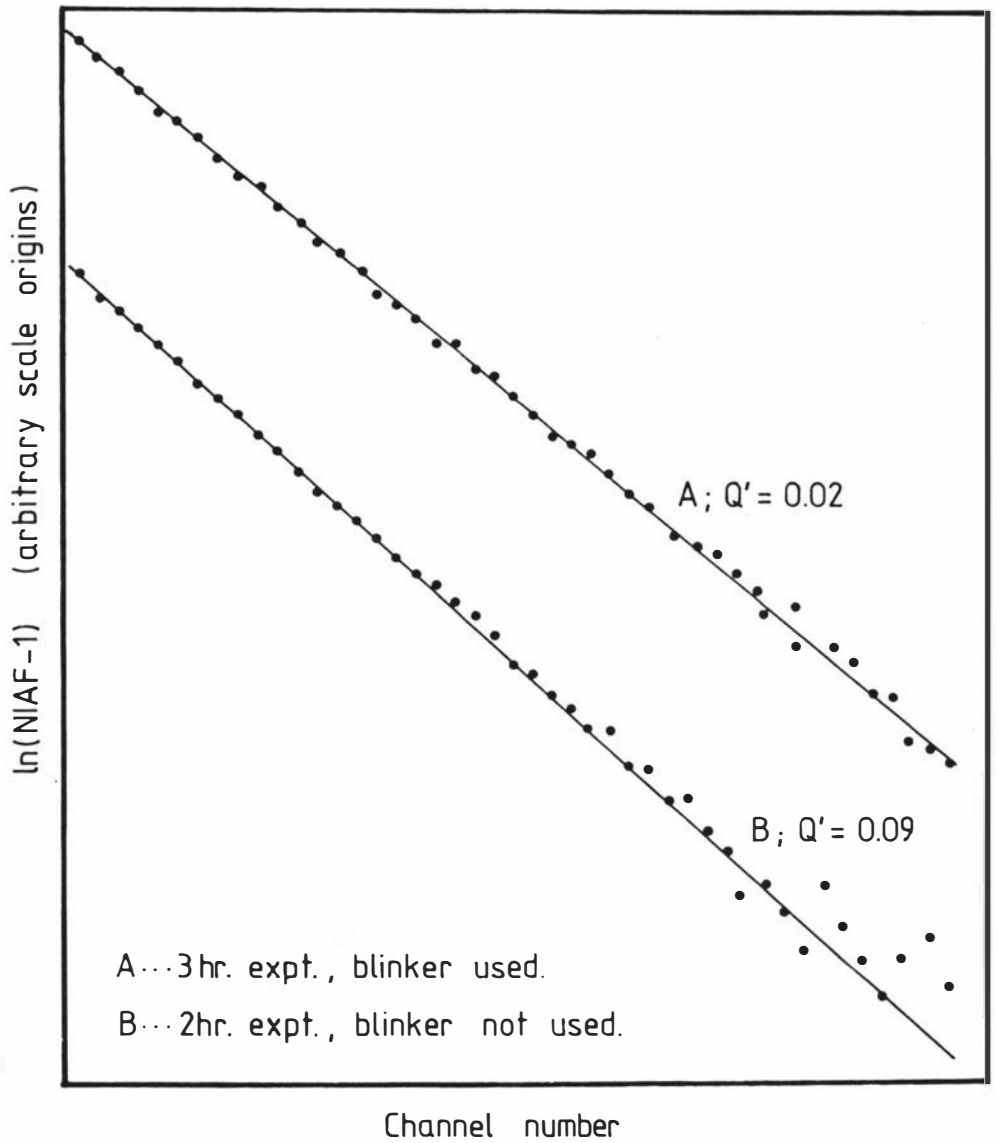


Figure 5.7. The signal-to-noise ratio obtained in several QELS experiments on a 0.26gm% solution of polystyrene in CCl_4. Plot A was obtained using the BFF method of blinker level setting. Plot B was obtained without recourse to the blinker. D_M calculated from the initial slope of curve B is ~10% smaller than D_M calculated from curve A, due to the effect of dust. (Note that the sample time, T, is not the same for the two plots.)

Polystyrene concentration (gm%)	Angle. (°)	Aco	D_M ($10^{-11} m^2 s^{-1}$)
0.26	12.8	1/5	2.98
0.26	13.7	1/5	2.93
0.26	17.3	1/5	2.99
0.26	18.2	1/5	3.05
0.26	27.2	1/5	3.01
2.0	13.7	1/3	2.94 ± 0.05**
2.0	18.2	1/3	2.9 ± 0.2**
2.0	27.2	1/3	2.7 ± 0.2**

** indicates analysis by the method of cumulants.

Table 5.1. Details of the data analysis for the samples 0.26gm% and 2.0gm% in CCl_4. The errors shown in D_M indicate the spread of D_M values. D_M was calculated from the small T values of S_M in the case of a cumulants analysis.

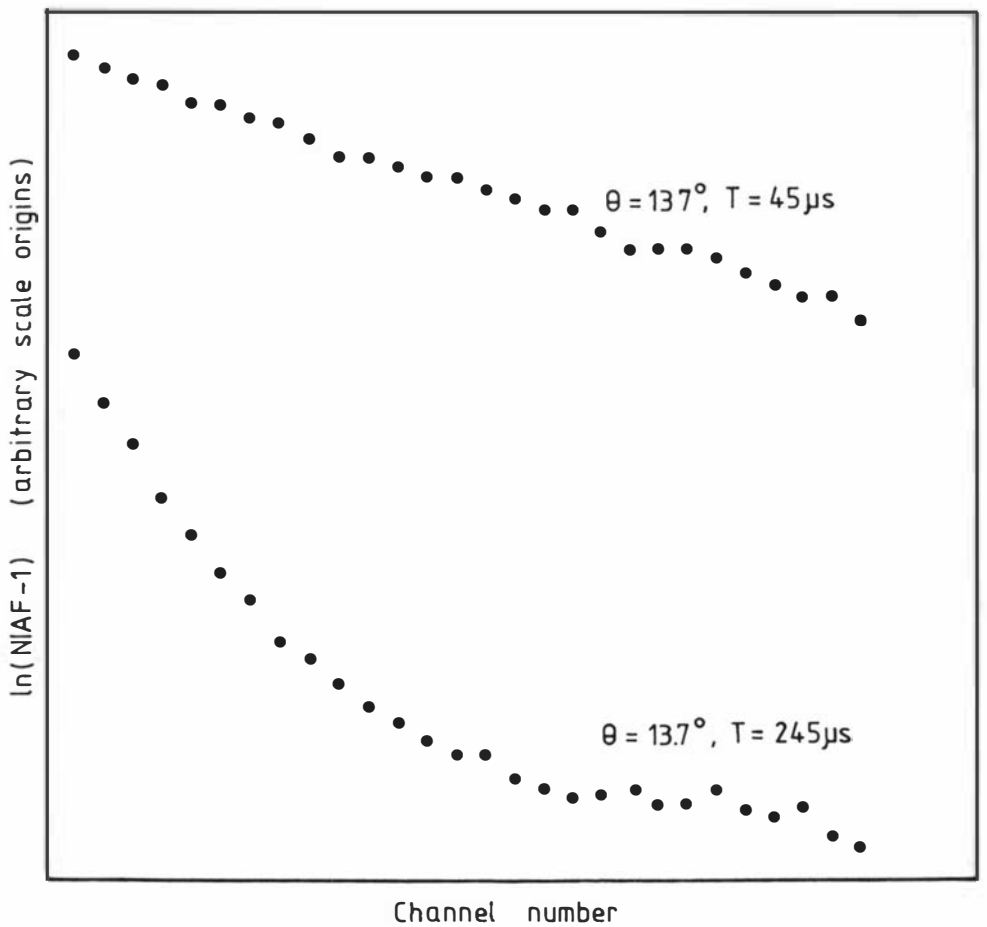


Figure 5.8. Plots of ℓn(NIAF-1) versus channel number for the 2.0gm% sample in CCl_4. The IAFs for this sample were multi-exponential ($Q' \simeq 0.8$), requiring analysis by the method of cumulants. The above plots indicate the signal-to-noise ratio obtainable at the largest and smallest values of T used in the cumulants study.

extrapolation of the initial slopes to T=0 yields an initial slope value free of systematic error. Pusey et al.[29] recommend that a range of T such that $0.4 \leq \bar{\Gamma}T_{max} \leq 4.0$ be used, although at the largest of the scattering angles employed in this study ($\theta=27.2^{o}$), $\bar{\Gamma}T_{max} = 0.4$ requires the use of a T too small to allow an IAF with an adequate signal-to-noise ratio to be obtained. However, as the cumulants analysis plots in Figure 5.9 show, the initial slope of the ℓn(NIAF-1) vs. time plots shows a T invariance for a range of accessible T values. This ensures accurate extrapolation to T=0. Further details of the data analysis for the 2.0gm% sample are given in Table 5.1, where the diffusion coefficient D_M has been calculated assuming the IAF initially decays as an exponential with exponent $(-2D_Mq^2)$. S_M, used previously to denote the slope of a ℓn(NIAF-1) versus time plot, denotes the initial slope (that obtained by extrapolation to T=0, as in Figure 5.9) of a ℓn(NIAF-1) versus time plot if cumulants analysis is used.

5.3.f. The Polystyrene Solution Mutual Diffusion Coefficients.

The D_M values obtained for solutions of $110,000M_w$ polystyrene in CCl_4 and $CDCl_3$ are presented in Figure 5.10, with tables of results given in Appendix 3 (Tables A.4 and A.5). A linear dependence of S_M on $\sin^2(\theta/2)$, shown in Appendix 4 (Figure A.2) for representative samples, was encountered for all polystyrene concentrations studied.

The viscous sample 8.0gm% in CCl_4 proved impossible to render dust free, resulting in a value of Aco $\lesssim$ 1/2. The IAFs obtained from this sample were thus rather noisy and this accounts for the larger error placed on the value of D_M for this sample. Dust problems were also encountered with the 1.0gm% and 2.0gm% polystyrene samples in the polar solvent $CDCl_3$, again leading to a poorer signal-to-noise ratio. This problem was compounded by the smaller values of T required to study the larger diffusion coefficient of polystyrene in $CDCl_3$.

The angular invariance of D_M is usually taken as the definative test of reliability in a QELS experiment. The range of angles over which D_M was determined in this work was rather small, spanning only $12^{o}<\theta<30^{o}$, with a smaller angular range than this in some cases. However, the angular invariance of D_M has been demonstrated for the

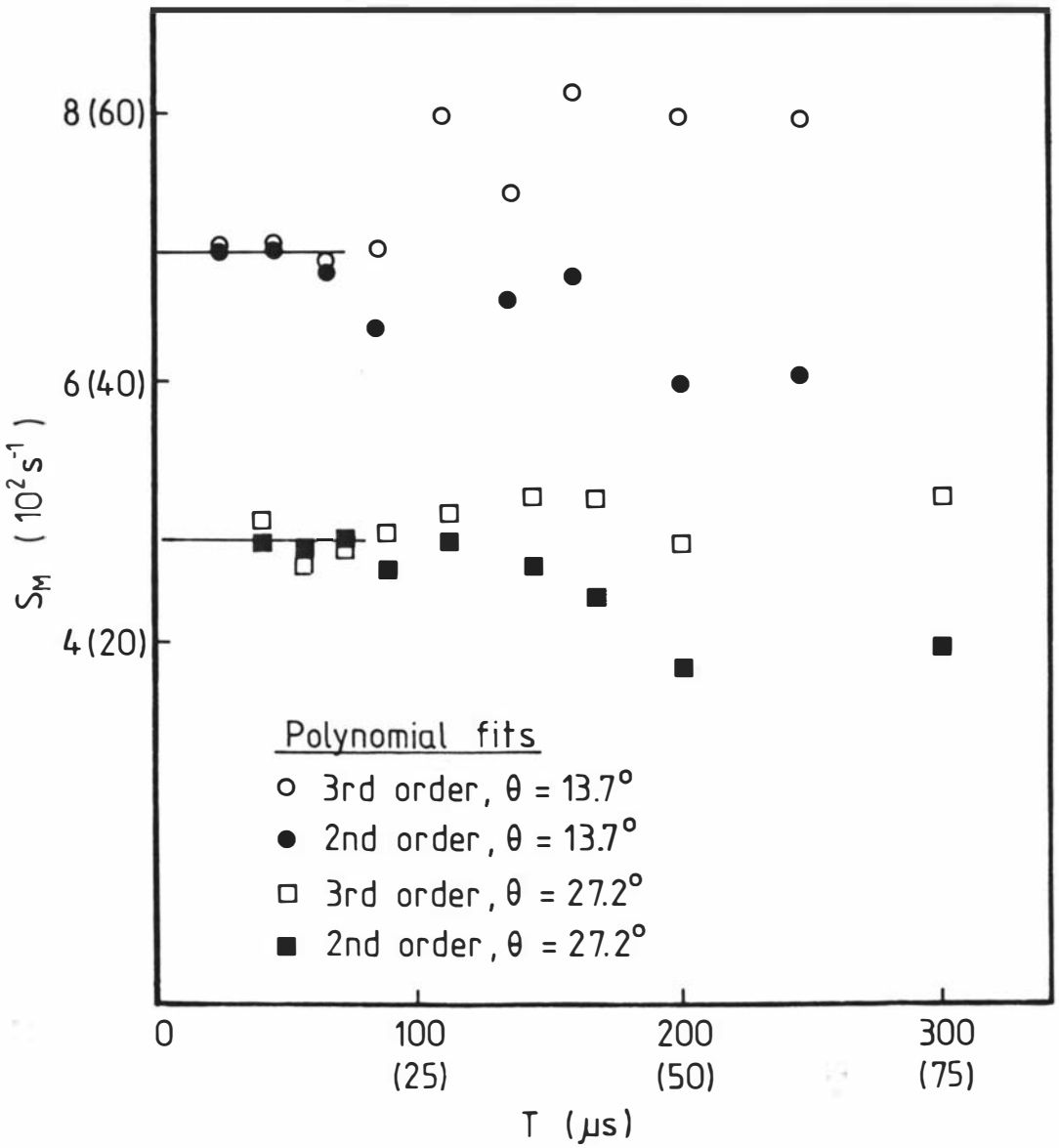


Figure 5.9. Cumulant plots for the sample 2.0gm% polystyrene in CCl_4. S_M is the initial slope obtained from ℓn(NIAF-1) versus time plots at various values of T. D_M is calculated from the value of S_M at T=0. The bracketed scales apply to the $\theta=27.2^o$ curves. The agreement between the values of S_M at T=0 for both the second and third order polynomial fits indicates an absence of systematic error in the curve fitting.

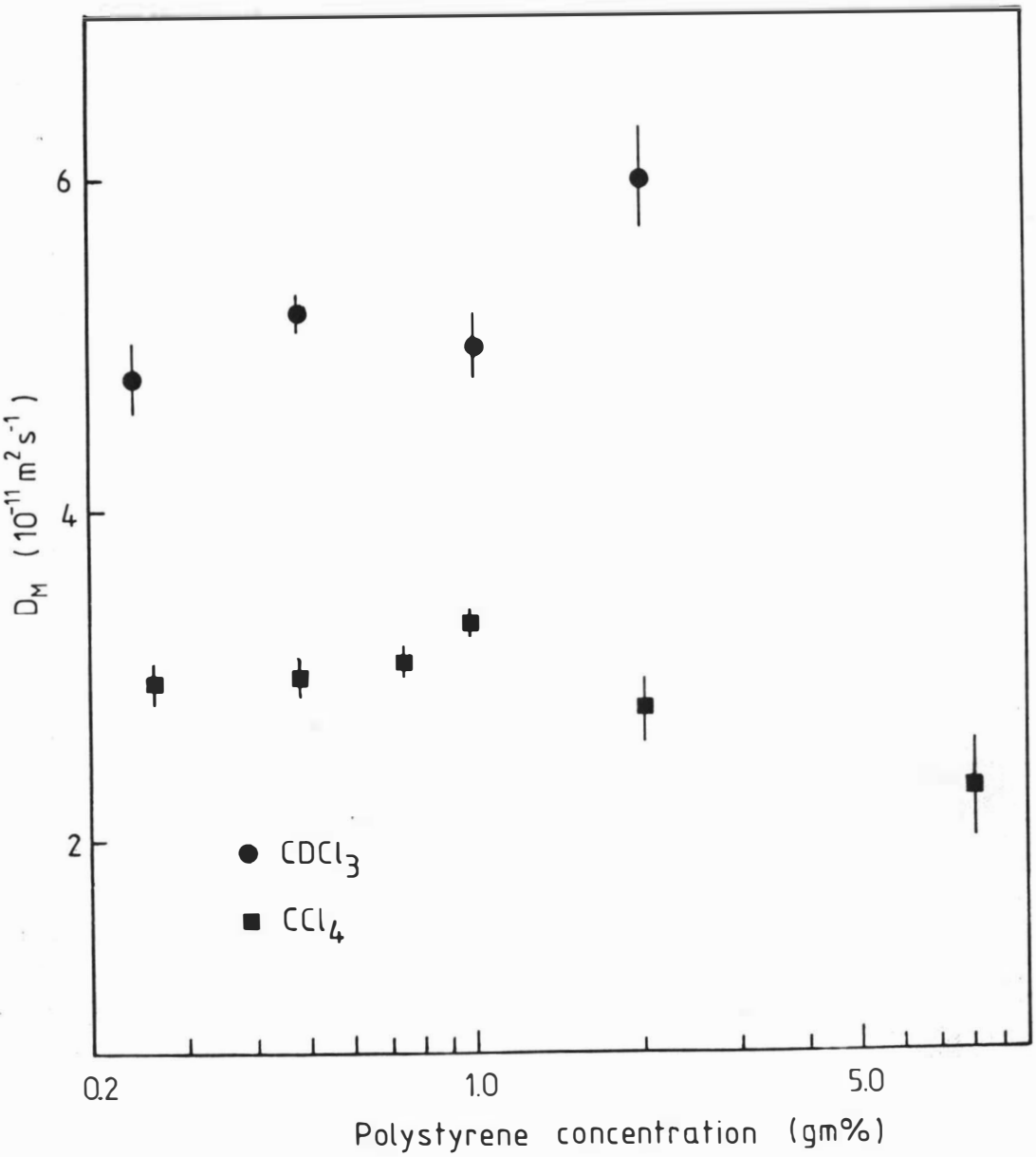


Figure 5.10. Mutual diffusion coefficients obtained by QELS for solutions of 110,000M_w polystyrene in the solvents $CDCl_3$ and CCl_4, as a function of polystyrene concentration. All experiments were conducted at 25.00±0.03°C.

similar system 390,000M_w polystyrene in butanone, studied over the more extended angular range $12^{\circ}<\theta<57^{\circ}$. Furthermore, it is dust which usually engenders a scattering-angle dependent D_M. Setting the blinker level by the BFF method precludes the possibility of dust lowering the values of D_M, but the ad hoc level setting method is not so precise, relying as it does upon visual sensing of an increasing scattered intensity.

The efficiency of the ad hoc method in removing dust-induced intensity fluctuations was assessed by studying the sample 0.96gm% in CCl_4. The ad hoc blinker level setting method yielded a value for D_M of $(3.33\pm0.08)\times10^{-12}m^2s^{-1}$. A trial application of the BFF method yielded a $Q'\simeq0.02$ at Aco = 1/3, indicating that setting the blinker level by this method is valid at this polystyrene concentration. The resultant value of D_M was $(3.38\pm0.04)\times10^{-12}m^2s^{-1}$ (BFF method), which is in excellent agreement with D_M obtained by the ad hoc method. Thus, dust is not expected to have significantly influenced any of the results presented in Figure 5.10, and these results would appear to be reliable in all other respects.

CHAPTER 6

DIFFUSION IN RANDOM-COIL POLYSTYRENE SOLUTIONS: DISCUSSION OF RESULTS

6.1 INTRODUCTION

Having measured the diffusion coefficients D_M and D_S for the systems polystyrene in CCl_4 and in $CDCl_3$, together with D_S for polystyrene in D-toluene, the comparisons previously given as research goals in Chapter 1.1 can be undertaken. The nature of these comparisons is now described.

For polymer solutions in which the random-coils are thoroughly overlapped, de Gennes[3] has predicted that D_S should vary as $c^{-1.75}$ (where c is the random-coil concentration). For polystyrene in benzene, Hervet et al.[7] have used the technique of Forced Rayleigh Scattering (FRS) to confirm that the concentration dependence of D_S does vary as $c^{-1.75}$ for $245{,}000M_w$ polystyrene in benzene. The D_S values determined in the PFGNMR study can be used to investigate the accuracy of the de Gennes' theory for other polymer/solvent systems.

Literature values of D_M and the indirectly determined polymer self-diffusion coefficient D_S^+, are available for the system $110{,}000M_w$ polystyrene in toluene[9]. The PFGNMR study of polystyrene self-diffusion in D-toluene was undertaken in order to effect a D_S/D_S^+ comparison. It should be noted that the effect of comparing diffusion coefficients obtained from studies in deuterated and undeuterated solvents must be evaluated.

The QELS results in this work have been obtained by using the blinker for dust minimisation, and small scattering angles have had to be used to obtain an acceptable signal-to-noise ratio. The reliability of the QELS-derived values of D_M can be firmly established through a comparison with macroscopically determined D_M values. For the polystyrene/CCl_4 system the QELS results can be compared with the interferometrically-derived D_M values obtained by Schick and Singer[67].

The final comparison is between the diffusion coefficients D_M and D_S. At low polystyrene concentrations ($c \lesssim 1$gm%), the effect of differing

solvents on D_S/D_M agreement is investigated.

6.2. THE dE GENNES' SCALING LAW FOR POLYMER SELF-DIFFUSION.

A description of polymer self-diffusion in polymer gels has been given by de Gennes. For the molecular weight of 110,000 , the polystyrene concentration must reach about 8gm% before the polymer gel regime is encountered[7]. In order to discuss the high concentration PFGNMR results, the theory of de Gennes'[3] is now briefly reviewed[7,66].

At very dilute polymer concentrations, the polymers behave as independent coils of (solvent-dependent) radius R_F. R_F is given by [66]

$$R_F = \ell(M/m)^{\nu} \qquad \nu=0.6 \qquad 6.1$$

where ℓ and m are respectively the length and molecular weight of a Kuhn statistical segment length (equal to about 3 monomer lengths[4]), M is the polymer molecular weight and ν is the (good solvent) Flory number. The macromolecules begin to overlap at a concentration c* such that the average distance between two neighbouring coil centres is equal to $2R_F$, thus defining c^* as

$$c^* = M/(R_F)^3 = (m/\ell^3)[M/m]^{(1-3\nu)^{\nu}} \qquad 6.2$$

In the concentration regime $c > c^*$, polymer chains interpenetrate and form a transient cross-linked network characterised by the average distance between entanglements, ξ (see Figure 6.1.a); and the chain disentanglement time, T_r (the time taken for a chain to adopt a completely new configuration). The parameter ξ is given by

$$\xi = R_F[c/c^*]^{[\nu/(1-3\nu)]} = (\ell/m\nu).(1-3\nu)^{-1}.c^{[\nu/(1-3\nu)]} \qquad 6.3$$

To evaluate T_r the concept of reptation is introduced[3]; that is to renew it's configuration a polymer chain has to slip in a tube of diameter ξ defined by its neighbours (see Figure 6.1.b). The tube can also suffer reorganisation (Figure 6.1.c) leading to additional relaxation of the polymer entanglements. de Gennes has shown that for a given polymer molecular weight, under the assumption that $\xi \gg \ell$,

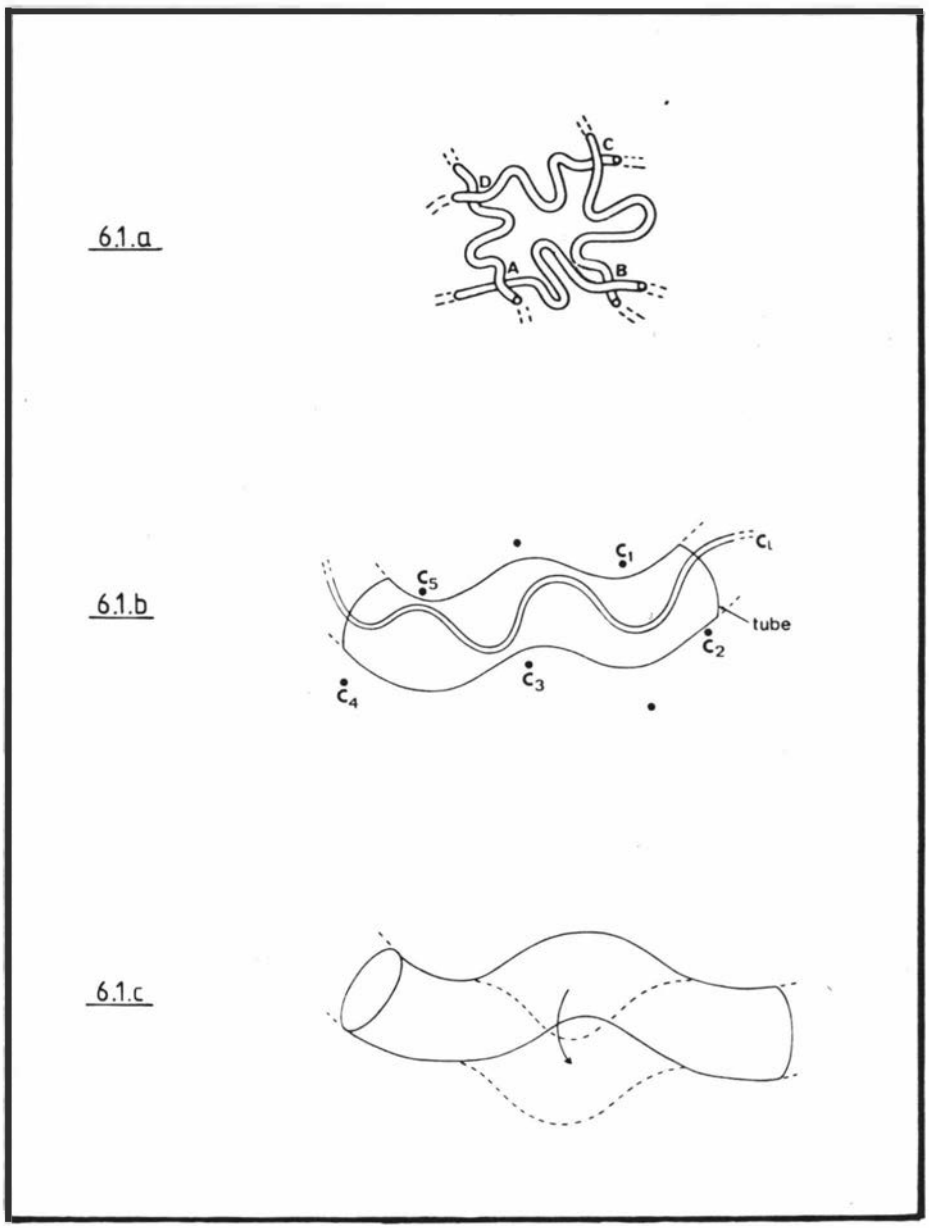


Figure 6.1. Entanglement phenomena in the polymer gel regime: the de Gennes' model - after de Gennes, reference 3.

6.1.a. Polymer entanglements. A, B, C ... are contact points between chains. The average distance between entanglement points is ξ.

6.1.b. One chain C_L trapped inside other chains C_1, C_2, C_3 ... . For not too long times, C_L is essentially confined inside a tube of radius $\sim \xi$.

6.1.c. Tube deformation: a region of size ξ moves over distances ξ.

T_r varies as

$$T_r \sim c^{1.5}$$

For an experiment conducted on a timescale long compared with T_r (such as PFGNMR experiments on 110,000M_w polystyrene [7], T_r can be taken as the elementary step of time in a 3-dimensional random walk[7]. The appropriate 3-dimensional elementary step of length is the end-to-end distance of the polymer chain[3,7]. For a given (low) molecular weight chain the self diffusion coefficient is then found to vary as [3,7]

$$D_S \sim c^{-1.75} \eta_0^{-1}$$

where η_0 is the solvent viscosity.

6.3 DIFFUSION IN RANDOM-COIL POLYSTYRENE SOLUTIONS: DISCUSSION OF RESULTS.

6.3.a. Experimental Results and the de Gennes' Scaling Law

In Figure 6.2 the data presented in Figure 5.3 have been re-plotted as $\log(D_S\eta_0)$ vs. $\log(c)$, so that the solvent viscosity effects are normalised. It is apparent that all three systems show a concentration range where the self-diffusion coefficient scales as $c^{-1.75}$ in accordance with the predictions of de Gennes'. The size of this range is greatest for CCl_4 and least for D-toluene. It is clear that in the entangled regime where the scaling laws operate, $D_S\eta_0$ is sensibly independent of the solvent, an entirely reasonable result for in this range of concentrations the main impediment to macromolecular motion is provided by intermolecular entanglements, and the entanglement renewal time T_r governs the diffusion rate.

For each solvent a breakdown of the scaling law is apparent for $c \gtrsim 20$gm%. The breakdown in the de Gennes' scaling law at high concentration arises from a fundamental assumption in the scaling law derivation; that is, the chain segments between entanglement points are assumed to have the same "flexibility" as a free chain. This is equivalent to requiring that these chain segments contain several Kuhn statistical units (i.e. $\xi >> \ell$), where the Kuhn statistical length ℓ is about 0.9nm for polystyrene[4]. At c = 25gm%, ξ = 3nm (from equation 6.3) and the requirement $\xi >> \ell$ breaks down. It can be seen from equation 6.3 that ξ is independent of the polymer molecular weight and so the breakdown of the D_S scaling law might be expected to occur at concentrations $\gtrsim$20gm% irrespective of the molecular weight of the polystyrene molecule.

At polymer concentrations below the polymer gel regime, some divergence of the data presented in Figure 6.2 is observed. This suggests that the random-coils have different hydrodynamic radii in the different solvents, with polystyrene in D-toluene having the smallest hydrodynamic radius. However, D-toluene is a good solvent for polystyrene and so the polymer radius of gyration is expected to be larger in this solvent than in the poorer solvents $CDCl_3$ and CCl_4. The results in Figure 6.2 indicate, therefore, that a larger radius of gyration (for

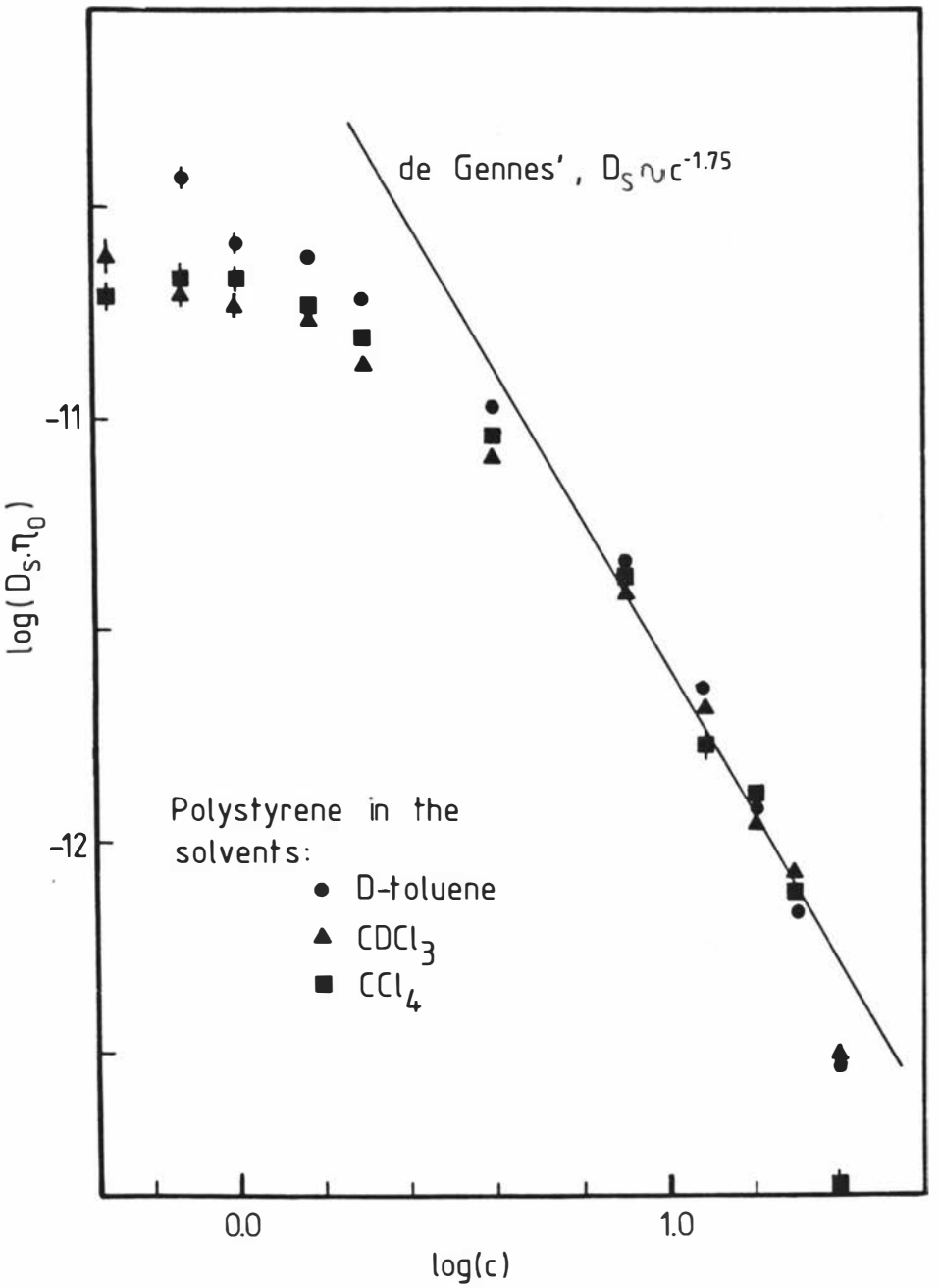


Figure 6.2. The self-diffusion coefficients of 110,000M_w polystyrene in various solvents, as a function of polystyrene concentration. The data have been normalised to solvent viscosity (η_0) and plotted as $\log(D_S\eta_0)$ versus log(c), where c is the polystyrene concentration. The units of the various quantities are centipoise (η_0), $10^{-11}m^2s^{-1}$ (D_S) and gm% (c). The data have been obtained by PFGNMR, and the straight line has the slope predicted by the de Gennes' scaling law for the polymer gel regime. Some divergence of the data is apparent at low concentrations which suggests different coil hydrodynamic radii in the different solvents.

a particular molecular weight polymer) is associated with a smaller frictional coefficient (a smaller hydrodynamic radius). A possible explanation for this effect is that the solvent, during polymer diffusive displacements, is less disturbed by flow through loosely-coiled, "swollen" polymers (those in good solvents) than by the process of flowing around more tightly-coiled polymers (those in poorer solvents).

6.3.b. Direct and Indirect Measurements of Polystyrene Self-Diffusion Coefficients

In the polymer gel region, polystyrene self-diffusion coefficients directly determined by the techniques of PFGNMR and FRS are consistent with the de Gennes' scaling law for D_S. Furthermore, at a given polystyrene concentration in the gel region, the quantity $D_S\eta_0$ is independent of the particular solvent used. It is of interest to consider whether or not indirectly determined polymer self-diffusion coefficients, those calculated from mutual-diffusion or sedimentation coefficients, also show that same scaling behaviour as D_S.

Roots et al.[9] have published D_S^+ values for 110,000M_w polystyrene in toluene. Sedimentation and mutual-diffusion measurements were made by Roots et al., with both techniques yielding mutually consistent values of D_S^+. The D_S^+ values are shown in Figure 6.3, where it is apparent that D_S^+ does not show the simple scaling law behaviour exhibited by directly measured self-diffusion coefficients. Figure 6.3 also shows that in the solvent toluene a large discrepancy exists between the magnitude of the directly and indirectly determined values of the polystyrene self-diffusion coefficient, especially at low solute concentrations where up to a 100% variation is observed.

Differences in the viscosities of deuterated and undeuterated toluene are too small to significantly influence polymer self-diffusion. However, the effect of deuteration on the expansion or contraction of random

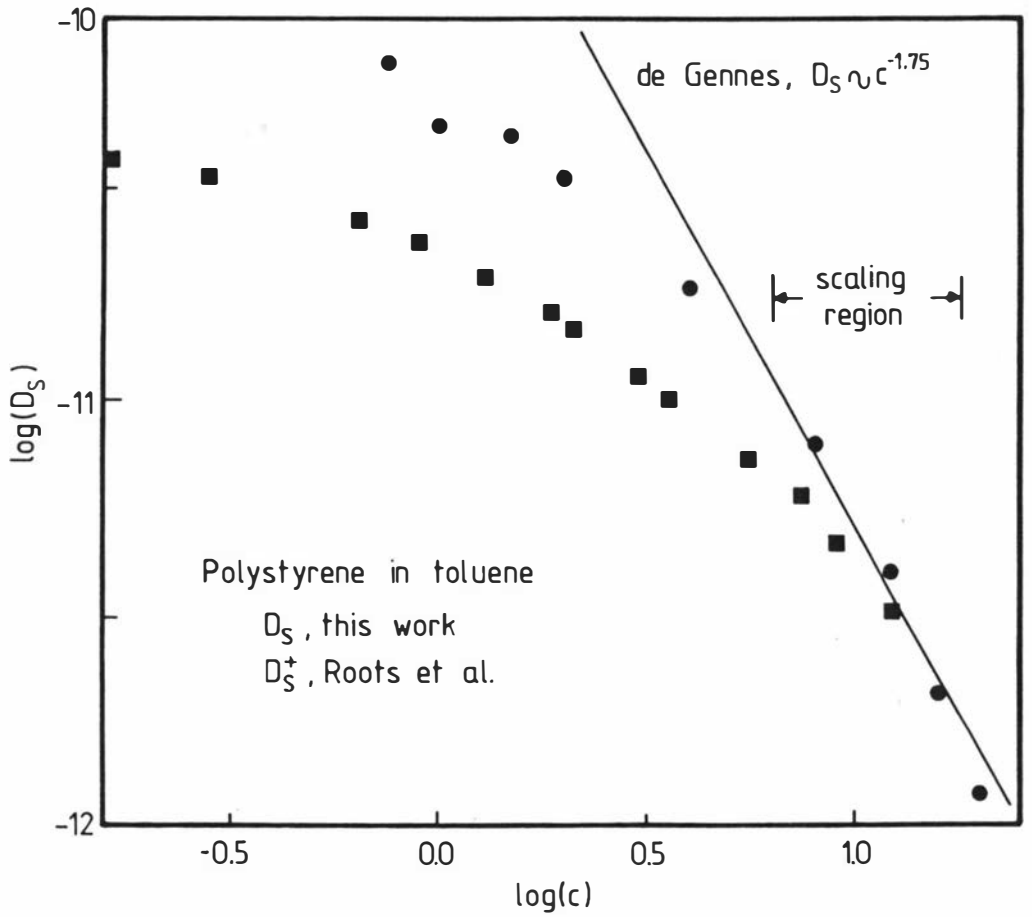


Figure 6.3. A comparison of random-coil polystyrene self-diffusion coefficients directly measured by PFGNMR (D_S; x 10^{-11} m^2 s^{-1}) with those determined from sedimentation coefficients (D_S^+; x 10^{-11} m^2 s^{-1}). A wide disagreement is apparent and only the D_S values scale according to the de Gennes' theory.

coils due to polymer/solvent interactions is not so clear, and it is perhaps radius of gyration changes which account, in part, for the variations observed in Figure 6.3. The effect of deuteration on the nature of the solvent can be assessed by comparing D_S for a polymer in a deuterated and undeuterated solvent. Hervet et al. have used FRS to measure D_S of 123,000M_w polystyrene in benzene. They obtain $D_S = (3.5\pm0.4)\times10^{-11} m^2 s^{-1}$ at 1.4gm%, and $D_S = (2.9\pm0.2)\times10^{-11} m^2 s^{-1}$ at 2.1gm%. For 110,000M_w (the closest molecular weight available here) polystyrene in deuterated benzene, a PFGNMR experiment yielded $D_S = (3.2\pm0.1)\times10^{-11} m^2 S^{-1}$ at 2.0gm%. The deuteration of a solvent thus appears to have little effect on D_S.

The results summarised in Figure 6.3 indicate, therefore, that the sedimentation/mutual-diffusion indirect approach to the calculation of D_S^+ must be inappropriate for random-coil macromolecules. Equations linking the mutual-diffusion and sedimentation coefficients to the polymer self-diffusion coefficient (equations 1.5 and 1.6 in Chapter 1) do not successfully predict D_S either in the polymer gel region (where entanglement phenomena predominate) or in more dilute polymer solutions (e.g. at c=0.5gm%) where the random-coils are well-separated on average (see Table 6.1).

6.3.c. A Comparison of Macroscopic and QELS Determinations of the Mutual Diffusion Coefficient

Schick and Singer[67] have presented D_0 and D_M values measured by interferometry, for various molecular weight polystyrenes in CCl_4 and butanone. Older studies of polymer diffusion (such as those by Schick and Singer; 1950) must be approached with some caution as the polymers used were often polydisperse. The molecular weights reported may thus not be appropriate for use in comparisons with the well characterised, monodisperse polystyrenes used in QELS studies.

The D_0 values of Schick and Singer, as a function of molecular weight, are presented in Figure 6.4 for polystyrene in CCl_4 and butanone. QELS values of D_0 for polystyrene in butanone, obtained from the work of King et al.[64], are also shown in Figure 6.4 and are in good agreement with the interferometry results. The polystyrenes used by Schick and Singer thus appear to be sufficiently monodisperse to allow

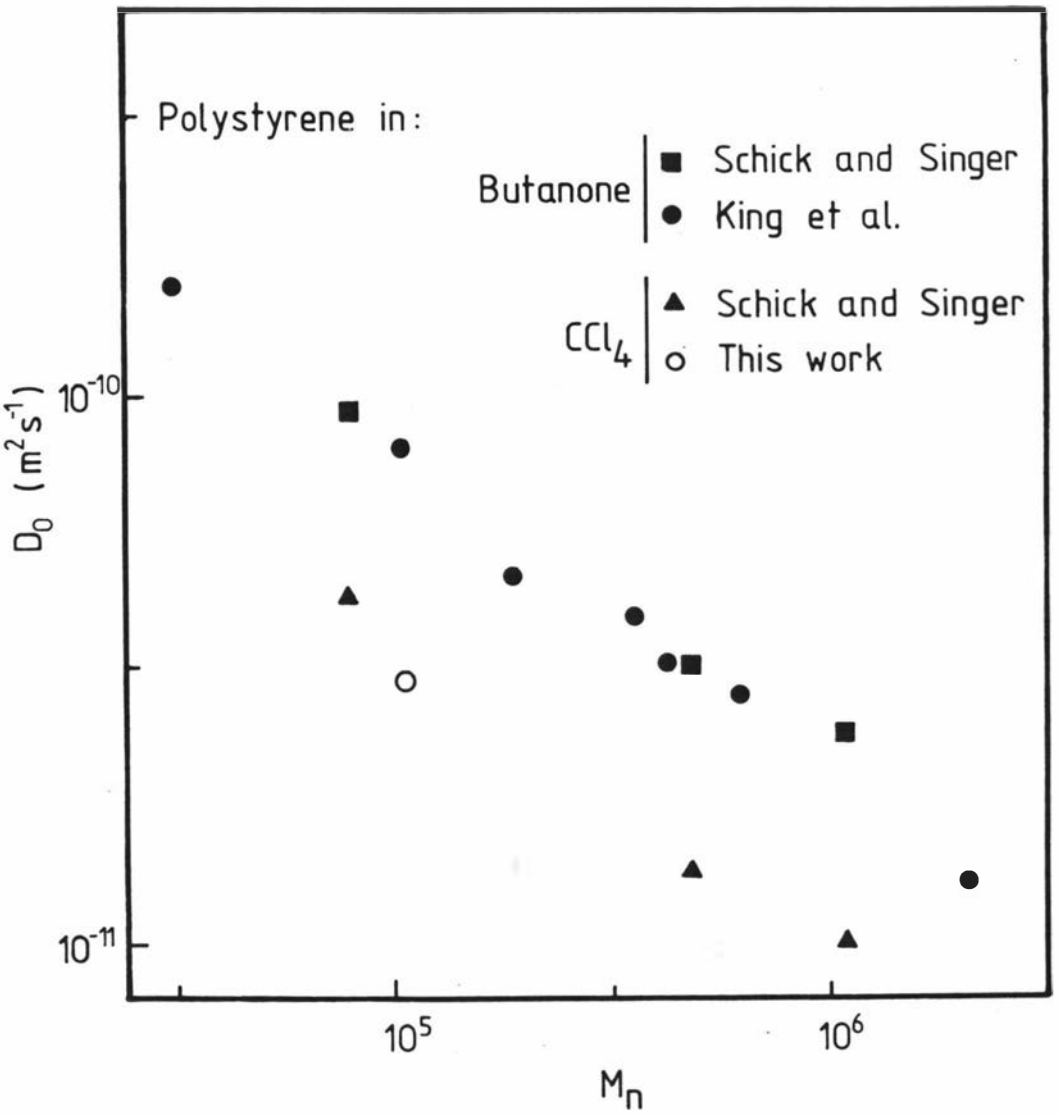


Figure 6.4. A comparison of D_0 values obtained by wedge interferometry (Schick and Singer) with results from QELS studies (King et al., and this work). The QELS/interferometry agreement obtained for polystyrene in butanone indicates that the polystyrenes used by Schick and Singer are sufficiently well characterised to allow comparisons with QELS studies, which use monodisperse polystyrenes of well known molecular weight. Extrapolation of the QELS results for polystyrene in CCl_4 (this work) to zero polymer concentration also yields a value of D_0 in good agreement with the macroscopically-determined results of Schick and Singer.

comparison with those used in QELS studies.

Schick and Singer have measured D_M over a limited polymer concentration range (0 to 0.5gm%) of polystyrene in CCl_4. For polystyrenes of molecular weight ~110,000 (in CCl_4), the interferometry results indicate that D_M is concentration independent below 0.5gm%. In the solvent CCl_4, the QELS values of D_M also show such a concentration independence (see Figure 5.10). Extrapolation of the QELS results to zero polymer concentration yields a value of D_0 in good agreement with the D_0 results of Schick and Singer, as shown in Figure 6.3. Thus, where comparisons are able to be made, good agreement is found between the values of D_M reported in this work and the macroscopically-determined D_M values.

6.3.d. A Comparison of Self and Mutual Diffusion Coefficients in Polymer Solutions.

Where solute-solute interactions dominate, the solvent-solute mutual diffusion coefficient and solute self-diffusion coefficients may differ markedly. However, in the limit of low solute concentrations such interactions vanish and the D_M and D_S values must reach the same infinite dilution limit. In Figures 6.5, 6.6 and 6.7 the mutual and the self diffusion coefficients for $110{,}000M_w$ polystyrene are plotted against a linear concentration scale for the solvents CCl_4, $CDCl_3$ and D-toluene (toluene for D_M). The mutual diffusion data for the last system are taken from the work of Roots et al.

Even at the lowest concentrations (0.5gm%) there is a wide discrepancy between the mutual and the self diffusion coefficients. In the case of the poorer solvents CCl_4 and $CDCl_3$, the low concentration values of D_M exceed the corresponding D_S values whilst for the good solvent toluene the opposite is true. As previously discussed, the independence of the measured D_S values on solvent deuteration removes solvent isotopic differences as a mechanism for the D_M/D_S disagreement in the case of toluene. Such a mechanism does not even arise for CCl_4 and $CDCl_3$, where the separation of D_M and D_S is still evident. The mutual and self diffusion coefficients must ultimately agree at some concentration below the lower limit of 0.5gm% studied here. (The concentration regime where $D_M \approx D_S$ has been termed "very dilute" in this work.)

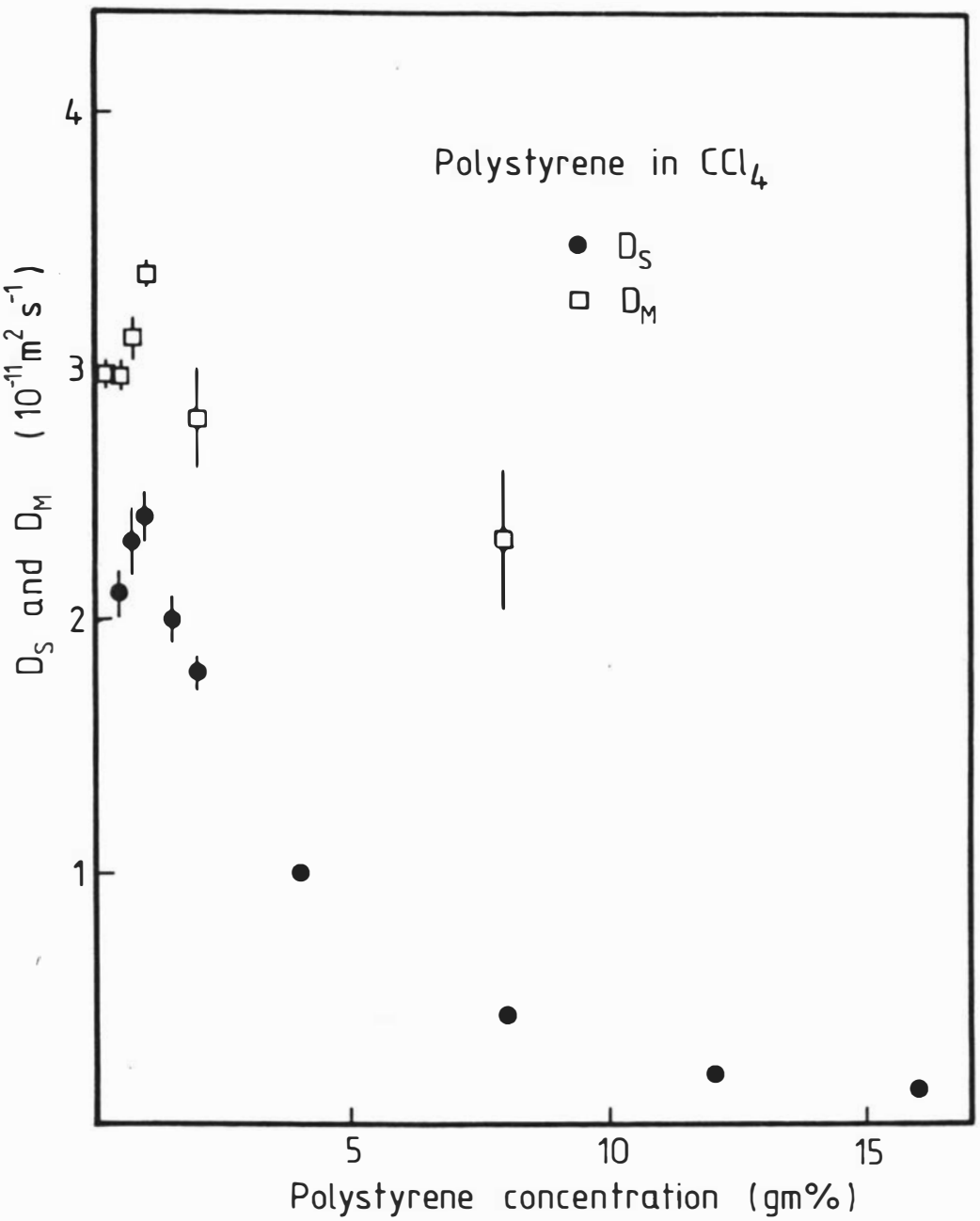


Figure 6.5. A comparison of mutual- and self-diffusion coefficients for 110,000M_w polystyrene in CCl_4. D_M values were obtained by QELS and D_S values by PFGNMR.

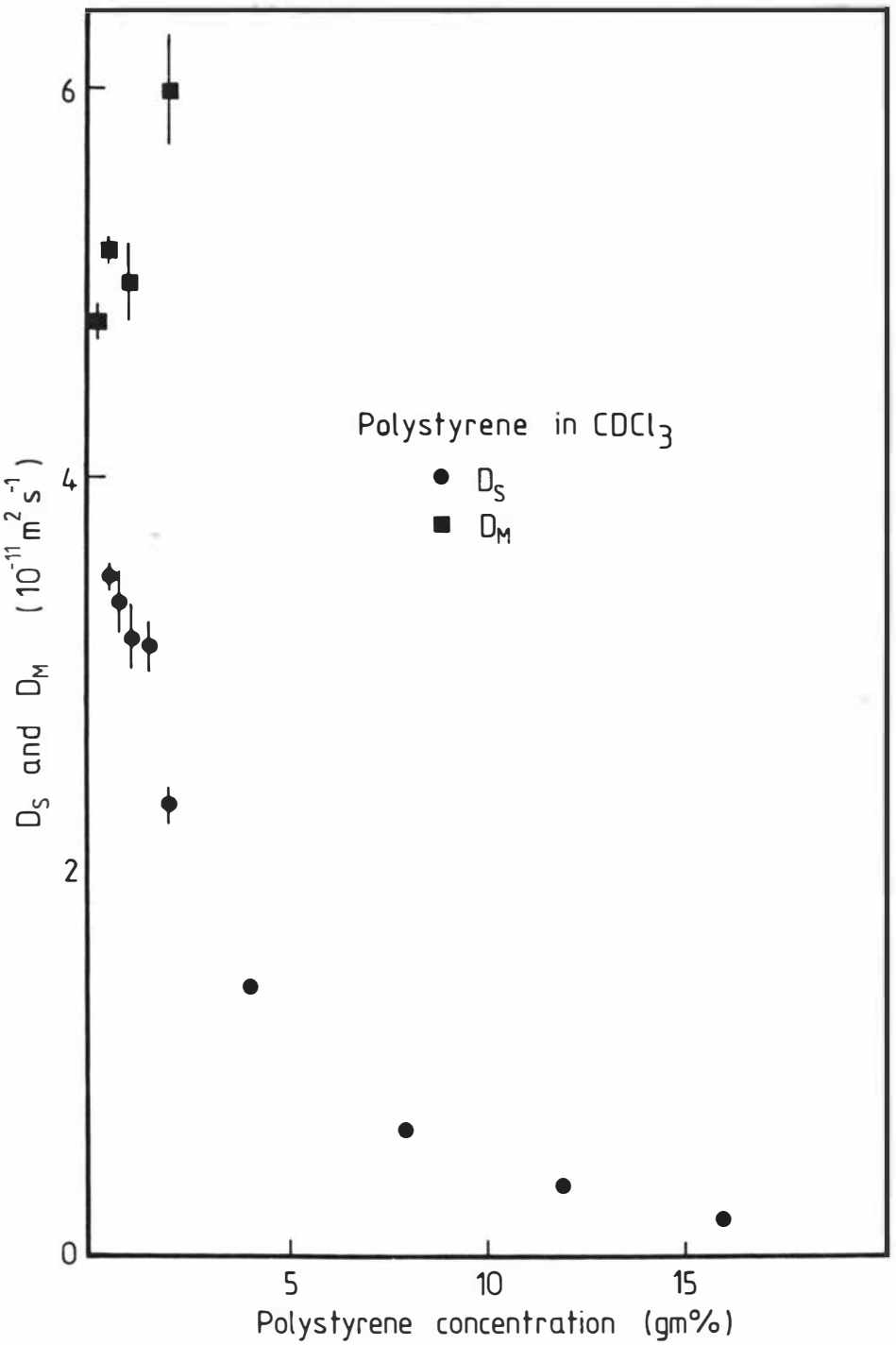


Figure 6.6. A comparison of mutual- and self-diffusion coefficients for 110,000M_w polystyrene in $CDCl_3$. D_M values were obtained by QELS and D_S values by PFGNMR.

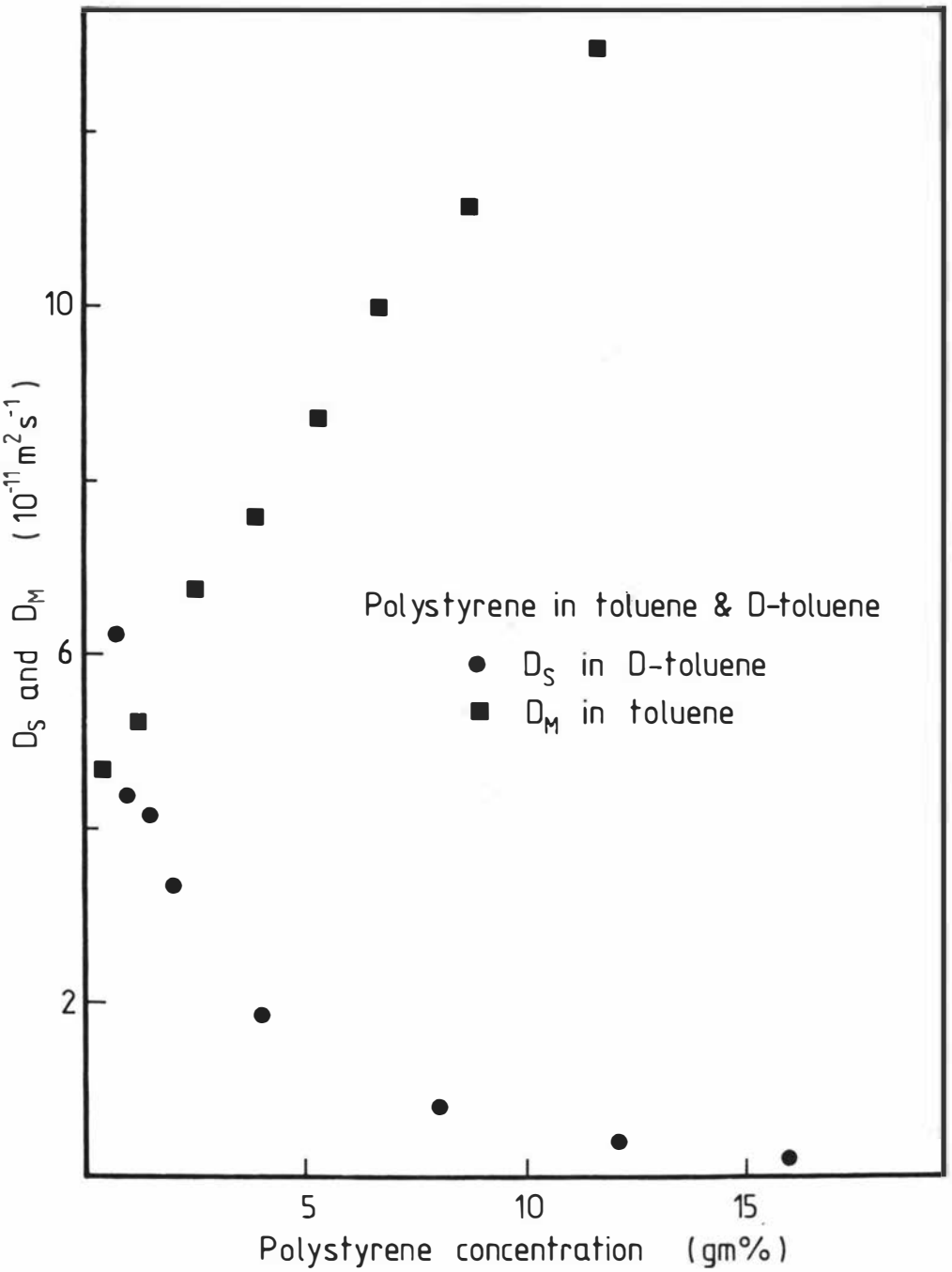


Figure 6.7. A comparison of mutual- and self-diffusion coefficients for 110,000M_w polystyrene in the solvents D-toluene (D_S measurements by PFGNMR) and toluene (D_M measurements by a diffusion cell technique). The D_M values are taken from the work of Roots et al.[9]

In the present investigation a discrepancy exists between mutual and self diffusion coefficients over the entire concentration regime available for study, implying that solute-solute interactions still play a significant role in polystyrene diffusion at rather low solute concentrations, where $c<<c^*$. The concentration region $c<c^*$, at least down to the lower limit of 0.5mg% studied here, is perhaps best termed "dilute" (as opposed to "very dilute") and solute interactions in this region can be envisaged as occurring in the following manner. At polymer concentrations of ~0.5gm%, polymer molecules are on average well separated. However, the experimental times over which D_M and D_S are measured by QELS and PFGNMR are long enough to allow diffusing molecules to meet and suffer intermolecular entanglements. Table 6.1 lists the characteristic lengths associated with QELS and PFGNMR diffusion coefficient determinations at the lowest polymer concentration susceptible to measurement by both techniques. It should be noted that the average displacement of the macromolecules during a measurement period is significantly greater than their average separation.

It may now be understood why the mutual/self-diffusion coefficient discrepancy is highly solvent dependent in the dilute regime. The extent to which entanglements occur in polymer-polymer encounters during the experimental time interval will depend on the relative surface free energy of the chain-chain and chain-solvent surfaces. In a good solvent such as toluene, polymers would show less tendency to entangle during intermolecular encounters than in a poorer solvent, thus leading to an increased D_S in a good solvent (relative to D_S in a poorer solvent, such as CCl_4). The trends shown in Figures 6.5, 6.6 and 6.7 for the D_M/D_S discrepancies are thus not entirely unexpected. The idea of a "dilute" concentration regime is not new, having previously been termed an "intermediate state" by Edwards[11] who writes that such a state is characterised by a "lumpy" density, as some macromolecules are entangled with their nearest neighbours, while others are not.

The possession of a smaller hydrodynamic radius by polystyrene in the good solvent D-toluene (see Figure 6.2) can now also be better explained in view of the fact that polymer-polymer interactions persist at the lowest polystyrene concentrations studied. In the dilute regime, polymer-polymer entanglements are expected to persist for longer periods of time when the random-coils are in a poor solvent; relative

Polystyrene concentration. (gm%)	0.5	8.0
R_M	33nm	13nm
R_g	9nm	9nm
$(\overline{r^2})^{\frac{1}{2}}_{QELS}$	200nm-500nm	200nm-500nm
$(\overline{r^2})^{\frac{1}{2}}_{PFGNMR}$	1100nm	730nm

Table 6.1. A comparison of the mean intermolecular spacing, R_m; the radius of gyration of the polystyrene random coil macromolecules, R_g; and the experimental displacements, $(\overline{r^2})^{\frac{1}{2}}_{QELS}$ and $(\overline{r^2})^{\frac{1}{2}}_{PFGNMR}$, at two different concentrations; one for $c<c^*$ and the other for $c>c^*$. R_g has been calculated according to King et al.[64].

to the persistence of entanglements in a good solvent. In the dilute polystyrene concentration regime this is expected to lead to a reduced D_S for polystyrene in poorer solvents, a trend which has been observed. This trend would be augmented by any tendency of the solvent to flow more easily through swollen polymers (as suggested in section 6.3.a).

CHAPTER 7

POLYSTYRENE LATEX SPHERE DIFFUSION: A LASER LIGHT-SCATTERING STUDY

7.1 INTRODUCTION

In Chapter 1 it was pointed out that in the case of concentrated solutions of charged macromolecules, further experiments were required to investigate the relationship between D_M and the apparent diffusion coefficient measured by QELS. This chapter presents the results of a QELS study of diffusion in solutions of polystyrene latex spheres at moderate ionic strength. The quantity with the dimensions of a diffusion coefficient that can be obtained from QELS studies is compared with values of D_M obtained from capillary penetration experiments on similar solutions of latex spheres.

Two latex sphere concentration regimes were studied as part of this work: the very dilute regime (latex sphere concentrations ranging from 0.004gm% to 0.025gm%) and the concentrated regime (> 0.4gm%). In the concentrated regime latex sphere solutions exhibit the phenomenon of multiple scattering; that is, a single photon encounters more than one latex sphere during passage through the sample cell[70]. The effect of multiple scattering on the QELS experiment must be assessed before QELS data obtained from a study of diffusion in concentrated latex sphere solutions can be interpreted with confidence.

One of the effects of placing latex spheres in solutions of moderate ionic strength is that long range electrostatic interactions between the latex spheres are screened out[71]. This ensures that the non-Brownian diffusion mechanisms associated with long range electrostatic interactions, of the type previously studied by Brown et al.[72] and Dalberg et al.[73], are absent. Non-Brownian diffusion gives rise to a scattering angle dependent diffusion coefficient in QELS experiments[72], thus making it difficult to assess the reliability of a QELS study. Unfortunately, screening the latex sphere surface charges also enhances the possibility of sphere aggregation, and so precautions must be taken to ensure that aggregates do not significantly alter the magnitude of the QELS-determined diffusion coefficients.

Anderson et al.[71] have determined the mutual diffusion coefficients of concentrated solutions of 0.091μm diameter latex spheres in 0.01M and 0.001M potassium chloride (KCl) The surfactant sodium dodecyl sulfate (SDS) was added to obviate sphere aggregation, and experiments were carried out on latex sphere solutions ranging in concentration from 0.5gm% to 6gm%. The only latex spheres available for the QELS study possessed a diameter of 0.085μm. Furthermore, although adding a surfactant to obviate sphere aggregation is a useful step, the SDS/KCl combination used by Anderson et al. should be avoided as the potassium salt of dodecyl sulpate is insoluable[74]. Apart from reducing the effectiveness of the surfactant in preventing sphere aggregation, the suspended precipitate in SDS/KCl solutions gives rise to undesirable scattering in a QELS experiment. Because of these effects, sodium chloride (NaCl) was used as the source of ionic strength in the QELS experiments. Solutions of 0.01M and 0.001M NaCl were used as "solvents" for the latex spheres, and SDS was added at a concentration of 0.0007M. The effect of the differing sphere diameters and differing surfactant concentrations on diffusion in latex sphere solutions must be taken into account when a D_M/QELS-measurement comparison is undertaken.

7.2. THE EFFECT OF MULTIPLE SCATTERING

The interpretation of QELS data collected from solutions displaying multiple scattering has been discussed in a number of recent theoretical and experimental studies[70, 73, 75-77]. The theoretical predictions have permitted interpretation of the initial decay of an IAF obtained from a system of non-interacting Brownian particles, when a scattered photon has suffered up to four scattering events[73]. This treatment has not yet been extended to more than four scattering events, and the effect of multiple scattering on the long time part of the IAF has also not been theoretically investigated. Since light scattered from concentrated latex sphere solutions is likely to contain more than four scattering events[70], the theoretical results are of little use here.

The experimental studies of several authors have indicated that while multiple scattering can alter the initial part of the IAF, the long time part of the IAF is unaffected[70], even when a high proportion of the light is multiply scattered[78]. We now consider the available experimental evidence in an effort to establish criteria for the interpretation of data collected from multiply scattering latex sphere solutions.

Pusey[70] has concluded that the major effect of multiply scattered light arising from the primary scattering volume is to add a rapid decay, characteristic of such light, to the slower decay associated with single scattering. The IAF thus contains a fast initial decay impressed upon the single exponential decay characteristic of singly scattered events. When the ratio of singly to multiply scattered light is small it is difficult to resolve these two processes. The ease of resolution of the two exponential decays also depends on the scattering angle as the two decay rates do not exhibit the same angular dependance. The initial decay rate has only a small angular dependance, showing less than a 20 percent variation as the scattering angle varies from 160^{o} to 20^{o}[70].

Multiple scattering also gives rise to a scattering volume which is larger than that encountered in an experiment concerned only with singly scattered events. For the scattering geometry employed in the Malvern 4300 spectrometer this results in the illumination of several coherence areas at the photomultiplier[70]. This leaves the decay rates of the IAF unchanged.

Colby et al.[75] have also investigated the behaviour of the initial decay rate of the IAF obtained from multiply (Rayleigh) scattering solutions of large non-interacting polystyrene spheres. This decay rate exhibited a marked non-linear dependance on q^2, in contrast to the linear dependance expected from singly scattering, non-interacting solutions of spheres. It was also found that at a given scattering angle the initial decay rate of a multiply scattering solution was dependent on the particular cell path length used in the study of the solution.

We may summarise the above observations as follows. The effect of moderate amounts of multiply scattered light on the IAF of a monodisperse polystyrene sphere solution is to introduce an additional fast decay to the longer, single exponential decay associated with single scattering. The long time decay, if resolvable, may be analysed according to usual singly scattered QELS theories (those presented in Chapter 2). Analysis of the initial decay of the IAF in systems where multiple scattering is known to exist shows that this decay rate is not a linear function of q^2[or equivalently $\sin^2(\theta/2)$]. Conversely, quantities derived from a decay rate exhibiting a linear q^2 dependence can be considered free of multiple scattering effects. A path length independent decay rate also indicates that multiple scattering effects are absent.

7.3. THE EXPERIMENTAL STUDY

7.3.a. Sample Preparation

Aqueous suspensions of polystyrene latex spheres of nominal diameter 0.085μm and nominal concentration 10gm% were supplied by the Dow Chemical Company (Indianapolis, USA). The SDS and NaCl were Analar grade, obtained from BDH chemicals (Poole, England.). The aqueous suspensions of latex spheres contain residual salts and surfactants, and so to standardise the ionic strength and surfactant concentrations in experimental solutions, the dialysis preparation scheme presented by Anderson et al. was used.

The concentrated solutions ($\gtrsim$ 0.5gm%) were prepared by forming an ~5gm% solution at the approximate ionic strength required, and then dialysing this solution for 48 hours against the appropriate 0.001M or 0.01M NaCl solution. SDS was also added at a level of 0.022gms per $100cm^3$ of solution, to both the ~5gm% and NaCl dialysis solutions. After dialysis, the following solutions were formed: ~2gm% (0.001M and 0.01M), ~4gm% (0.001M) and ~2.5gm% (0.01M). All solutions were stored at 4^oC until used, and to further minimise aggregation effects, experiments on the 0.001M solutions were completed before dialysis of the 0.01M solution was carried out. The dilute solutions ($\lesssim$ 0.025gm%) were formed by simple dilution of the Dow aqueous suspension with 0.001M or 0.01M NaCl solutions, as appropriate.

Sample concentrations were determined by U.V. spectrophotometry at a wavelength of 265nm with a Shimadzu (Kyoto, Japan) MPS-5000 spectrophotometer. The samples were diluted to ~0.004gm% and the absorbance readings compared with calibration curves prepared by diluting the neat Dow latex sphere suspension. The concentration of the Dow suspension, determined by drying $1cm^3$ of neat solution to constant weight at 60^oC, was (10.15±0.05)gm%. Absorbance readings for duplicate samples were reproducible to about 0.5%, indicating that sample concentrations quoted in this work could contain an error of up to 2%.

Since the latex spheres are very much better scatterers than $110,000M_w$

random-coil polystyrene molecules, a much simpler cell and solution clearing sequence than that presented in Chapter 6 could be employed. Having first removed any residual chemical traces from the cells by ultrasonication in hot detergent, followed by copious rinsing with re-distilled water; the following procedure was used for preparation of a new sample. The cell was rinsed with ten volumes of each of the following; a hot detergent solution, hot tap water, re-distilled water and 0.22μm filtered (using a Millipore filter) re-distilled water. This last rinsing step was performed in an atmosphere of 0.22μm filtered air, where the cell was also transferred to a dessicator and subsequently dried *in vacuo*. A small Millipore filter holder (using 13mm diameter filters), suitable for attaching to the end of a syringe, was also subjected to the above rinsing and drying steps. Light scattering samples were prepared by directly filtering the latex sphere solutions into a sample cell using the 13mm, 0.22μm pore size Millipore filters. These filters had been pre-washed (and dried) to remove any contaminant salts or surfactants deposited in the filter during the manufacturing process. Intermediate latex sphere concentrations were obtained by diluting the ~2gm% or ~2.5gm% solutions with a NaCl/SDS solution filtered directly into the sample cell. Sample cells were weighed at each stage so that accurate concentration calculations could be made once an aliquot of the most dilute solution in the cell had been analysed by U.V. spectrophotometry. All solution transfers and dilutions were carried out in an atmosphere of 0.22μm filtered air.

The QELS experiments were performed using the laser spectrometer described in Chapter 2. Where appropriate, the experimental details outlined in Chapter 6 have been taken into consideration (sample thermal equilibration times, etc).

7.3.b. Use of the Blinker

Preliminary experiments without the blinker indicated that the IAFs obtained from a study of a concentrated latex sphere solution exhibited both a short initial decay and a long, quasi-single-exponential decay. The long time decay assumed single exponentiality (i.e. $Q' \lesssim 0.02$) when the blinker was set by the ad hoc method. However, setting the blinker level in this way is rather tedious, and it was considerably

simpler to manipulate the blinker level until the long time decay assumed single exponentiality as judged from a ℓn(NIAF-1) vs. t plot. That such an adjustment scheme is permitted can be seen from the fact that during preliminary experiments the blinker held the correlator off for as little as 1 second in 10. A correlator accumulation period of 9 seconds represents a time extremely long compared with any statistical fluctuations in the light intensity falling on the photomultiplier, and so the intensity fluctuations causing the blinker to act may be assumed to be due to the presence of dust in the scattering volume. The preceding argument is expected to hold even when the correlator accumulates for as little as, say, 1 in 2 seconds, although such dusty samples result in poor utilisation of the available experimental time. The applicability of the blinker level setting method outlined above will be further discussed in section 7.4.a.

7.3.c. Data Analysis

In this section we discuss, as an example, the data obtained from a solution of 2.15gm% latex spheres in 0.001M NaCl. This solution exhibits the complications typically encountered in the interpretation of data from the concentrated solutions of spheres studied in this work. A solution of 2.71gm% latex spheres in 0.01M NaCl is also discussed, and data obtained from this solution used to justify the blinker setting scheme outlined in the last section.

The 2.15gm% sample was studied in a 1.000cm path length cell and visual inspection indicated severe multiple scattering; indeed the laser beam was attenuated to approximately 3% of the incident beam intensity on passage through the sample cell. Several plots of ℓn(NIAF-1) versus channel number for the 2.15gm% sample are shown in Figure 7.1. The theoretical background (equation 2.17) was used to obtain the NIAFs for all data presented in this work. Despite the intense multiple scattering associated with the 2.15gm% sample, it should be noted that the low angle NIAFs in Figure 7.1 exhibit a short initial decay followed by a longer, single exponential decay. This longer decay was attributed to single scattered events.

The NIAFs shown in Figure 7.1 were obtained by using the blinker to

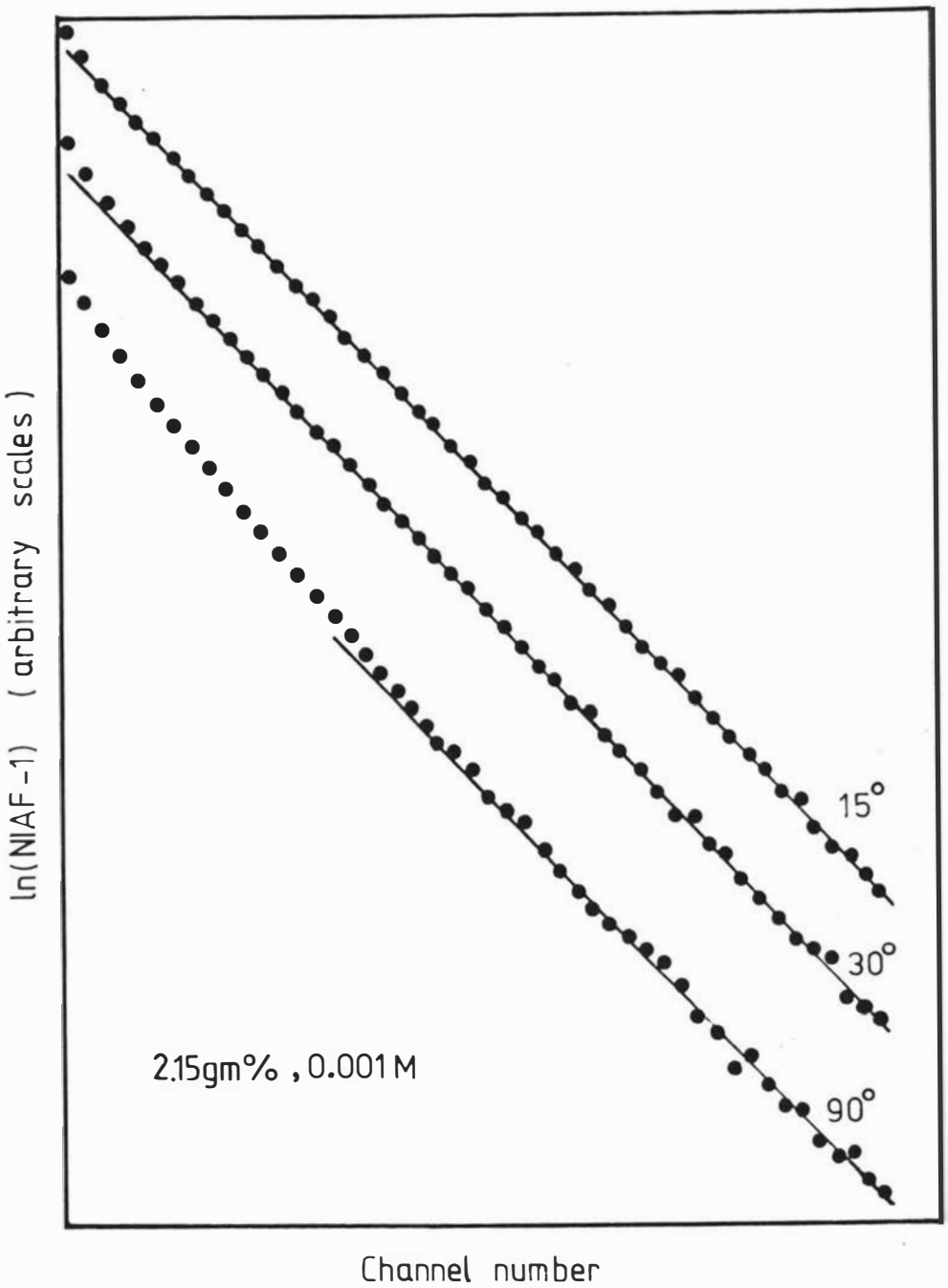


Figure 7.1. Plots of ℓn(NIAF-1) versus channel number showing the presence of long and short decays in the NIAF, for the sample 2.15gm% polystyrene latex spheres in 0.001M NaCl. The long decay exhibits single exponential behaviour ($Q' \lesssim 0.02$). The long and short decays are not separable at a scattering angle of 90°.

θ	Sample	Aco	Q'
15^{o}	2.15gm%	1/4	0.012
30^{o}	2.15gm%	1/6	0.011
15^{o}	2.71gm%	1/12	0.010
30^{o}	2.71gm%	1/10	0.005

Table 7.1. Examples of correlator off-to-on times (Aco) encountered in the concentrated latex sphere study. The 2.15gm% (0.001M) sample gives typical values of Aco; while the 2.71gm% (0.01M) sample was the cleanest studied. Note that small Q' values are obtained even when the blinker is infrequently triggered. The experimental run times were 15-30 minutes, depending upon the particular sample under study.

remove any spurious intensity fluctuations from the scattered light. That the intensity fluctuations removed were, in fact, spurious can be seen from the ratio of the average correlator off-to-on times shown in Table 7.1. Also presented in Table 7.1 are the values of Q' obtained from the very clean sample 2.71gm% in 0.01M NaCl. The blinker was seldom triggered during accumulation of the IAFs for this sample, yet single exponential behaviour of the long time part of the NIAF was observed (i.e. $Q' \lesssim 0.02$). This supports the earlier conclusion that the spurious intensity fluctuations which trigger the blinker are caused by dust in the scattering volume, and are not caused by processes of experimental interest.

The count rates observed for this sample were high although the signal-to-noise ratio was much poorer than would ordinarily be expected of such count rates. From this it was concluded that most of the multiply scattered light was uncorrelated and so did not mask the small amount of correlated singly scattered light present. A similar conclusion was reached by Chu et al.[78] in studies of critical opalescence in binary solutions. At larger scattering angles it was more difficult to measure the long time decay rate owing to both the decreased amounts of single scattered light and the poorer resolution between the long and short decays present in the IAF. Figure 7.1 illustrates these trends and indicates that the long and short decays can not be reliably separated at a scattering angle of 90°. Only data displaying two clearly separable components have been analysed ($\theta \leq 30^{\circ}$ for the 2.15gm% sample).

The long time decay rate, S_L, is the slope of the long time part of a plot of ℓn(NIAF-1) versus time. The assumption that the long, single exponential decay is related to a singly scattered process is supported by the linear dependance of S_L on $\sin^2(\theta/2)$, shown in Figure 7.2. Details of the data analysis for the 2.15gm% sample are presented in Table 7.2. The quantity D_L has been calculated assuming the long time decay of the NIAF is a single exponential with exponent $(-2D_Lq^2)$. Although the range of angles over which the 2.15gm% sample was studied was rather small, more dilute samples with a much extended angular range show good agreement between high and low angle values of the observed diffusion coefficient (see Figure 7.4).

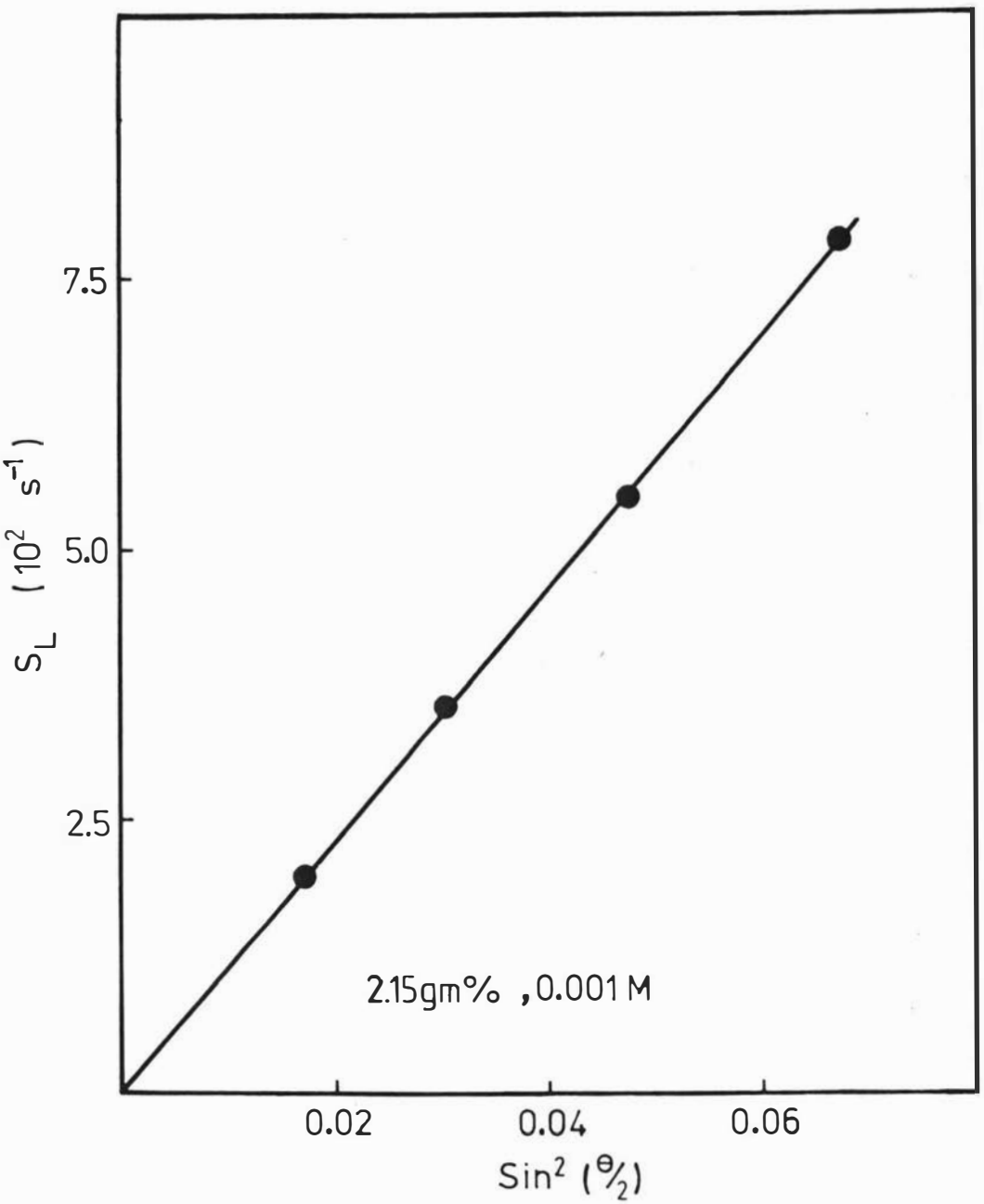


Figure 7.2. A plot showing the linear dependence of the long-time decay rate, S_L, on $\sin^2(\theta/2)$ for the sample 2.15gm% in 0.001M NaCl. S_L was obtained from the long time part of a ℓn(NIAF-1) versus time graph, and the linear dependence on $\sin^2(\theta/2)$ indicates that single-scattering processes characterised by a single diffusion coefficient are being observed.

θ	Channels analysed	Q'	D_L ($10^{-12} m^2 s^{-1}$)
15^o	8-51	0.020	8.49
20^o	9-51	0.018	8.50
25^o	10-51	0.012	8.36
30^o	12-51	0.025	8.42

Table 7.2. Details of the data analysis for the sample 2.15gm% in 0.001M NaCl. Only the low angle IAFs ($\theta \leq 30^o$) show two clearly resolvable exponentials. The values of Q' are small enough to consider the long time part of the IAF as being represented by a single exponential decay[29].

7.3.d. The Concentrated Solution Results

The D_L values obtained for solutions $\gtrsim$ 0.4gm% are presented in Figure 7.3 and Appendix 3 (Table A.6), with the angular dependence of the long time decay rate of the NIAFs shown in Figures 7.4 and 7.5 for representative samples. Unless otherwise noted, experiments were carried out at 25°C. With the exception of the 4.46gm% sample (the most concentrated sample studied) the long time decay was well represented by a single exponential for all latex sphere concentrations in both the 0.01M and 0.001M NaCl solutions, and the lowest value of Aco encountered was 1/3.

In the case of the 4.46gm% solution, which was studied in a 0.500cm path length cell to minimise multiple scattering, the long time part of the first NIAF obtained (at $\theta = 30^\circ$) exhibited significant curvature ($Q' \simeq 0.3$), yet did not appear to be dusty when the IAF was observed during accumulation. Setting the blinker by the ad hoc method revealed that the long time decay was multi-exponential at all scattering angles studied. Calculations show that the average inter-sphere spacing is only ~0.1μm (about a sphere diameter) in the 4.46gm% sample, and so it is probably the influence of short-range sphere interactions which are reflected in the multi-exponential nature of the long time decays. The method of cumulants was used to extract the initial decay rate of the long time part of the NIAF after channels containing the multiple scattering data were discounted. No systematic variations in D_L with angle were found for this sample (see Figure 7.5). The difficulty of estimating the number of channels to analyse as the "true" long time part of the NIAF is reflected in the increased error associated with the value of D_L for this 4.46gm% sample (see Figure 7.3).

Figures 7.4 and 7.5 indicate that the long time decays were not affected by multiple scattering. To confirm that multiple scattering did not affect the measured value of D_L a 2.20gm%, 0.01M solution was prepared from freshly dialysed stock, and studied in a 0.500cm path length spectrophotometer cell. This solution was also diluted to form the 1.17gm% and 0.55gm% solutions. The D_L values determined for these solutions are also shown in Figure 7.3 and are in good agreement with the trends exemplified by the 2.5gm%, 1.44gm% and 0.51gm% solutions in 0.01M sodium chloride studied earlier in a 1.00cm path length cell. The diffusion coefficient of the 0.55gm% sample showed no change when

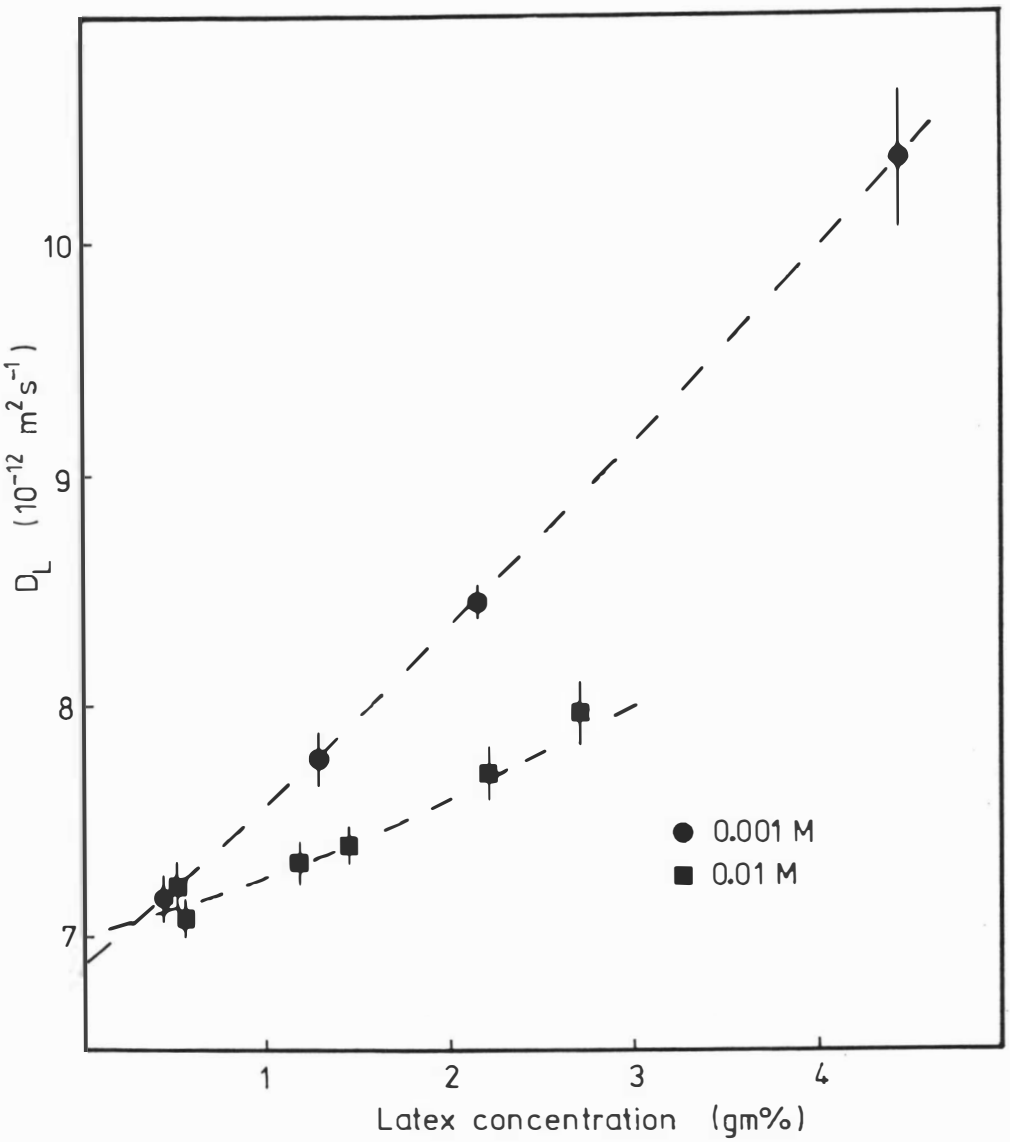


Figure 7.3. The concentration dependence of the diffusion coefficient determined by QELS assuming the long-time slope of the ℓn(NIAF-1) versus time plot is given by $(-2D_Lq^2)$. The value of D_L shown for each particular concentration was obtained by calculating D_L at each of the investigated angles and averaging the results. The errors shown represent the spread of experimental values.

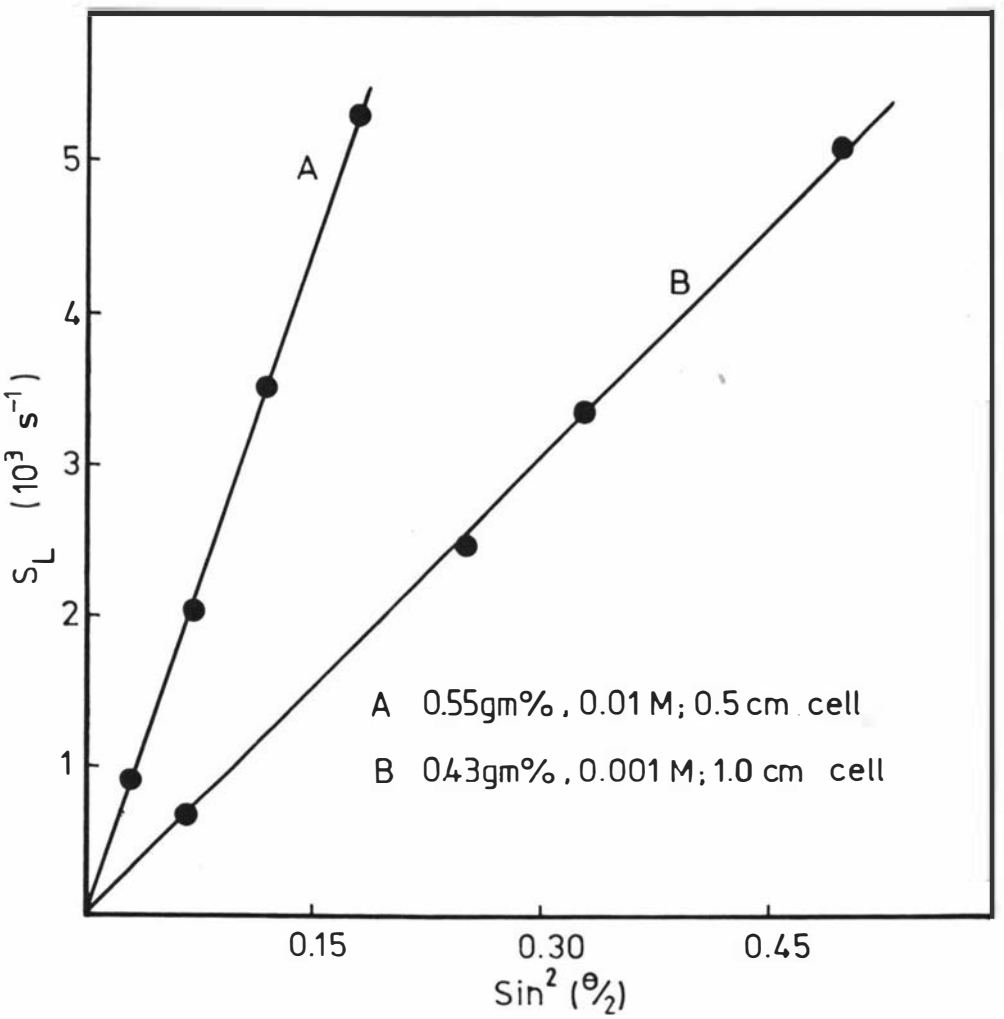


Figure 7.4. Plots showing the linear dependence of S_L on $\sin^2(\theta/2)$ for representative solutions. The vertical scale shown has been divided by three when plotting the results obtained for solution A.

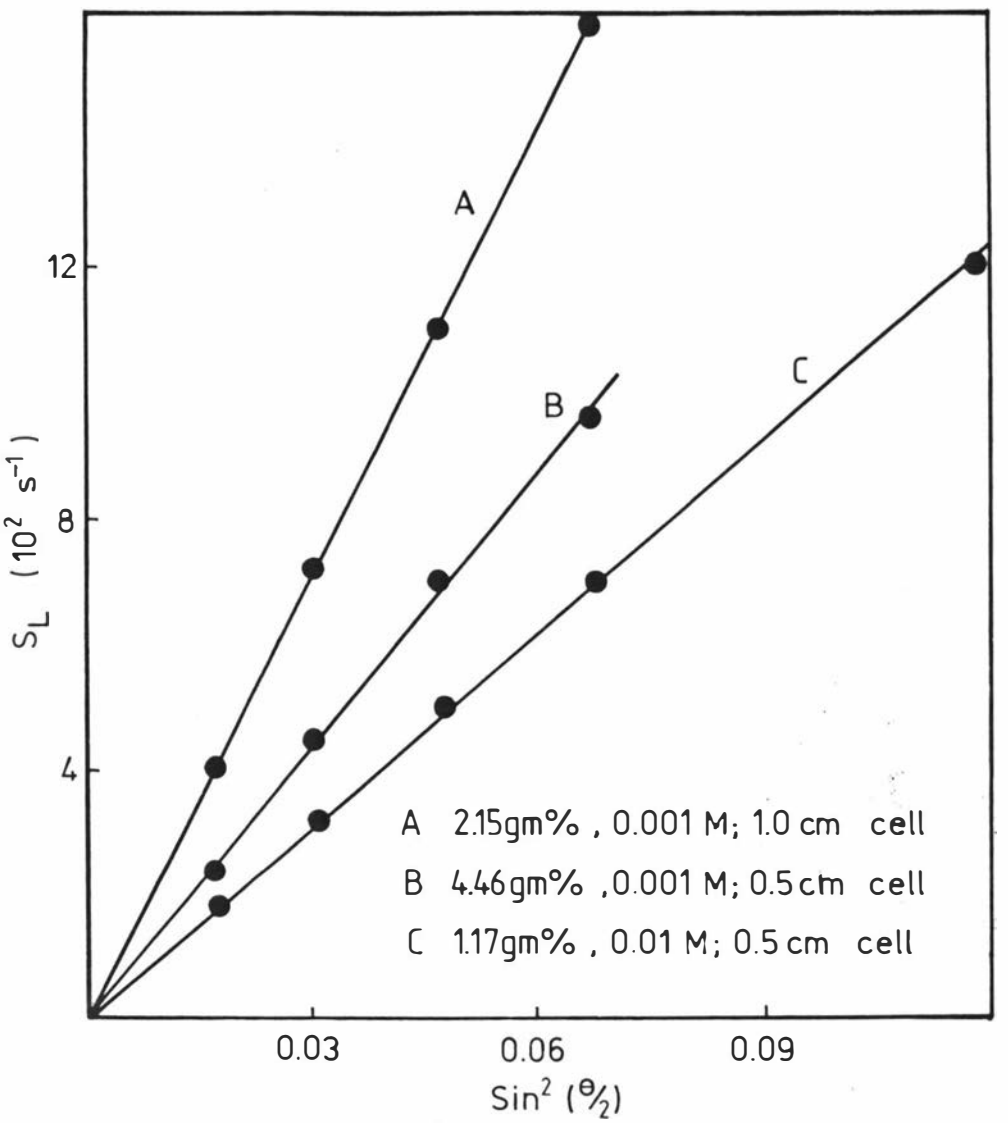


Figure 7.5. Plots showing the linear dependence of S_L on $\sin^2(\theta/2)$ for representative solutions. The vertical scale shown has been divided by two when plotting the results obtained for solution A.

measured 4 days after the original determination, indicating that sample aggregation is not a problem in this study.

Two concentrations, 0.43gm% (0.001M NaCl) and 1.44gm% (0.01M NaCl), were also studied at 20°C. The differences in the experimental values of D_L at the two temperatures (20°C and 25°C) are adequately described by the change in solvent viscosity. At infinite dilution the Stokes-Einstein equation indicates that the diffusion coefficient is proportional to the reciprocal of the solvent viscosity, and the fact that the same proportionality exists for both the 1.44gm% and the 0.43gm% samples indicates that solvent viscosity still provides the dominant activation energy requirement at quite high latex sphere concentrations.

7.3.e. The Very Dilute Solution Results.

In the very dilute latex sphere concentration regime, the QELS technique provides a direct measure of D_0. The very dilute regime study was carried out to assess the accuracy of the values of D_0 obtained by extrapolation of D_L to zero latex sphere concentration.

Figure 7.6 presents the results obtained from the very dilute regime QELS study. The values of these diffusion coefficients are listed in Appendix 3 (in Table A.7). All samples were prepared by simple dilution of the original Dow latex sphere suspension. The ionic strength of a latex sphere solution has been taken as that of the dilutent.

To examine the reproducibility of the diffusion coefficients obtained in the dilute regime, most samples were prepared in the following manner: a given latex sphere concentration was made up in either water or 0.001M NaCl. $1cm^3$ of this solution was accurately added to a sample cell, and the diffusion coefficient of the sample was measured. 10µl of a previously filtered NaCl solution was then added to raise the ionic strength to the desired value without appreciably altering the latex sphere concentration. Such families of samples prepared by the addition of sodium chloride, or by subsequent intra-cell dilution are indicated in Figure 7.6 by lettered subscripts. Multiple scattering effects were not apparent in any of the IAFs obtained from these dilute solutions. The range of scattering angles studied was 30° - 105° in all cases,

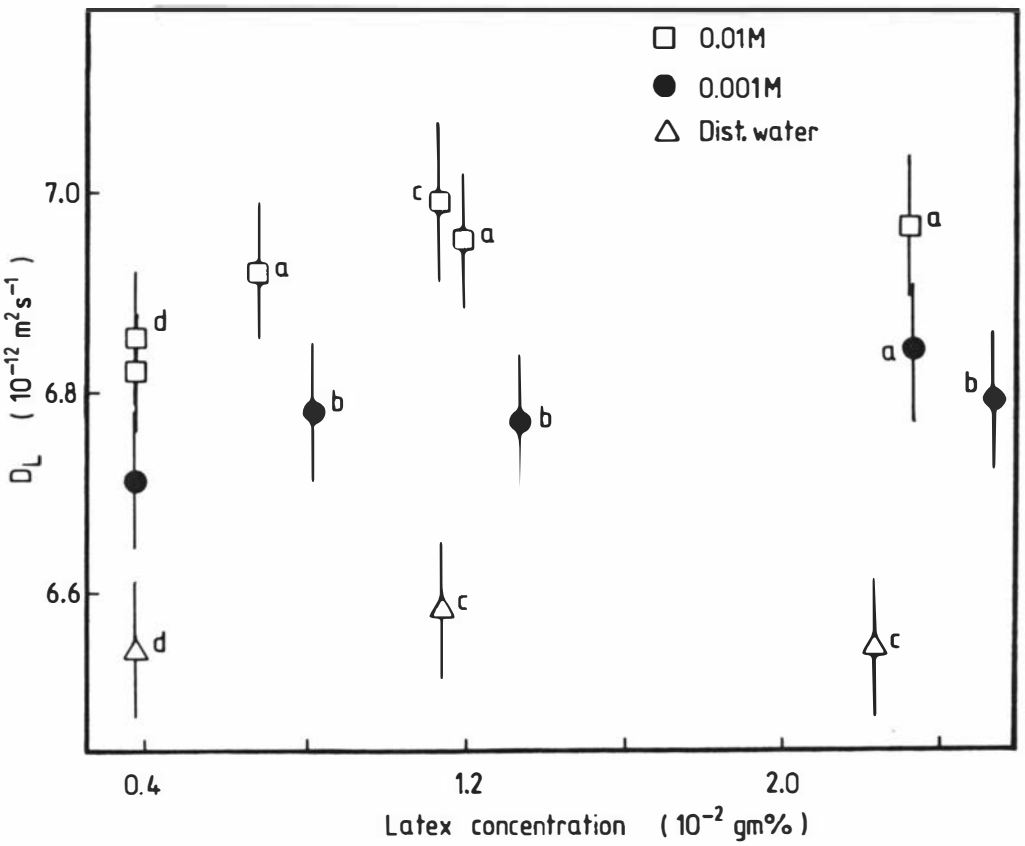


Figure 7.6. The very dilute regime latex sphere diffusion coefficients as a function of sphere concentration and ionic strength. The diffusion coefficients show appreciable ionic strength dependence but no significant concentration dependence (within the ±1% error bars). Families of samples generated from a common parent solution are denoted by lettered subscripts. These solutions were formed either by intracell dilution with solvent, or by the addition of 10µl.ml^{-1} quantities of an appropriate, concentrated salt solution.

and the error bars shown in Figure 7.6 indicate the spread of experimental results.

Table 7.3 presents parameters for latex sphere concentrations of 0.004gm% and ~0.023gm%. The hydrodynamic radius, R_H, was calculated from the Stokes-Einstein equation, and R_S is the calculated mean latex sphere separation. An estimate of the experimental rms displacement of a sphere, $(\overline{r^2})^{\frac{1}{2}}$, may be obtained from

$$\overline{r^2} = 6D_0t$$

where t is the experimental observation time. In a QELS experiment, t is of the order of the time required for a NIAF to decay to the 1/e point[27].

Interparticle collisions are not expected to play a major part in diffusion at these concentrations, for even at the largest concentrations considered here $R_S/(\overline{r^2})^{\frac{1}{2}} > 10$. Further, Figure 7.6 indicates that for the lowest ionic strength solutions the diffusion coefficient is not concentration dependent in the dilute regime (within the approximately 1% errors) and so the spheres may be considered free of electrostatic interactions. However, the diffusion coefficient of the spheres is noticeably ionic strength dependent, whereas the diffusion of hard spheres is not expected to be ionic strength dependent in the very dilute regime[79]. This suggests that the experimentally determined ionic strength dependence of the diffusion coefficient observed here may be due to a physical size change of the spheres, possibly induced by shielding of the surface charges from one another at moderate ionic strengths. Further, increasing the ionic strength above 0.01M in sodium chloride did not increase the measured diffusion coefficient. Such a saturation effect would be expected if electrostatic shielding were occurring.

We may examine the possibility of shielding effects causing changes in sphere size by calculating the change in radius which occurs when the strain, caused by electrostatic interactions between sulphate groups located on the surface of a sphere, is relaxed by shielding of these groups. A sphere with surface charges suffers a stress of magnitude

$$\text{Stress} = \sigma^2/(2\varepsilon)$$

Solvent.	Distilled water.	0.01M NaCl.	Distilled water.	0.01M NaCl.
Latex Conc. (gm%)	0.004	0.004	0.022	0.023
D_0 ($10^{-12} m^2 s^{-1}$)	6.52 ± 0.07	6.87 ± 0.07	6.54 ± 0.07	6.96 ± 0.08
R_H (μm)	0.0375	0.0357	0.0374	0.0352
R_S (μm)	1.8	1.8	1.0	1.0
$(\overline{r^2})^{\frac{1}{2}}$ (μm)	0.077	0.079	0.077	0.080

Table 7.3. Details of the diffusion coefficient determined by QELS at latex sphere concentrations of 0.004gm% and ~0.023gm% at various ionic strengths. R_H was calculated from the Stokes-Einstein equation, and R_S is the calculated mean inter-sphere spacing. The root-mean-square displacement, $(\overline{r^2})^{\frac{1}{2}}$, was calculated from the equation $(\overline{r^2})^{\frac{1}{2}} = 6D_0 t$.

where σ is the surface charge density and ε is the permittivity of the sphere. The change in sphere radius, da, which occurs upon relaxation of that stress is calculated from

$$\text{Strain} = 3(da/a) = \sigma^2(2\varepsilon B_M)$$

where a is the sphere radius and B_M the bulk modulus. Using a value for the surface charge density of $10\mu Ccm^{-2}$ [71], a permittivity of $2.5\ \varepsilon_0$ [80] and a bulk modulus of 3×10^9 [80], the calculated change in sphere radius is 2.5 percent for the transition from a fully strained to a fully relaxed state. Such a change is close to the experimentally observed change of 5 ± 2 percent. However, it should be noted that the permittivity and bulk modulus values quoted are for disordered bulk polystyrene. We have used these in the absence of more appropriate values for charged latex spheres. In addition, the bulk modulus is unlikely to remain constant up to strains of several percent, and thus a smaller value of bulk modulus is probably more appropriate. It is clearly desirable to directly measure the sphere radius as a function of ionic strength by, for example, low angle X-ray scattering, in order to confirm that sphere radius changes can account for the diffusion coefficient variations observed.

The diameter of the spheres studied in this work is given by the manufacturer as 0.085μm with a standard deviation of 0.0055μm. The QELS experiment yields a diameter of $0.075 \pm 0.001\mu m$ in distilled water. Other authors have reported similar discrepancies between the quoted sphere diameter and a Stokes-Einstein diameter obtained from QELS measurements [75,81]. However, for completeness samples of the nominally 0.085μm spheres were examined by transmission electron microscope and the diameter distribution was determined, as shown in Figure 7.7. An average diameter, appropriately weighted for a QELS experiment (i.e. weighting proportional to a^6 to account for the variation in scattered intensity with sphere radius), was then calculated according to the formula of Brown et al.[72]. The calculated diameter was 0.075μm, with an estimated random error of 3%, and shows excellent agreement with the Stokes-Einstein value obtained from the high dilution QELS results (see Table 7.3).

Finally, the variation of diffusion coefficient with ionic strength in the very dilute regime is not peculiar to the 0.075μm diameter sphere sample. A cursory study of a dilute solution of 0.091μm diameter spheres showed that a change of approximately 3% occurred in the diffusion coefficient upon changing the ionic strength from that of

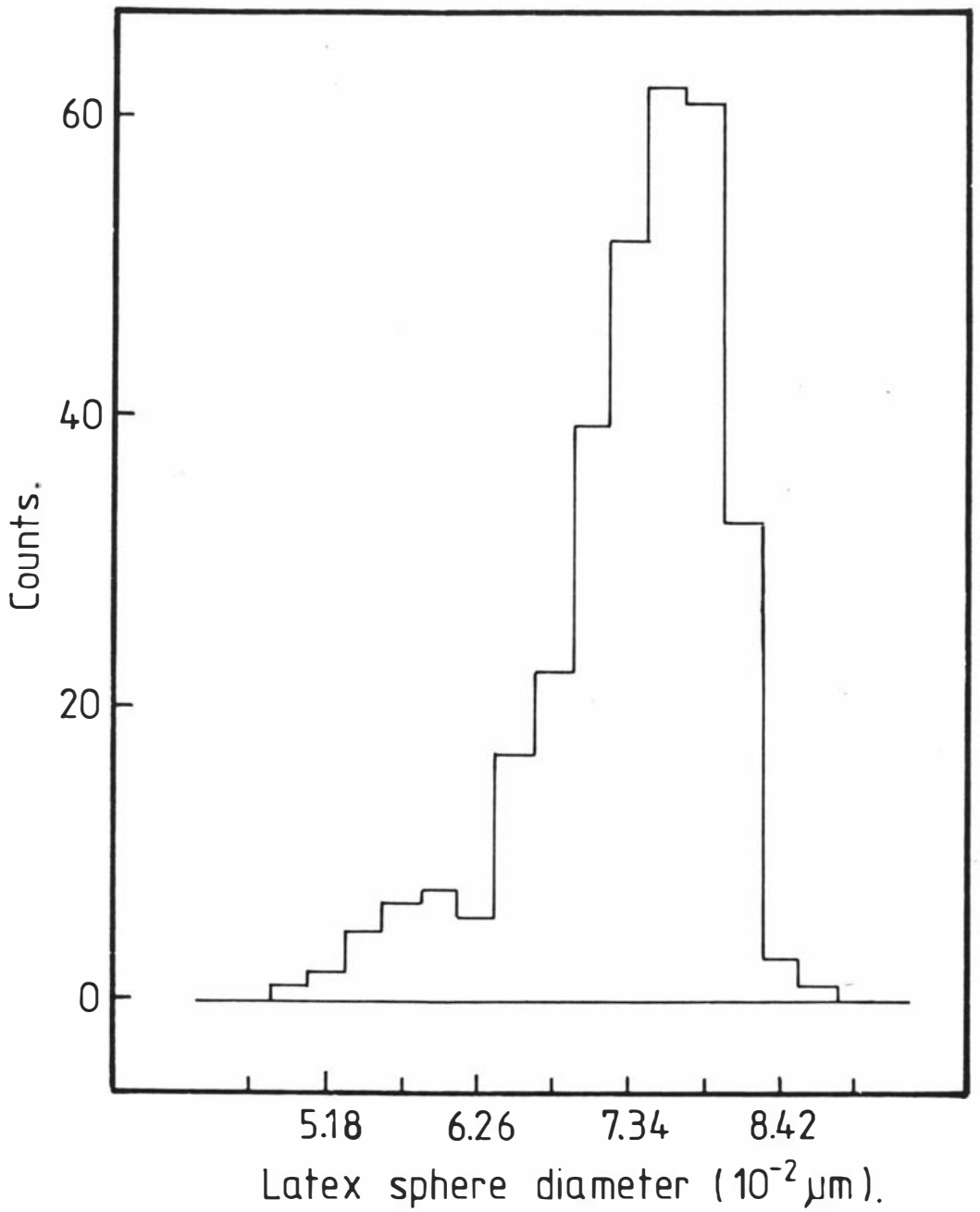


Figure 7.7. The diameter distribution of the nominally 0.085µm diameter spheres as determined by transmission electron microscopy. The (weighted) average diameter calculated from the distribution data was 0.075µm. This value is in excellent agreement with the diameter calculated from the Stokes-Einstein equation, using the QELS results for latex spheres in water.

distilled water to 0.01M in sodium chloride. An extended study of the 0.091μm spheres was precluded owing to a paucity of available sample.

7.4 COMPARISON OF RESULTS

7.4.a. Theories of Macro-ion Transport in the Presence of a Concentration Gradient

In the preceeding sections of this chapter it has been shown that QELS is able to provide a measure of the unique, reproducible quantity D_L, a quantity which is unaffected by multiple scattering (since D_L exhibits linear S_L versus q^2 plots, and is scattering cell path length independent). It remains to compare D_L, the apparent diffusion coefficient obtained by QELS, with mutual diffusion coefficients determined by the observation of the relaxation of a macroscopic concentration gradient, as reported by Anderson et al. Unfortunately, the spheres used in the QELS study have a diameter 20% smaller than the spheres of nominal diameter 0.091μm used by Anderson et al. A further difference is that the effective surfactant concentration encountered in this work is expected to be somewhat higher than that encountered in the solutions of Anderson et al. because surfactant precipitation was prevented in the QELS study by employing NaCl as the source of ionic strength. Since the adsorption of surfactant ions can affect the surface charge density of the spheres[70], the surface charge densities of the 0.075μm and 0.091μm spheres possibly differ. Thus, a direct comparison of results is prevented and instead interpretation through available macro-ion transport theory is sought.

The concentration dependence of D_M for solutions of charged latex spheres (the macro-ions) can be expressed in the virial form

$$D_M(c) = D_0(1 + k.c + ...) \qquad 7.1$$

Theories of macro-ion transport give an expression for k that is derived under the assumption that the solution is "dilute"; that is, only binary interactions between the macro-ions are important. Under these conditions an expression for k can be obtained which is a function of only the macro-ion radius, macro-ion surface charge density and the solution ionic strength. Two theories[82,83] which have had some success[71] in predicting experimental values for k are now briefly discussed, with the intention of using these theories to predict a

value of k for the latex sphere solutions used in the QELS study. The slope of a (D_L/D_0) versus c plot provides the experimental value of "k" in the case of the QELS experiments, and equivalence of the theoretical and experimental values of k would indicate that D_L can be identified with D_M.

The theory of Anderson and Reed[82] was developed from a microscopic analysis of the dynamics of Brownian particles. It was assumed that particle interactions give rise to two additional (over and above the solvent-particle interactions encountered in very dilute solutions), uncorrelated forces acting on each particle: a random solvent force arising from solvent disturbance by surrounding particles, and a force resulting from direct (electro-static) interactions of a particle with its neighbours. By considering only binary interactions (equivalent to assuming a "dilute" solution) the direct forces between each particle and its neighbours were evaluated in terms of a pair potential energy E(r) which exists for two charged particles separated by a centre-to centre distance r; the term I in equation 7.2 accounts for these interactions. The hydrodynamic effect of the neighbours was considered to give rise to an additional frictional coefficient and is represented by the term Λ below. Anderson and Reed showed that given only E(r) for $r \geq 2a$ (where a is the particle radius), the linear coefficient k can be calculated from

$$k = 8(I-\Lambda)/\rho \qquad 7.2$$

where ρ is the particle density. Expressions for I and Λ are given in equations 16 of reference 71, and for reasons of brevity are not reproduced here.

The alternative successful theory, that of Batchelor[83], combines macroscopic and microscopic ideas by assuming that a gradient in chemical potential gives rise to an equivalent mean force per particle. An analogy is then drawn between this particle flux and sedimentation, and analysis of the hydrodynamic interactions among particles in the latter phenomenon leads to the expression

$$k = [1.45+8(G-P)]/\rho \qquad 7.3$$

The parameter G accounts for the hydrodynamic forces among sedimenting particles, and the long range forces due to the macroscopic concentration gradient are accounted for by P. Expressions for P and G are given in equations 17 of reference 71.

The theories of both Anderson and Reed, and Batchelor, each provide an expression for k in terms of the interaction energy, E(r), although E(r) must be obtained from the work of other authors. For a given (appropriate) interaction energy, Anderson et al.[71] have shown that both theories predict similar values for k for systems as diverse as BSA and polystyrene latex spheres. The predicted values for k (k_{theo}) are in good qualitative agreement with experimental k values (k_{exptl}) over a range of ionic strengths, although quantitative agreement between k_{theo} and k_{exptl} was only obtained at moderately high electrolyte concentrations (~0.01M 1:1 electrolyte solutions). Since k_{theo} and k_{exptl} agree at electrolyte concentrations where an accurate expression for E(r) is relatively unimportant due to screening of the latex sphere charges, the hydrodynamic contribution to k has probably been correctly formulated. However, the particular expressions chosen by Anderson et al. to represent E(r) do not appear to be adequate, since agreement is not obtained between k_{theo} and k_{exptl} at the lower electrolyte concentrations where an accurate description of E(r) becomes important.

The expression chosen by Anderson et al. to represent E(r) in the case of polystyrene latex spheres, was derived by Hogg et al.[84] for the Gouy-Chapman model of the electrical double layer around a colloidal particle (a large charged, solid particle surrounded by a diffuse layer of electrolyte ions of opposite charge). Under the assumptions that the surface potential (ψ_0) of the charged spheres is small ($\lesssim$ 60mV), the electrostatic double layer is thin in comparison with the sphere radius (equivalent to assuming the spheres can be treated as flat plates), and the solution is "dilute"; Hogg et al. have shown that the interaction energy between two charged spheres can be written as

$$E(r) = (\varepsilon a \psi_0^2/2) \ln[1+\exp(-2\kappa a R)] \qquad 7.4$$

where

$$\psi_0 = (2k_B T/e).\sinh^{-1}[2\pi e \kappa^{-1} \sigma/(\varepsilon k_B T)] \qquad 7.5$$

and

$$R = r/(2a) - 1$$

The other parameters are; the permittivity ε of the solvent supporting the electrolyte, the Boltzmann constant k_B, the electronic charge e, the absolute temperature T, the surface charge density σ and the Debye-Hückel shielding length κ^{-1}.

The above expression for the interaction energy, while satisfactory for latex spheres in 0.01M electrolyte solutions is, however, invalid for 0.001M solutions for two reasons. First, the values of the surface charge density possessed by latex spheres are too large (>100mV) to allow E(r) to be represented by equation 7.4. Second, the flat plate approximation breaks down for 1:1 electrolyte concentrations <0.005M[85] (for spheres with $a \leq 0.05\mu m$). However, there are alternative expressions available for E(r). When considering the low ionic strength measurements the expression for E(r) developed by Stigter and Hill[86], which was based on the work of Verwey and Overbeek[87] and Hoskin[88], should more closely represent the experimental situation since this theory does not suffer from restrictions on ψ_0, nor are the latex spheres assumed to be flat plates. For "dilute" solutions Stigter and Hill have shown that

$$E(r) = \varepsilon a \psi_0^2 f.\exp(-2\kappa a R)/[2\Xi^2(R+1)] \qquad 7.6$$

where the symbols have been defined earlier, except for Ξ (which can be obtained from tables in Hoskin, in conjunction with various equations in references 86, 87) and f (which can be obtained from tables in Verwey and Overbeek).

7.4.b. Application of Macro-ion Transport Theories to Latex Sphere Solutions.

A summary of both the QELS and capillary penetration (Anderson et al.) results, together with various theoretical predictions, is presented in Table 7.4. Parameters used to evaluate expressions for E(r) (equations 7.4 and 7.6) are given in Appendix 3 (Table A.8), and computer programs were written to numerically evaluate k_{theo} via equations 7.2 and 7.3.

For each sphere size and solution ionic strength a range of k_{theo} values has been calculated since a range of surface charge densities appears in the literature for polystyrene spheres. Following Anderson et al. values of k_{theo} have been calculated for surface charge densities varying from 3 to 10μC cm^{-2} (although values as low as 1.2μC cm^{-2} have been reported[72] for smaller spheres with a = 0.023μm). These values for the surface charge density have been obtained from potentiometric titration studies of latex spheres in extremely low ionic strength solutions[89]. However, when any macro-ion in placed in a solution of moderate ionic strength, a layer of counter-ions (the Stern layer) becomes absorbed to the macro-ion surface[85] and it is this ionic-strength dependent absorption of counter-ions which determines the effective surface charge density of the macro-ion[90]. The surface charge density appropriate for inclusion in equation 7.6 in thus not well-defined at moderate ionic strength since the extent of counter-ion absorption is not known, although charge densities approaching 10μC cm^{-2} are not expected to be appropriate. It would thus be rather difficult to test the accuracy of equation 7.6 although, as will shortly be discussed, equation 7.6 can be expected to be useful in the comparative situation under consideration in this work, provided that the two sets of spheres (those used in the QELS and capillary penetration studies) possess similar surface charge densities.

The surface charge densities of the two sets of spheres could differ since different surfactant concentrations and spheres of different diameters were utilised in the QELS and capillary penetration studies. The sphere surface charge density has been found to vary with sphere radius, although the radius differences encountered in this comparison are not expected to result in significant surface charge density variations[89]. The effect of adding surfactant to the latex sphere solutions is more complicated. In the capillary penetration study the surfactant is precipitated and so needs no further consideration. However, in the QELS study, the effect of the surfactant is three-fold. First, the addition of surfactant <u>increases</u> the effective ionic strength of the latex sphere solution. Second, the increased ionic strength of the solution <u>reduces</u> the sphere surface charge density due to increased counter-ion absorption. Third, the sphere surface charge density is <u>increased</u> due to absorption of the negatively charged surfactant on to the sphere surface. The second and third effects will tend to cancel, thus leaving the sphere surface charge density, to a <u>first approximation, unchanged</u>

by surfactant addition. The above discussion indicates, therefore, that the latex spheres used in the QELS and capillary penetration studies are expected to possess similar charge densities. Under this assertion, the nature of the diffusion coefficient measured by QELS is now evaluated.

7.4.c. Interpretation of Data Obtained at High Ionic Strength.

The QELS results for the 0.075μm latex spheres in 0.01M solutions are summarised in Table 7.4 (see also Figure 7.8). The capillary penetration results of Anderson et al. are also given in Table 7.4 together with various theoretical predictions for the value of k. As the data in Table 7.4 shows, both the QELS and capillary penetration results are in quantitative agreement with the values of k_{theo} predicted by the theory of Batchelor[83] at a surface charge density of $3\mu C\,cm^{-2}$. The interaction energy expression due to Hogg et al. was used to calculate k_{theo} since at these higher ionic strengths, and at lower charge densities, the approximations leading to equation 7.4 are met. The electrolyte concentration in both the capillary penetration and QELS study was assumed to be 0.01M; that is the contribution to solution ionic strength by surfactant (in the QELS study) was neglected. This approximation leads to insignificant changes in k_{theo} when compared to the errors in k_{expt1}.

The theory of Batchelor predicts values of k_{theo} (using $\sigma=3\mu C\,cm^{-2}$ and $\kappa^{-1} = 30\text{Å}$) in quantitative agreement with both macroscopic and QELS diffusion data. This indicates that the QELS technique is able to provide a measure of the macroscopic mutual diffusion coefficient in high ionic strength solutions, at least up to sphere concentrations of ~3gm%. Theoretical justification of the QELS results aside, we note that the QELS results satisfy our intuitive expectations of the diffusion behaviour of charged spheres in a good charge screening medium; that is, the smaller spheres used in the QELS study should exhibit a value for k greater than or equal to the value of k obtained for the larger spheres studied by Anderson et al.

Salt concentration (M)	Sphere diameter (μm)	k_{exptl} ($cm^3 g^{-1}$)	k_{theo} ($cm^3 g^{-1}$)		
			a	b	c
0.01	0.075	5.5 ± 0.6	4.3-5.5	5.6-6.7	-
0.01	0.091	5.0	3.3-4.2	4.9-5.7	-
0.001	0.075	11.7 ± 0.4	35-41	34-41	24-26
0.001	0.091	18	24-30	26-30	20-22
0.002*	0.075	11.7 ± 0.4	-	-	14.3*

a...model of Anderson & Reed[82], interaction energy of Hogg et al.[84]
b...model of Batchelor[83], interaction energy of Hogg et al.[84]
c...model of Batchelor[83], interaction energy of Stigter and Hill[86].

Table 7.4. Theoretical and experimental values for k. The range of values quoted for k_{theo} corresponds to a range of surface charge densities from 3μCcm^{-2} to 10μCcm^{-2}. The * indicates that the effect of added surfactant has been taken into account when calculating these values.

7.4.d. Interpretation of Data Obtained at Low Ionic Strength.

Theoretical predictions of k for latex spheres in low ionic strength solutions are shown in Table 7.4. The Debye-Hückel shielding length is much larger (~0.01μm) in 0.001M salt solutions, so demanding a much more accurate formulation of the electrostatic interaction energy term than in the case of 0.01M solutions, if quantitative predictions of k_{theo} are required. Thus, as expected, there are variations in both the range and magnitude of k_{theo} obtained for a given range of surface charge density, depending upon the expression used for the interaction energy. Table 7.4 also contains the capillary penetration results of Anderson et al. for the 0.091μm spheres in 0.001M solutions. The experimental results of Anderson et al. (see Figure 7.8) for this ionic strength are quite scattered, but show reasonable agreement with theory when the interaction energy is calculated using equation 7.6.

The QELS results are also presented in Table 7.4. The individual experimental points show little scatter (see Figure 7.8) but are in much poorer agreement with the theoretical predictions if the salt concentration is taken as 0.001M. This poor agreement could indicate that the QELS technique fails to measure the mutual diffusion coefficient of charged spheres in low ionic strength solutions, whereas the technique apparently does measure this diffusion coefficient in high ionic strength solutions. However, the ionic strength of the solutions used in the low ionic strength QELS study contains important contributions from both NaCl (0.001M) and SDS (0.0007M). Since SDS is a 1:1 electrolyte, the effective salt concentration encountered in the QELS study is 0.0017M.

The increased effective ionic strength present in the QELS study can be accounted for by calculating a new value for k_{theo}. The salt concentration was approximated as 0.002M in order to simplify evaluation of equation 7.6, and a charge density of $3\mu C\,cm^{-2}$ was assumed. Under these conditions a value of $14.3 cm^3 g^{-1}$ was obtained for k_{theo} for the spheres and solution conditions encountered in the QELS study. The relatively good agreement obtained between k_{theo} and k_{exptl} in the capillary penetration study, where D_M was measured, is now also obtained for the QELS measurements. Thus, the QELS results are consistent with the view that D_L provides a measure of the macroscopic mutual

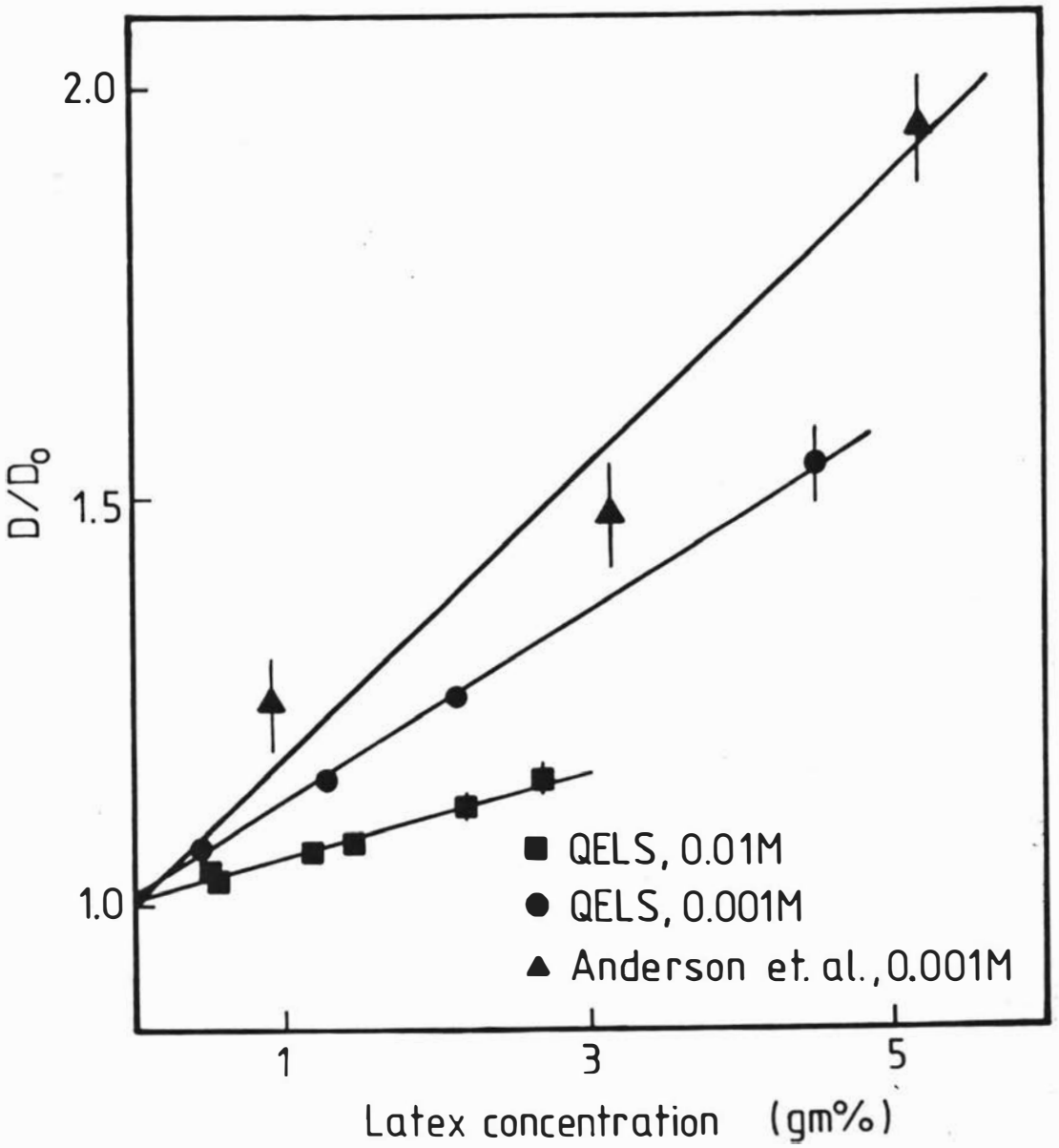


Figure 7.8. The diffusion coefficients (D_L) show a linear concentration dependence in both 0.001M and 0.01M NaCl solutions. The D_0 value used was obtained from the relevant ionic strength data in Figure 7.6. The results of Anderson et al. are also shown for 0.091μm latex spheres in 0.001M potassium chloride. These values were calculated from experimental data[71,91] using equation 13 of reference 71. The errors shown represent the spread of experimental values for both the QELS results and the results of Anderson et al.[71,91]. The experimental results of Anderson et al. for the 0.01M solutions, although not reproduced here, are in close agreement with the QELS results.

diffusion coefficient. It should be noted that this conclusion rests upon the assumption that the surface charge densities of the 0.091μm and 0.075μm diameter latex spheres are approximately equal. This assumption would appear to be valid for the solution conditions encountered in the QELS and capillary penetration studies of latex sphere diffusion. We now consider why it is that previous D_M/QELS - measurement comparisons have indicated that QELS does not measure D_M for solutions of charged macromolecules.

7.4.e. Comparison With Other Work.

A comparison of the results obtained from studies of diffusion in solutions of the charged protein BSA has indicated that QELS does not measure the mutual diffusion coefficient as determined by a diffusion cell technique[13] (see Figure 1.1). However, the diffusion cell work has recently been called into some question[69] due to the use of a non-rigid membrane in the experiments purporting to measure D_M.

For solutions of BSA, the concentration dependence of both the mutual and self diffusion coefficients has been independently determined in 0.2M sodium chloride solutions at pH ≃ 5.4[92] by Kitchen et al. These results can be used as alternative macroscopic measurements with which to compare the earlier QELS study[13] of BSA diffusion in 0.25M solutions.

Kitchen et al. have determined the self-diffusion coefficient of BSA by a radiotracer-capillary-penetration technique which has yielded values in good agreement with independent determinations in 0.1M solutions at pH ≃ 4.7[13]. Such agreement is expected between self diffusion coefficients determined at the different pH and ionic strengths because the conformation of BSA does not change significantly over the pH range 4.5 - 11.0[93], and the differences in the viscosities of the 0.2M and 0.1M salt solutions used in the two investigations are also too small to appreciably influence self diffusion. The mutual diffusion data presented by Kitchen et al. was obtained by utilising two independent techniques (a capillary penetration and an ultra-centrifugation method) which yielded values for the mutual diffusion coefficient which were in agreement within the precision of the experiments. Thus, both the self and mutual diffusion coefficient

data of Kitchen et al. appear to be consistent.

Several points of interest arise from the work of Kitchen et al. First, it was found that D_M exhibited only a very weak concentration dependence (i.e. $k \approx 0$) at pH≈5.4. Phillies et al., using the QELS technique, also found k to be small near this pH for solutions of BSA studied over a similar concentration range (up to ~25gm%). Second, Kitchen et al. found that values of the mutual and self diffusion coefficients were related within the precision of the experiments, by the equation

$$D_M = D_S\left(\frac{\partial \Pi}{\partial c}\right)_{p,T}(1-\Phi) \qquad (7.7)$$

where D_S is the self-diffusion coefficient, Φ is the volume fraction and $\left(\frac{\partial \Pi}{\partial c}\right)_{p,T}$ is the isothermal osmotic compressibility which can be obtained from the work of Scatchard et al.[94]. Equation 7.7 can also be used together with suitable values for D_S and $\left(\frac{\partial \Pi}{\partial c}\right)_{p,T}$[13,94], to predict values of D_M for the experimental conditions encountered in the earlier QELS study of BSA diffusion[13]. Within the expected errors of the comparison, the diffusion coefficients obtained by QELS are in agreement with values of D_M predicted from equation 7.7 over the entire pH range studied (pH 4.5 - 7.6) in the QELS investigation[95]. Thus when the diffusion coefficients obtained from the QELS study of Phillies et al. are compared with macroscopic D_M determinations (both experimental and theoretical) derived from the work of Kitchen et al., good agreement is obtained. This indicates that QELS provides a measure of D_M for these solutions of charged macromolecules; a result which is in agreement with the conclusion reached in the last section.

CHAPTER 8

CONCLUSIONS

8.1.a. Concluding Remarks

The work presented in this thesis can be divided into three main areas: the development of the PFGNMR instrumentation, the study of diffusion in random-coil polystyrene solutions by the techniques of both PFGNMR and QELS, and the application of QELS to the study of diffusion in moderate ionic strength solutions of charged latex spheres. The outcome of research in these areas is now reviewed.

The development of the PFGNMR apparatus was undertaken to provide a method for the rapid and accurate measurement of random-coil polymer self-diffusion coefficients. It has been shown in this work that appropriate apparatus design has enabled self-diffusion coefficients to be measured to an accuracy of ~1%. Experiments involving signal-averaging have been performed without the need for the spin-echo acceptance/rejection schemes which have often, in the past, been used in PFGNMR experiments to overcome the lack of spin-echo signal stability. Thus, the result of this work is that the PFGNMR method has been developed to a stage where accurate self-diffusion coefficient measurements can be routinely made on a wide range of systems. However, while the accuracy of the PFGNMR experiment has been improved to a satisfactory level, the experiments in this thesis have been hindered, in some instances, by a lack of precision (i.e. an inadequate signal-to-noise ratio). Increasing the signal-to-noise ratio in the PFGNMR experiment (other than by sample volume increases) is seen as being the next important area in the development of the PFGNMR technique. This aspect of the PFGNMR experiment is considered in some detail in section 8.1.b.

The second area of investigation in this thesis was the study of diffusion in random-coil polystyrene solutions. The techniques of PFGNMR and QELS were used to measure D_S and D_M respectively. The behaviour of D_S in the polymer gel regime is now relatively well understood. It is evident from the studies in this thesis, and from the FRS studies of Hervet et al., that it is reptation which provides the dominant mechanism

for polymer entanglement relaxation in the polymer gel regime. de Gennes' has successfully predicted the observed concentration dependence of D_S in the polymer gel regime; at least for polymer concentrations up to ~20gm%. At larger concentrations some of the assumptions made by de Gennes' regarding polymer chain configurations are violated, and the concentration dependence of D_S is no longer correctly predicted. Thus, there is a need for further theoretical, and also experimental, investigation into the self-diffusion of random-coil polymers at concentrations above 20gm%. Application of PFGNMR to such studies will require that the experimental signal-to-noise ratio be maximised since the relatively rapid T_2 relaxation in polymer gels will reduce the magnitude of the spin-echo signal. Also, to measure the smaller coefficients encountered in polymer gels, the magnitude of the field gradient pulses will have to be increased if pulses of resonable length (i.e. consistent with the T_2 limitations) are to be used. However, gradient pulses of larger magnitude can be expected to complicate the PFGNMR experiment because of eddy current generation, and so there are practical limitations to providing accurate D_S measurements at large polymer concentrations. This problem is considered further in section 8.1.b.

The value of the QELS study of diffusion in random-coil polystyrene solutions has been to provide D_M measurements which, when compared with D_S measurements, have indicated that polymer-polymer interactions are important at even the lowest polystyrene concentrations available to joint PFGNMR-QELS study.

The interactions implied by the D_M/D_S disagreement evident in the dilute concentration regime may account for the observation that in this regime D_S does not necessarily monotonically decrease with increasing polymer concentration. The concentration dependence of D_S in the dilute regime appears to be solvent dependent, although the limited precision afforded by the PFGNMR apparatus precludes definite conclusions from being drawn. Therefore, it is essential that improved apparatus be designed with the aim of providing accurate D_S measurements at polymer concentrations extending into the very dilute regime. The concentration dependence of D_S could then be compared for a series of solvents of increasing "goodness" (from a theta-solvent to a very good solvent). With the present PFGNMR apparatus, it is possible to obtain

more accurate D_S measurements in the dilute regime if a smaller molecular weight polystyrene with a correspondingly higher c^* value is employed (e.g. $4000M_w$ polystyrene, which has $c^* \simeq 10$gm%). However, as the concentration dependence of D_S could be molecular weight dependent, studies on smaller molecular weight polystyrenes are not an adequate substitute for an increase in experimental precision.

The outcome of recent studies on the sedimentation of random-coil polymers has made it possible to appreciate how the D_S/D_S^+ discrepancies, encountered in the present work on random-coils, could eventuate. Brochard and de Gennes[96] have considered the sedimentation process in the polymer-gel regime of random-coil polymer solutions, and have modelled this process in terms of the flow of solvent through a network of fixed polymer entanglements,a so-called "porous-plug" model ; that is, the contribution to polymer motion due to reptation is neglected in the presence of the much larger displacements due to sedimentation. Under this approach Brochard and de Gennes have predicted that in the polymer gel regime, the sedimentation coefficient should scale as $c^{-0.5}$ in a non-theta solvent, or as $c^{-1.0}$ in a theta solvent. Roots and Nystrom[97] have found that in a non-theta solvent, the random-coil polystyrene sedimentation coefficient exhibits $c^{-0.8}$ scaling behaviour, while in a theta solvent the predicted $c^{-1.0}$ behaviour is observed. This partial agreement between theory and experiment indicates that the process of solvent flow through a fixed polymer network is important in a sedimentation experiment, whereas in a self-diffusion experiment, D_S behaviour in the gel regime can be accounted for solely in terms of a relaxing, transient polymer network. Therefore, it is not surprising that D_S and D_S^+ should show some differences as different physical processes are operating in the self-diffusion and sedimentation experiments. D_M measurements are also fundamentally concerned with the flow of solvent through the entangled polymers, and so the D_S/D_S^+ discrepancy encountered for D_S^+ derived from D_M measurements[9] might also be anticipated. It should be noted that entanglements are not expected to play a significant role in interactions between "hard-sphere" macromolecules and so D_S/D_S^+ agreement is expected in this case, on the basis of the above argument. It is interesting to note that in studies of the self-diffusion of the globular protein Bovine Serum Albumin in 0.2M sodium chloride, agreement was found between D_S and D_S^+ (within the limits of experimental error) over a wide range of protein

concentrations[69]. It is clear that the differences between directly and indirectly determined self-diffusion coefficients encountered for random-coil polymers represents an area for continuing experimental and theoretical investigation, particularly in the dilute regime.

The final investigation in this thesis was the QELS study of diffusion in concentrated solutions of charged latex spheres. From this study it was concluded that QELS measures D_M for these solutions, a conclusion which rests upon the assumption that the surface charge density of the latex spheres used in this work is approximately equal to that encountered for the spheres used in the macroscopic-displacement, mutual diffusion studies of Anderson et al. Although this assumption appears to be well-founded, it is still clearly desirable to undertake a QELS/macroscopic-D_M comparison on identical sphere solutions. Compared with protein solutions, polystyrene latex sphere solutions offer the advantages of simple preparation (i.e. non-rigorous dust removal steps can be used) and freedom from aggregation problems. It has been shown in this work that the QELS experimental data obtained from latex sphere studies can be reliably interpreted, even though a significant proportion of the scattered light is multiply scattered. However, interpretation of the QELS results would be simplified (and larger scattering angles could be used) if multiple scattering was reduced. Therefore, future studies should use, if possible, smaller diameter latex spheres.

8.1.b. Towards an Improved PFGNMR Experiment

The study of diffusion in random-coil polystyrene solutions has indicated a need for measurements to be made at polystyrene concentrations below the 0.5gm% lower limit accessible to the present PFGNMR apparatus. The provision of a better signal-to-noise ratio in the PFGNMR experiment appears, at first sight, to be a relatively simple matter. If quadrupolar magnetic field gradient coils[47,54] are used, the sample volume can be increased by a factor of ~8 (compared with the present apparatus), whilst maintaining a field gradient uniformity similar to that encountered with the Helmholtz coils used in this work. Improved preamplifier designs are also available[55]. These should allow a further factor of two increase in the NMR signal-to-noise ratio. Thus, polystyrene concentrations down to about 0.05gm% are potentially

available for study at good precision (D_S to ~3%) by incorporating existing apparatus improvements. However, at polystyrene concentrations as small as 0.05gm%, few solvents possess sufficiently low levels of ^1H contamination to allow simple interpretation of the PFGNMR experimental results, as the signal attenuation ratio must be considered in terms of a weighted combination of D_S and D_{Solv}. Frequency domain analysis could be used to separately analyse the solvent and polymer NMR signals if sufficient resolution is available, and so it is desirable to improve the resolution of the PFGNMR experiment up to the limit obtainable for a stationary sample; about 1Hz for ^1H nuclei in a magnetic field of magnitude 1.4 Tesla. Such a resolution would also provide an increase in the experimental signal-to-noise ratio of ~15, compared with the present apparatus.

In principle, the resolution requirement is easily met by including suitable homogeneity coils[53] in the NMR probe. However, making a probe with adequate resolution results in an increase in the amount of metal near the magnetic field gradient coils. This could lead to the generation of large eddy-currents which in turn would invalidate the Stejskal-Tanner[43] spin-echo attenuation formula, due to the gradient pulses assuming a non-rectangular shape. Eddy currents would be a particular problem if the magnitude of the field gradient pulses was to be further increased to facilitate the study of self-diffusion in the polymer-gel regime.

Eddy currents are only associated with magnetic field gradient pulse turn-on and turn-off and so by limiting the rise and fall times of the gradient pulses to the form of a ramp, eddy-current effects can be minimised. A magnetic field gradient ramped-pulse sequence is shown in Figure 8.1, where the rf pulses shown represent a standard spin-echo sequence. By suitable choice of the time β, eddy-currents can be made negligibly small. The expression for the spin-echo attenuation under the action of the gradient pulses shown in Figure 8.1 is most easily derived according to the approach presented by Stejskal and Tanner[43]. This derivation is given in Appendix 6, where it is shown that the spin-echo attenuation at $t=2\tau$ is given by

$$\ell n[A(G)/A(0)] = -\gamma^2 G^2 D_S [\delta^2(\Delta-\delta/3) + \beta^2(\beta/30-\delta/6)].$$

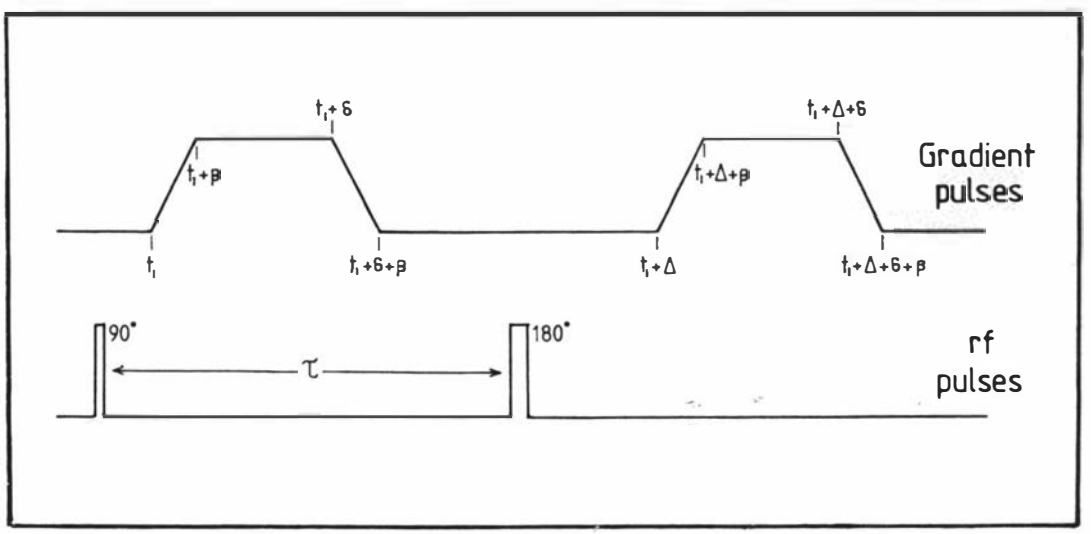


Figure 8.1. A ramped-pulse magnetic field gradient pulse sequence for eddy current minimisation. The rf pulses form a standard spin-echo sequence.

The symbols have their usual meanings, and β is defined in Figure 8.1. As β tends to zero, the expression for the spin-echo attenuation ratio reduces to the familiar Stejskal-Tanner formula (equation 3.7.), as required.

PFGNMR has the potential to measure self-diffusion coefficients in many liquid systems, and offers particular advantages in the study of individual components in multi-component systems when used in conjunction with frequency-domain analysis. Improving the resolution of the PFGNMR experiment to ~1Hz would allow a much wider range of multicomponent systems to be studied, and would also improve the experimental signal-to-noise ratio. Apart from obviating eddy-current induced problems in PFGNMR experiments, the ramped-pulse gradient sequence also has the advantage that it can be generated using lower bandwidth instrumentation than in the case of rectangular gradient pulses, thus simplifying the design of current pulse-supply output stages.

APPENDIX 1

THE MAGNETIC FIELD DUE TO AN OPPOSED HELMHOLTZ PAIR IN THE PRESENCE OF MAGNET POLE PIECES

It is well known[42] that two current loops (with opposed current flows) give rise to a large area of uniform magnetic field gradient along their common axis. Figure A.1.a. depicts two such current loops of radius r_0, equally spaced a distance z_0 about a plane at right angles to the z-axis, centred on z=0. The z component of the magnetic field magnitude at the point P(r,z), B_{zr}, can be obtained by using the Biot-Savart law. For a coil with n turns

$$B_{zr} = \mu_0 In(r_0-r)/2\ ((r_0-r)^2+(z_0-z)^2)^{-3/2}-((r_0-r)^2+(z_0+z)^2)^{-3/2} \quad (A.1)$$

where I is the current and μ_0 is the permeability of free space. From the coil configuration shown in Figure A.1.a., a necessary and sufficient condition for a uniform z-axis field gradient at the origin is

$$(d^3B_{zr}/dz^3)_{r=0=z} = 0 \quad (A.2)$$

Application of the above condition to equation A.1 yields $r_0/z_0 = 2/\sqrt{3}$ as the coil configuration which would produce the largest region of uniform field gradient at the origin.

Tanner[46] has indicated that the effect on B_{zr} of two magnet pole-pieces located at $z=\pm l$ is amenable to analysis by the method of images[56]. The geometry of the image problem is shown in Figure A.1.b. and the expression for B_{zr} now becomes

$$B_{zr} = \mu_0 In(r_0-r)^2/2\ .\ ((r_0-r)^2+(z_0-z)^2)^{-3/2}-((r_0-r)^2+(z_0+z)^2)^{-3/2}$$
$$+\ ((r_0-r)^2+(2l-z_0-z)^2)^{-3/2}-((r_0-r)^2+(2l-z_0+z)^2)^{-3/2} \quad (A.3)$$

where only the first order induction terms have been included (i.e. the effect of the nearest pole piece only). Application of the condition imposed by equation A.2 to equation A.3 yields

$$3Z(R^2+Z^2)^{-7/2}\ 7Z^3(R^2+Z^2)^{-9/2} + 3(2-z)\ R^2+(2-z)^2\ ^{-7/2}$$
$$-\ 7(2-z)^3\ R^2+(2-z)^2\ ^{-9/2} = 0 \quad (A.4)$$

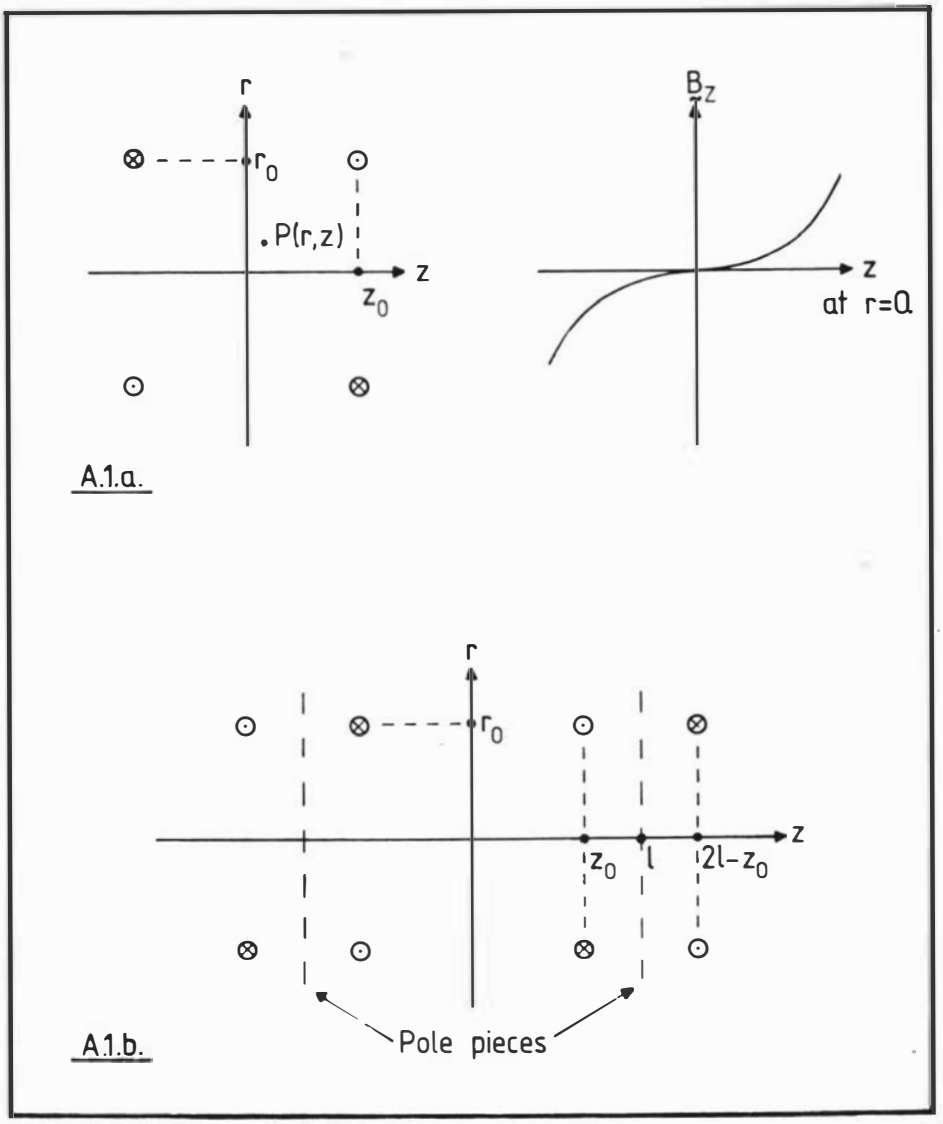


Figure A.1. The magnetic field gradient due to an opposed Helmholtz pair.

A.1.a. Two opposed current loops and their associated magnetic field.

A.1.b. The geometry for the image field calculation. The primary current loops are located at $z=\pm z_0$, the pole-pieces at $z=\pm l$ and the image current loops at $z=\pm(2l-z_0)$.

where the dimensionless quantities $R = r_0/l$, $Z = z_0/l$ have been employed. Second order induction terms can easily be included in equation A.4, but our calculations have shown that these terms contribute less than 1% to the value of R for a given Z and hence can be neglected (within the winding error). Figure 4.2 details the correction to be made to R, for a given Z, in the presence of nearby pole-pieces. Equation A.4 is represented in Figure 4.2 as curve A.

APPENDIX 2

THE DIGITAL PULSE PROGRAMMER

The pulse programmer essentially consists of three sections: the divider chain and associated timing pulse selection circuitry; the d, Δ and δ down counters; and the control circuitry. With the aid of Figures 4.4 the workings of sections one and two are self evident. However, the control circuitry, consisting of sundry D flip-flops and several monostables (74123s), merits a little further explanation.

The problem of providing sequentially timed intervals is generally complicated by the presence of propagation delays, and it is the function of the control circuitry to circumvent any inaccuracies such delays might otherwise cause. In sequential timing, the edge of a clock pulse which marks the end of an interval also marks time zero for the next interval. The second interval's counters will always miss their time zero pulse if they are activated at the end of the first interval due to propagation delays associated with the activation process.

Down counters, including the 74190 counter, often have a so-called "look ahead" feature for use in sequential timing. This is an output pin whose logic state changes upon a count of one and this change may be used to activate the next interval's counters as the next clock pulse will mark time zero for this interval. Unfortunately the precision of the pulsed field gradient experiment often demands that there be order-of-magnitude differences in the frequencies of the clock pulses driving the Δ and δ counters, with δ having the higher-frequency pulses. Thus activation of the δ counters by some "look-ahead" feature could result in δ being incorrectly timed.

In the present application these problems are overcome by inhibiting those counters not immediately concerned with timing a particular interval. This is achieved by placing a logic zero at the CLK input of the initial counter in the cascade via a D flip-flop. Immediately a timed interval is completed, the next appropriate counters are activated, and the previous counters inactivated, by clocking the

appropriate flip-flops (those connected to the counters' CLK inputs). The monostables are also triggered at this stage and provide a pulse sequence to the divider chain which causes all divider chain outputs to go to the count of nine, then zero. This reset-nine, reset-zero sequence has the effect of mimicking a timing pulse at the CLK input of any activated down counters and so time zero is restored and timing proceeds with no loss in accuracy. (All control circuitry activation occurs in the period during which the 1MHz master clock is at logic one.) For the case when 1μs pulses are selected, the D flip-flop marked as 7474* in Figure 4.4.a provides the necessary time zero pulse.

APPENDIX 3

AUXILIARY TABLES

Polystyrene concentration (gm%)	δ (ms)	Δ (ms)	D_S ($10^{-11} m^2 s^{-1}$)
0.50	7	13	2.1±0.1
0.75	7	13	2.3±0.2
1.00	7	13	2.4±0.1
1.50	8	14	2.0±0.1
2.00	9	15	1.81±0.06
4.00	10	16	1.00±0.03
8.00	14	20	0.44±0.01
12.0	19	25	0.194±0.006
16.0	22	28	0.144±0.006
19.5	18	22	0.083±0.003
25.0	32	46	0.017±0.001

Table A.1. The self-diffusion coefficients of 110,000M_w polystyrene in CCl_4, at 25°C. The error in D_S is obtained from the standard deviation in the slope of the attenuation plot, plus the gradient calibration error (1.2%).

Polystyrene concentration (gm%)	δ (ms)	Δ (ms)	D_S ($10^{-11} m^2 s^{-1}$)
0.54	7	13	3.5±0.3
0.51	7	13	3.2±0.2
0.75	7	13	3.4±0.2
0.75	7	13	3.6±0.2
1.05	7	13	3.2±0.2
1.48	8	14	3.2±0.1
1.48	9	15	2.9±0.1
2.05	9	15	2.3±0.1
4.06	10	16	1.39±0.04
7.98	13	20	0.67±0.02
12.0	15	26	0.375±0.009
16.0	17	28	0.197±0.005
20.0	20	28	0.0132±0.0004
25.0	24	36	0.0057±0.0002

Table A.2. The self-diffusion coefficients of 110,000M_w polystyrene in $CDCl_3$, at 25°C. (Errors as in Table A.1 caption.)

Polystyrene concentration (gm%)	δ (ms)	Δ (ms)	D_S ($10^{-11} m^2 s^{-1}$)
0.75	5	11	6.2±0.3
1.00	6	12	4.5±0.2
1.50	6	12	4.2±0.2
2.00	6	12	3.35±0.09
4.03	10	16	1.84±0.07
8.05	12	19	0.79±0.02
12.0	14	21	0.40±0.01
16.0	15	24	0.207±0.007
20.0	20	31	0.115±0.004
25.0	26	39	0.053±0.002

Table A.3. The self-diffusion coefficients of 110,000M_w polystyrene in D-toluene, at 25°C. (Errors as in Table A.1 caption.)

Polystyrene concentration. (gm%).	Q'	Average D_M. ($10^{-11} m^2 s^{-1}$).	Number of D_M determinations used to find average.
0.26	0.02	2.98±0.07	10, using 5 angles.
0.48	0.01	3.0±0.1	4, using 4 angles.
0.74	0.02	3.1±0.1	3, using 3 angles.
0.97	0.06	3.33±0.08*	25, using 5 angles.
2.0	~0.8	2.8±0.2*	27, using 3 angles.
8.0	~3	2.3±0.3*	35, using 3 angles.

* --- Calculated by the method of cumulants.

Table A.4. Mutual diffusion coefficients for solutions of 110,000M_w random-coil polystyrene in CCl_4, at 25°C. The value of Q' is an estimate based on experimental values obtained at the smallest time scales used in the study of a particular concentration. D_M has been calculated from the initial slope of a ln(NIAF-1) versus time graph in the case of a cumulants fit, and from the straight line ln(NIAF-1) plot in the case of Q' $\lesssim$0.02. The errors given for D_M represent the spread of values obtained.

Polystyrene concentration (gm%).	Q'	Average D_M. ($10^{-11} m^2 s^{-1}$).	Number of D_M determinations used to find average.
0.24	0.02	4.8±0.2	4, using 4 angles.
0.48	0.02	5.2±0.1	5, using 5 angles.
1.0	~0.6	5.0±0.2*	20, using 2 angles.
2.0	~1.0	6.0±0.3*	10, using 1 angle.

* --- indicates analysis by the method of cumulants.

Table A.5. Mutual diffusion coefficients for solutions of 110,000M_w random-coil polystyrene in $CDCl_3$. (Other comments as in Table A.4 caption.)

Salt concentration (M)	Sphere concentration (gm%)	D_L ($10^{-12} m^2 s^{-1}$)	Comments
0.001	0.43	7.2±0.1	
0.001	1.28	7.8±0.1	
0.001	2.15	8.44±0.06	
0.001	4.46	10.4±0.3	0.5cm cell.
0.001	0.43	6.30±0.06	20°C
0.01	0.51	7.2±0.1	
0.01	0.55	7.07±0.07	0.5cm cell.
0.01	1.17	7.3±0.1	0.5cm cell.
0.01	1.44	7.43±0.07	
0.01	2.20	7.7±0.1	0.5cm cell.
0.01	2.71	8.0±0.2	
0.01	1.44	6.55±0.07	20°C

Table A.6. The concentrated polystyrene latex sphere solutions results, at 25°C (with several values at 20°C).

Salt concentration (M)	Sphere concentration (gm%)	D_0 ($10^{-12} m^2 s^{-1}$)	Comments
0.001	0.0234	6.84±0.07	
0.01	0.0234	6.96±0.07	A series
0.01	0.0119	6.95±0.07	
0.01	0.0069	6.92±0.07	
0.001	0.0254	6.79±0.08	
0.001	0.0134	6.77±0.07	B series
0.001	0.0082	6.78±0.07	
water	0.0224	6.54±0.07	
water	0.0114	6.58±0.07	C series
0.01	0.0114	6.99±0.07	
water	0.0038	6.54±0.07	D series
0.01	0.0038	6.85±0.07	
0.001	0.0038	6.71±0.07	
0.01	0.0038	6.81±0.07	
0.001	0.070	6.88±0.07	
0.01	0.070	7.01±0.07	

Table A.7. The polystyrene latex sphere dilute solution results, at 25°C.

Salt concentration (M)	Surface charge density (μCcm^{-2})	Sphere radius (μm)	Parameters ψ_0 (V)	κ ($\mathring{A}$)	Ξ
0.001	10	0.0455	0.205	96	1.905
0.001	3	0.0455	0.143	96	1.462
0.001	10	0.0375	0.205	96	1.844
0.001	3	0.0375	0.143	96	1.450
0.002	3	0.0375	0.126	68	1.420

0.075μm diameter spheres		0.091μm diameter spheres.	
R	f	R	f
0.000	0.7133	0.000	0.7678
0.010	0.7281	0.010	0.7872
0.025	0.7496	0.025	0.8139
0.050	0.7824	0.050	0.8489
0.100	0.8381	0.100	0.9100
0.150	0.8894	0.150	0.9463
0.200	0.9139	0.200	0.9684
0.350	0.9684	0.350	0.9939
0.500	0.9916	0.500	0.9989
0.750	0.9985	0.750	0.9997
100	1.000	100	100

Tables A.8. Parameters used to evaluate E(r) at low ionic strength.

APPENDIX 4.

AUXILARY FIGURES.

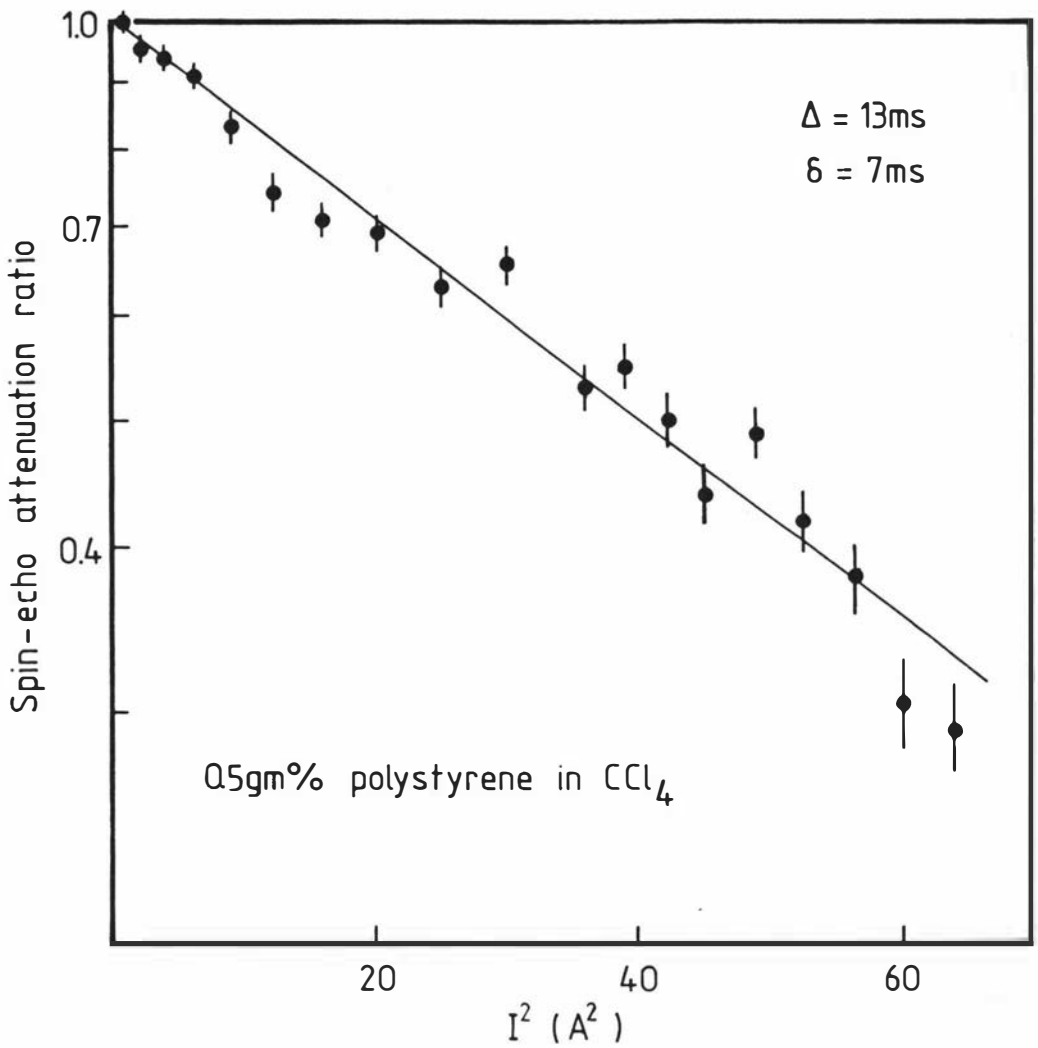


Figure A.1. The spin-echo attenuation plot for the smallest 110,000M_w polystyrene concentration studied.

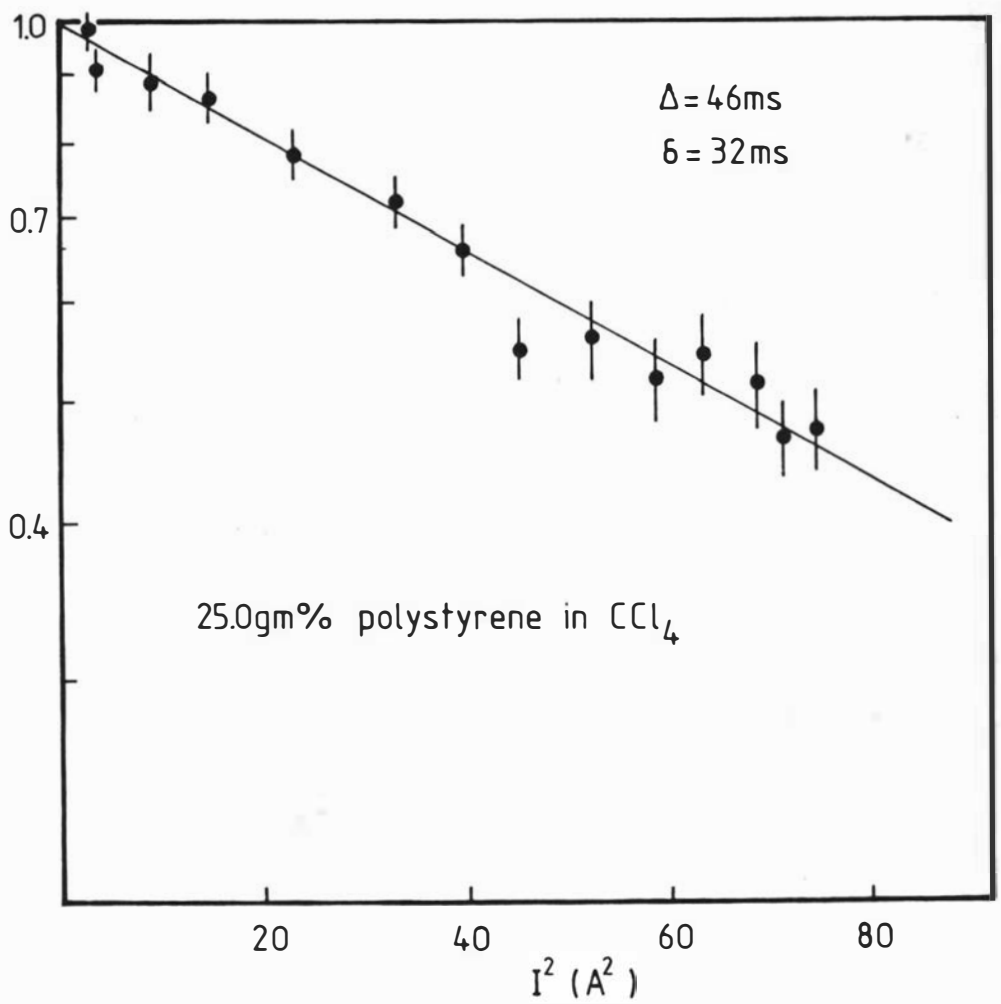


Figure A.2. The spin-echo attenuation plot for the largest 110,000M_w polystyrene concentration studied.

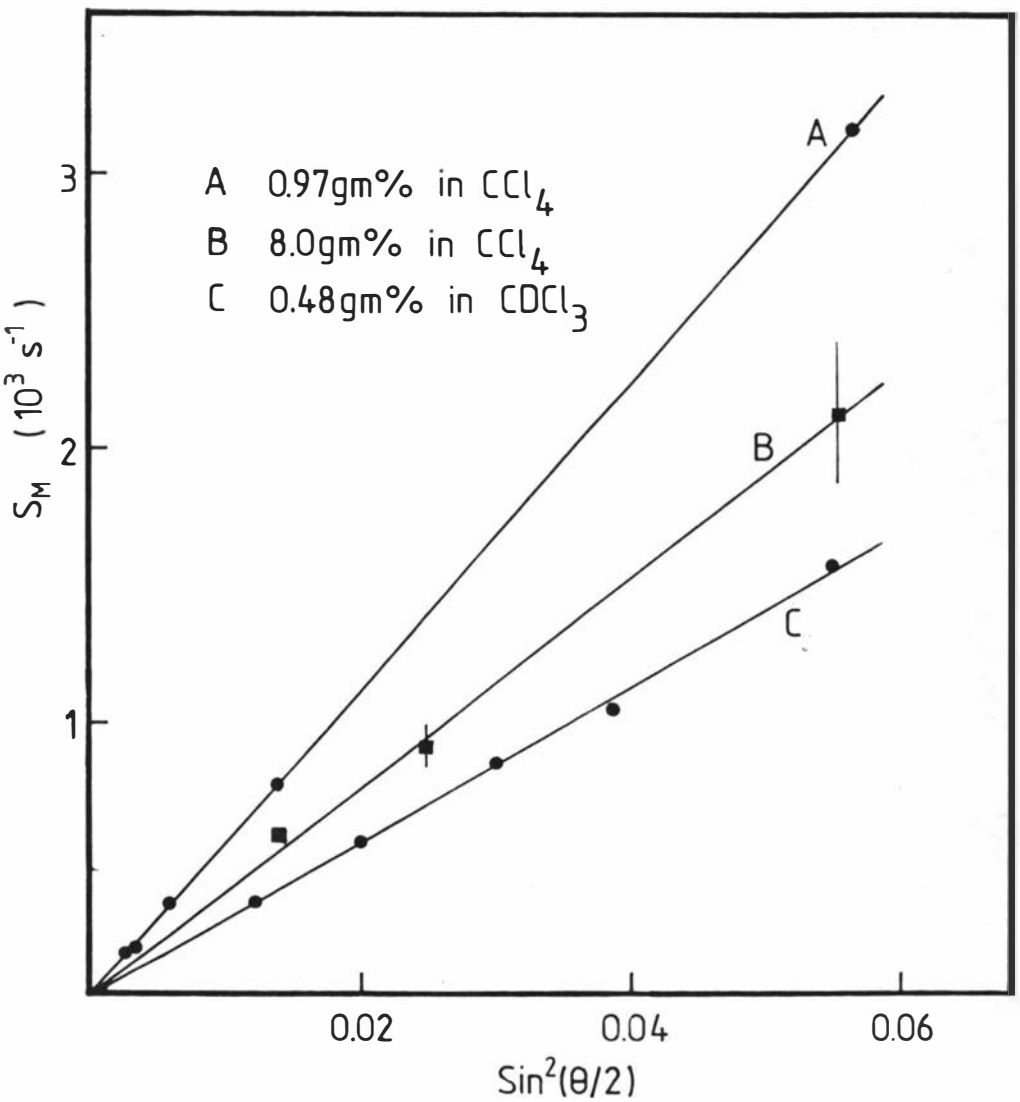


Figure A.3. Representative plots showing the linear dependence of S_M on $\sin^2(\theta/2)$. This linear dependence indicates that a simple Brownian diffusion process is being studied. When plotting the results obtained for sample A, both the vertical and horizontal scales shown have been multiplied by four. The vertical scale shown has been multiplied by three when plotting the results obtained for sample C.

APPENDIX 5

A 20MHz DIGITAL-ANALOGUE RATEMETER.

The schematic circuit diagram of the ratemeter developed to facilitate the setting of the zero degree scattering angle (as discussed in Chapter 5) is shown in Figure A.5.a. The output photocount pulses from the photomultiplier/discriminator assembly are passed to a 50Ω input impedance preamplifier (designed by Precision Devices; Malvern, England) to generate TTL logic compatible voltage levels; with 0V and -5V corresponding to "1" and "0" respectively. These amplified pulses then enter a divider chain consisting of 7400 series decade counters (7490s). Outputs from the divider chain are available in a divide-by 2,4,10,20,40,... sequence, and NAND gates are used to select an appropriate division factor.

To set the zero degree scattering angle, the photomultiplier alignment is varied until the maximum photocount-rate is observed. Maximisation of this count-rate is most easily achieved if it is displayed in an analogue form. The monostable multivibrator, zener-diode and milliammeter shown in Figure A.5.a form a simple frequency-to-current converter. The monostable output pulse width is adjusted until a full-scale deflection reading is obtained on the milliammeter for a monostable input frequency of 500Hz. With the divider chain outputs available, this allows selection of full scale photocount-per-second rates of 1000 to 20×10^6; in a 1,2,5 sequence.

The monostable $\overline{Q}$ output (normally at logic "1", i.e. at about -1.2V) is connected to the meter via a 3.3V zener diode. This diode prevents current flowing through the meter in the absence of monostable pulses, thus giving a true zero count-rate indication. The diode also serves to limit the current through the meter by reducing the voltage drop across the meter during a monostable pulse.

Pulses emitted from the photomultiplier/discriminator assembly will show a random distribution in time, and so it is possible that not all pulses will be counted, as pulses arriving at the monostable input are ignored if a monostable output pulse is occurring. However, as the

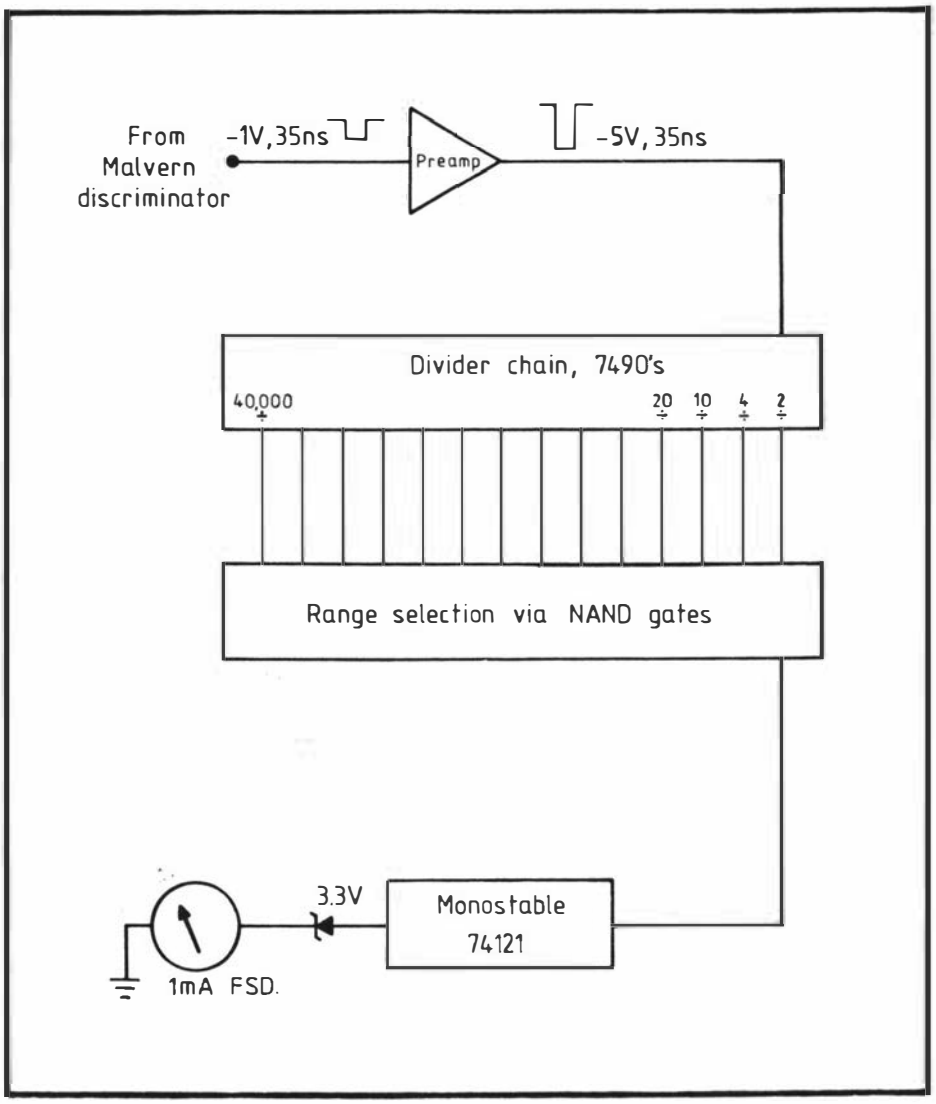


Figure A.5.a. Schematic circuit diagram for a 20MHz digital-analogue ratemeter. A 2,4,10,20 ... 40,000 division sequence was used to give 1,2,5,10kHz ... 20MHz count-rate ranges. The monostable multivibrator output pulse width is 0.6ms. The meter is a 1mA FSD, DC ammeter with an internal resistance of 300Ω. The 3.3V zener diode prevents the meter showing a small offset in the absence of input pulses.

alignment of the photomultiplier only requires an indication of the relative count-rate, and not the absolute count-rate, the random arrival of monostable input pulses is not a problem. In any event, the count-rate displayed by the rate-meter is not expected to be greatly in error since some averaging of the input pulse train occurs as the pulses pass through the divider chain. Also, the monostable output pulse width is small enough to allow a 1:1 correspondence between the monostable input and output pulses to be maintained for bursts of pulses at frequencies of up to 1500Hz (c.f. 500Hz for full scale deflection).

APPENDIX 6

A PULSED FIELD GRADIENT SEQUENCE FOR EDDY CURRENT MINIMISATION

The time-dependent behaviour of the macroscopic nuclear magnetisation in the x-y plane (i.e. following a 90^{o} rf pulse) was first classically described by Bloch[40]. Torrey[96], treating the magnetisation as a macroscopic fluid, added to Bloch's analysis by including the effect that diffusion has on the time rate of change of the magnetisation. The resultant equation describing the behaviour of $\underset{\sim}{M}$ in the x-y plane is known as the Bloch-Torrey equation, which is given by[96]

$$\partial \underset{\sim}{M}(\underset{\sim}{r},t)/\partial t = \gamma \underset{\sim}{M} \times \underset{\sim}{B}(\underset{\sim}{r},t) - (M_x \underset{\sim}{i} + M_y \underset{\sim}{j})/T_2 - (M_z - M_0)\underset{\sim}{k}/T_1 + D\nabla^2 \underset{\sim}{M} \qquad A.5$$

where $\underset{\sim}{M}(\underset{\sim}{r},t)$ is the macroscopic magnetisation in the inhomogeneous field $\underset{\sim}{B}(\underset{\sim}{r},t)$; M_x, M_y and M_z are the x,y and z components of the magnetisation at t=0; and M_0 is the equilibrium magnetisation. D is the self-diffusion coefficient of the fluid, and other parameters are as previously defined in Chapter 3.

Torrey considered the behaviour of the magnetisation in the x-y plane in the presence of a steady magnetic field gradient. An expression for the attenuation of a spin-echo due to diffusion in the presence of this field gradient was derived by Torrey (from equation A.5), and found to be identical to the equation obtained earlier by Carr and Purcell from a random walk model. Thus, either a macroscopic (Bloch-Torrey) or microscopic (Carr-Purcell) approach is valid for obtaining an expression for the diffusion-attenuated spin-echo.

In 1964, Stejskal and Tanner[6], following the macroscopic approach of Torrey, considered the behaviour of the x-y plane magnetisation under the action of a time-dependent magnetic field gradient, $\underset{\sim}{G}(t)$. For a spin-echo experiment, Stejskal and Tanner showed that the spin-echo attenuation due to diffusion is given by

$$\ell n[A(G)/A(0)] = -\gamma^2 D \left[\int_0^{2\tau} F^2 dt - 4\underset{\sim}{f} \cdot \int_{\tau}^{2\tau} \underset{\sim}{F} dt + 4f^2 \tau \right] \qquad A.6$$

where

$$\underset{\sim}{f} = \underset{\sim}{F}(\tau) \qquad \text{A.7}$$

and

$$\underset{\sim}{F}(t) = \int_0^t \underset{\sim}{G}(t')dt' \qquad \text{A.8}$$

For the pulsed field gradient experiments of interest to this work, $\underset{\sim}{G}(t)$ is a one-dimensional gradient applied along the sample z-axis, that is $\underset{\sim}{G}(t) = G(t)\underset{\sim}{k}$. Also, it is assumed here that G(t) is very much larger than any gradients due to inhomogeneities in the steady magnetic field $\underset{\sim}{B}_0 = B_0\underset{\sim}{k}$. The ramped-pulse magnetic field gradient sequence shown in Figure 8.1 can thus be expressed as

$$\begin{aligned}
G(t) &= 0 && 0 \leq t \leq t_1 \\
&= (G/\beta)(t-t_1) && t_1 < t < t_1+\beta \\
&= G && t_1+\beta < t < t_1+\delta \\
&= G[1-(1/\beta)(t-t_1-\delta)] && t_1+\delta < t \leq t_1+\delta+\beta \\
&= 0 && t_1+\delta+\beta < t \leq t_1+\Delta \\
&= (G/\beta)(t-t_1-\Delta) && t_1+\Delta < t \leq t_1+\Delta+\beta \\
&= G && t_1+\Delta+\beta < t \leq t_1+\Delta+\delta \\
&= G[1-(1/\beta)(t-t_1-\delta-\Delta)] && t_1+\Delta+\delta < t \leq t_1+\Delta+\delta+\beta \\
&= 0 && t > t_1+\Delta+\delta+\beta.
\end{aligned}$$

Equations A.7 and A.8 can be evaluated for this choice of G(t), and substituted into equation A.6 to yield

$$\ell n[A(G)/A(0)] = -\gamma^2G^2D[\delta^2(\Delta-\delta/3) + \beta^2(\beta/30-\delta/6)] \qquad \text{A.9}$$

which reduces to the Stejskal-Tanner square pulse expression as the ramp-time, β, tends to zero.

The reduction of the functions $\int F(t)$ and $\int F(t)^2$ to their final forms (as given in Table A.6.a) requires that over a thousand terms be collected up and cancelled out. There is, of course, ample opportunity for errors to occur in the term reduction process. To check the accuracy of equation A.9 a numerical integration program was written to evaluate equation A.6 directly from the interval equations for F(t) and $F(t)^2$ (see Table A.6.a). For a given D,τ,δ,Δ and β, the attenuation ratio calculated numerically from equation A.6 was compared with that calculated from the analytic expression, equation A.9. The attenuation ratios calculated from the two equations were in perfect agreement over the

Time Interval	F(t)	$\int F(t)$	$\int F(t)^2$
$0 < t \leq A$	0		0
$A < t \leq B$	$g/(2\beta)\ (t-A)^2$	-	$g^2\beta^3/20$
$B < t \leq C$	$g\beta/2 + g(t-B)$	-	$g^2(-\beta^3/12 + \beta^2\delta/4 - \beta\delta^2/2 + \delta^3/8)$
$C < t \leq D$	$g\delta - g/(2\beta)\ (D-t)^2$	-	$g^2(\delta^2\beta - \delta\beta^2/3 + \beta^3/20)$
$D < t \leq E$	$g\delta$	$g(\Delta\delta-\delta\tau)$**	$g^2\delta^2(\Delta-\delta-\beta)$
$E < t \leq F$	$g\delta + g/(2\beta)\ (t-E)^2$	$g(\delta\beta+\beta^2/6)$	$g^2(\beta^3/20 + \delta^2\beta + \delta\beta^2/3)$
$F < t \leq G$	$g\beta/2 + g\delta + g(t-F)$	$g(-3\beta\delta/2 + 3\delta^2/2)$	$g^2(\beta^2\delta/4 - \beta^3/12 + 7\delta^3/3 - 5\beta\delta^2/2)$
$G < t \leq H$	$2g\delta - g/(2\beta)\ (H-t)^2$	$g(2\delta\beta-\beta^2/6)$	$g^2(4\delta^2\beta - 2\delta\beta^2/3 + \beta^3/20)$
$H < t \leq 2\tau$	$2g\delta$	$g(4\delta\tau-2\Delta\delta-2\delta^2-2\delta\beta)$	$g^2(8\delta^2\tau - 4\delta^3 - 4\delta^2\Delta - 4\delta^2\beta)$

Table A.6.a. Evaluation of the integrals used to calculate the spin-echo attenuation ratio. The letters A,B,C, ... H denote the times t_1, $t_1+\beta$, $t_1+\delta$ ⋯ $t_1+\Delta+\delta+\beta$ respectively, as shown in Figure 8.1. The limits for the entry marked ** are actually $\tau < t \leq t_1+\Delta$, rather than those indicated in the time interval column.

very wide range of values of τ, δ, Δ and β that were examined. Equation A.9 is thus deemed to have been correctly derived.

APPENDIX 7.

PUBLISHED WORK.

JOURNAL OF MAGNETIC RESONANCE 37, 247–259 (1980)

A Pulsed Field Gradient System for a Fourier Transform Spectrometer

P. T. CALLAGHAN, C. M. TROTTER AND K. W. JOLLEY

Department of Chemistry, Biochemistry & Biophysics, Massey University, Palmerston North, New Zealand

Received November 16, 1978; revised February 5, 1979

The construction and performance of a pulsed field gradient system for use with a commercial high-resolution pulse–Fourier transform NMR spectrometer is described. The diffusion coefficient of benzene as measured by the system lies within 0.9% of the current literature value. The use of an external ^{2}H lock in conjunction with signal averaging facilitates the measurement of diffusion coefficients for solution components present in small concentrations and data are presented for a 0.5% (w/v) solution of polystyrene ($M_r = 110{,}000$) in carbon tetrachloride. The ability of the system to investigate slow diffusion is demonstrated by measurements made on a 10% (w/v) solution of polystyrene ($M_r = 230{,}000$) in carbon tetrachloride. Homogeneity coils in the ^{1}H probe enable the self-diffusion of single components in multicomponent systems to be investigated, and results for the binary system butanol–benzene are presented.

INTRODUCTION

The NMR spin-echo technique for measuring self-diffusion has been used extensively since it was first suggested by Hahn (*1*). The advantages associated with the technique over conventional methods have been offset by poor experimental accuracy. A recent paper, however (*2*), demonstrated a reproducibility of ± 1% and an overall accuracy of ± 2% using a steady gradient technique to measure the self-diffusion coefficients of water in electrolyte solutions.

An alternative method of studying self-diffusion in liquids is the pulsed field gradient technique. Stejskal and Tanner (*3*) have shown that two identical rectangular pulses applied before and after the 180° refocusing rf pulse give an echo

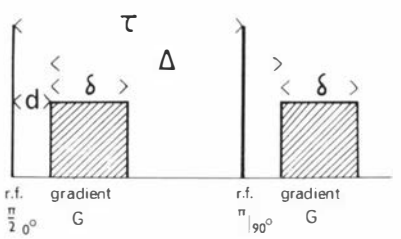


FIG. 1. Pulsed field gradient sequence showing the times τ, d, Δ, and δ which can be independently set in an experiment.

0022-2364/80/020247-13$02.00/0
Copyright © 1980 by Academic Press, Inc.
All rights of reproduction in any form reserved.
Printed in Great Britain

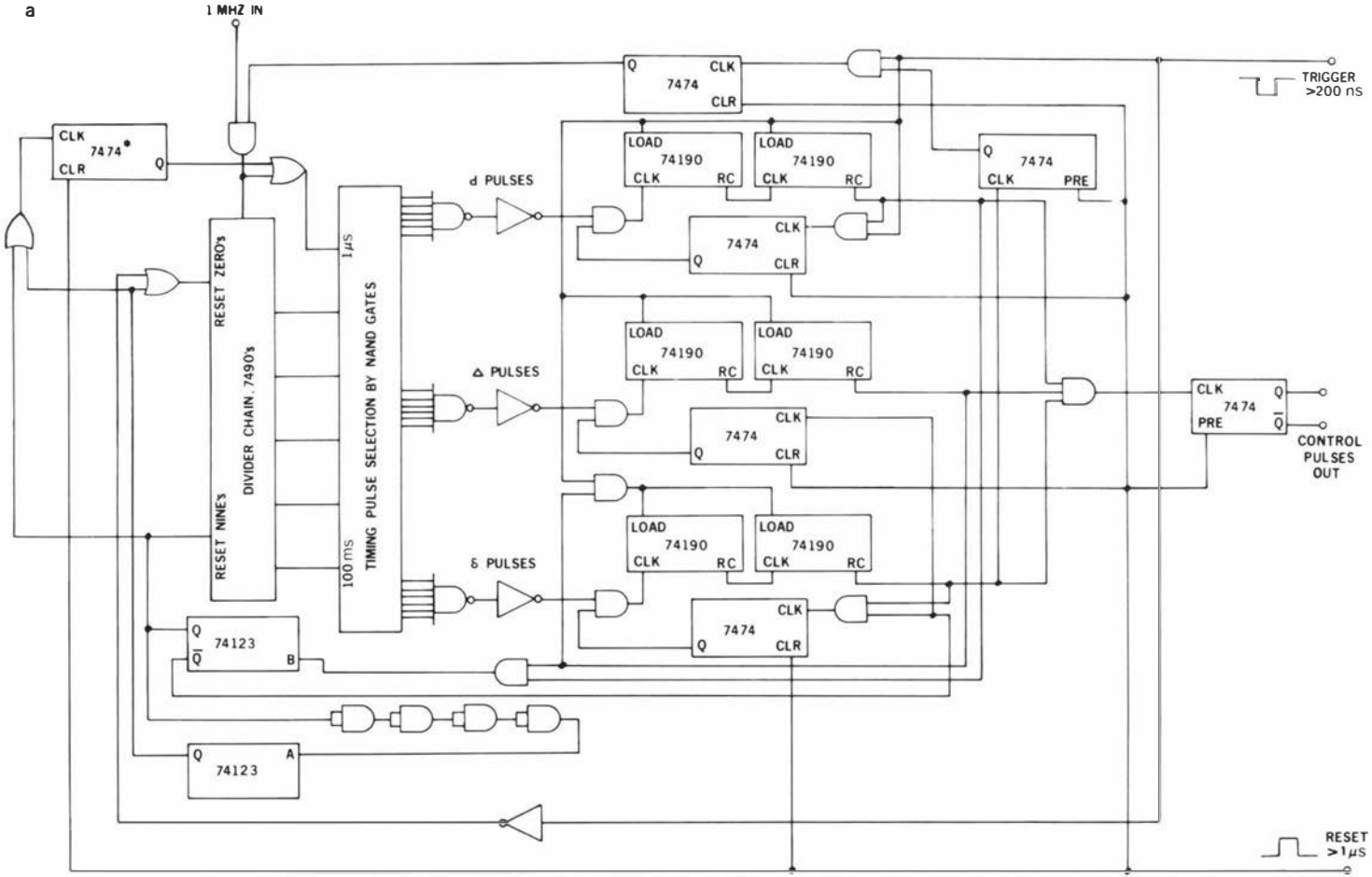


FIG. 2a. Schematic circuit diagram for the pulse programmer.

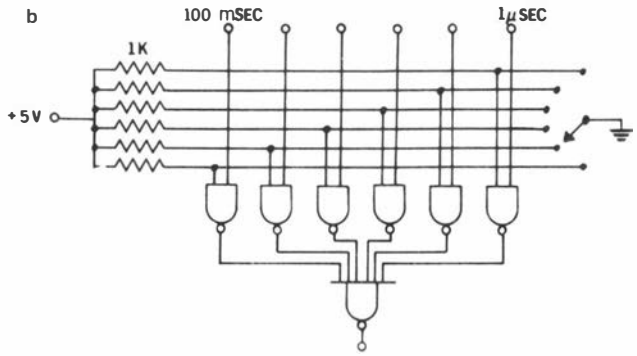


FIG. 2b. Timing pulse selection circuit.

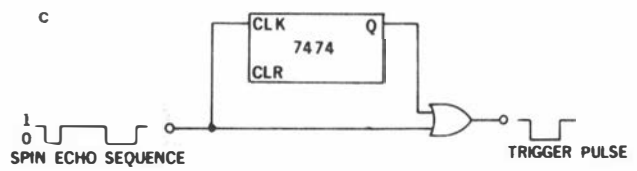


FIG. 2c. Circuit modification required when using a two-pulse spin-echo sequence as a trigger.

attenuation of

$$A(G)/A(0) = \exp[-D\gamma^2 G^2 \delta^2 (\Delta - \delta/3)],$$

where $A(G)$ and $A(0)$ are the echo amplitudes with and without the field gradient pulses, respectively. The magnitude of the gradient in the polarizing field is G and by a suitable choice of coil may be applied as a gradient with respect to the x, y, or z direction. The quantity D is the self-diffusion coefficient of the nuclear spins along the gradient direction defined by the relationship

$$D = \bar{z}^2/2t,$$

where $\bar{z}^2$ is the mean-square distance traveled along the gradient axis in time t. The quantity γ is the magnetogyric ratio of the nuclei being observed and δ and Δ are pulse spacings defined in Fig. 1.

There are considerable advantages in using the pulsed field gradient technique for the measurement of self-diffusion coefficients. These include the sampling of nuclear spin echoes in the absence of a gradient (an essential requirement when frequency resolution is required), the ability to measure slower diffusion, and the detection of non-Gaussian diffusion by the use of various interpulse spacings (*4, 5*).

We describe here a pulsed field gradient system controlled by the rf gate pulse of a commercial high-resolution pulse–Fourier transform spectrometer (JEOL FX-60).

THE PULSE PROGRAMMER

A digital pulse programmer has been designed so that the experimental parameters Δ and δ, as well as the time d (see Fig. 1), may be set directly on

BCD-coded thumbwheel switches. The circuit, which utilizes 7400 series TTL devices throughout, is shown in Fig. 2a. A 1-MHz signal, derived from the JEOL spectrometer crystal clock, provides the clock pulses entering the divider chain. Timing pulses appropriate to any particular experiment may be selected using NAND gates as detailed in Fig. 2b. The precision of the output pulse timing is determined by the number of up/down counters (74190s) in cascade. Figure 2 thus represents a programmer with a precision of two digits in each of the intervals d, Δ, and δ. Such a precision has been found to be quite adequate for our pulsed field gradient experiments. The up/down counters are utilized in the down counting mode, and are directly programmed with the thumbwheel switches.

The function of the pulse programmer is to provide the accurate, sequentially timed intervals d, δ, and Δ. The TTL devices are used in a manner which avoids the problem of propagation delays so that the accuracy of all timed intervals is better than 1 μsec.

At power turn-on, a reset pulse (>1 μsec) must be provided to the appropriate PRE or CLR inputs (see Fig. 2b) of the 7474s to set their initial states. The trigger pulse is provided by the spectrometer pulse programmer, and as such is a two-pulse sequence for a spin-echo experiment. This two-pulse sequence is easily turned into the required single-trigger pulse by the inclusion of the circuitry shown in Fig. 2c before the trigger input.

The 1-MHz clock access to the divider chain is automatically disabled when the two-pulse sequence reaches completion. The appearance of the falling edge of the next trigger pulse readies the system for a new sequence, and timing proceeds from the rising edge of the trigger pulse. The circuit presented does not require the NAND gate range switches to be debounced, or to make before break, as false clocking of the counters is prevented by their inhibited CLK inputs. More details concerning the pulse programmer are given in the Appendix.

CURRENT CONTROL

The pulse programmer logic output is used to externally switch the current supplied by a commercial operational power supply (KEPCO JQE 25-10M) operating in the constant current mode. This power supply was modified to give reduced response time by removal of the output capacitor, and the addition of several phase shifting networks around the error amplifier to prevent oscillation.[1]

Transistors in a three-stage Darlington configuration, shown in Fig. 3, are used to generate the field gradient pulses by externally switching the current path. During δ, the Q_A transistors are turned on and Q_B are off, thus allowing current to flow through the gradient coils. At all other times Q_A are off and Q_B are on, thus isolating the coils from the circuit. At all times the current magnitude is controlled by the power supply feedback amplifier. This has the advantage that the gradient pulse amplitude may be measured at any time by noting the voltage drop across the 50-W, 0.1Ω precision resistor, R_S. The actual current pulses flowing in the coils may be monitored across resistor R using an oscilloscope with a differential input amplifier.

[1] This brings the specifications up to the equivalent high-speed model OPS 25-10M upon whose circuitry the modifications were based.

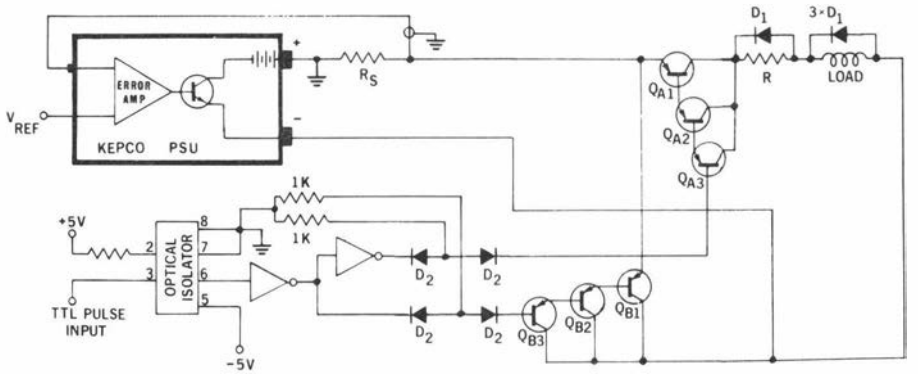


FIG. 3. Current switching circuit for the field gradient coils. The transistors used are TIP 36A (Q_{A1}, Q_{B1}), TIP 30A (Q_{A2}, Q_{B2}), and 2N3906 (Q_{A3}, Q_{B3}).

The optical isolator provides a convenient (−5 V, 0 V), to (0 V, +5 V) logic voltage level translation as well as protection for the TTL pulse programmer. A 2-A fuse is included to protect the coils in the case of system failure. The current supply output transistors are protected from large voltage spikes generated during current turn-off by the high-speed rectifier diodes in parallel with the coils.

The current pulses produced by this system, using the Helmholtz coils as a load, are shown in Fig. 4a. The current regulation is better than 0.02% over the operating range (100 mA to 10 A) and the pulses are precisely matched in shape. Any error in

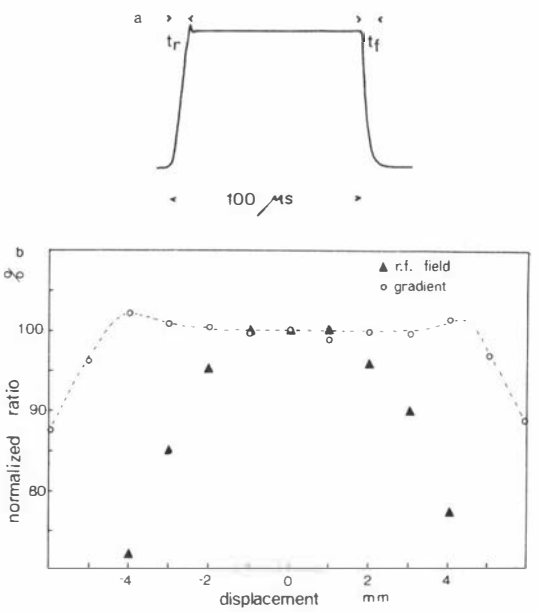


FIG. 4. (a) Gradient pulse shape for a 1.5 T m^{-1} pulse determined by measuring the voltage across resistor R in Fig. 3. The rise and fall times are independent of the pulse height and duration. (b) Radiofrequency field and field gradient profiles measured along the y axis of the sample space.

measuring diffusion coefficients caused by deviation from the rectangular pulse shape is insignificant ($<0.1\%$) for values of $\delta \geqslant 500$ μsec.

External switching of the current to provide the gradient pulses avoids the possibility of current flowing through the coils other than during times δ. Systems employing feedback amplifiers for current stabilization are susceptible to pickup on the sensing resistor during the rf pulse. This may cause small amounts of gradient current to be present during the rf pulse. We have found, by experimenting with other switching systems, that these small gradients can cause a distortion in the echo envelope and phase, effects mentioned by other authors (*6, 7*). Isolation of the coils during times other than δ avoids this problem.

THE PROBE

A 60-MHz low-resolution ^{1}H probe was built to incorporate 0.15 T m^{-1} A^{-1} field gradient coils. The entire unit was made to fit in the 32-mm gap between the polarizing magnet pole faces.

The rf section of the probe consists of a single coil series resonant circuit designed according to the criteria set out by Clark and McNeil (*8*). The circuit diagram is shown in Fig. 5. We have used a JEOL 60-MHz FET preamplifier in the receiver stage although any other single-stage tuned preamplifier would suffice (*9*). Resistor R_1 has been included to limit the coil Q during the ring down stage after the 60-V pp rf pulse. In order to obtain maximum power transfer the length of the 50-Ω coaxial transmission line was set (*8*) to give a load impedance, when tuned at C_1, equal to the transmitter output impedance.

The sample coil, L_2, was designed to give good homogeneity of the rf field and a good filling factor but with an inductance and Q limited to the desired low values. We have followed the method of Lowe and Tarr (*10*) and have wound a two-turn 7-mm-long, 9-mm-diameter coil from 0.17-mm copper shim. After the series capacitor C_1 was tuned the ^{1}H 90° flip time was 23 μsec under a 60-V pp rf pulse at 60 MHz. The coil was wound on the glass Dewar shown in Fig. 6 using Teflon tape to hold it in place. Sample tubes are inserted in the 5-mm-diameter cavity down the axis

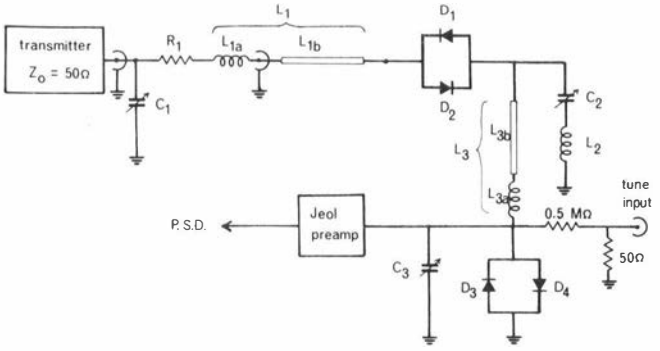


FIG. 5. Series resonant circuit after Clark and McNeill (*8*). Resistor R_1 is included to reduce ring down times to ~1.5 μsec and L_1 is adjusted to present a 50-Ω load to the rf transmitter. L_1C_1, L_2C_2, and L_3C_3 are tuned pairs. The diodes shown are high-speed silicon.

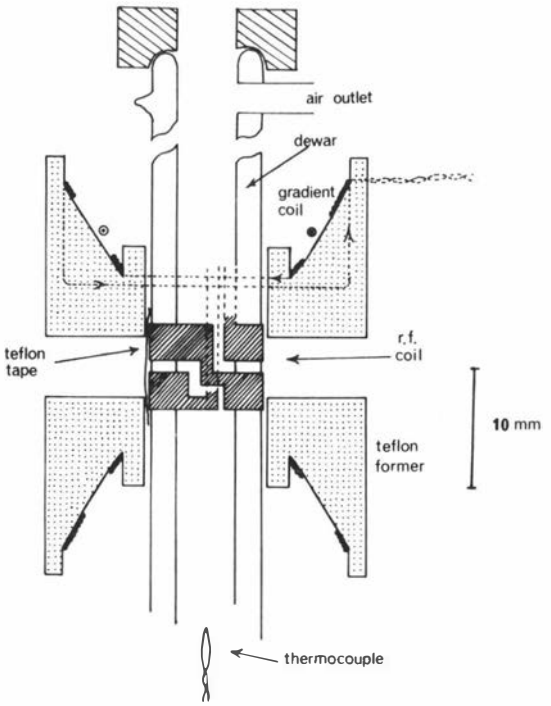


FIG. 6. Sample space geometry. The viewing port along the axis of the Helmholtz coil allows the rf coil to be accurately centered.

of the Dewar and sample temperature is controlled using a copper–constantan thermocouple sensor in a conventional hot-air feedback system. The temperature variation over the sample volume is ≤ 0.5°C. The rf profile measured along the y axis of the sample space is shown in Fig. 4b. The rf pulse strength was determined by measuring the 180° flip time in a very small water sample.

The main $\partial B_z/\partial z$ gradient coils for diffusion measurements are an opposed Helmholtz pair wound with 19 turns per coil using 26-swg enameled copper wire on a Teflon former. During an experiment the coils are maintained at a constant temperature by a steady stream of air directed at their base. Helmholtz coils offer good gradient uniformity over the small sample volumes employed in this system, but for extended cylindrical volumes quadrupolar coils are superior (*11*). The shape of the Helmholtz former follows the equation of Tanner (*12*) and minimizes second-order ($\partial^2 B_z/\partial z^2$) gradients over the sample space. The gradient uniformity in our coil is calculated to be better than 1% over the sample space 4.5 mm in diameter and 4.5 mm in length. The calculated y-axis profile has been confirmed experimentally by measuring the echo attenuation of a small water sample as a function of its position along the y axis (see Fig. 4b).

We have included in the probe a set of $\partial B_z/\partial x$, $\partial B_z/\partial y$, and $\partial B_z/\partial z$ homogeneity coils. These coils give a residual gradient, g_0, of 0.1 mT m^{-1}. This gradient is sufficiently small to resolve ^{1}H resonances ~ 60 Hz apart which allows for independent measurement of diffusion rates in some multicomponent mixtures, and provides

a valuable increase in signal to noise when working with dilute molecular species. An excellent set of design criteria has been given by Anderson (*13*).

Where possible we have used Teflon, laminated plastic, and Perspex as construction materials in the probe to minimize any eddy currents associated with switching on and off the field gradient pulses. These currents can distort the gradient time dependence from the desired square shape. By examining the ^{1}H free-induction decay in the eddy current "tail" following a maximum 1.5 T m^{-1} gradient pulse we have determined that eddy effects contribute $\leqslant 0.03$ mT m^{-1} at 500 μsec following a gradient pulse and $\leqslant 0.01$ mT m^{-1} at 1000 μsec. Despite the small operating gap between the magnet pole pieces, gradients associated with eddy currents are entirely insignificant for diffusion experiments over the entire experimental range, $\delta \geqslant 0.5$ msec, $\Delta \geqslant 2$ msec.

RESULTS

^{1}H spin-echo signals are sampled with an AD converter and processed in the minicomputer of the JEOL spectrometer. Data are analyzed by plotting the natural logarithm of the echo attenuation versus $I^2\delta^2(\Delta - \delta/3)$ and performing a least-squares fit to the resulting straight line. Using a water sample at 25°C and taking Mills' value (*14*) for the diffusion coefficient of water at this temperature (2.266×10^{-9} m^2 sec^{-1}) we obtain a coil gradient of 0.1512 ± 0.0005 T m^{-1} A^{-1}, which is within 1% of that calculated from a knowledge of the coil dimensions. With this value for the field gradient the diffusion coefficient of Analar benzene at 25°C is

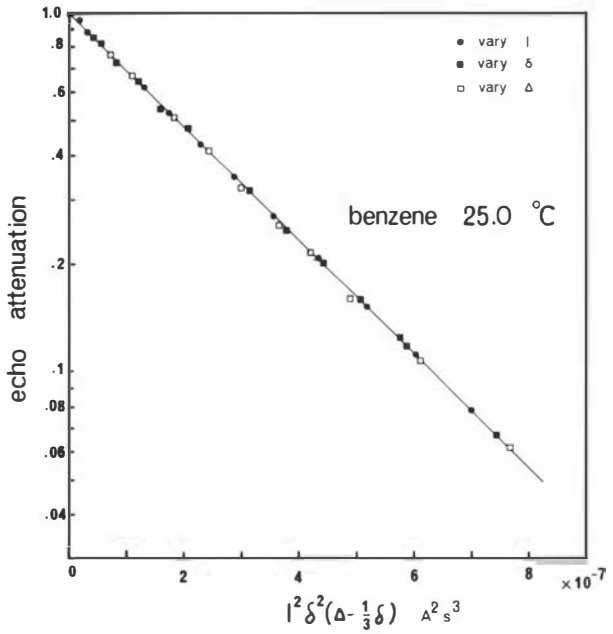


FIG. 7. Echo attenuation plot for Analar benzene at 25.0°C in which all three experimental parameters, G, Δ, and δ, are varied.

$(2.23 \pm 0.02) \times 10^{-9}$ m^2 sec^{-1}, compared to the literature value (*15*) of 2.210×10^{-9} m^2 sec^{-1}. Figure 7 shows an echo attenuation plot for benzene at 25°C obtained by varying all three parameters G, Δ, and δ. These data are consistent with the Skejskal and Tanner formula (*3*), the diffusion coefficient being independent of δ and Δ within experimental precision. The data intercept also agrees with the measured zero gradient amplitude.

The ability to accumulate data in a signal-averaging mode is a major advantage with modern NMR spectrometers. Use of an external ^{2}H lock (JEOL NM 3900) allows for the accumulation of signals under pulsed field gradient conditions since we find that the lock signal recovers from the field gradient pulse in $\leq$ 2msec. We have found that when adding successive spin echoes it is essential to remove any small

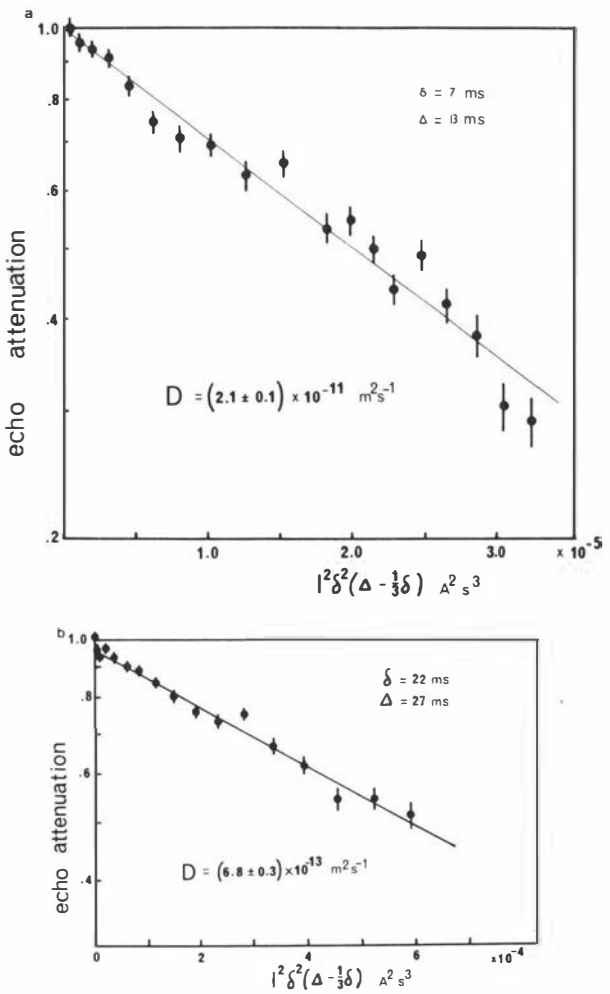


FIG. 8. (a) Echo attenuation data for a solution of 0.5% (w/v) polystyrene (M_r = 110,000) in CCl_4 at 25.0°C. The line shown is obtained by a linear least-squares fit. (b) 10% (w/v) polystyrene (M_r = 230,000) in CCl_4 at 25.0°C.

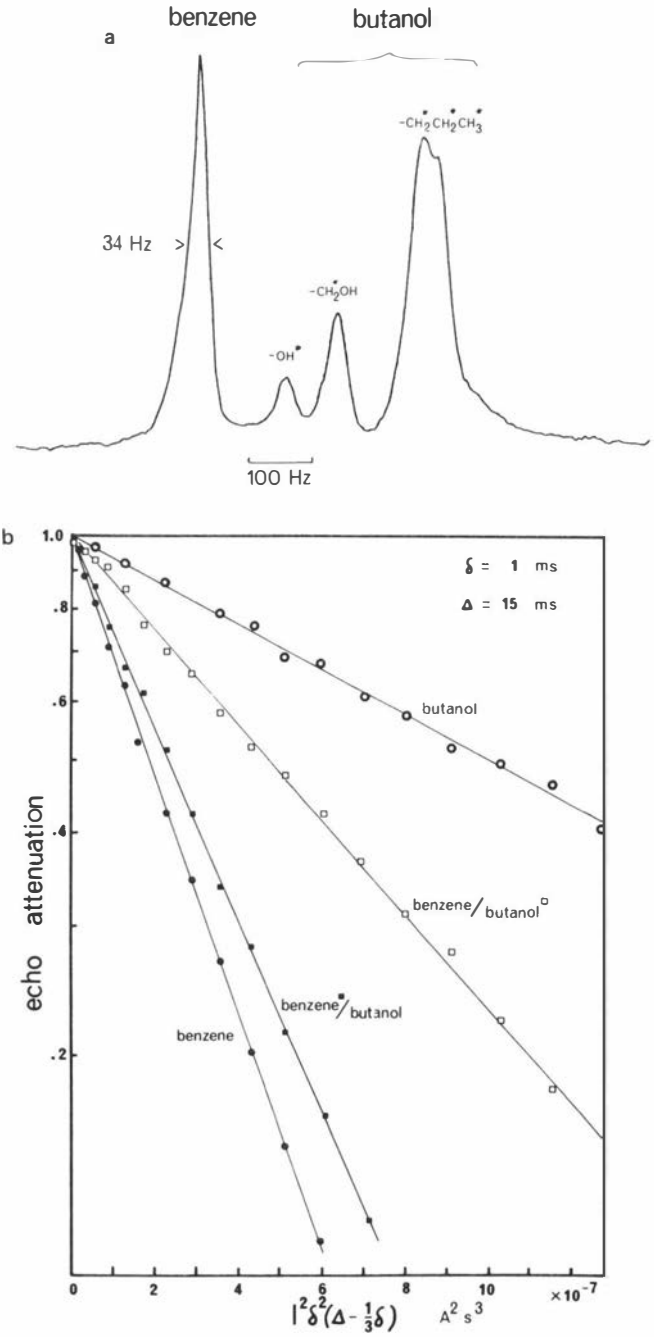


FIG. 9. (a) ^{1}H frequency spectrum for 5-mm-long, 4.5-mm-diameter sample consisting of an equimolar mixture of benzene and butanol at 25.0°C. (b) Echo attenuation data for pure benzene, pure butanol, and the benzene and butanol components in an equimolar mixture. All data were obtained at 25.0°C and the self-diffusion coefficients are respectively $(2.23 \pm 0.02) \times 10^{-9}$, $(0.43 \pm 0.01) \times 10^{-9}$, $(1.83 \pm 0.02) \times 10^{-9}$, and $(0.90 \pm 0.01) \times 10^{-9}$ m^2 sec^{-1}.

spurious dc signal component. On our machine this is accomplished by phase-inverting successive spin-echo pulse pairs while at the same time alternating the sign of the AD converter. In Fig. 8a, the echo attenuation plot for 0.5% (w/v) polystyrene ($M_r = 110{,}000$) in carbon tetrachloride at 25°C is shown. Each data point represents 400 accumulations. Previous published diffusion measurements on polystyrene solutions using pulsed field gradient NMR have been restricted to concentrations greater than 30% (*16*). In conjunction with photon correlation spectroscopy methods (*17*) we are proceeding with comparative diffusion measurements over a wide concentration range using a variety of polystyrenes and solvents of different molecular weights.

Figure 8b shows the echo attenuation plot for a 10% (w/v) solution of polystyrene ($M_r = 230{,}000$) in carbon tetrachloride at 25°C. The discrepancy between the data intercept and the zero gradient amplitude is caused by slow lock signal recovery in the time $\tau - \delta$ (5 msec following the long, 22-msec) gradient pulse. It is eliminated by increasing $\tau - \delta$. The diffusion rate of $(6.8 \pm 0.3) \times 10^{-13}\ m^2\ sec^{-1}$ is near the slow limit for the technique and although other authors (*18–20*) have reported slower diffusion measurements in the vicinity of $10^{-13}\ m^2\ sec^{-1}$, the present result does represent a considerable improvement in sensitivity and precision in this range.

The above results were obtained by measuring the amplitude of the spin echoes directly from the time domain signal. An alternative way is to start the signal sampling at the center of the echo so that the data may be Fourier-transformed into the frequency domain. Provided that the components of a mixture have resolvable resonances it then becomes possible to measure the self-diffusion rates of the various molecular species (*21*). Figure 9a shows the ^1H frequency spectrum of an equimolar mixture of benzene and butanol. It can be seen that the homogeneity coils incorporated in the probe give a resolution of ~ 35 Hz over the sample volume and the benzene and butanol resonances are resolved. The echo attenuation data for pure butanol, pure benzene, and the equimolar mixture are shown in Fig. 9b. We intend to compare self-diffusion coefficients in various molar mixtures of this and other binary solutions with mutual diffusion rates obtained by the photon correlation spectroscopy facility in this department (*17*).

CONCLUSION

We have shown that the pulse field gradient device described above gives excellent agreement with the accepted literature values for the diffusion coefficient of benzene (*15*). We have also demonstrated the advantages to be gained by interfacing such a device to a high-resolution pulse–Fourier transform spectrometer, the computer software of which facilitates spectrum accumulation and reduction. Data accumulation enables measurements to be made on dilute solutions as is demonstrated by the 0.5% polystyrene solution results, and the Fourier transform capability enables the frequency spectrum to be obtained provided sampling is commenced at the center of the echo. This allows for the measurement of diffusion coefficients for single-solution components in multicomponent systems provided their resonances are resolvable. The high-resolution magnet and the simple homogeneity coils incorporated in the

probe provide a resolution of about 35 Hz, which is sufficient to resolve components whose chemical shift is ≥ 1 ppm at 60 MHz.

APPENDIX

The pulse programmer consists of three sections: the divider chain and associated pulse selection circuitry; the d, Δ, and δ down counters; and the control circuitry. With the aid of Fig. 2, the workings of sections 1 and 2 are self-evident. However, the control circuitry, consisting of sundry D flip-flops (7474s) and several monostables, merits a little further explanation.

The problem of providing sequentially timed intervals is generally complicated by the presence of propagation delays, and it is the function of the control circuitry to circumvent any inaccuracies such delays might otherwise cause.

In sequential timing, the edge of a clock pulse which marks the end of an interval also marks time zero for the next interval. The second interval's counters will always miss their time zero pulse if they are activated at the end of the first interval due to propagation delays associated with the activation process.

Down counters, including the 74190 counter, often have a so-called "look ahead" feature for use in sequential timing. This is an output pin whose logic state changes upon a count of one and this change may be used to activate the next interval's counters as the next clock pulse will mark time zero for this interval. Unfortunately the precision of the pulsed field gradient experiment often demands that there be order-of-magnitude differences in the frequencies of the clock pulses driving the Δ and δ counters, with δ having the higher-frequency pulses. Thus activation of the δ counters by some "look-ahead" feature could result in δ being incorrectly timed.

In the present application these problems are overcome by inhibiting those counters not immediately concerned with timing a particular interval. This is achieved by placing a logic one at the CLK input of the initial counter in the cascade via a D flip-flop. Immediately a timed interval is completed, the next appropriate counters are activated, and the previous counters inactivated, by clocking the appropriate flip-flops (those connected to the counters' CLK inputs). The monostables (74123s) are also triggered at this stage and provide a pulse sequence to the divider chain which causes all outputs to go to the count of nine, then one. This reset-nine, reset-zero sequence has the effect of mimicking a timing pulse at the CLK input of any activated down counters and so time zero is restored and timing proceeds with no loss in accuracy.

For the case when 1-μsec pulses are selected the D flip-flop, marked as 7474* in Fig. 2a, provides the necessary zero time pulse.

ACKNOWLEDGMENTS

The authors are indebted to Mr. R. C. O'Driscoll and Dr. D. N. Pinder for valuable discussions and to Mr. K. Smith and Mr. R. Parsons for technical assistance.

REFERENCES

1. E. HAHN, *Phys. Rev.* **80,** 580 (1950).
2. K. R. HARRIS, R. MILLS, P. J. BACK, AND D. S. WEBSTER, *J. Magn. Reson.* **29,** 473 (1978).
3. E. O. STEJSKAL AND J. E. TANNER, *J. Chem. Phys.* **42,** 288 (1965).
4. E. O. STEJSKAL, *J. Chem. Phys.* **43,** 3597 (1965).
5. J. E. TANNER AND E. O. STEJSKAL, *J. Chem. Phys.* **49,** 1768 (1968).
6. G. B. MATSON, *Rev. Sci. Instrum.* **43,** 1504 (1971).
7. L. MCLACHLAN, Institute of Nuclear Sciences, DSIR, Wellington, N.Z., private communication.
8. W. G. CLARK AND J. A. MCNEIL, *Rev. Sci. Instrum.* **44,** 844 (1973).
9. D. J. ADDUCI, P. A. HORNUNG, AND D. R. TORGESON, *Rev. Sci. Instrum.* **47,** 1503 (1976).
10. J. LOWE AND C. E. TARR, *J. Phys. E.* **1,** 320 (1968).
11. D. S. WEBSTER AND K. H. MARSDEN, *Rev. Sci. Instrum.* **45,** 1232 (1974).
12. J. E. TANNER, *Rev. Sci. Instrum.* **36,** 1086 (1965).
13. W. A. ANDERSON, *Rev. Sci. Instrum.* **32,** 241 (1961).
14. R. MILLS, *J. Phys. Chem.* **77,** 687 (1973).
15. K. R. HARRIS, C. K. N. PUA, AND P. J. DUNLOP, *J. Phys. Chem.*, 3524 (1970).
16. T. COSGROVE AND R. F. WARREN, *Polymer* **18,** 255 (1977).
17. D. N. PINDER AND R. C. O'DRISCOLL, *J. Phys. E.* **10,** 400 (1977).
18. B. D. BOSS, E. O. STEJSKAL, AND J. D. FERRY, *J. Phys. Chem.* **71,** 1501 (1967).
19. J. E. TANNER, KANG-JEN LIU, AND J. E. ANDERSON, *Macromolecules* **4,** 586 (1971).
20. J. E. TANNER, *Macromolecules* **4,** 748 (1971).
21. T. L. JAMES AND G. G. MCDONALD, *J. Magn. Reson.* **11,** 58 (1973).

JOURNAL OF MAGNETIC RESONANCE 40, 000–000 (1980)

Stable and Accurate Spin Echos in Pulsed Field Gradient NMR

In a recent paper von Meerwall *et al.* (*1*) suggest that pulsed gradient NMR requires an experienced operator who can visually locate the echo and correctly position it at $t = 2\tau$ by applying gradient pulse width corrections. Even with such corrections applied these authors find rf phase and envelope position instabilities in the echo. Similar effects have been mentioned by Tanner (*2*), who used manual addition and rejection of echos. Von Meerwall *et al.* adopt computer echo inspection and rejection in their system.

In building our system we identified four sources of echo phase and envelope instability. These are eddy-current-associated gradients, sample movement, field/frequency variations, and spurious gradient current stimulated by rf pulse radiation and other pickup (e.g., mains ac) on the sensing resistor of the current supply. Eddy currents are eliminated by using laminated plastic and Perspex construction in the probe, our 4.5-mm sample tubes are held firmly in a well-seated holding ring, and an external ^{2}D lock is used to minimize field/frequency instability. We suspect that the fourth item, the spurious gradient current associated with sensing resistor pickup, is overlooked in the apparatus of other workers and is the source of many of the problems mentioned in the literature. The switching system used in our apparatus (*3*) overcomes pickup effects by diverting any residual current through a dummy load when the desired gradient pulses are off. This system was developed because of the phase and envelope distortion and fluctuation present in our first apparatus, which employed conventional feedback switching (*4*). Using our switching system no pulse width correction is necessary in order to locate the echo at $t = 2\tau$ and automatic data accumulation takes place under conditions of near-perfect phase and envelope stability.

Figure 1 shows off-resonant ($\Delta\nu$ = 500 Hz) spin echos obtained for glycerol with and without gradient pulses (G = 1.35 T m^{-1} Δ = 15 msec, δ = 10 msec, 2τ = 30 msec). Application of the gradient pulse shifts the zero-phase point P by less than 50 μsec, representing a phase angle shift of less than 9°. In successive accumulations under the action of the gradient pulses, P is stable to $\lesssim$20 μsec ($\lesssim$4°). The echo envelope position shows a similar consistency. Another indication of the reliability of the experiment is given by the accuracy of the accumulated echo height. The consistency between the height after 20 accumulations and the height for a single accumulation is within the experimental noise ($\pm$2%). This order of stability is essential for samples with very low signal-to-noise ratios where echo observation and manipulation after each accumulation are impossible. This is the situation for a solution of 0.5% w/v polystyrene in carbon tetrachloride. We have been able to measure the diffusion coefficient of the polystyrene in such a solution to a precision of better than 5% (*3*), limited only by available signal to noise.

In conclusion we do not agree with von Meerwall *et al.* (*1*) and Cantor and Jonas (*5*), who suggest that D values cannot be obtained with the same pre-

0022-2364/80/000000-00$02.00/0
Copyright © 1980 by Academic Press, Inc.
All rights of reproduction in any form reserved.

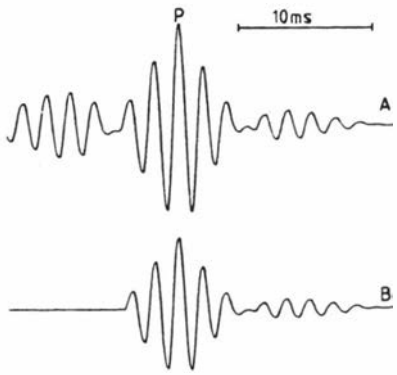


FIG. 1. Off-resonant ($\Delta\nu$ = 500 Hz) spin echos (2τ = 30 msec) obtained from glycerol. (A) No field gradient pulses. (B) G = 1.35 T m^{-1}, Δ = 15 msec, δ = 10 msec, d = 500 μsec. The symbolism is that of Ref. (*3*).

cision as relaxation times and give 5 to 10% as a typical reproducibility. The factor limiting reproducibility in an experiment which involves adding successive spin echo signals is the phenomenon of unstable echos. This in turn leads to a deterioration in experimental precision and accuracy. Echo distortion will also cause deterioration in accuracy. Once these problems are solved there is no reason why one should not obtain a precision and, by calibration with a standard molecular species, an accuracy similar to that associated with the steady gradient method. Harris *et al.* (*6*) have obtained a precision of better than 1% using the steady gradient method with water and benzene and we have demonstrated a similar capability with pulsed gradient NMR (*3*). In the slow diffusion region the precision should not significantly deteriorate. Figure 2 shows our echo attenuation plot for glycerol at 25°C. We obtain D = 2.15(4) × 10^{-12} m^2 sec^{-1}, which agrees well with the published value (*7*).

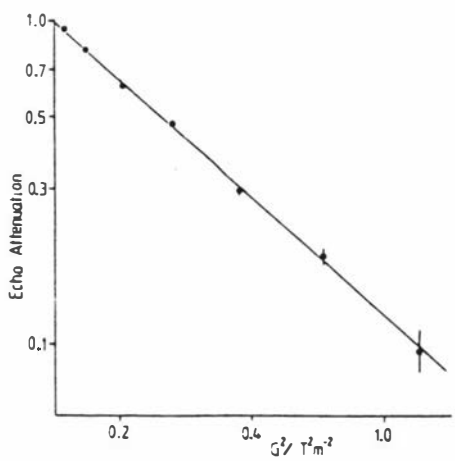


FIG. 2. Echo attenuation plot for glycerol at 25°C. 2τ = 60 msec. Δ = 30 msec, δ = 25 msec, d = 500 μsec.

REFERENCES

1. E. VON MEERWALL, R. D. BURGAN, AND R. D. FERGUSON, *J. Magn. Reson.* **34**, 339 (1979).
2. J. E. TANNER, Ph.D. dissertation, Department of Chemistry, University of Wisconsin, 1966.
3. P. T. CALLAGHAN, C. M. TROTTER, AND K. W. JOLLEY, *J. Magn. Reson.* **37**, 247 (1980).
4. G. B. MATSON, *Rev. Sci. Instrum.* **43**, 1504 (1971).
5. D. M. CANTOR AND J. JONAS, *J. Magn. Reson.* **28**, 157 (1977).
6. K. R. HARRIS, R. MILLS, P. J. BACK, AND D. S. WEBSTER, *J. Magn. Reson.* **29**, 473 (1978).
7. D. J. TOMLINSON, *Mol. Phys.* **25**, 735 (1972).

P. T. CALLAGHAN
K. W. JOLLEY
C. M. TROTTER

Department of Chemistry,
Biochemistry and Biophysics
Massey University
Palmerston North, New Zealand

Received December, 1979; revised March 27, 1980

Laser light scattering from concentrated solutions of polystyrene latex spheres: A comparative study

C. M. Trotter and D. N. Pinder

PROOF ONLY.

Department of Chemistry, Biochemistry and Biophysics, Massey University, Palmerston North, New Zealand
(Received 12 March 1980; accepted 2 June 1980)

Quasielastic light scattering was used to measure the mutual diffusion coefficient of polystyrene latex spheres over the concentration range 0.004 to 4.46 gm per 100 ml. Measurements were made at 25.0 °C in solutions of 0.01 M and 0.001 M sodium chloride, with several low sphere concentration measurements also being made in triply distilled water. The diffusion coefficient was found to be ionic strength dependent over the entire concentration range studied. Solutions of polystyrene spheres at moderate concentrations exhibit the phenomenon of multiple scattering. The available literature on multiple scattering is reviewed and criteria adopted for the reliable extraction of data from these solutions. The diffusion coefficients so obtained show substantial agreement with the macroscopic capillary penetration results of Anderson *et al.* The conclusion reached in this work is that quasielastic light scattering is able to provide a measure of the macroscopic mutual diffusion coefficient at moderate sphere concentrations and moderate ionic strengths. This conclusion is seen to be in accord with earlier QELS studies on cyanomethemoglobin and Bovine Serum Albumin, provided that a reassessment of available macroscopic diffusion data on these systems is undertaken.

INTRODUCTION

In recent years quasielastic light scattering spectroscopy (QELS) has been extensively used to study the diffusion of both random coil macromolecules in suitable solvents and small synthetic polystyrene latex spheres in water. In very dilute solutions intermolecular interactions may be neglected, and provided the random coil macromolecules are too small to engender internal mode contributions, the intensity autocorrelation function (IAF) of the scattered light decays as a single exponential with exponent $(-2D_0q^2)$, where D_0 is the infinite dilution translational diffusion coefficient of the macromolecules and q is the scattering vector.[1]

The diffusion of random coil polystyrene has been studied by various interferometric techniques, all of which measure the translational mutual diffusion coefficient D_M. Extrapolation of D_M to infinite dilution yields D_θ, and values for D_0 obtained by extrapolation of interferometry measurements are in good agreement with those derived from QELS studies.[2,3] Dilute solutions of small latex spheres of known diameter, also studied by QELS, yield self diffusion coefficients in good agreement with those predicted from the Stokes–Einstein equation.

Extension of the QELS technique to concentrated polymer solutions has been the subject of several investigations.[4–7] The simple QELS theory is not applicable to solutions when the macromolecular concentration is so large that macromolecular interactions cause the IAF to become multiexponential. In this case it has been suggested that a cumulant analysis[8,9] may be applied to the IAF, with the first cumulant being related to the translational mutual diffusion coefficient of the macromolecular solution through the relationship $\bar{\Gamma} = (-2D_{ML}q^2)$, where $\bar{\Gamma}$ is the first cumulant of the IAF and D_{ML} is the diffusion coefficient as determined by QELS. However, it is not certain that the diffusion coefficient determined by the essentially microscopic QELS technique, in the presence of particle interactions, can be identified with the classical macroscopic translational mutual diffusion coefficient D_M. In order to clarify the relationship between D_{ML} and D_M, several experimental investigations have been carried out.

Pusey *et al.* have used QELS to study the diffusion of monodisperse random coil polystyrene macromolecules in toluene as a function of concentration and compared D_{ML} with D_M values obtained from the wedge interferometry studies of Rehage.[10] The effects of the differing polymer molecular weights used in the comparison were partially offset by the different temperatures used in the QELS and interferometric studies. Both sets of diffusion data show the same behavior with concentration, suggesting that at moderate polymer concentrations D_{ML} can be identified with the macroscopic mutual diffusion coefficient. This conclusion has since been validated by the recent work of Roots *et al.*,[11] who, using the same molecular weight polystyrene as the earlier QELS study by Pusey *et al.*, obtained values for D_M in good agreement with the earlier D_{ML} determinations.

A comparison of D_M and D_{ML} has also been attempted for charged macromolecules. Alpert and Banks[6] have used QELS to study the diffusion of cyanomethemoglobin over a wide concentration range (up to protein volume fractions of about 0.4). The values of D_{ML} obtained showed only a small decrease with concentration, a result in sharp contrast to the rapid decrease of D_M with concentration found from the classical diffusion cell measurements of Keller *et al.*[12] Similar discrepancies were also found in a concentrated solution study of bovine serum albumin (BSA), where the QELS results of Phillies *et al.*[7] were again compared with diffusion cell measurements.[12] We leave a discussion of the apparent discrepancies between D_M and D_{ML} obtained for solutions of charged macromolecules until later in this paper.

Protein solutions are not, however, ideal systems for comparative studies. The difficulties of preparing monodisperse protein solutions are well known and samples with some degrees of polydispersity (normally dimers, trimers, etc.) are usually presented for study. Sample variability can also be a problem, particularly

in the case of BSA where investigations have shown that different samples of BSA, studied under identical conditions, can show variations in the diffusion coefficient of up to 10%.[13] (This variation has been ascribed to differences in the amount of fatty acid bound to the BSA.[14]) The complications of polydispersity and sample variability, together with possible protein aggregation effects and the dependence of protein charge on *p*H, all lead to uncertainties in the interpretation of comparative diffusion results. Polystyrene latex spheres would appear to be a more useful system for comparative studies because these synthetic spheres are monodisperse, relatively free from aggregation effects, and possess a fixed charge little affected by *p*H changes. The mutual diffusion coefficients of concentrated solutions of 0.091 μm spheres in 0.01 and 0.001*M* KCl can be obtained from the capillary penetration measurements of Anderson *et al.*[15]

This paper compares results obtained by QELS with those obtained by Anderson *et al.* For all measurements made, we have used the independence of the measured diffusion coefficient with q^2 as the criterion of experimental data reliability. Attempts have been made to ensure that multiple scattering has not affected the quantities derived from the IAF. The reproducibility of data has been examined to ensure that possible aggregation effects lie within the stated error bounds of the experiments.

SAMPLE PREPARATION AND INSTRUMENTATION

Aqueous suspensions of polystyrene latex spheres of nominal diameter of 0.085 μm and nominal concentration of 10 g per 100 ml of solution had previously been obtained from the Dow Chemical Company. The preparation of experimental solutions utilized the dialysis scheme of Anderson *et al.* except that solution ionic strength was provided by sodium chloride, instead of potassium chloride, to avoid the formation of the insoluble potassium salt of any surfactant not bound to the spheres. The surfactant used was sodium dodecyl sulfate (SDS), supplied by B.D.H. Chemicals (U.K.). Latex sphere solution concentrations in this paper will be given in grams of latex spheres per 100 ml of solution, denoted by a % symbol.

The concentrated solutions (≳0.5%) were prepared by forming a 5% solution at the approximate ionic strength required, and then dialyzing this solution for 48 h against the appropriate 0.001 or 0.01*M* sodium chloride solution. SDS was added at a level of 0.022 g per 100 ml to both the 5% and the sodium chloride dialysis solutions to obviate coagulation of the spheres. After dialysis, the following solutions of spheres were formed: ~2% (0.001 and 0.01*M*), ~4% (0.001*M*), and ~2.5% (0.01*M*). All solutions were stored at 4°C until used and to further minimize aggregation effects, experiments on the 0.001*M* solutions were completed before dialysis of the 0.01*M* solution was started. The dilute solutions (≲0.1%) were formed by simple dilution of the Dow aqueous suspension with 0.001 or 0.01*M* sodium chloride solutions, as appropriate.

Light scattering samples were prepared by filtering the sample solutions through a prewashed and dried 0.22 μm Millipore filter into a sample cell of 1.00 or 0.50 cm path length. These sample cells had previously been well rinsed with 0.22 μm filtered redistilled water and subsequently dried *in vacuo*. Intermediate sample concentrations were obtained by diluting the ~2% or ~2.5% solutions with a filtered sodium chloride/SDS solution which was added directly to the sample cell. Sample cells were weighed at each stage so that accurate concentration calculations could be made. All solution transfers, dilutions, and the final cell rinsing steps were carried out in an atmosphere of 0.22 μm filtered air.

Sample concentrations were determined by UV spectrophotometry at a wavelength at 265 nm with a Shimadzu MPS-5000 spectrophotometer. Absorbance readings were compared with a calibration curve prepared by diluting the neat Dow latex suspension. The concentration of the Dow latex suspension, determined by drying 1 ml of neat solution to constant weight at 60°C, was 10.15% ± 0.05%. Absorbance readings for duplicate samples were reproducible to about 0.5 / Solution concentrations quoted in this paper could therefore contain an error of up to 2 percent. percent.

The experiments were performed using a Spectra Physics 125A He–Ne laser in conjunction with a 4300 spectrometer (Precision Devices, Malvern, U.K.) and an ITT FW130 photomultiplier. The index matching fluid in the thermal bath surrounding the sample was 0.22 μm filtered water to which the antibacterial agent sodium azide had been added at a level of 0.04 g per 100 ml. This additive has been very effective in maintaining the cleanliness of the index matching medium. The temperature of the thermal bath was regulated to better than ±0.03°C by a Precision Devices temperature controller.

Data processing was carried out by a 48 channel clipping and scaling digital correlator,[16] which also includes three additional channels to monitor total counts, clipped counts, and the number of elapsed sample times. The monitor channels were used to calculate the theoretical background and so obtain the normalized intensity autocorrelation function (nIAF). The accumulation of the IAF was observed on an oscilloscope, and the correlator was also interfaced to a PDP 11-03 digital computer for data analysis purposes. Plots of the IAF were obtained using a computer controlled Hewlett-Packard 7015B chart recorder.

The samples prepared in the manner outlined earlier generally showed such low dust levels that experiments could be performed at forward scattering angles down to 15° (see Figs. 2, 4, and 5). For those solutions which contained the occasional dust particle an automated data rejection scheme was used to delete any incoming data with an abnormally high average count rate. Full details of this rejection scheme have been given in a recent paper.[16]

RESULTS AND DISCUSSION

Multiple scattering effects

The interpretation of data collected from concentrated solutions of polystyrene spheres is complicated by the

presence of significant amounts of multiply scattered light. An additional complication, long range electrostatic interactions of the type previously studied by Brown *et al.*[17] and Dalberg *et al.*,[18] should be avoided in this work since the concentrated samples of spheres have been studied in solutions of moderate ionic strength. However, the addition of salts to a solution enhances the possibility of sphere aggregation and care must be exercised in the interpretation of data collected from such solutions.

The interpretation of QELS data collected from solutions displaying multiple scattering has been discussed in a number of recent theoretical and experimental studies.[19–22] The theoretical predictions have allowed corrections to be made to the initial decay of an IAF, obtained from a system of noninteracting Brownian particles,[18] when the scattered light has suffered up to four scattering events. The theoretical treatment has not yet been extended to include the effects of multiple scattering on the long time part of the IAF. However, the experimental studies of several authors have indicated that the long time part of the IAF is unaffected by multiple scattering.[22,23] We now consider the available experimental evidence so that criteria can be established for the interpretation of data collected in the presence of multiple scattering.

Pusey[22] has concluded that the major effect of multiply scattered light arising from the primary scattering volume is to add a rapid decay, characteristic of such light, to the slower decay associated with single scattering. The IAF thus contains a fast initial decay impressed upon the single exponential decay characteristic of singly scattered events. When the ratio of singly to multiply scattered light is small it is difficult to resolve these two processes. The ease of resolution of the two exponential decays also depends on the scattering angle as the two decay rates do not exhibit the same angular dependence. The initial decay rate has only a small angular dependence, showing less than a 20% variation as the scattering angle (θ) varies from 160° to 20°.[22]

Colby *et al.*[19] have also investigated the behavior of the initial decay rate of the IAF obtained from multiply scattering solutions of noninteracting polystyrene spheres. The decay rate exhibited a marked nonlinear dependence on q^2, in contrast to the linear dependence expected from singly scattering, noninteracting solutions of spheres. It was also found that at a given scattering angle the initial decay rate of a multiply scattering solution was dependent on the particular cell path length used in the study of the solution.

Multiple scattering also gives rise to a scattering volume which is larger than that encountered in a singly scattered experiment. For the scattering geometry employed in the Malvern 4300 spectrometer this results in the illumination of several coherence areas at the photomultiplier.[22] The effect of accepting light over several coherence areas is to reduce the signal to noise ratio of the detected scattered light; however, the decay rates of the IAF remain unchanged.

We may summarize the above observations as:

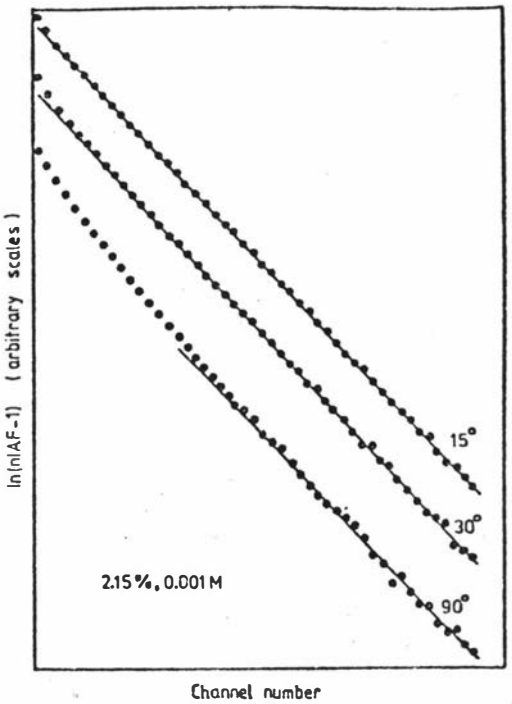


FIG. 1. Plots of ln(nIAF − 1) showing the presence of long and short decays in the nIAF, for the sample 2.15% in 0.001*M* sodium chloride. The long decay exhibits single exponential behavior.

The effect of moderate amounts of multiply scattered light on the IAF of a monodisperse polystyrene sphere solution is to introduce an additional fast decay to the longer, single exponential decay associated with single scattering. The long time decay, if resolvable, may be analyzed according to usual QELS theories. Analysis of the initial decay of the IAF in systems where multiple scattering is known to exist shows that this decay rate is not a linear function of q^2 [or equivalently $\sin^2(\theta/2)$]. Conversely, quantities derived from a single exponential decay rate exhibiting a linear q^2 dependence can be considered free of multiple scattering effects. A path length independent decay rate also ensures that multiple scattering effects are absent.

Data analysis

In this section we discuss, as an example, the data obtained from the 2.15% polystyrene sphere solution in 0.001*M* sodium chloride. This sample exhibits the complications typically encountered in the interpretation of data from the concentrated solutions of spheres studied in this paper. The theoretical background has been used to obtain the nIAF for all samples studied.

The 2.15% sample was studied in a 1.00 cm path length cell and visual inspection indicated severe multiple scattering; indeed the laser beam was attenuated to approximately 3% of the incident beam intensity on passage through the sample cell. Several plots of ln(nIAF-1) versus channel number for the 2.15% sample are shown in Fig. 1. Despite the intense multiple scattering associated with the 2.15% sample, it should be noted that the

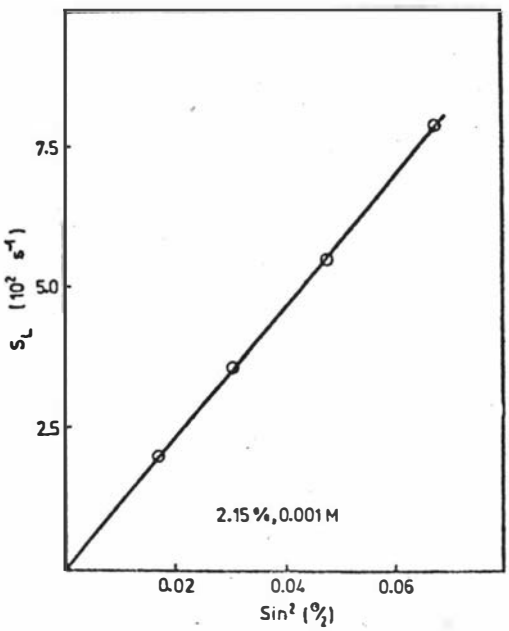


FIG. 2. Plot showing the linear dependence of the long time decay rate (S_L) on $\sin^2(\theta/2)$ for the sample 2.15% in 0.001M sodium chloride. S_L has been obtained from the long time part of a ln(nIAF − 1) versus time graph.

nIAFs
low angle | exhibit a short initial decay followed by a longer, single exponential decay. We associated this longer decay with single scattered events.

The count rates observed for this sample were high although the signal to noise ratio was much poorer than would ordinarily be expected of each count rates. From this we conclude that most of the multiply scattered light was uncorrelated and so did not mask the small amount of coherent singly scattered light present. A similar conclusion was reached by Chu *et al.*[23] in studies of critical opalescence in binary solutions. At larger scattering angles it was more difficult to measure the long time decay rate owing to decreasing amounts of singly scattered light and the poorer resolution between the long and short decays present in the IAF. Figure 1 illustrates these trends and indicates that the long and short decays can not be reliably separated at a scattering angle of 90°. Only data displaying two clearly separable components have been analyzed.

TABLE I. Details of the data analysis for the sample 2.15% in 0.001M sodium chloride. Only the low angle IAF's show two clearly resolvable exponentials. The values of $\mu_2/\bar{\Gamma}^2$ are small enough to consider the long time part of the IAF as being represented by a single exponential decay.[8]

θ	Channels analyzed	$2D_Lq^2$	$\mu_2/\bar{\Gamma}^2$	D_L (10^{-12} m^2s^{-1})
15°	8–51	−203	0.020	8.49
20°	9–51	−360	0.018	8.50
25°	10–51	−550	0.012	8.36
30°	12–51	−732	0.025	8.42

The long time decay rate S_L is the slope of the long time part of a plot of ln(nIAF-1) versus time. The assumption that the long, single exponential decay is related to a singly scattered process is supported by the linear dependence of S_L on $\sin^2(\theta/2)$, shown in Fig. 2. Details of the data analysis for the 2.15% sample are presented in Table I. The quantity D_L has been calculated assuming the long time decay of the nIAF is a single exponential with exponent $(-2D_Lq^2)$. As Table I shows, there is no systematic variation in the quantity D_L with angle as would be expected of samples exhibiting aggregation effects. Although the range of angles over which the 2.15% sample was studied was rather small, more dilute samples with a much extended angular range show good agreement between high and low angle values of the observed diffusion coefficient (see Fig. 4).

Concentrated solution results

The observed D_L values for solutions ≥ 0.5% are presented in Fig. 3, with the angular dependence of the long time decay of the nIAF's shown in Figs. 4 and 5 for representative samples. In all cases (except the 4.46% sample) the long time decay is well represented by a single exponential. Calculations show that the average separation of spheres in the 4.46% sample is 0.1 μm (about a sphere diameter) and the influence of particle interactions is reflected in a multiexponential long time decay. To minimize multiple scattering effects, the 4.46% sample was studied in a 0.5 cm path length cell,

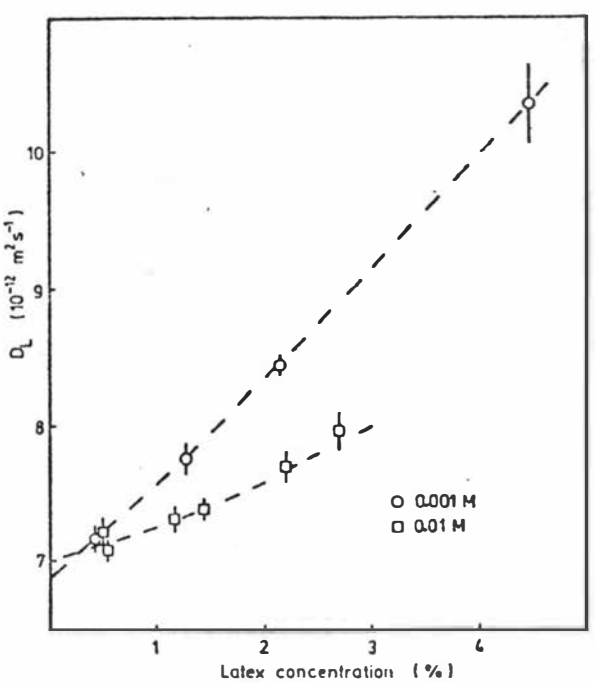


FIG. 3. The concentration dependence of the diffusion coefficient determined by QELS assuming the long time slope of a ln(nIAF − 1) versus time plot is given by $(-2D_Lq^2)$. The value of D_L shown for a particular concentration was obtained by calculating D_L at each of the investigated angles and averaging the results. The errors shown represent the spread of experimental values.

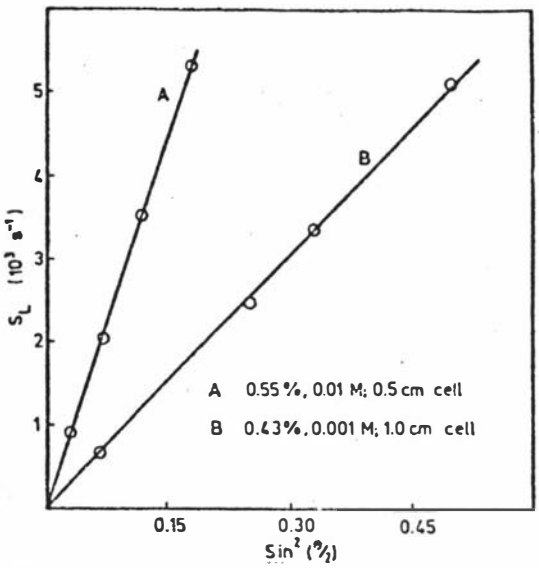


FIG. 4. Plots showing the linear dependence of S_L on $\sin^2(\theta/2)$ for representative solutions. The vertical scale shown has been divided by three when plotting the results obtained for solution A.

and the method of cumulants was used to extract the initial decay rate of the long time part of the nIAF after channels containing the multiple scattering data were discounted. The difficulty of estimating the number of channels to analyze as the true long time part of the nIAF is reflected in the increased error placed on the value of D_L for this concentration.

Figures 4 and 5 indicate that the long time decays were not affected by multiple scattering. To further confirm that multiple scattering did not affect the measured value of D_L a 2.5%, 0.01M solution was prepared from freshly dialyzed stock, and studied in a 0.50 cm path length, 1 cm wide (frosted sides) spectrophotometer cell. This solution was also diluted to form the 1.17% and 0.55% solutions. The D_L values determined for these solutions are shown in Fig. 3 and are in good agreement with the trends exemplified by the 2.5%, 1.44%, and 0.51% solutions in 0.01M sodium chloride studied earlier in a 1.00 cm path length cell. The diffusion coefficient of the 0.55% sample showed no change when measured 4 days after the original determination, indicating that sample aggregation is not a problem in this study. (The linearity of the plots in Figs. 4 and 5 also indicates an absence of aggregation effects.)

Two concentrations [0.43% (0.001M NaCl) and 1.44% (0.01M NaCl)] were also studied at 20°C. The differences in the experimental values for D_L at the two temperatures are adequately described by the change in solvent viscosity. At infinite dilution the Stokes–Einstein equation indicates that the diffusion coefficient is proportional to the reciprocal of the solvent viscosity, and the fact that the same proportionality exists for both the 1.44% and the 0.43% samples indicates that solvent viscosity still provides the dominant activation energy requirement at quite high latex sphere concentrations.

Dilute solution results

The investigation of this regime was initially attempted using samples diluted from the original dialyzed solutions, which had been stored at 4°C for several weeks. However, the reproducibility of such samples showed variations of up to ±4% and after 4 weeks some of these samples showed aggregates visible to the naked eye. The study of these samples was abandoned.

Figure 6 presents the results obtained for samples prepared by a simple dilution of the original Dow latex sphere suspension. To examine the reproducibility of the diffusion coefficients obtained in the dilute regime, most samples were prepared in the following manner: A given latex sphere concentration was made up in either water or 0.001M sodium chloride, 1 ml of this solution was accurately added to a sample cell, and the diffusion coefficient of the sample was measured. 10 μl of a previously filtered sodium chloride solution was then added to raise the ionic strength to the desired value without appreciably altering the concentration. Such families of samples prepared by the addition of sodium chloride, or by subsequent intracell dilution, are indicated in Fig. 6 by lettered subscripts. Multiple scattering effects were not apparent in any of the IAF's obtained from these dilute solutions. The range of scattering angles studied was 30°–105° in all cases, and the error bars shown in Fig. 6 indicate the spread of experimental results.

Table II presents parameters for latex sphere concentrations of 0.004% and 0.024%. The hydrodynamic radius R_H was calculated from the Stokes–Einstein equation, and R_s is the calculated mean latex sphere separation. The experimental rms displacement of a sphere $\langle r^2 \rangle^{1/2}$ may be obtained from

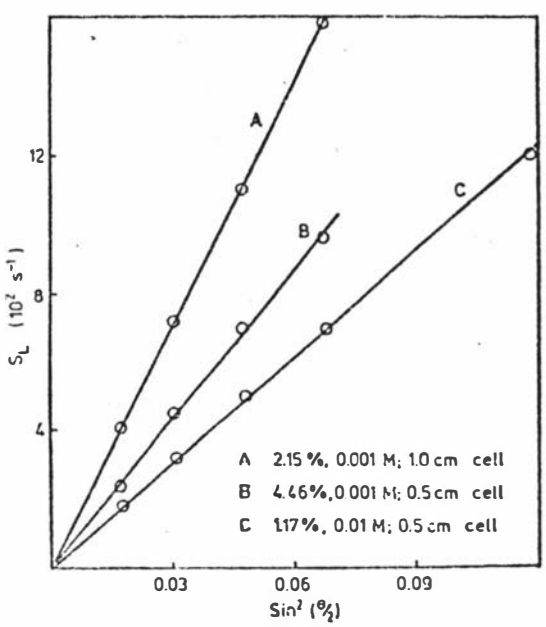


FIG. 5. Plots showing the linear dependence of S_L on $\sin^2(\theta/2)$ for representative solutions. The vertical scale shown has been divided by two when plotting the results obtained for solution A.

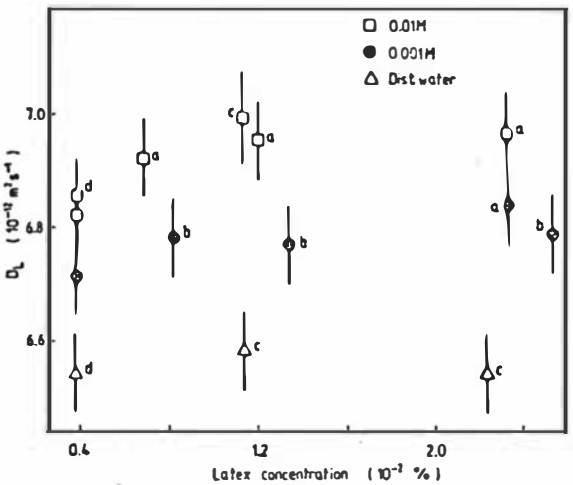


FIG. 6. The dilute regime latex sphere diffusion coefficient as a function of sphere concentration and ionic strength. Families of samples generated from a common parent solution are denoted by lettered subscripts. These solutions were formed either by intracell dilution with solvent, or by the addition of 10 μl ml^{-1} quantities of an appropriate, concentrated salt solution. The errors shown include both the spread and reproducibility of the results.

$$\langle r^2 \rangle = 6 D_0 t \,, \qquad (1)$$

where t is the experimental observation time. In a QELS experiment, t is the time required for a nIAF to decay to the $1/e$ point.

Interparticle collisions are not expected to play a major part in diffusion at these concentrations, for even at the largest concentrations considered here $\langle r^2 \rangle^{1/2}/R_S < 1/10$. Further, Fig. 6 indicates that for the lowest ionic strength solutions the diffusion coefficient is not concentration dependent in the dilute regime (within the approximately 1% errors) and the spheres may be considered free of electrostatic interactions. However, the diffusion coefficient of the spheres is noticeably ionic strength dependent, whereas the diffusion of hard spheres is not expected to be ionic strength dependent at infinite dilution.[24] This suggests that the experimentally determined ionic strength dependence of the diffusion coefficient observed here may be due to a physical size change of the spheres, possibly induced by shielding of the surface charges from one another at moderate ionic strengths. Further, increasing the ionic strength above 0.01M in sodium chloride did not increase the measured diffusion coefficient. Such a saturation effect would be expected if electrostatic shielding were occurring.

We may examine the possibility of shielding effects causing changes in sphere size by calculating the change in radius which occurs when the strain, caused by electrostatic interactions between sulfate groups located on the surface of a sphere, is relaxed by shielding of these groups. Using a value for the surface charge density of 10 μC cm^{-2},[15] a permittivity of $2.5\varepsilon_0$,[25] and a bulk modulus of 3×10^9,[25] the calculated change in sphere radius is 2.5% for the transition from a fully strained to a fully relaxed state. Such a change is close to the experimentally observed change of (5±2) percent. However, it should be noted that the permittivity and bulk modulus values quoted are for disordered bulk polystyrene. We have used these in the absence of more appropriate values for charged latex spheres. In addition, the bulk modulus is unlikely to remain constant up to strains of several percent, and thus a smaller value of the bulk modulus is probably more appropriate. We further note that although solvent mobility tends to preclude solvent ordering in the region about a charged latex sphere, the present investigation does not allow us to completely dismiss possible solvent ordering effects as being responsible for the trends detailed in Fig. 6.

The diameter of the spheres studied in this work is given by the manufacturer as 0.085 μm with a standard deviation of 0.0055 μm. The QELS experiment yields a diameter of 0.075 ± 0.001 μm in distilled water. Other authors have reported similar discrepancies between the quoted sphere diameter and a Stokes–Einstein diameter obtained from QELS measurements.[13,26] However, for completeness samples of the nominally 0.085 μm spheres were examined by transmission electron microscope and the moments of the radius distribution were determined. An average diameter, appropriately weighted for a QELS experiment, was then calculated according to the formula of Brown *et al.*[17] The calculated diameter was 0.075 μm, with an estimated random error of 3%, and shows excellent agreement with the Stokes–Einstein value obtained from the high dilution QELS results (see Table II).

Finally, the variation of diffusion coefficient with ionic strength in the very dilute regime is not peculiar to the nominally 0.085 μm sample of spheres. A cursory study of a dilute solution of 0.091 μm diameter spheres showed that a change of approximately 3 percent occurred in the diffusion coefficient upon changing the ionic strength from that of distilled water to 0.01M in sodium chloride. An extended study of the 0.091 μm spheres was precluded owing to a paucity of available sample.

TABLE II. Details of the diffusion coefficient determined by QELS at latex sphere concentrations of 0.004% and ~0.023%, at various ionic strengths. R_H was calculated from the Stokes–Einstein equation, and R_S is the calculated mean intersphere spacing. The root mean square displacement $\langle r^2 \rangle^{1/2}$ was calculated from Eq. (1).

Solvent	Distilled water	0.01M NaCl
Latex conc.	0.004% 0.022%	0.004% 0.023%
D_0 (10^{-12} m^2 s^{-1})	6.52 ± 0.07 6.54 ± 0.07	6.87 ± 0.07 6.96 ± 0.08
R_H (μm)	0.0375 0.0374	0.0357 0.0352
R_S (μm)	1.8 1.0	1.8 1.0
$\langle r^2 \rangle^{1/2}$ (μm)	0.077 0.077	0.079 0.080

COMPARISON OF RESULTS

Theoretical predictions of diffusion behavior

The original aim of this paper was to compare the apparent diffusion coefficient obtained by QELS with mutual diffusion coefficients determined by the observation of the relaxation of a macroscopic concentration gradient, as reported by Anderson *et al.* Unfortunately, the spheres used in the QELS study have a diameter 20% smaller than the spheres of nominal diameter 0.091 μm used by Anderson *et al.* A further difference is that the effective surfactant concentration encountered in this work is expected to be somewhat higher than that encountered in the solutions of Anderson *et al.* because surfactant precipitation was prevented in the QELS study by employing sodium chloride as the source of ionic strength. Since the adsorption of surfactant ions can affect the surface charge density of the spheres,[22] the surface charge densities of the 0.075 and 0.091 μm spheres probably differ. Thus, a direct comparison of results is prevented and instead we seek interpretation through available theory.

The theoretical work available assumes the sphere concentration to be so low that only binary interactions need be considered, and the concentration dependence of the diffusion coefficient can be represented by the truncated virial form[15]

$$D(c) = D_0(1 + kc) .$$

There are at least two distinct aspects to any theory which seeks to account for the rate of change k of the mutual diffusion coefficient with concentration of charged spherical particles.[15] The first is an accurate expression for the interaction energy E between two charged spheres in an electrolyte in terms of the assumed charge density on the spheres. The second is an expression for k in terms of the interaction energy. For a given interaction energy, the theories of both Anderson and Reed[28] and Batchelor[29] predict similar values for k. When examining solutions of BSA, and also solutions of polystyrene spheres, the particular expressions chosen by Anderson *et al.* to represent the interaction energy yield theoretical values for k which are in quantitative agreement with experiment only at high ionic strengths (0.01M). For the polystyrene spheres, Anderson *et al.*[30] used an expression for the interaction energy between two flat plates as an approximation to that between two large spheres. However, for ionic strengths as low as 0.001M such an approximation is invalid.[31]

There are alternative expressions for the interaction energy between charged spheres. When considering the low ionic strength measurements we have chosen to use that developed by Stigter and Hill,[32] which is based on the work of Hoskin[33] and Verwey and Overbeek,[34] i.e.,

$$E = \varepsilon a^2 \frac{\psi_0^2 f}{\delta^2 R} \exp\{-\kappa(R - 2a)\} \qquad (2)$$

where the symbols have their usual meanings,[15,32] and δ and f can be obtained from tables in Hoskin, and Verwey and Overbeek. Even this expression for E is only approximate and best represents the interaction energy for larger rather than smaller particle separations; consequently, the expression pertains to only dilute solution of charged spheres.

TABLE III. Theoretical and experimental values for k. The range of values quoted for $k_{theor.}$ corresponds to a range of surface charge densities from 3 to 10 μC cm^{-2}.

Salt concentration (M)	Sphere diameter (μm)	$k_{expt.}$ (cm^3 g^{-1})	$k_{theor.}$ (cm^3 g^{-1}) a	b	c
0.001[d]	0.075	11.7 ± 0.4	35–41	34–41	24–26[d]
0.001	0.091	18	24–30	26–30	20–22
0.01	0.075	5.5 ± 0.6	4.3–5.5	5.6–6.7	···
0.01	0.091	5.0	3.3–4.2	4.9–5.7	···

[a] Model of Anderson and Reed,[15,27] and interaction energy of Hogg *et al.*[30]
[b] Model of Batchelor,[28] and interaction energy of Hogg *et al.*[30]
[c] Model of Batchelor,[28] and interaction energy of Stigter and Hill.[32]
[d] See the discussion in the text regarding the validity of these values.

Comparison of results with theory

A summary of both QELS and capillary penetration (Anderson *et al.*) results together with various theoretical predictions is presented in Table III. For each sphere size and ionic strength we have calculated a range of theoretical values for k ($k_{theor.}$) since a range of surface charge densities appears in the literature for polystyrene spheres. Following Anderson *et al.*, we have calculated values for $k_{theor.}$ for surface charge densities ranging from 3 to 10 μC cm^{-2} (although values as low as 1.2 μC cm^{-2} and even 0.47 μC cm^{-2} have been reported[17,35]). These values for the surface charge density (with the exception of the 0.47 μC cm^{-2} value) have been obtained from potentiometric titration studies of latex spheres in extremely low ionic strength solutions.[36] When any macroion is placed in a solution of moderate ionic strength, however, a layer of counterions (the Stern layer) becomes absorbed to the macroion surface.[37] The surface charge density appropriate for inclusion in Eq. (2) is thus not well defined at moderate ionic strength since the extent of counterion absorption is not known (although charge density values approaching 10 μC cm^{-2} would not be expected to be appropriate). It would be rather difficult to test the accuracy of Eq. (2), although, as will shortly be discussed, Eq. (2) is useful in the comparative situation under consideration in this work.

The high ionic strength solutions

The QELS results for the 0.075 μm latex spheres in 0.01M solutions are summarized in Table III (see also Fig. 7). The capillary penetration results of Anderson *et al.* are also shown in Table III, together with various theoretical predictions for the value of k. As the data in Table III show, both the QELS and capillary penetration results are in quantitative agreement with the values of $k_{theor.}$ predicted by the theory of Batchelor[29] at a surface charge density of 3 μC cm^{-2}.

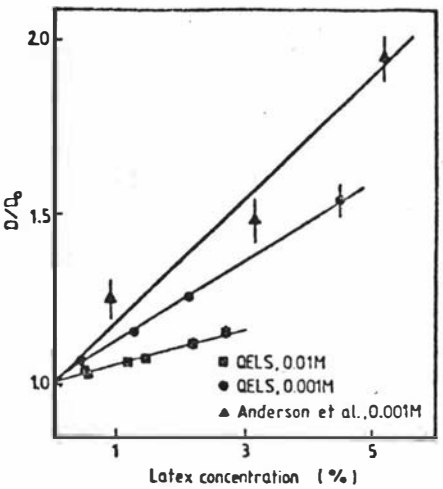


FIG. 7. The diffusion coefficients as determined by QELS show a linear concentration dependence in both 0.001 and 0.01M sodium chloride solutions. The D_0 value used was obtained from the data in Fig. 6. The results of Anderson *et al.* are also shown for 0.091 μm latex spheres in 0.001M potassium chloride. These results were calculated from experimental data[15,37] using Eq. (13) of Ref. 15, together with the D_0 value from Fig. 6 of Ref. 15. The errors shown indicate the spread of experimental values for both the QELS results and the results of Anderson *et al.*[15,37] The experimental results of Anderson *et al.* for the 0.01M solutions are in agreement with the QELS results and so are not reproduced here.

The surface charge densities of the two sets of spheres could differ since different surfactant concentrations and spheres of different diameters were utilized in the QELS and capillary penetration studies. Also, the sphere surface charge density has been found to vary with sphere radius, although the radius differences encountered in this comparison are not expected to result in significant surface charge variations.[36] A surfactant, which can also influence the surface charge density of the spheres, was used at a concentration of 0.0007M in both the QELS and capillary penetration studies. In the QELS study surfactant ions would have become absorbed onto the sphere surface and so increased the effective surface charge density. In the capillary penetration investigation, the insoluble potassium salt of SDS would have formed, with a resultant decrease in the overall ionic strength of the solution, and increased sphere interaction. However, it is the absorption of counterions which determines the effective surface charge density of macroions in solution,[27] with the ionic strength of the solution determining the magnitude of the electrostatic interaction energy for a given latex sphere charge. Only small variations in the total ionic strength of these concentrated salt solutions (0.01M) would result from surfactant precipitation and so it is to be expected that the spheres used in the capillary penetration study would experience electrostatic interactions similar to the latex spheres used in the QELS study. It is appropriate, therefore, that the same value of the surface charge density (3 μC cm^{-2}) should yield values of $k_{theor.}$ in quantitative agreement with both QELS and capillary penetration results.

The above discussion indicates that QELS is able to provide a measure of the macroscopic mutual diffusion coefficient in high ionic strength solutions, up to sphere concentrations of ~3%. Theoretical justification of the QELS results aside, we note that the QELS results satisfy our intuitive expectations of the diffusion behavior of charged spheres in a good charge screening medium, i.e., the smaller spheres used in the QELS study should exhibit a value for k greater than or equal to the value of k obtained for the larger spheres studied by Anderson *et al.*

The low ionic strength solutions

Theoretical predictions of k for latex spheres in low ionic strength solutions are shown in Table III. The Debye–Hückel shielding length is much larger (~0.01 μm) in 0.001M salt solutions, so demanding a much more accurate formulation of the electrostatic interaction energy term than in the case of 0.01M solutions, if quantitative predictions of $k_{theor.}$ are required. Thus, as expected, there are variations in both the range and magnitude of $k_{theor.}$ obtained for a given range of surface charge density, depending upon the expression used for the interaction energy. Table III also contains the capillary penetration results of Anderson *et al.* for the 0.091 μm spheres of 0.001M solutions. The experimental results of Anderson *et al.* (see Fig. 7) for this ionic strength are quite scattered, but show reasonable agreement with theory when the interaction energy is calculated using Eq. (2).

The QELS results are also presented in Table III. The individual experimental points show little scatter (see Fig. 7) but are in much poorer agreement with the theoretical predictions. This poor agreement could indicate that the QELS technique fails to measure the mutual diffusion coefficient of charged spheres in low ionic strength solutions, whereas the technique apparently does measure this diffusion coefficient in high ionic strength solutions. However, the diffusion coefficient measured by the QELS technique is independent of scattering angle and this is usually indicative of a single diffusive process, so possible alternative explanations for this poor agreement with theory are investigated.

The ionic strength of the solutions used in the low ionic strength QELS study contains important contributions from both sodium chloride (0.001M) and SDS (0.0007M) whereas the formation of insoluble potassium dodecyl sulfate in the capillary penetration study would have resulted in only a salt solution of 0.001M providing solution ionic strength. The increased ionic strength of the QELS study can be accounted for by calculating a new value for $k_{theor.}$.

Using Eq. (2) to represent the electrostatic interaction term (together with a surface charge density of 3 μC cm^{-2}, and approximating the electrolyte concentration as 0.002M), a value of 14.3 was obtained for $k_{theor.}$ for the spheres used in the QELS study. This clearly indicates that the experimental value for k obtained for the 0.075 μm spheres should be smaller than the value of k for the 0.091 μm spheres for the solution conditions encountered in this comparison. We note that an

important parameter which must be assumed in these calculations is the surface charge density on the spheres. The magnitude of this parameter is not well defined and it is strongly dependent on the solution conditions. The charged surfactant absorbed on the 0.075 μm spheres would tend to increase the surface charge density (with respect to the 0.091 μm spheres) although the resultant increase in the hydrophobic nature of the sphere surface caused by surfactant should aid counterion absorption,[27] and so serve to reduce the sphere charge. The higher effective ionic strength encountered in the QELS study probably further aids counterion absorption. In view of these contributing factors the 20% difference which exists between the experimental and theoretical values for k for the 0.075 μm spheres is not considered serious. (A 10% difference also exists between $k_{theor.}$ and the experimental value for k obtained for the 0.091 μm spheres.)

Comparison with other work

It is appropriate at this stage to consider the earlier comparative studies carried out on cyanomethemoglobin and BSA, where results from QELS experiments were compared with the diffusion cell data of Keller *et al.*[6,7,12] Those comparisons indicated that the QELS and macroscopic determinations of the mutual diffusion coefficient were apparently in marked disagreement at large protein concentrations. However, the work of Keller *et al.* has been called into some question by Kitchen *et al.*,[38] who caution that a systematic error may have been present in the mutual diffusion coefficient determinations.

In the case of BSA, the concentration dependence of both the mutual and self diffusion coefficients has been experimentally determined in 0.2M sodium chloride solutions at pH ≃ 5.4[39] by Kitchen *et al.* These results can be used as alternative macroscopic measurements with which to compare the earlier QELS study[7] of BSA diffusion in 0.25M solutions.

Kitchen *et al.* have determined the self-diffusion coefficient of BSA by a radiotracer–capillary–penetration technique which has yielded values in good agreement with independent determinations in 0.1M solutions at pH ≃ 4.7.[12] Such agreement is expected between self-diffusion coefficients determined at the different pH's and ionic strengths because the conformation of BSA does not change significantly over the pH range 4.5–11.0,[40] and the differences in the viscosities of the 0.2 and 0.1M salt solutions used in the two investigations are also too small to appreciably influence self-diffusion. The mutual diffusion data presented by Kitchen *et al.* were obtained by utilizing two independent techniques (a capillary penetration and an ultracentrifugation method) which yielded values for the mutual diffusion coefficient which were in agreement within the precision of the experiments. Thus, both the self- and mutual diffusion coefficient data of Kitchen *et al.* appear to be reliable.

Several points of interest arise from the work of Kitchen *et al.* First it was found that D_M exhibited only a very weak concentration dependence at this pH. Second, Kitchen *et al.* found that values of the mutual and self-diffusion coefficients were related within the precision of the experiments by the equation

$$D_M = D_S \left(\frac{\delta\pi}{\delta c}\right)_{p,T} (1 - \Phi) , \qquad (4)$$

where D_S is the self diffusion coefficient, Φ is the volume fraction, and $(\delta\pi/\delta c)_{p,T}$ is the isothermal osmotic compressibility which can be obtained from the work of Scatchard *et al.*[41] Equation (4) can also be used, together with suitable values for D_S and $(\delta\pi/\delta c)_{p,T}$,[12,41] to predict values of D_M for the experimental conditions encountered in the earlier QELS study of BSA diffusion.[7] Within the expected errors of the comparison, the D_{ML} values obtained by QELS are in agreement with values of D_M predicted from Eq. (4) over the entire pH range studied (pH 4.5–7.6) in the QELS investigation.[7,42] Thus, when values of D_{ML} obtained from the QELS study of Phillies *et al.* are compared with macroscopic D_M determinations (both experimental and theoretical) derived from the work of Kitchen *et al.*, good agreement is obtained.

CONCLUSIONS

Concentrated solutions of polystyrene spheres at moderate ionic strength exhibit IAF's which are characterized by a short, initial decay followed by a longer, single exponential decay. A review of earlier studies indicates that the short decay is attributable to multiple scattering. Invoking single scattered theory to analyze the long time part of the IAF yields a unique, reproducible diffusion coefficient which exhibits an angular independence characteristic of a simple Brownian diffusion process. The diffusion coefficient so determined is highly ionic strength dependent, while a dilute solution study indicates that the high dilution diffusion coefficient is also ionic strength dependent.

A direct comparison of the concentration dependence of the latex sphere diffusion coefficient determined by QELS with capillary penetration data is prevented, owing to the different diameter spheres and different effective ionic strengths used in the QELS and capillary penetration studies. However, there exist several theories which predict values for the change in the macroscopic mutual diffusion coefficient with concentration. These theories are formulated in terms of the macroion radius and solution ionic strength, and predict values for k in good agreement with the macroscopic diffusion data of Anderson *et al.* These same theories predict values for k which are also in substantial agreement with the experimental values of k obtained from the QELS study, indicating that QELS is probably able to provide a value for the macroscopic mutual diffusion coefficient of latex spheres in solutions of moderate ionic strength.

Earlier comparisons of QELS and macroscopic diffusion coefficient determinations have been carried out using solutions of BSA,[7,12] and apparent disagreement was found between QELS and macroscopic measurements at high protein concentrations. However, if the QELS data are compared with more recent, independently verifiable values for the macroscopic mutual diffusion coefficient,[38] good agreement is found. This indicates that

the QELS technique also provides a measure of D_M for BSA solutions.

Finally, if further comparative experiments are to be performed using polystyrene latex spheres in moderate ionic strength solutions, every effort should be made to ensure that the QELS and classical studies are conducted on a common sample of spheres, under the same solution conditions. If SDS is to be used as a surfactant, sodium chloride and not potassium chloride should be used as a source of ionic strength. This will prevent formation of the insoluble potassium salt of SDS[13] which, if in suspension, could give rise to significant scattering and so interfere with the QELS experiment.

[1]H. Z. Cummins and H. C. Swinney, in Prog. Opt. 8, 135 (1970).
[2]A. F. Schick and S. J. Singer, J. Phys. Chem. 54, 1028 (1950)
[3]T. A. King, A. Knox, and J. D. G. McAdam, Polymer 14, 293 (1973).
[4]P. N. Pusey, J. M. Vaughan, and G. Williams, J. Chem. Soc. Faraday Trans. 11, 1696 (1974).
[5]D. Bailey, T. A. King, and D. N. Pinder, Chem. Phys. 12, 161 (1976).
[6]S. Alpert and G. Banks, Biophys. Chem. 4, 287 (1976).
[7]G. D. J. Phillies, G. B. Benedek, and N. A. Mazer, J. Chem. Phys. 65, 1883 (1976).
[8]P. N. Pusey, D. E. Koppel, D. W. Schaefer, R. D. Camerini-Otero, and S. Y. Koenig, Biochemistry 13, 952 (1974).
[9]D. E. Koppel, J. Chem. Phys. 57, 4814 (1972).
[10]G. Rehage, O. Ernst, and J. Furmann, Discuss. Faraday Soc. 49, 208 (1970).
[11]J. Roots, B. Nystrom, L. Sundelofand, and B. Porsch, Polymer 20, 337 (1979).
[12]K. H. Keller, E. R. Canales, and S. I. Yum, J. Phys. Chem. 75, 379 (1971).
[13]M. Champagne, J. Chim. Phys. Phys. Chim. Biol. 54, 378 (1957); 54, 393 (1957).
[14]J. F. Foster, in *The Plasma Proteins*, edited by Frank W. Putman (Academic, New York, 1960).
[15]J. L. Anderson, F. Rauth, and A. Morales, J. Phys. Chem. 82, 608 (1978).
[16]R. C. O'Driscoll and D. N. Pinder, J. Phys. E 13, 192 (1980). Also, for application of the dust rejection scheme to the solutions in this work see C. M. Trotter, Ph. D. Thesis, Massey University (1980).
[17]J. C. Brown, P. N. Pusey, J. W. Goodwin, and R. H. O'Hewill, J. Phys. A 8, 664 (1975).
[18]P. S. Dalburg, A. Boe, K. A. Strand, and T. Sikkeland, J. Chem. Phys. 69, 5473 (1978).
[19]P. C. Colby, L. M. Narducci, V. Bluemel, and J. Baer, Phys. Rev. A 12, 1530 (1975).
[20]A. Boe and T. Sikkeland, Phys. Rev. A 16, 2051 (1977).
[21]C. M. Sorenson, R. C. Mockler, and W. J. O'Sullivan, Phys. Rev. A 16, 365 (1977).
[22]P. N. Pusey, J. Phys. A 11, 119 (1978).
[23]B. Chu, D. Thiel, W. Tscharnuter, and D. V. Fenby, J. Phys. (Paris) Suppl. 33, 111 (1972).
[24]D. L. Ermak, J. Chem. Phys. 62, 4189 (1975); 62, 4197 (1975).
[25]*Polymer Handbook*, edited by J. Brandrup and E. H. Immergut (Wiley-Interscience, London,
[26]S. P. Lee, W. Tscharnuter, and B. Chu, J. Polym. Sci. 10, 2453 (1972).
[27]D. J. Shaw, *Introduction to Colloid and Surface Chemistry* (Butterworths, London, 1970), 2nd edition.
[28]J. L. Anderson and C. C. Reed, J. Chem. Phys. 64, 3240 (1976); 64, 4336 (1976).
[29]G. K. Batchelor, J. Fluid Mech. 74, 1 (1976).
[30]R. Hogg, T. W. Healy, and D. W. Fuerstenau, Trans. Faraday Soc. 62, 1638 (1966).
[31]K. J. Mysels, *Introduction to Colloid Chemistry* (Wiley-Interscience, London, 1959).
[32]D. Stigter and T. L. Hill, J. Phys. Chem. 63, 551 (1959).
[33]N. E. Hoskin, Trans. Faraday Soc. 49, 1471 (1953).
[34]E. J. W. Verwey and J. Th. G. Overbeek, *Theory of the Stability of Lyophobic Colloids* (Elsevier, Amsterdam, 1948).
[35]D. W. Schaefer and B. J. Berne, Phys. Rev. Lett. 32, 1110 (1974).
[36]H. J. Van der Hull and J. W. Vanderhoff, J. Colloid Interface Sci. 28, 336 (1968).
[37]J. L. Anderson (private communication).
[38]R. G. Kitchen, B. N. Preston, and J. D. Wells, J. Polym. Sci. Symp. 55, 39 (1976).
[39]Although Kitchen *et al.* have not reported the *p*H at which measurements were made, they have taken thermodynamic data from Scatchard *et al.* (Ref. 41) corresponding to a *p*H of ~5.4 and so it is assumed that this is the *p*H at which experiments were conducted.
[40]P. A. Charlwood and A. Ens, Can. J. Chem. 35, 99 (1957).
[41]G. Scatchard, A. C. Batchelder, and A. Brown, J. Am. Chem. Soc. 68, 2315 (1946); 68, 2320 (1946).
[42]G. D. J. Phillies, J. Chem. Phys. 62, 3925 (1975).
[43]L. P. Nelles and J. R. Bamburg, Anal. Biochem. 73, 524 (1976).

BIBLIOGRAPHY

1. J. E. Tanner, Ph.D. dissertation, Department of Chemistry, University of Winsconsin (1966) .

2. E. von Meerwall, D. D. Burgan and R.D. Ferguson, J. Magn. Reson.34, 339 (1979).

3. P. G. de Gennes, Macromolecules. 9, 594 (1976).

4. C. Tanford, Physical Chemistry of Macromolecules. (Wiley and Sons, New York, 1961).

5. H. Yamakawa, Modern Theory of Polymer Solutions. (Harper and Row, New York, 1971).

6. E.O. Stejaskal and J. E. Tanner, J. Chem. Phys. 42, 288 (1965).

7. H. Hervet, L. Leger and F. Rondelez, Phys. Rev. Letts. 42, 1681 (1979).

8. H. Z. Cummins, N. Knable and Y. Yeh, Phys. Rev. Letts. 12, 150 (1964).

9. J. Roots, B. Nystrom, L. O. Sundelof and B. Porsch, Polymer. 20, 337 (1979).

10. P.N. Pusey, J. M. Vaughan and G. Williams, J. Chem. Soc. Faraday Trans. 11, 1969 (1974).

11. D. Bailey, T. A. King and D. N. Pinder, J. Phys. 12, 161 (1976).

12. G. Rehage, O. Ernst and J. Fuhrmann, Disc. Faraday Soc. 49, 208(1970).

13. G. D. J. Phillies, G. B. Benedek and N. A. Mazer, J. Chem. Phys. 65, 1883 (1976).

14. K. H. Keller, E. R. Canales and Su Il Yum, J. Phys. Chem. 75, 379 (1971).

15. J. F. Foster in The Plasma Proteins. (Edited by J.W. Putman, Academic Press, New York, 1960).

16. J. S. Murday, J. Magn. Reson. 10, 111(1973).

17. K. R. Harris, R. Mills, P. J. Back and D. S. Webster, J. Magn, Reson. 29, 473 (1978).

18. R. Pecora, J. Chem. Phys. 40, 1604 (1964).

19. L. van Hove, Phys. Rev. 95, 249 (1954).

20. A. T. Forrester, J. Opt. Soc. Am. 51, 253 (1961).

21. A. Javan, W. R. Bennett and D. R. Herriot, Phys. Rev. Letts. 6, 106 (1961).

22. H. Z. Cummins, N. Knable and Y. Yeh, Phys. Rev. Letts. 12, 150 (1964).

23. E. Jakeman and E. R. Pike, J. Phys. A. 2, 411 (1969). See references in articles by E. Jakeman, and E. R. Pike, in Photon Correlation and Light Beating Spectroscopy. (Edited by H. Z. Cummins and E. R. Pike, Plenum Press, New York, 1974).

24. D. E. Koppel, J. Appl. Phys. 42, 3216 (1971).

25. D. E. Koppel , J. Chem. Phys. 57, 4814 (1972).

26. J. C. Brown, P. N. Pusey and R. Dietz, J. Chem. Phys. 62, 1136 (1975).

27. B. Chu, Laser Light Scattering. (Academic Press, New York, 1974).

28. B. J. Berne and R. Pecora, Dynamic Light Scattering. J. Wiley and Sons, New York (1976).

29. P. N. Pusey, D. E. Koppel, D. W. Schafer, R. D. Camerini-Otero and S. H. Koenig, Biochemistry. 13, 4171 (1974).

30. R. Foord, E. Jakeman, C. J. Oliver, E. R. Pike, R. J. Blagrove, E. Wood and A. R. Peacocke, Nature. 227, 242 (1970).

31. L. Mandel and E. Wolf, Rev. Mod. Phys. 37, 231 (1965).

32. C. J. Oliver in Photon Correlation and Light Beating Spectroscopy. (Edited by H. Z. Cummins and E. R. Pike, Plenum Press, New York, 1974).

33. J. H. Van Vleck and D. Middleton, Proc. IEEE. 54, 2 (1966).

34. If T becomes comparable to the coherence time of the scattered intensity, the NIAF ceases to yield information regarding the intensity fluctuations. See also reference 23.

35. E. Jakeman, E. R. Pike and S. Swain, J. Phys. A. 4, 517 (1971).

36. P. G. Guest, Numerical Methods of Curve Fitting. (Cambridge University Press, 1961).

37. R. C. O'Driscoll and D. N. Pinder, J. Phys. E. 13, 192 (1980).

38. R. C. O'Driscoll, J. Phys. E. 13 (in press).

39. A. Abragam, The Principles of Nuclear Magnetism. (Clarendon Press, Oxford, 1961).

40. F. Bloch, W. W. Hansen and M. Packard, Phys. Rev. 70, 474 (1964).

41. E. Hahn, Phys. Rev. 80, 580 (1950).

42. H. Y. Carr and E. M. Purcell, Phys. Rev. 94, 630 (1954).

43. E. O. Stejskal and J. E. Tanner, J. Chem. Phys. 42, 288 (1965).

44. J. E. Tanner, Kang-Jen Liu and J. E. Anderson, Macromolecules. 4, 586 (1971).

45. P. T. Callaghan. Private Communication.

46. J. E. Tanner, Rev. Sci. Instrum. 36, 1086 (1965).

47. D. S. Webster and K. H. Marsden, Rev. Sci. Instrum. 45, 1232 (1974).

48. R. Mills, J. Phys. Chem. 77, 687 (1973).

49. K. R. Harris, C. K. N. Pua and P. J. Dunlop, J. Phys. Chem., 3524 (1970).

50. L. G. Longsworth, J. Phys. Chem. 64, 1914 (1960).

51. W. A. Clark and J. A. McNeil, Rev. Sci. Instrum. 44, 844 (1973).

52. J. Lowe and C. E. Tarr, J. Phys. E. 1, 320 (1968).

53. W. A. Anderson, Rev. Sci. Instrum. 32, 241 (1961).

54. G. Odberg and L. Odberg, J. Magn. Reson. 16, 342 (1974).

55. H. D. Kipnich, R. Esche and W. Maurer, J. Magn. Reson. 22, 161 (1976).

56. I. S. Grant and W. R. Phillips, Electromagnetism. (J. Wiley and Sons, New York, 1975).

57. Motorola Linear Integrated Circuits Handbook, 6, 8-332 (1975).

58. G. B. Matson, Rev. Sci. Instrum. 43, 1504 (1971).

59. C. Bell, T. Cosgrove and R. F. Warren, J. Phys. E. 7, 969 (1974) This power supply has adequate frequency response and current regulation, but suffers from some restrictuions on allowable pulse widths and spacings.

60. T. C. Farrar and E. D. Becker, Pulse and Fourier Transform NMR. (Academic Press, New York, 1971).

61. D. J. Tomlinson, Mol. Phys. 25, 735 (1972).

62. P. T. Callaghan, C. M. Trotter and K. W. Jolley, J. Magn. Reson. 37, 247 (1980).

63. L. Odberg, K. Goffloo and J. Schlegal,Chemica Scripta. 4, 107 (1973).

64. T. A. King, A. Knox and J. D. C. McAdam, Polymer. 14, 293 (1973).

65. J. Harvey, Auckland University, N.Z. - private Communication.

66. M. Adams and M. Delsanti, Macromolecules. 10, 1226 (1977).

67. A. F. Schick and S. J. Singer, J. Phys. Chem. 54, 1028 (1950).

68. S. F. Edwards, Proc. Phys. Soc. 88, 265 (1966).

69. R. G. Kitchen, B. N. Preston and J. D. Wells, J. Polym. Sci. Symp. 55, 39 (1976).

70. P. N. Pusey, J. Phys. A. 11, 119 (1978).

71. J. L. Anderson, F. Rauth and A. Morales, J. Phys. Chem. 82, 608 (1978).

72. J. C. Brown, P. N. Pusey, J. W. Goodwin and R. H. Ottewill, J. Phys. A. 8, 664 (1975).

73. P. S. Dalburg, A. Boe, K. A. Strand and T. Sikkeland, J. Chem. Phys. 69, 5473 (1978).

74. L. P. Nelles and R. Bamburg, Anal. Biochem. 73, 524 (1976).

75. P. C. Colby, L. M. Narducci, V. Bluemel and J. Baer, Phys. Rev. A. 12, 1530 (1975).

76. A. Boe and T. Sikkeland, Phys. Rev. A. 16, 2105 (1977).

77. C. M. Sorenson, R. C. Mockler and W. J. O'Sullivan, Phys. Rev. A. 16, 365 (1977).

78. B. Chu, D. Thiel, W. Tscharnuter and D. V. Fenby, J. Phys. (Paris) Suppl. 33, 111 (1972).

79. D. L. Ermak, J. Chem. Phys. 62, 4189 (1975), J. Chem. Phys. 62, 4197 (1975) .

80. Polymer Handbook. (Edited by J. Brandrup and E. H. Immergut, Wiley Interscience, London, 1974).

81. S. P. Lee, W. Tscharnuter and B. Chu, J. Polym. Sci. 10, 2453 (1972).

82. J. L. Anderson and C. C. Reed, J. Chem. Phys. 64, 3240 (1976); J. Chem. Phys. 64, 4336 (1976).

83. G. K. Batchelor, J. Fluid. Mech. 74, 1 (1976).

84. R. Hogg, T. W. Healy and D. W. Fuerstenau, Trans. Faraday Soc, 62, 1638 (1966).

85. K. J. Mysels, Introduction to Colloid Chemistry. (Wiley-Interscience, London, 1959).

86. D. Stigter and T. L. Hill, J. Phys. Chem. 63, 551 (1959).

87. E. J. W. Verwey and J. Th. G. Overbeek, Theory of the Stability of Lyophobic Colloids. (Elsevier-Amsterdam, 1948).

88. N. E. Hoskin, Trans. Faraday Soc. 49, 1471 (1953).

89. H. J. Van der Hull and J. W. Vanderhoff, J. Colloid. Interface Sci. 28, 336 (1968).

90. D. J. Shaw, Introduction to Colloid and Surface Chemistry. (2nd Edn., Butterworths, London, 1970).

91. J. L. Anderson, Carnegie - Mellon University, Pittsburgh, U.S.A.- private communication.

92. Although Kitchen et al. have not reported the pH at which measurements were made, they have taken thermodynamic data from Scatchard et al. (ref.94) corresponding to a pH of ~5.4 and so it is assumed that this is the pH at which experiments were conducted.

93. P. A. Charlwood and A. Ens, Can. J. Chem. 35, 99 (1957).

94. G. Scatchard, A. C. Batchelder and A. Brown, J. Am. Chem. Soc. 68, 2315 (1946); J. Am. Chem. Soc. 68, 2320 (1946).

95. G. D. J. Phillies, J. Chem. Phys. 62, 3925 (1975).

96. F. Brochard and P.G. de Gennes, Macromolecules 10, 1157 (1977).

97. J. Roots and B. Nystrom, Polymer. 20, 148 (1979).